CRUST AND UPPER MANTLE STRUCTURE

OF

THE NORTHEASTERN UNITED STATES

by

Steven R. Taylor

B.S., Ohio University, Athens, Ohio

(1975)

SUBMITTED IN PARTIAL FULFILLMENT

OF THE REQUIREMENTS FOR THE DEGREE OF

DOCTOR OF PHILOSOPHY

at the

May, 1980

Signature of Author.....
Department of Earth and Planetary Sciences
May 1980

Certified by.....
Thesis Supervisor

Accepted by.....
Chairman, Departmental Committee on Graduate Students

CRUST AND UPPER MANTLE STRUCTURE

OF

THE NORTHEASTERN UNITED STATES

by

Steven R. Taylor

Submitted to the Department of Earth and Planetary Sciences on May 9, 1980, in partial fulfillment of the requirements for the degree of Doctor of Philosophy

ABSTRACT

Recognition that mountain belts are places where oceans have closed implies that continental structure differs across them. Using the northeastern United States (NEUS) seismic network, it is shown that this applies to the northern Appalachians by investigating the crustal structure of the Precambrian Grenville Province in New York state and the New England Paleozoic Appalachian Province. The crust and upper mantle structure of the NEUS is studied by combining teleseismic and regional body wave observations with surface wave dispersion measurements.

The velocity models suggest that structures down to possibly 200 km and greater can be correlated with surficial geologic and tectonic features and that the two orogenic belts show marked differences in crustal structure. This has the important implication that major orogenic belts have effects that reach well into the lithosphere which are stable for extended periods of time, perhaps as long as 1 b.y.

Regional travel times recorded across the NEUS seismic network indicate that the northern Appalachians are characterized by a well-defined two layer crust, with a relatively high velocity lower layer. The upper crustal layer, approximately 15 km thick with P and S velocities of 6.1 and 3.6 km/s, respectively, overlies a high velocity lower crust with P and S velocities of 7.0 and 4.1 km/s. The average crustal thickness is approximately 40 km. The crust of the Grenville Province is vertically homogeneous with nearly constant P and S velocities of 6.6 and 3.7 km/s, respectively, and an average crustal thickness of 37 km.

Analysis of Rayleigh wave phase and group velocities yields structural models that are relatively consistent with the models derived from regional travel times. A method for calculating interstation phase and group velocities from the interstation transfer function using Wiener deconvolution is

presented. The Rayleigh wave phase and group velocities along different paths are inverted simultaneously using a maximum-likelihood technique. Phase and group velocities are also calculated across the MIT short-period network in southeastern New England by estimating the frequency-wavenumber power spectra.

Lateral variations in structure are studied using time term analysis and teleseismic P wave residuals. A region of thick or low-velocity crust trends northeast across eastern New York, western Massachusetts, southeast Vermont, central New Hampshire, and central Maine. In eastern New York this zone correlates with Bouguer gravity lows and with the Taconic klippen; a thick pile of thrusts emplaced during the mid-Ordovician Taconic orogeny. The crustal thickening beneath central New England correlates well with Bouguer gravity lows and is found in the region of highest topography indicating an isostatically compensated highland area.

The suture between the Grenville and Appalachian Province in the NEUS probably occurs along a north-northeast trending belt extending from northwestern Vermont to southwestern Connecticut. High crustal velocities and/or crustal thinning, a linear gravity high, a serpentinite belt, Precambrian uplifts, and the Taconic thrusts are found along much of this belt which shows many similarities to the Ivera zone in northern Italy.

There is also the possibility of a second suture located in the eastern section of the study area separating the central orogenic belt from an eastern block (Avalonia). Refraction models, and Pn and teleseismic P wave residuals indicate that the crust of the eastern block is probably thinner than that of the central belt and may be missing the high velocity lower crustal layer. In eastern Massachusetts, these two regions are separated by prominent fault zones across which no formations can be traced.

Three-dimensional inversion of teleseismic P wave residuals indicates that a relatively low velocity anomaly extending to depths in excess of 200 km and dipping to the northwest shows a spatial correlation with the Bronson Hill - Boundary Mountains Anticlinorium in central New Hampshire and Maine. These structures occupy the sites of a complex series of island arc sequences last active in Early Devonian time prior to the Acadian orogeny. This low-velocity region may represent subducted oceanic lithosphere which has undergone post-orogenic radioactive heating. Alternatively, the oceanic lithosphere may have been totally subducted resulting in lower velocity material filling the vacated Benioff zone.

The observed differences in crustal structure between the Grenville and Appalachian Provinces are probably the result in variations of petrology, chemistry, water content, temperature, and tectonic evolution. Comparison of seismic velocities with resistivity measurements suggests that the lower crust of the Grenville Province may be composed of

rocks with hydrous mineral phases resulting in lowered velocities and a higher Poisson's ratio. Alternatively, the rocks of the lower crust beneath the Grenville Province may be similar to those found on the surface while higher velocity, mafic mineralogies are prevalent in the lower crust of the Appalachians. This is consistent with the hypothesis that the Grenville crust underwent substantial reactivation, thickened, and became vertically uniform during the Grenville orogeny. In contrast, the rocks of the Appalachian belt probably were associated with a cycle of oceanic opening and closure which suggests an ensimatic origin of the lower crust in this region.

Thesis Advisor: M. Nafi Toksöz
Professor of Geophysics

ACKNOWLEDGEMENTS

The old adage "giving the tie off ones neck" literally applies to my advisor M. Nafi Toksoz who gave me a tremendous amount of help and support over the years. His insight for identifying interesting geophysical problems and defining ways to solve them made things much easier for me. I will remain indebted to Nafi.

Ed Chiburis of Weston Observatory at Boston College and Yash Aggarwal, Mary Golisano, and Lynn Sykes of Lamont-Doherty Geological Observatory freely provided short period data used in many aspects of this thesis. Many geological discussions with B. C. Burchfiel, Pat Barosh, and Frank Spear are also greatly appreciated.

My fellow partners-in-crime kept my spirits up and aided me in all aspects of my work. My fuzzy-faced office-mate Michael Clair Fehler demonstrated to me that a person can finish a thesis at M.I.T. without becoming a babbling idiot. MCF is a real star, and although he specialized in the more sensual aspects of geophysics such as the study of jerky and wet cracks, and hot dry rocks, he would always take time to listen to my problems, then say something like "You don't know that? It's simply the correspondence principle." and then set me straight. I'll always miss his stern over-the-glasses looks, his funny accent, his binoculars, and his stink executive command. Arthur C. H. Cheng, the man of many talents, can tell you about dominant diagonal

matrices and the lie of Rick Middleton's hockey stick in the same breath (unless he's reading the sports page...in which case he won't tell you anything.) Although George Zandt stinks and can't tell the difference between a phone line glitch and a deep earthquake (both have a high apparent velocity), I hope that our continued search for mysterious blocks in the lithosphere and resurgent domes causes us to cross paths. Clifford H. Thurber, my theoretical-type office-mate, sits over there at his desk and continues to frustrate me with his efficency. His programs work the first time, he write lots of papers on every different topic in geophysics, and he continues to maintain a healthy attitude on life. Never once did he give me a hard time for stealing cookies out of his desk drawer.

Norm Burr, Bill Ellsworth, and Randy Richardson were a major influence during my formative years at M.I.T. Norm introduced me to the wonders of computer hacking, to LLL, and most importantly to Hilltop Steak House. Bill sort of took me under his wing and helped with 3-D inversions and told me "Yes, Steve there is a U Lambda V-transpose". Without intending to, Randy convinced me to let somebody else figure out the state of stress in the lithosphere.

In later years, I had fun and interesting discussions along the way with John Nabelek, Jay Pulli, Jim Muller, Albert Hsui, Sean Solomon, Wai Ying Chung, Gerardo Suarez, Mike Chaplin, Rob Comer, and Mark Willis. I also highly recommend drinking and giggling with Steve Roecker,

especially on a mountain.

Of course, I shan't forget my stellar seismology students, Roger Buck, Ken Tubman, Rob Stewart, Dan Davis, Lynn Hall, and all the others. Ken Tubman also provided much input into the surface wave analysis and good old RB kept my ego pumped up. These guys are all going to be superstars.

There are also the "real" people scattered about the fifth floor. Sara Brydges seemed to be doing me favors everytime I turned around and in addition to everything else, helped me keep up on local gossip. George Keough, Al Taylor, and Dave Johnston provided much assistance with the maintenance and operation of the M.I.T seismic network. Then there's always the other two crazies at the end of the hall, Judy Roos and Sharyn Belk.

Of course, none of this would have been possible without the love, help, and support from both sets of my parents, my sister-ugly who sent me funny rocks from the Canadian Rockies, and the rest of the Goff family.

Pino's Pizza (End your quest, at Pino's you've found the best) supplied me with my weekly grease quota.

And without getting mushy, I thank Heather for everything.

This research was supported by the Nuclear Regulatory Commission contract NRC-04-76-209 and the Advanced Research Projects Agency, monitored by the Air Force office of Scientific Research under contract F44620-75-C-0064.

TABLE OF CONTENTS

PAGE

CHAPTER 1

INTRODUCTION

With the northeastern United States (NEUS) seismic network in operation since 1975, it became possible to investigate for the first time the crust and upper mantle structure of the Precambrian Grenville Province in New York state and the New England Paleozoic Appalachian Province. The region under study in this thesis is actually one small segment of an impressive Paleozoic mountain chain that extends at least 3,000 km from the southeastern United States through New England and into Newfoundland.

The tectonic history of ancient mountain belts is usually interpreted in terms of the reigning evolutionary models for neo-tectonic belts such as the Himalayas, the Alps, or the Zagros. However, the geology and geophysics of older mountain belts is often known in great detail and it is difficult to formulate even a simple first order evolutionary model because of the numerous complications encountered. Ancient orogenic belts represent deeply eroded cores of more recent mountain chains and detailed geologic and geophysical studies of these older belts such as the Appalachians should provide important constraints for interpreting the younger belts.

Many of the geologic, tectonic, and geophysical problems

associated with the northern Appalachians were discussed at the Zen-Zietz Penrose Conference of the Geological Society of America in 1972, and are summarized by Zietz and Zen (1973). During the conference, it became clear that detailed seismic work would be necessary to aid in solving geologic and tectonic problems. A detailed seismic refraction survey was judged to be too expensive.

> "Without it, however, calculations based on gravity data are too unconstrained to lead to much more than inconclusive speculation. Lynn Sykes suggested that some of the desired information on velocity structure might be obtained at vastly less cost by a long-term program of earthquake observations using arrays of geophones linked by telephone; this suggestion seemed to arouse much interest, although in the core area, because of the convergence of phyical properties (largely through metamorphism and intrusion) of the supracrustal rocks and the basement, one may doubt that remote physical measurements could lead to reasonable discrimination of these rocks.
>
> Cross-sections extending to the base of the crust and preferably lower, are, nonetheless, a potentially profitable meeting ground for geologists and geophysicists because these sections help to define the geometric problems of a foldbelt. Geologists can use structural,

> lithologic, and metamorphic data obtained at the surface to predict geologic conditions several kilometers below the surface and to reconstruct physical conditions of the past, including such things as the structure and volume of rocks now eroded and estimates of crustal shortening. Geophysicists can give important assistance to some types of downward projection in the near-surface environment and can provide almost the only information available for deeper parts of the crust and mantle."

The above quote taken from Zietz and Zen (1973) summarizes some of the goals of this thesis; i.e. to collect body and surface wave data from a regional seismic network, derive a structural model, and interpret the model in terms of geologic and other geophysical information.

Chapter 2 is mainly a literature review summarizing the geologic setting of New England and other relevant geophysical observations such as seismic, gravity, magnetic, heat flow, and electrical measurements.

In Chapter 3, refraction profiles from timed quarry blasts are first presented and contrasts between the Precambrian Grenville Province in New York State and the Paleozoic Appalachian Province are explored using travel times from regional earthquakes recorded by the NEUS network. Lateral variations in structure across the NEUS are then analyzed by a time term analysis of the Pn branch

of the travel time curve. The last section in Chapter 3 compares the derived velocity models with other models from both the northern and southern Appalachians.

Surface wave dispersion measurements are presented in Chapter 4 for a number of different paths across northeastern North America. Interstation phase and group velocities are measured from the interstation transfer function which is calculated using Wiener deconvolution. Rayleigh wave phase and group velocities are also measured across the MIT short-period seismic network from the frequency-wavenumber power spectra. For each path, the observed phase and group velocities are inverted simultaneously using a maximum-likelihood technique in order to derive a shear velocity with depth profile.

In Chapter 5, teleseismic P wave residuals recorded across the NEUS seismic network are analyzed to determine lateral variations in crust and upper mantle structure beneath the region. The residuals are compared with gravity and the time term observations and a three-dimensional model for the crust and upper mantle is presented using the technique of Aki et al., (1977).

In Chapter 6, the results from previous chapters are first summarized. Then the crust and upper mantle structure between the Grenville and Appalachian Provinces is compared in terms of variations in composition and tectonic evolution.

Contrasts in geologic and geophysical structures are then

made between the northern and southern Appalachians. The COCORP findings across the Blue Ridge and Piedmont in Georgia, North Carolina, and Tennessee have solved numerous long-standing geologic and tectonic problems in the southern Appalachians and are included in the discussion.

Finally, a first order plate tectonic model of the New England Appalachians is presented which satisfies many geologic and geophysical constraints.

CHAPTER 2

GEOLOGIC AND GEOPHYSICAL SETTING

In this chapter, the geologic setting of the northeastern United States is reviewed and a simple model for its tectonic evolution will be presented in Chapter 6. Because only regional, large-scale structures are analyzed using seismic techniques in the following chapters, the discussions are kept quite general. Then, previous geophysical studies utilizing seismic, gravity, magnetic, heat flow, and electrical techniques are reviewed.

2.1 GEOLOGIC SETTING

The northern Appalachians have undergone a long and extremely complex geological development. Table 6.1 lists major orogenic episodes in the Appalachians and the maximum manifestation in the area of influence (from Rodgers, 1970). Dating and stratigraphic correlation between regions has been complicated by numerous orogenic episodes. The northern Appalachians can be divided into three major tectonic units (Bird and Dewey, 1970; Naylor, 1975): a western belt and an eastern belt possibly representing the margins of two once convergent continental masses surround a

central orogenic belt composed mainly of eugeoclinal lithologies (Figure 2.1). The western unit is mainly underlain by rocks of the Precambrian Grenville Province which are exposed in the Adirondacks and outlying massifs such as the Green Mountains, Berkshires, and the Hudson Highlands. Unconformably overlying the Grenville basement is an Eocambrian to Cambrian platform sequence which grades upward into a Lower Ordovician clastic sequence. Found above are the Taconic klippe which consist primarily of deep-water shales, sandstones, and graywackes. Paleontological evidence suggests that they were deposited contemporaneously with the shelf sediments (Zen, 1972).

The central orogenic belt consists of a number of broad structural warps. The Connecticut Valley Synclinorium (CVS) is found to the east of the previously discussed Precambrian massifs and can be traced from Connecticut through Quebec to the Gulf of St. Lawrence. The CVS contains a thick, highly metamorphosed eugeoclinal sequence divided into two members separated by a major Middle Ordovician unconformity. A linear serpentinite belt follows the western flanks of the CVS.

East of CVS lies the Bronson Hill Anticlinorium (BHA) which consists of a chain of elliptical gneissic domes (Oliverian Plutonic series in New Hampshire). The structure can be traced from Connecticut through northern New Hampshire and is probably continuous with the Boundary Mountains Anticlinorium in Maine. Mantling the domes is a

series of mafic metavolcanics associated with felsic metavolcanics and metasediments (Ammonoosuc Volcanics in New Hampshire) of Middle Ordovician age or older (440 ± 30 m.y.; Naylor, 1975). Unconformably overlying the Ammonoosucs is a series of Silurian to Lower Devonian highly metamorphosed clastics with some carbonates and volcanics.

Eastward of the BHA lies the Merrimack Synclinorium (MS) which is a major northeast-trending tectonic feature extending from eastern Connecticut through Maine and into New Brunswick. It is the site of thick accumulations of Ordovician to Lower Devonian metasediments typically metamorphosed to sillimanite grade. These metasediments (Devonian Littleton Formation) can be correlated with Devonian strata at the top of the BHA. The MS also contains large volumes of intrusives belonging to the Middle Devonian New Hampshire Plutonic Series and the Mesozoic White Mountain Magma series.

On the eastern flank of the MS a major northeast-trending thrust belt (Clinton-Newbury, Bloody Bluff, and Lake Char Faults) extends from southern Connecticut through eastern Massachusetts (Skehan, 1969). Magnetic anomalies associated with the formations in the thrust belt suggest that the faults continue offshore in an east-northeast direction into the Gulf of Maine (Weston Geophysical, 1976; Alvord et al., 1976) and possibly into New Brunswick (Nelson, 1976). In eastern Massachusetts the northwest dipping thrusts greatly offset metamorphic isograds and no stratigraphic units can

be traced across them (P. Barosh, personal commun.). Deformation and metamorphism in the MS probably delineate a zone of maximum intensity of the Middle Devonian Acadian orogeny (Rodgers, 1970).

The Eastern Basement is exposed to the east of the above described thrust belt. These units are probably correlative with rocks of the Avalon Zone in Newfoundland and southeastern New Brunswick (Bird and Dewey, 1970; Nelson, 1976). The region in eastern Massachusetts is characterized by plutonic, metasedimentary and metavolcanic rocks metamorphosed mainly to chlorite grade ranging in age from late Precambrian to Carboniferous. Unfossiliferous strata and scattered age dating have made geologic interpretations enigmatic (Naylor, 1975; Zarrow et al., 1978). However, according to Naylor (1975), no rocks have been assigned an age greater than 650 m.y. which is significantly younger than the Grenville age rocks (1,100 m.y.) in the western belt.

2.2 GEOPHYSICAL SETTING

To date, very little seismological work pertaining to crust and mantle structure has been done in the northeastern United States. Early studies involving analysis of local earthquake data and timed quarry blasts include those by Leet (1941), Linehan (1962), Katz (1955), and Nakamura and

Howell (1964). More recently, some refraction work has been published by Chiburis and Graham (1978), Aggarwal in Schnerk et al., (1976), and Taylor and Toksoz (1979a). These studies along with other refraction models from neighboring regions are summarized in Table 3.5 and discussed in section 3.4.

Some observations have been made on teleseismic P waves recorded in the NEUS by Wu and Allen (1972) who directly measured $dT/d\Delta$ across the five original Boston College stations and by Fletcher et al., (1978), who observed teleseismic P wave residuals across the eastern U.S. and Canada. Although the study by Fletcher et al., (1978) involves readings from only a few nuclear explosions, their observations are quite similar to those discussed in Chapter 5. Early arrivals are observed for stations in the Grenville Province relative to those in the Appalachians especially for sources from the northwest.

Surface wave studies in the NEUS are limited to those by Brune and Dorman (1963), Dorman and Ewing (1962), and Taylor and Toksoz (1979b) and are consistent with refraction results and are discussed in Chapter 4.

2.2.1 GRAVITY AND MAGNETICS

Gravity and magnetic anomalies show very good correlations with geologic features in the eastern United

States. Their prominent features will be described in this section and their fit into the tectonic framework of the eastern U.S. will be discussed in Chapter 6. Detailed gravity and areomagnetic maps are available over much of the NEUS. A generalized Bouguer gravity map after Kane et al., (1972) is shown in Figure 2.2a for the NEUS and in Figure 2.2b for the eastern U.S. (Diment et al., (1972)). The prominant features observed in the regional gravity field in the NEUS are a low over the Taconic klippen in eastern New York, a low over the White Mountains in northern New Hampshire, and a northeast-trending low over the CVS in Vermont and western Maine. A north-northeast trending gravity high is found in western Connecticut, western Massachusetts, western Vermont, and into Quebec and is associated with the Precambrian uplifts and the serpentinite belt. There is also a gravity high found in the northern Adirondacks and along the Atlantic coast. As noted by Kane et al., (1972), more detailed maps show a discontinuity in regional trends where broad northeast-striking gravity elements of eastern and northern New England are separated from the more northernly-trending anomalies of western New England along a line extending from Rhode Island to north-central Vermont.

Excellent areomagnetic data is available over much of the NEUS. Because a dipolar field falls of as r^{-3} as opposed to r^{-2} for the gravity data, the magnetic anomalies are of much higher wavenumber and show a very impressive

correlation with surface geologic features (Figure 2.3). Areomagnetic data has been crutial for mapping important structural and stratigraphic contacts where they are often obscured by glacial sediments or water (Alvord et al., 1976; Weston Geophys. Res. Inc., 1976). Prominant features observed on the areomagnetic maps are the Clinton-Newbury and Bloody Bluff Fault zone in eastern Massachusetts and eastern Connecticut, rocks of the White Mountain Plutonic series, diabase dikes associated with Triassic rifting, the Oliverian domes and gneiss domes of the BHA. In general, Cambrian-Ordovician rocks such as the Nashoba Formation within the Clinton-Newbury and Bloody Bluff Fault Zone have a stronger magnetic signiture than Silurian-Devonian rocks.

2.2.2 HEAT FLOW AND RESISTIVITY

Heat flow measurements in the NEUS are few and are subject to many effects which are difficult to correct for such as climatic variations, thermal conductivity, and radiogenic heat production. Diment et al., (1972) summarizes early heat flow measurements and makes corrections for Pleistocene climatic variations (Figure 2.4). More recent measurements which include corrections for radioactivity were made by Jaupart (1979). Figure 2.4 indicates that central New England is characterized by a north-northeast trending zone of high heat flow. Although

many of these measurements are taken from highly radioactive plutons, Jaupart (1979) concludes that these trends persist after corrections for radioactivity which suggests that the anomalies may be caused by differences in mantle temperature.

Resistivity measurements in the NEUS suggest the presense of a highly conductive lower crust in the Adirondack Mountains in New York state (Connerney et al., 1979), while a resistive lower crust underlies a slightly conductive, approximately 15 km thick upper crust in New England (Kasameyer, 1974). Using geomagnetic sounding, Bailey et al., (1978) found evidence for high telluric current flow in central New England which they attributed to a 200 degree thermal anomaly and low resistivity at the base of the crust. However, the anomaly they observe may actually be caused by highly conductive formations found in the Merrimack Synclinorium such as the Brimfield Schist which contain abundant graphite and iron sulfides (T. Madden, pers. comm.).

In the next three chapters, body wave data from regional and teleseismic events and surface wave dispersion measurements will be presented. In Chapter 6, the results will be jointly interpreted with the geologic and geophysical information summarized in this chapter.

FIGURE CAPTIONS

Figure 2.1a — Generalized geologic map of northeastern United States. Modified from King (1969).

Figure 2.1b — Major tectonic structure in northeastern United States. Shaded regions correspond to sillimanite-grade metamorphic zones.

Figure 2.2a — Bouguer gravity in northeastern United States. Areas with positive gravity anomalies are shaded. Modified from Kane et al. (1972).

Figure 2.2b — Bouguer gravity in eastern United States; from Diment et al. (1972).

Figure 2.3 — Areomagnetic map of New England. Contour interval is 100 gammas.

Figure 2.4 — Heat flow corrected for Pleistocene climatic variations; from Diment et al., (1972).

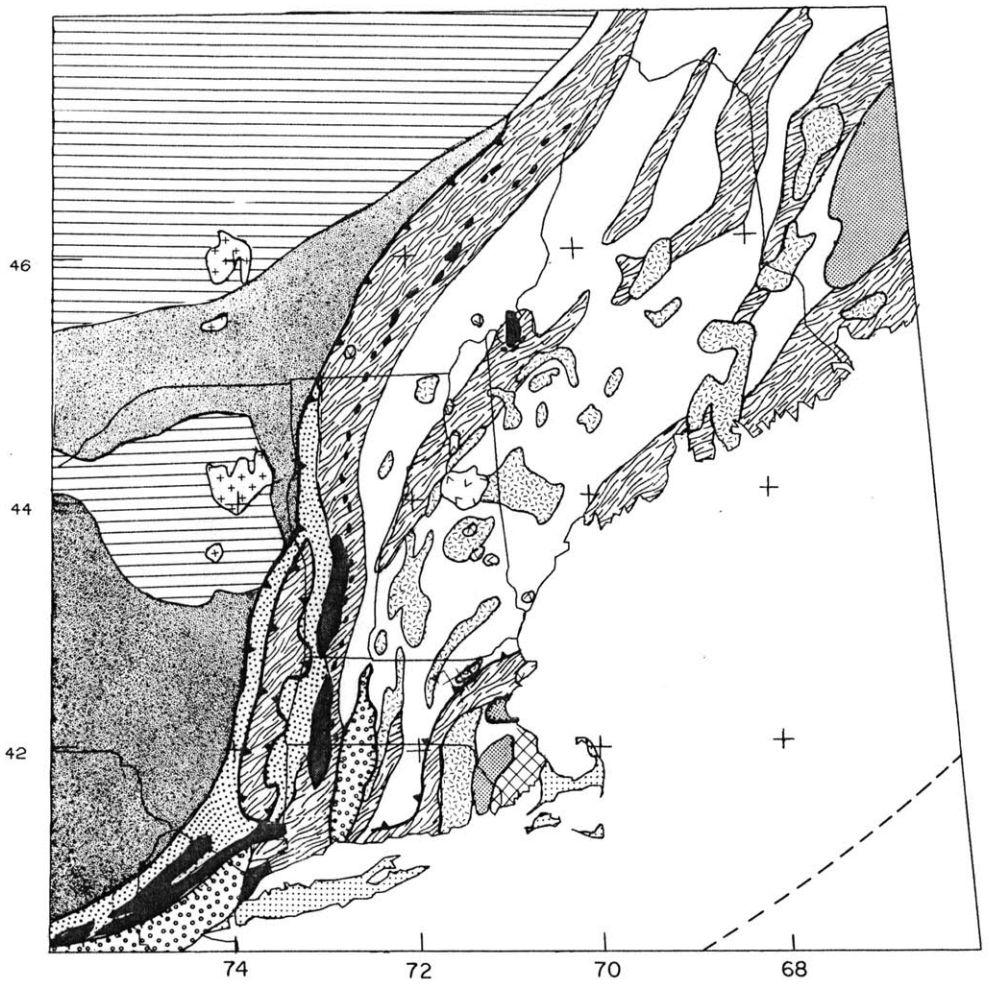

EXPLANATION

Thrust fault, barbs on upper block

Normal fault, hachures on downthrown side

STRATIFIED ROCKS

- Cenozoic glacial deposits
- Triassic red beds
- Carboniferous
- Silurian - Devonian eugeoclinal rocks
- Cambrian - Ordovician foreland rocks
- Cambrian - Ordovician deformed miogeoclinal rocks
- Cambrian - Ordovician eugeoclinal rocks
- Precambrian rocks of the eastern block
- Precambrian uplifts, Grenville basement
- Precambrian Grenville basement

IGNEOUS ROCKS

- Mesozoic White Mountain Plutonic Series
- Devonian New Hampshire Plutonic Series
- Cambrian - Ordovician serpentinites, ultramafics
- Precambrian anorthosites

Figure 2.1a

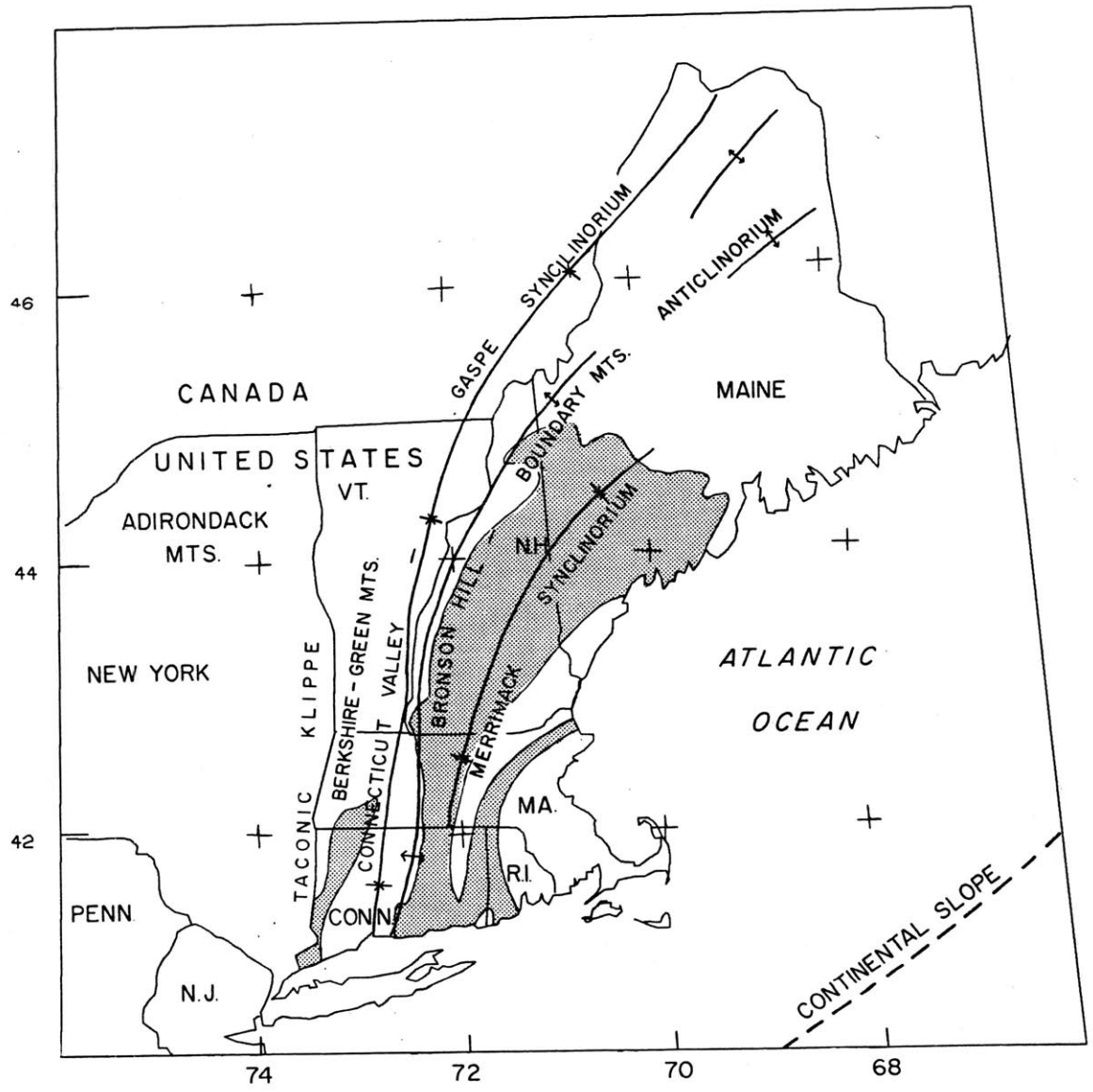
CANADA
UNITED STATES
VT.
ADIRONDACK MTS.
NEW YORK
PENN.
N.J.
MAINE
N.H.
MA.
R.I.
CONN.
ATLANTIC OCEAN
GASPE SYNCLINORIUM
ANTICLINORIUM
BOUNDARY MTS.
BRONSON HILL
MERRIMACK SYNCLINORIUM
CONNECTICUT VALLEY
BERKSHIRE - GREEN MTS.
KLIPPE
TACONIC
CONTINENTAL SLOPE
46
44
42
74
72
70
68

Figure 2.1b

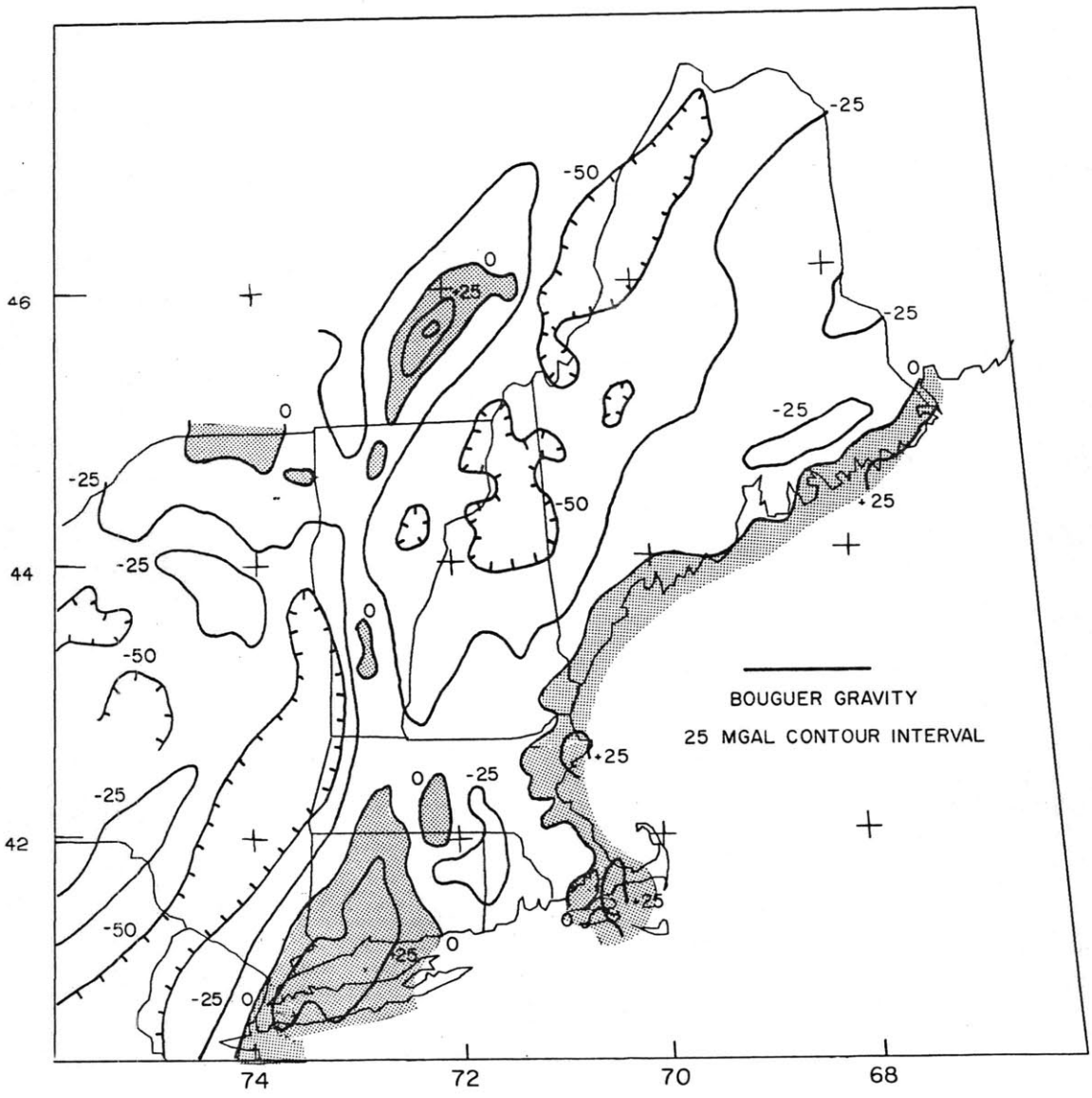
46
44
42
74
72
70
68
-25
-50
0
+25
BOUGUER GRAVITY
25 MGAL CONTOUR INTERVAL

Figure 2.2a

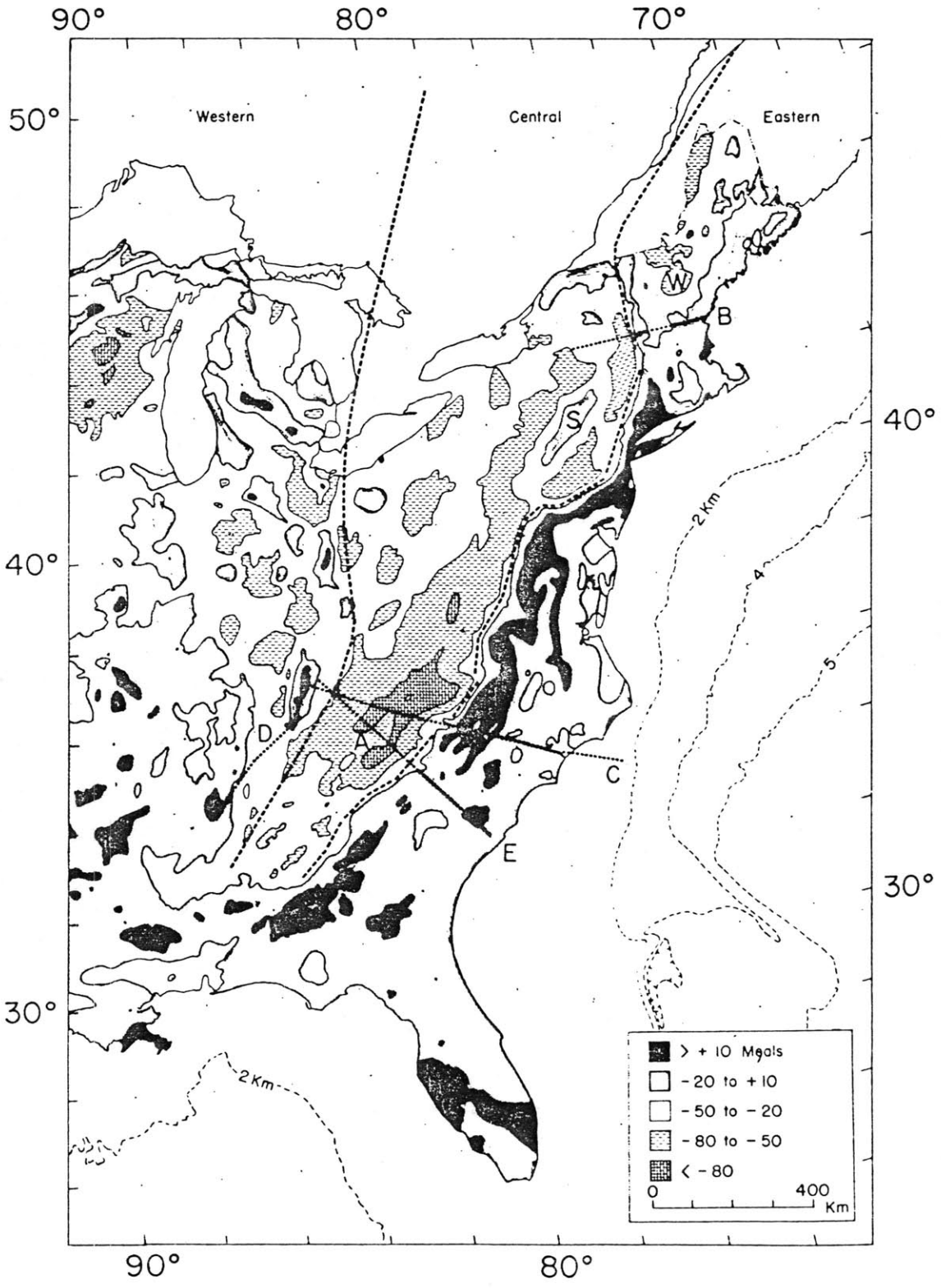
90°
80°
70°
50°
40°
30°
Western
Central
Eastern
W
B
S
A
D
C
E
2 Km
4
5
> + 10 Meals
- 20 to + 10
- 50 to - 20
- 80 to - 50
< - 80
0
400
Km

Figure 2.2b

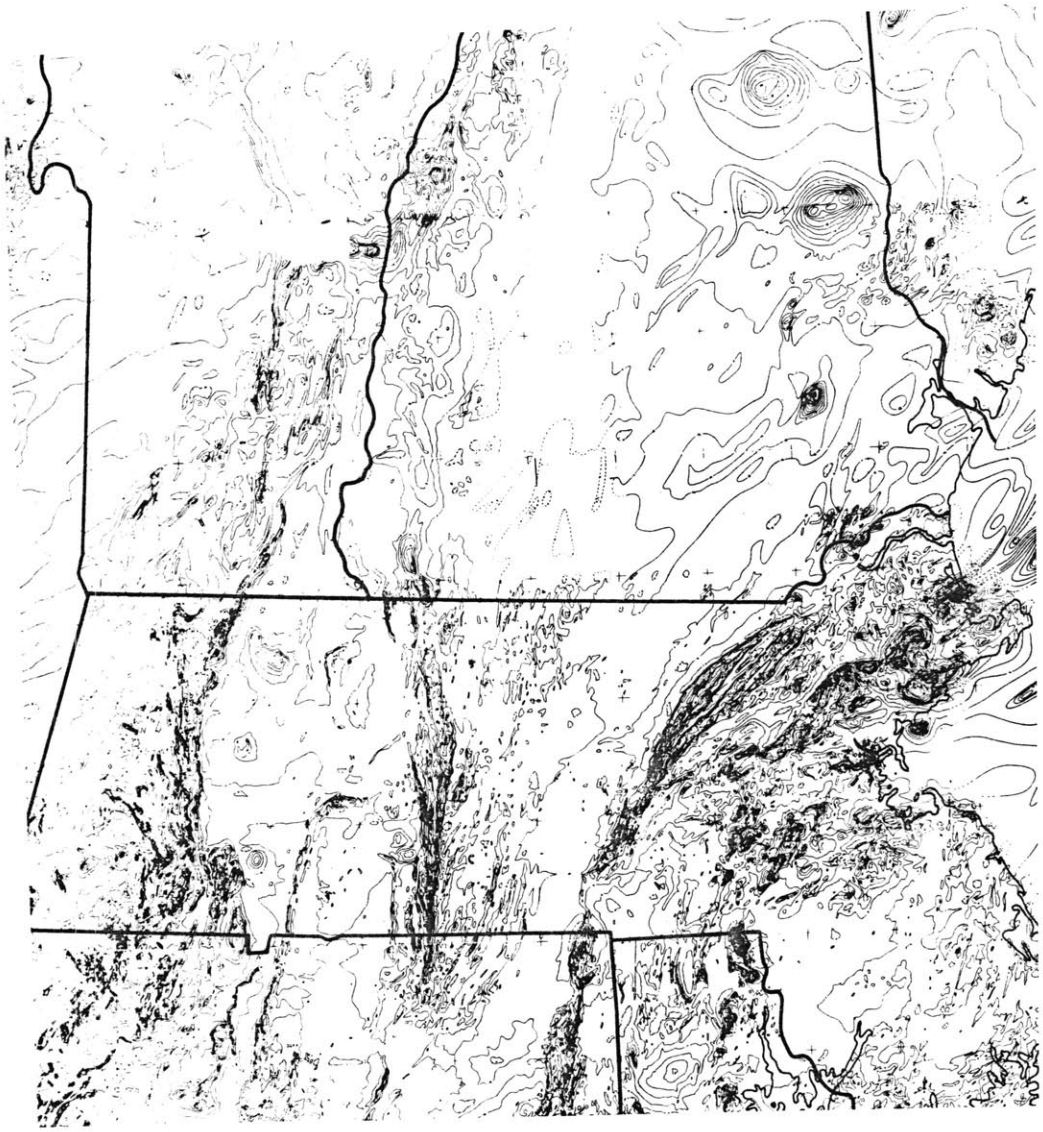

Figure 2.3

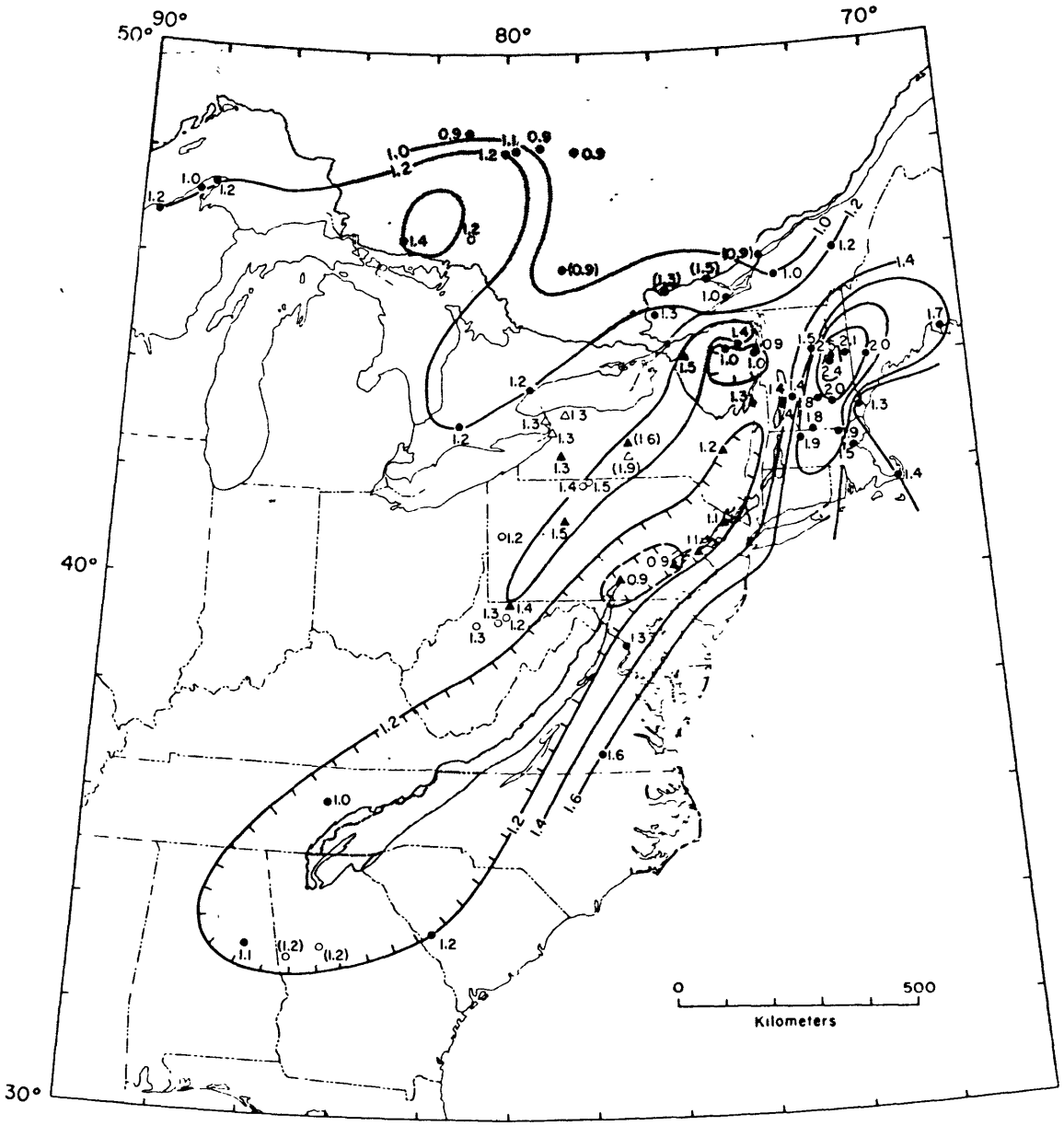

Figure 2.4

CHAPTER 3

CRUSTAL STRUCTURE FROM REGIONAL TRAVEL TIMES

Analysis of travel times from quarry blasts and earthquakes in the northeastern United States have been limited in scope and have yielded inconsistent results, indicating the complicated structure in the region. Leet (1941) and Linehan (1962) published early results in New England using data from regional earthquakes recorded on a small network. Katz (1955) published refraction results in New York State from interpretation of a few timed quarry blasts recorded along linear arrays. More recently, some refraction work has been reported by Chiburis and Graham (1978), Aggarwal (in Schnerk et al., 1976), and Taylor and Toksoz (1979).

In this chapter, results from timed quarry blasts are presented using data from portable stations and the NEUS seismic network. Average compressional and shear wave velocity structure using regional earthquakes are derived using data from the NEUS network, and lateral variations in structure are studied by performing a time term analysis of the Pn travel time branch. Finally, the results are contrasted with other travel time studies in other portions of the Appalachians and eastern North America.

3.1 STRUCTURE FROM MEASURED QUARRY BLASTS

Ten quarry blasts have been timed in New England and Canada and recorded on both portable and permanent seismic stations. The blasts and stations used are shown in Figure 3.1, and the origin times, and blast locations are listed in Table 3.1. About half of the blasts were located in southern New England, and the rest in the large, open pit asbestoes mines in Quebec. Three shots were also recorded in Vermont.

Instruments used both for collecting origin times and as portable stations consisted of Sprengnether MEQ-800's recording on smoked paper drums, and USGS J-302 VCO's recording FM signals on cassette tapes. Drum recordings were made with a speed of 240 mm/min where reading precision for sharp arrivals has a standard error of about 0.05 sec. The cassette recordings could be discrimminated and played back at very high speeds (3 cm/s or greater) and reading precision is on the order of a few milliseconds. For these readings, accuracy was limited by the drift of the crystal oscillator clock, whose timing corrections were less than 20 ms/day, and the impulsiveness of the signal.

The quarry and roadcut blasts ranged in size from approximately 5,000-20,000 kg. Shot configurations were generally an array of 40-200 drillholes, each 15-20 m deep and 8-10 cm in diameter. The delay time along the string was up to 0.5 sec and the explosive was usually a mixture of

ammonium-nitrate and fuel oil. The 5,000 Kg shots generally produced clear arrivals out to 150 km and readings beyond this distance are few and are limited to only the larger blasts.

A composite refraction profile and compressional velocity model is shown in Figure 3.2 and listed in Table 3.2. One of the most notable features discovered upon analysis of the travel times is the extreme regional variability of the uppermost crustal layer. Velocities in eastern Massachusetts range from less than 5 km/s to 5.8 km/s, and a 6.0 km/s upper layer was identified in southern Maine. Because the blasts produced few impulsive arrivals at distances greater than 150 km, the crustal thickness and the velocities of the lower layers are not well constrained. However, it does appear that the lower crust is characterized by velocities greater than 7.0 km/s and that the cross-over distance for the Pn branch is greater than 160 km, indicating crustal thicknesses in excess of 35 km.

3.2 AVERAGE STRUCTURE USING P AND S ARRIVALS FROM REGIONAL EARTHQUAKES

Refraction models derived from timed blasts are very useful in determining crustal structure and as discussed in the previous section indicate a high degree of structural complexity in the NEUS. However, there are a number of

difficulties in working solely with the seismic refraction surveys. First, the data collection can be difficult, expensive, and time-consuming. A number of refraction lines were set up by the author only to find that the blast either occurred much earlier than expected or was delayed, or was too small to produce usable recordings. Second, and more importantly, most of the blasts were too small to generate impulsive Pn arrivals which are essential in estimating crustal thickness. Interpretation of the refraction profiles was also complicated by the paucity of data at certain crutial distance intervals. In constrast, a wealth of information can be derived by analyzing readings from the large number of earthquakes recorded and cataloged over the past four or five years since the NEUS seismic network was initiated. Although the earthquake-generated dataset contains errors which are due to effects of mislocations and errors in origin times, it represents a much more complete collection of arrival-time information than the refraction surveys using explosive sources. In this section, the earthquake dataset and the method of analysis is discussed along with a description of the results.

3.2.1 DATA

A dataset of 1545 P-wave and 546 S-wave readings from 170 regional earthquakes with eqicentral distances up to 600 km

was selected from earthquake bulletins of the NEUS seismic network (Chiburis et al., 1975-1979). The earthquakes used are shown in Figure 3.4. The magnitude range was between 1.5 and 3.8, and small magnitude events and swarms with poor epicentral control were eliminated. A few events with well-constrained focal depths of about 10 km in the Adirondacks were deleted from the dataset. These events were characterized by "depth" hyperbolae (Figure 3.5a) from readings at nearby stations which would cause positive errors in velocity estimates of upper crustal layers unless depth corrections were made. Some relatively deep events (d>10 km) were located by the Canadian network in Quebec. However, as discussed below, the effects that these focal depths have on the travel times to the distant NEUS stations is small. Because most events are shallow (less than 10 km) a surface focus was assumed, and travel times were computed with respect to published epicenters and origin times.

Travel time plots were constructed for various event-station combinations and it became readily apparent that significant differences in travel time curves existed between stations lying above Grenville basement and stations lying in the New England Appalachians. The serpentinite belt and the Precambrian uplifts were used to separate stations into the two regions (Figure 2.1a). Reduced travel time plots using P and S travel times for stations lying above Grenville and Appalachian basement are plotted separately and shown in Figures 3.6 and 3.7. The

Appalachian and Grenville stations show similar travel times past epicentral distances of about 200 km. However, overlays of the travel time curves demonstrate that significant crustal differences exist between the two regions. For distances less than 200 km, the Grenville travel time curve is remarkably linear, while the Appalachian curve shows lower velocities out to at least 100 km where arrival times on the separate plots begin to rapidly converge.

Although readings made from the enlarged develocorder films generally have a standard error of 0.1 sec, scatter in the travel time plots arise from errors in hypocenter and origin time, misidentification of phases, and lateral complexities in structure.

3.2.2 ANALYSIS OF TRAVEL TIME CURVES

A number of different techniques are available for interpretation of the travel time profiles shown in Figure 3.6. A simultaneous inversion for hypocenters and velocity structure was considered following the technique described by Aki and Lee (1976). However, the distribution of events and stations in the NEUS is not suitable for this type of analysis. Many of the events used occur outside of the region being modeled and were originally located using the Canadian Seismic Network. There is also a lack of deep

events and the resolution of deeper crustal layers would be very poor.

A Wiechert-Herglotz or tau inversion was also considered. However, because of the scatter in the data these inversion techniques were judged to be too eloquent. On the other extreme, identifying and fitting straight line segments to travel time branches is very subjective and may not achieve a best solution in a least squares sense.

A more systematic, yet simple approach following the technique of Mitchell and Hashim (1977) was selected (see Appendix B for details). Given a set of travel time data, a nonlinear least squares method is used to solve for apparent velocities, critical distances, and corresponding intercept times for a plane layered earth model. The method solves a system of equations containing nonlinear terms involving critical distance divided by refractor velocity (see Appendix B and Figure 3.3).

Because a least squares technique is used, critical distances, their corresponding times, and apparent velocities are perturbed about a trial model. The initial model was selected by estimating critical distances and corresponding times from reduced travel time plots with expanded time scales. Trial apparent velocities were then calculated by taking the inverse slope of a least squares line fit to the data along the selected distance interval.

3.2.3 ERROR ANALYSIS

The travel time data generally had a standard deviation of about 0.7 sec. This scatter is probably caused mostly by errors in epicentral location, focal depth, and origin time. Reading errors, phase misidentification, and differences in travel time with azimuth caused by lateral variations in structure and anisotropy are probably also important factors.

Epicentral locations for most events are probably accurate to within 5 km. Location errors of 5 km will cause travel time errors of less than one second.

Effects of errors in earthquake depth on travel times was also investigated. With the exception of one area in the Adirondacks and La Malbaie, Quebec, most earthquakes in the study area have foci of less than 10 km (Sbar and Sykes, 1977). Recently, accurate location of aftershocks near Bath, Maine indicated depths of less than 7 km (Graham and Chiburis, 1980). For a homogeneous upper crust, the partial derivatives of travel time with respect to depth, z, can be approximated by

$$\frac{\partial T}{\partial z} = \frac{z}{V_0\sqrt{z^2+x^2}} \qquad (3.1)$$

where V0 is the crustal velocity, x is the epicentral distance. These partial derivatives for various depths are plotted as a function of distance in Figure 3.5b for V0 = 6.5 km/s. For depth errors of 5 km, the errors in travel

time will be less than 1 second and will be negligible for distances greater than about 40 km.

It is possible that the velocity model used in locating the earthquakes introduces some bias into the interpretation. Most of the earthquake locations and origin times used in the NEUS were calculated using the same velocity model (Chiburis et al., 1975-1979). The earthquakes in Canada were located by combining readings from the NEUS stations with the Canadian network using a different velocity model. In a region with reasonably dense station coverage and without strong lateral variations in velocity such as eastern North America, small differences in the velocity model should not have a significant effect on the appearence of the travel time curves shown in Figure 3.6. As demonstrated by Anderson (1979), fairly accurate epicenter locations within an array can be obtained by simply constructing a series of station bisectors based on relative arrival times with no information on velocities. Although most of the earthquakes are located using the same velocity model, the differences in travel times observed between Appalachian and Grenville stations (Figure 3.6, 3.7) gives further support that the location velocity model introduces little bias into the final interpretation.

3.2.4 RESULTS

The final velocity models, and fit to the data for Appalachian and Grenville P and S travel time curves are shown out to 300 km in Figure 3.7. The critical distances, corresponding times, apparent velocities, layer thicknesses, and model errors are listed in Table 3.3. As will be discussed in section 3.4, the results obtained from interpretation of the travel time profiles are consistent with previous refraction models and show large contrasts between the two orogenic belts. The crust of the Grenville Province appears to be very homogeneous with nearly constant P and S wave velocities of about 6.6 and 3.7 km/s, respectively, with an average crustal thickness of 37 km. In contrast, the Appalachians are characterized by a slightly thicker (approximately 40 km) crust with two well-defined layers. The upper crust in the Appalachians shows relatively low P and S velocities of about 6.1 and 3.6 km/s, respectively, to about 15 km where an abrupt increase to 7.0 km/s and 4.1 km/s occurs. Both regions show similar Pn velocities of 8.0 km/s for the Grenville and 8.1 km/s for the Appalachians.

3.3 LATERAL STRUCTURE FROM TIME TERM ANALYSIS OF THE Pn BRANCH

The least squares technique discussed in the previous section represents an average crustal model for two large

regions and cannot adequately portray lateral variations in crustal structure. To study these lateral variations in crustal structure, a time term analysis was applied to the Pn branch of the travel time curve for all stations simultaneously (D > 200 km).

Previous time term studies in eastern North America include those by James et al. (1968) in the Middle Atlantic States, Berry and West (1966) from the Lake Superior refraction experiment, and Berry and Fuchs (1973) in eastern Canada.

3.3.1 METHOD

The time term method (Scheiddegger and Willmore, 1957; Willmore and Bancroft, 1960) is based on the fact that the travel time, Tij, between a source i and station j can be represented by the sum of a source and receiver term and the distance, Dij, divided by the average refractor velocity (in this case the Pn velocity) Vpn (Figure 3.8)

$$T_{ij} = S_i + R_j + \frac{D_{ij}}{V_{Pn}} \qquad (3.2)$$

Because the sum of the source and receiver terms equal a constant (the zero-distance intercept time of the travel time branch), there are infinitely many solutions and the system is singular (see Appendix C). Thus, the generalized inverse operator for the system was computed and the one

zero eigenvalue resulting from the non-uniqueness of the source and receiver term was truncated (Wiggins, 1972).

A number of crutial assumptions are made in the derivation of equation 3.2. First, it is assumed that the dip of the refractor is small. Without an adequate azimuthal distribution of sources, problems similar to those of an unreversed seismic refraction profile can result and there can be systematic errors in the time terms and refractor velocity. However, as can be seen from Figure 3.4, there is a reasonably good azimuthal distribution of events. Also, in an older, stable geologic province such as that in the NEUS, the regional dips of the Moho are expected to be small. Similar errors can occur if there exist large regional variations in the refractor velocity. As discussed in the previous section, although the Grenville and New England Appalachians show regional differences in the crust, the Pn velocities appear to be quite similar.

It is also assumed that effects of velocity anisotropy are small and that a large velocity gradient does not exist in the upper mantle (i.e. the second derivative of the Pn travel time branch is small). Velocity anisotropy can be examined by including azimuthal terms involving sines and cosines into the time term equation (McCollom and Crosson, 1975). Berry and Fuchs (1973) found only weak, poorly defined anisotropy in the Grenville Province. Velocity gradients can be modeled by incorporating higher order distance terms into equation 3.2. However, as can be seen

from Figure 3.6, the Pn travel time branch is fairly linear, and the coefficients of the higher order terms would be small.

3.3.2 RESULTS AND INTERPRETATION

Earthquakes were selected from those of Figure 3.4 which yielded three or more Pn arrivals in the distance range of 200-600 km. In all, 71 events, 61 stations and 343 readings were used. For each event, epicentral distances and moveout times from the nearest station were calculated. Relative station time terms, $\bar{R}_i^{P_n}$, were computed by subtracting off the mean time term from each station time term, R_i, using

$$\bar{R}_i^{P_n} = R_i - \frac{1}{N}\sum_{i=1}^{N} R_i \qquad (3.3)$$

where N is the number of stations.

The calculated Pn velocity is 8.04 km/s and the relative station time terms, standard errors, and number of readings are listed in Table 3.4 and shown in Figure 3.9 for stations with four or more readings.

As will be discussed in Chapter 5, the station time terms have fewer readings and therefore are less constrained than the average relative teleseismic P-wave residuals, although the two sets of residuals do show a relatively good correlation. A trend of positive time terms (late arrivals) are observed in part of eastern New York, western

Massachusetts, southeast Vermont, central New Hampshire, and central Maine. Negative time terms (early arrivals) are observed in northeastern New York and northwestern Vermont and also along much of the coastline.

As discussed in Appendix C, for a layer over a half-space model, the station time terms are functions of crustal thickness, velocity, and upper mantle velocity. Thus, unless some constraints can be placed on the problem, the station time terms can be interpreted a number of different ways.

Because the Pn velocities appear to be relatively constant and the average crustal velocities are similar across the NEUS, it was decided to model the time terms as a function of crustal thickness. Inverting absolute time terms for crustal thickness requires the direct measurement of the source terms, Sj, at a given site j, by recording the origin time and measuring the intercept time from the resulting travel time vs. distance plot. It would then be necessary to record a Pn arrival at the same site, calculate the resulting "station term", Rj, and equate Sj = Rj. Because all of the station terms are relative, this would assign absolute values to them, which could be used to invert for absolute crustal thickness assuming a crustal velocity function.

Only relative time terms were calculated in this study, so the crust and upper mantle parameters from this and the previous section could be used to obtain, at best, a first

order approximation of crustal thickness variations. To obtain the crustal thickness values at each station site from the relative time terms, a single layer over a half space model is used where the crustal thickness is

$$h = h_0 + \frac{R_i V_a}{\cos\theta} \qquad (3.4)$$

and

$$\theta = \sin^{-1} \frac{V_a}{V_{pn}}$$

where Vpn = 8.04, Va = 6.6, h0 = 38 km for Grenville stations and 39 km for Appalachian stations. Note that the estimate of the average crustal velocity is slightly high so the crustal thickness variations are probably the maximum to be expected. The crustal thickness map is shown in Figure 3.10.

As indicated by observing the relative station time terms in Figure 3.9, the crustal thickness appears to be greatest (and/or velocities are lowest) in a northeast trending belt running from eastern New York, through central New Hampshire, and into Maine. This belt shows a remarkable correlation with the belt of Bouguer gravity lows shown in Figure 2.2. Crustal thinning (and/or high crustal velocities) is found in northwestern Vermont and northeastern New York and along the Atlantic coast.

The crustal thickness map is based on an overly simplified model and represents at best a first order approximation. Many factors contribute to erroneous crustal thickness estimations many of which are described in detail

by Bath (1978).

3.4 COMPARISON WITH OTHER REFRACTION MODELS IN EASTERN NORTH AMERICA

Results from observations of regional travel times suggests that significant differences in crustal structure exist between the Grenville and Appalachian Provinces. In this section, the models presented in this chapter will be compared with other refraction models measured in eastern North America. The tectonic implications of the structural differences will be examined in Chapter 6.

Refraction models for the northern and southern Appalachians and the Grenville Province are contrasted in Table 3.5. The northern Appalachians appear to be composed of a relatively thick, 40 km crust with two well-defined layers. The lower crust is characterized by relatively high velocities of 7 km/s. This is consistent with refraction models of Leet (1941) and Steinhart et al., (1962) in the NEUS, R.L.Street (pers. comm.) in central New Hampshire, and Dainty et al. (1966) in Newfoundland. Two models presented by Chiburis and Graham (1978) in southeastern New England and Nakamura and Howell (1964) in eastern Maine suggests crustal thinning and a missing high velocity lower layer along the Atlantic coast. The region where the Chiburis and Graham (1978) model was compiled is located in a region

characterized by a zone of negative time terms and apparent crustal thinning (Figures 3.9 and 3.10). Interestingly, these surveys may have sampled rocks of the eastern Block (or Avalon zone) discussed in Chapter 2.

Refraction models from the Grenville Province appear to be fairly similar along its length from the southeastern U.S. to eastern Canada. In eastern Canada the high velocity lower crustal layer is absent or weakly developed (Dainty et al., 1966; Berry and Fuchs, 1973). It also appears that the Grenville crust thickens from about 36 km at its eastern edge to about 45 km at its western edge in the vicinity of the Grenville Front. In New York state, the Grenville crust appears to be uniform, about 36 km thick, with velocities ranging from 6.4 to 6.6 km/s (Katz, 1955; Aggarwal in Schnerk et al., 1976).

Further south, west of the Blue Ridge, the Grenville crust appears to have two layers but the lower crustal layer is about 6.7 km/s which is low relative to the northern Appalachians (Steinhart and Meyer, 1961). The 14 km thick upper layer could by composed of the allochthonous miogeoclinal rocks.

The southern Appalachians appear to show velocity structures that are more like the Grenville models than those of the northern Appalachians because of the lack of the high velocity lower crustal layer (Long, 1979; Warren, 1968; Bollinger et al., 1980). This has very important implications that will be discussed in Chapter 6.

Table 3.1

Blast Locations and Origin Times

Date	Location	Lat.	Long.	O.T.
8/25/76	Keating Quarry	42.539	71.689	21:24:51.53
10/4/76	"	"	"	21:36:20.0
4/7/77	"	"	"	21:29:42.2
8/30/76	Beneyento Sand & Gravel	42.588	71.138	19:28:08.25
5/3/77	Cook Concrete	43.698	70.262	17:30:47.65
6/17/77	East Barret, Vt. I-91 roadcut blast	44.323	72.041	19:25:08.1
6/22/79	National Mines, Que.	46.140	71.225	19:44:02.61
6/27/79	John Mansville Mines, Que	45.771	71.949	19:47:42.24
8/1/79	Vermont Asbestoes	44.76	72.53	18:31:50.75
8/14/79	"	"	"	18:47:11.25

TABLE 3.2

Refraction Model From Timed Quarry Blasts

DEPTH (Km)	V_p (Km/s)
0. - 22.1	6.0
22.1 - 44.6	7.1
Moho	8.1

Table 3.3

Travel Time Models V_0=6.4 km/s

	Appalachians		Grenville	
	P	S	P	S
# events	128	96	82	58
T_{i1}	0.1	0.2	0.4	0.4
T_{i2}	2.9	6.2	0.8	0.8
T_{i3}	6.9	11.4	5.9	12.5
t_1	22.0±1.0	39.4±1.6	17.6±6.1	16.8±4.1
t_2	30.0	57.3	34.2	60.3
X_{c1}	133.6±6.5	139.3±5.6	112.4±40.0	59.2±14.9
X_{c2}	189.3±7.9	214.4±9.0	223.0±11.5	220.0±10.9
V_1	6.1	3.6	6.6	3.7
V_2	7.0	4.2	6.6	3.7
V_3	8.2	4.7	8.0	4.6
Z_0	2.2	2.1	3.1	1.9
Z_1	10.9±0.5	14.9±0.6	0.7±0.2	0.3±0.7
Z_2	26.7±1.1	24.8±1.0	32.0±1.7	35.6±1.6
Z_{total}	39.8	41.8	35.8	37.8
data Std. Dev.	0.73	0.72	0.60	0.87

(See Figure 3.3 for symbol definitions)

Table 3.4

Station Time Terms, Errors, and Number of Readings

V_{pn} = 8.04 km/s 71 events 343 readings

Station	Relative Time Term	No. Readings	Std. Error
AGM	-0.1	5	.05
APT	-0.2	2	.08
BCT	-0.2	12	.03
BML	0.1	12	.06
BNH	0.4	18	.03
CBM	-0.3	8	.04
COV	-0.2	3	.06
D3A	-0.1	11	.04
DANY	-0.2	2	.08
DNH	-0.2	8	.04
ECT	0.4	20	.02
EMM	-0.6	34	.03
ESJ	-0.2	1	.10
FLET	-0.4	2	.08
FLR	-0.1	2	.08
GFN	0.2	4	.06
GLO	-0.5	5	.05
HDM	-0.4	4	.06
HKM	0.0	1	.10
HNH	0.0	5	.05
HRV	-0.2	5	.05
JKM	0.6	4	.06
LNX	1.1	4	.06
MARL	0.2	5	.05
MDV	-0.1	4	.06
MIM	-0.4	26	.03
MPVT	-0.2	3	.06
NSC	-0.4	6	.05
ONH	0.1	3	.07
PNH	0.5	5	.05
PNY	0.1	4	.06
PTN	0.5	3	.06
QUA	0.4	8	.04
TBR	-0.1	5	.05
TMT	0.3	5	.04
TRM	0.3	9	.04
UCT	-0.3	11	.04
WES	-0.5	9	.04
WFM	-0.2	6	.05
WND	0.8	3	.06
WNH	0.2	8	.05
WNY	-0.1	3	.06
WPNY	0.6	2	.08
WPR	0.0	5	.05

Table 3.5

Generalized Refraction Models in Eastern North America

Canadian Appalachians

Grenville

Berry and Fuchs (1973)

Depth (km)	V_p (km/s)
0.-20.	6.3
20.-40.	6.6-6.9
Moho	8.06

Dainty et al. (1966)

0.-37.	6.25
Moho	8.18

Appalachians

Dainty et al. (1966)

Depth	V_p
0.-15.	5.9
15.-25.	6.3
25.-42.	7.2
Moho	8.1

Cont. Margin

Dainty et al. (1966)

Depth	V_p
0.-9.	5.4
9.-35.	6.25
Moho	8.0

Northeastern United States

Grenville

Katz (1954)

0.-35.	6.4
Moho	8.14

Aggarwal in (Schnerk et al. 1976)

0.-4.0	6.1
4.0-35.0	6.6
Moho	8.1

Appalachians

Street (1976)

0.-2.5	5.76
2.5-26.0	6.40
26.0-42.1	7.47
Moho	8.13

Taylor and Toksöz (1979)

0.-7.3	5.7
7.3-26.1	6.3
26.1-39.0	7.3
Moho	8.13

Leet (1941)

0.-16.0	6.13
16.0-29.0	6.77
29.0-36.0	7.17
Moho	8.43

Steinhart et al. (1962) (Gulf of Me. to Me. interior)

0.-20.0	6.0
20.0-40.0	7.0
40.0	8.0

Cont. Margin

Nakamura and Howell (1964)

0.-30.	6.0
Moho	8.1

Chiburus and Graham (1978)

0.-3.0	5.6
3.0-13.0	6.1
13.-31.0	6.6
Moho	8.1

Table 3.5 (continued)

Southern Appalachians

Grenville

Steinhart and Meyer (1961)

Depth (km)	V_p (km/s)
0.-13.7	6.20
13.7-45.3	6.73
Moho	8.06

Warren (1968)

0.-23.0	6.1
23.0-40.0	6.7
Moho	8.0

Bollinger et al. (1980)

0.-10.0	5.63
10.0-49.0	6.53
Moho	8.18

Appalachians (east of Blue Ridge)

Bollinger et al. (1980)*

Depth (km)	V_p (km/s)
0.-15.0	6.09
15.0-39.0	6.50
Moho	8.18

Warren (1968)

0.-20.0	6.0
20.0-38.0	6.7
Moho	8.1

Long (1979)+

0.-5.0	6.3
5.0-35.0	6.5
Moho	8.1

* Crust thins to 31 km to the east beneath central Piedmont

\+ Crust varies from 30-37 km thickness

FIGURE CAPTIONS

Figure 3.1 Blasts, portable and permanent stations used in refraction surveys.

Figure 3.2 Travel times from blasts and model fit.

Figure 3.3 Terminology used for two-layer over a half-space model (see Appendix B).

Figure 3.4 Events used in travel time analysis.

Figure 3.5a Travel times from Grenville earthquakes. Solid lines correspond to travel times from depths of 5 and 10 km.

Figure 3.5b Partial derivatives of travel time with depth for layer over a half space model.

Figure 3.6a Reduced P-wave travel times to 600 km for Appalachian stations.

Figure 3.6b Same as Figure 3.6a for Grenville stations.

Figure 3.6c S-wave travel times to 600 km for Appalachian stations.

Figure 3.6d Same as Figure 3.6c for Grenville stations.

Figure 3.7 Same as Figure 3.6 to 300 km with velocity models and model fit.

Figure 3.8 Terminology used for time term analysis discussion (see Appendix C).

Figure 3.9 Map of relative station Pn time terms in seconds.

Figure 3.10 Crustal thickness from relative time terms.

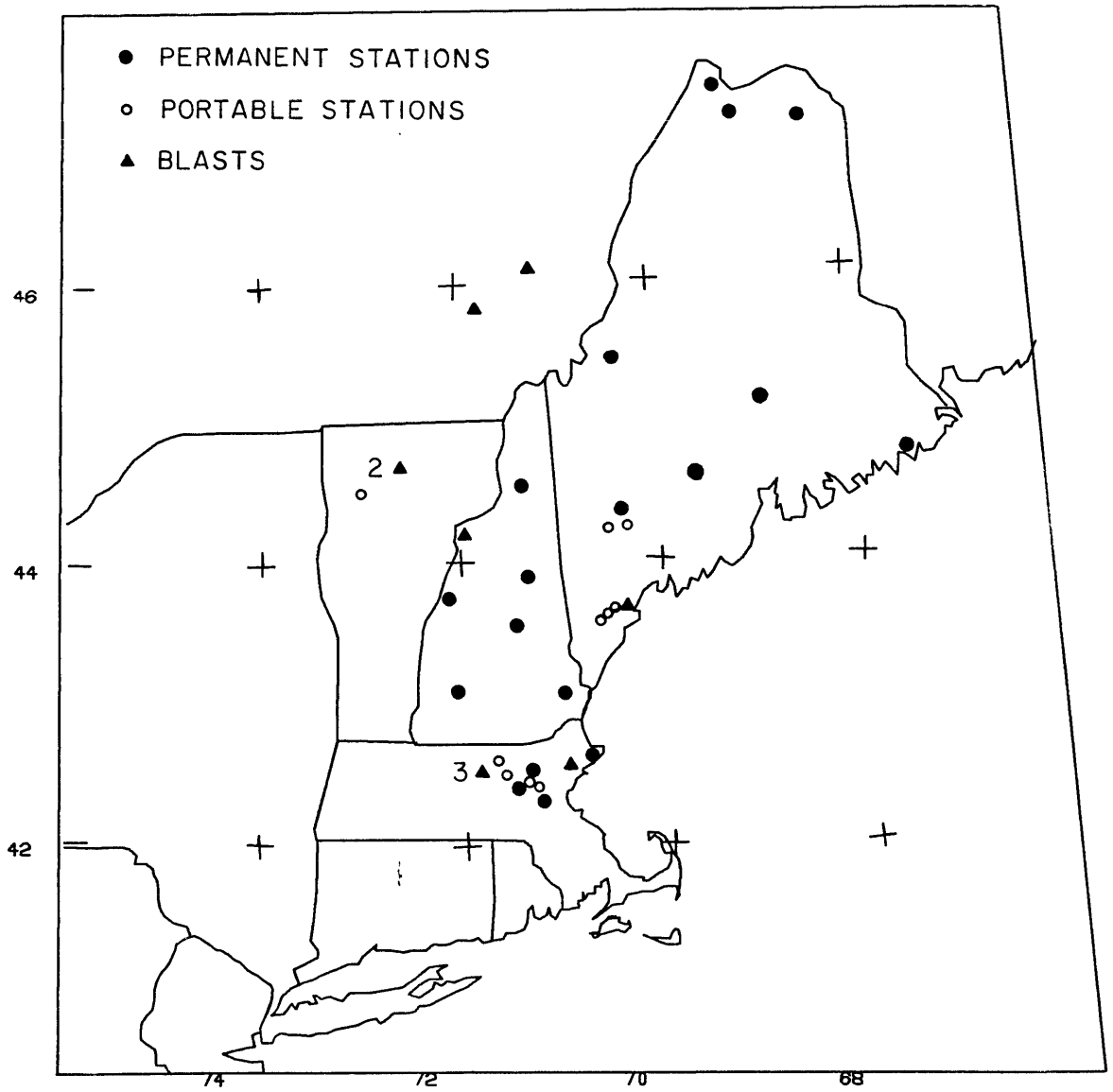
PERMANENT STATIONS
PORTABLE STATIONS
BLASTS
46
44
42
74
72
70
68
2
3

Figure 3.1

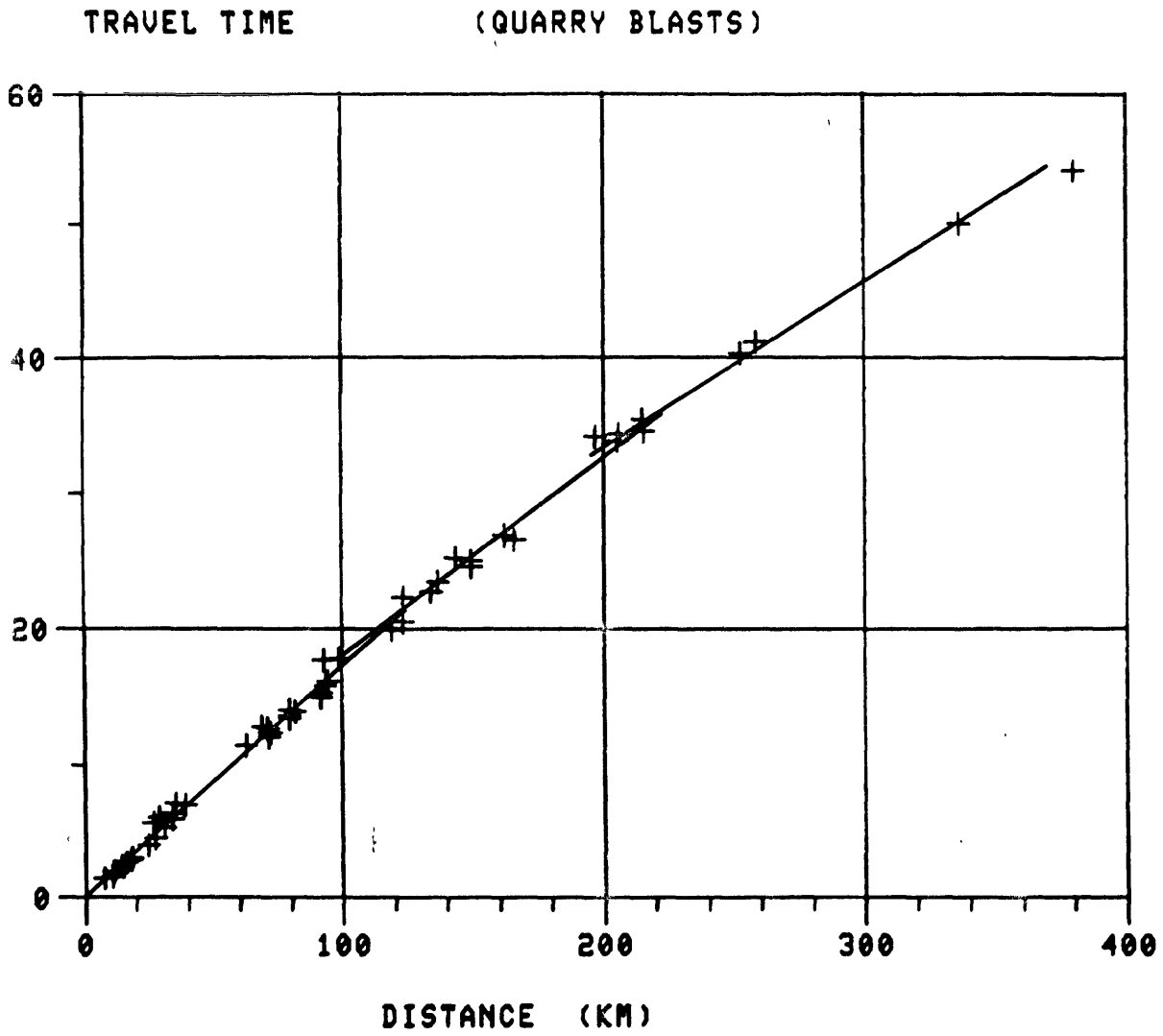
TRAVEL TIME (QUARRY BLASTS)
60
40
20
0
0
100
200
300
400
DISTANCE (KM)

Figure 3.2

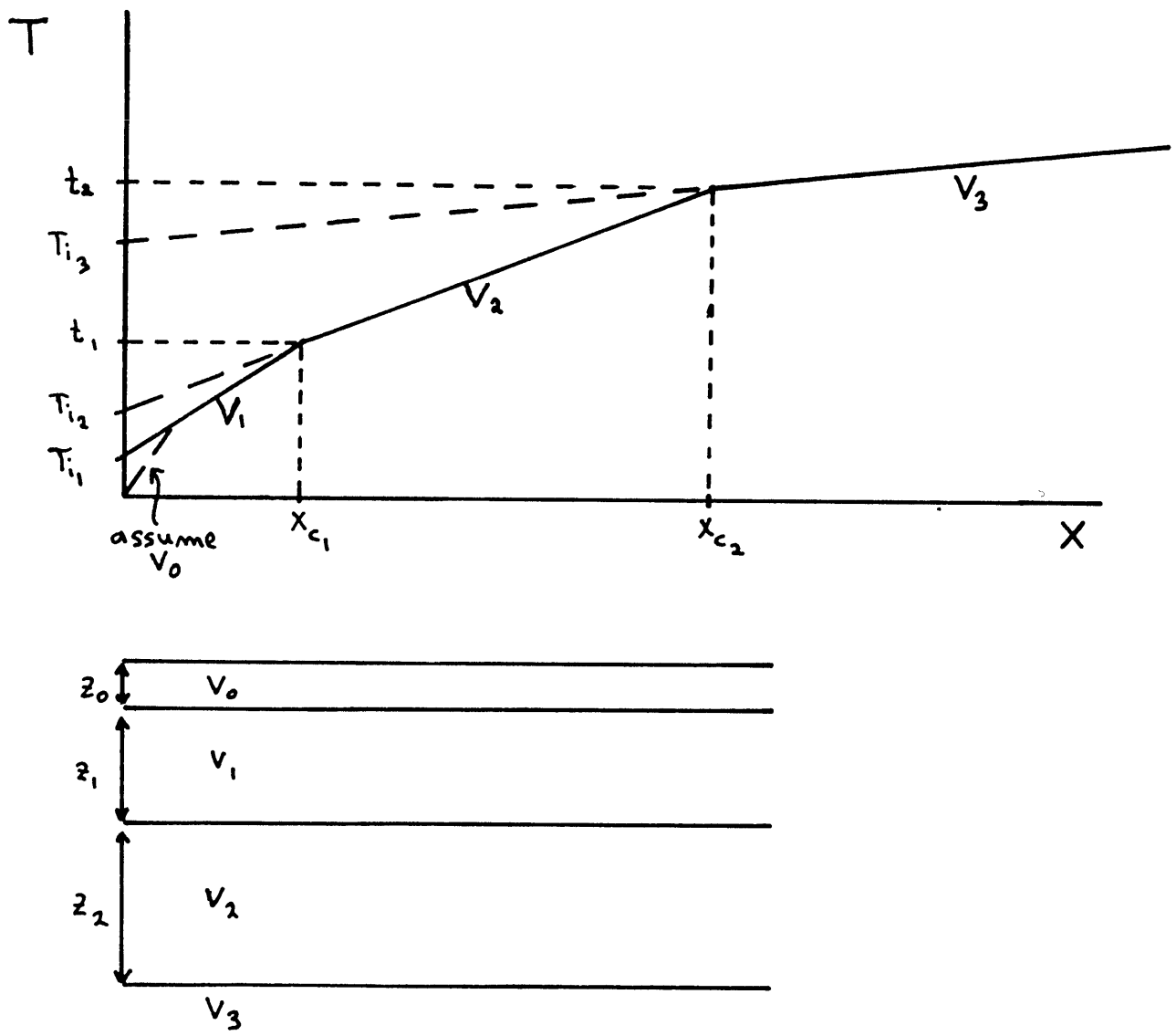

Figure 3.3

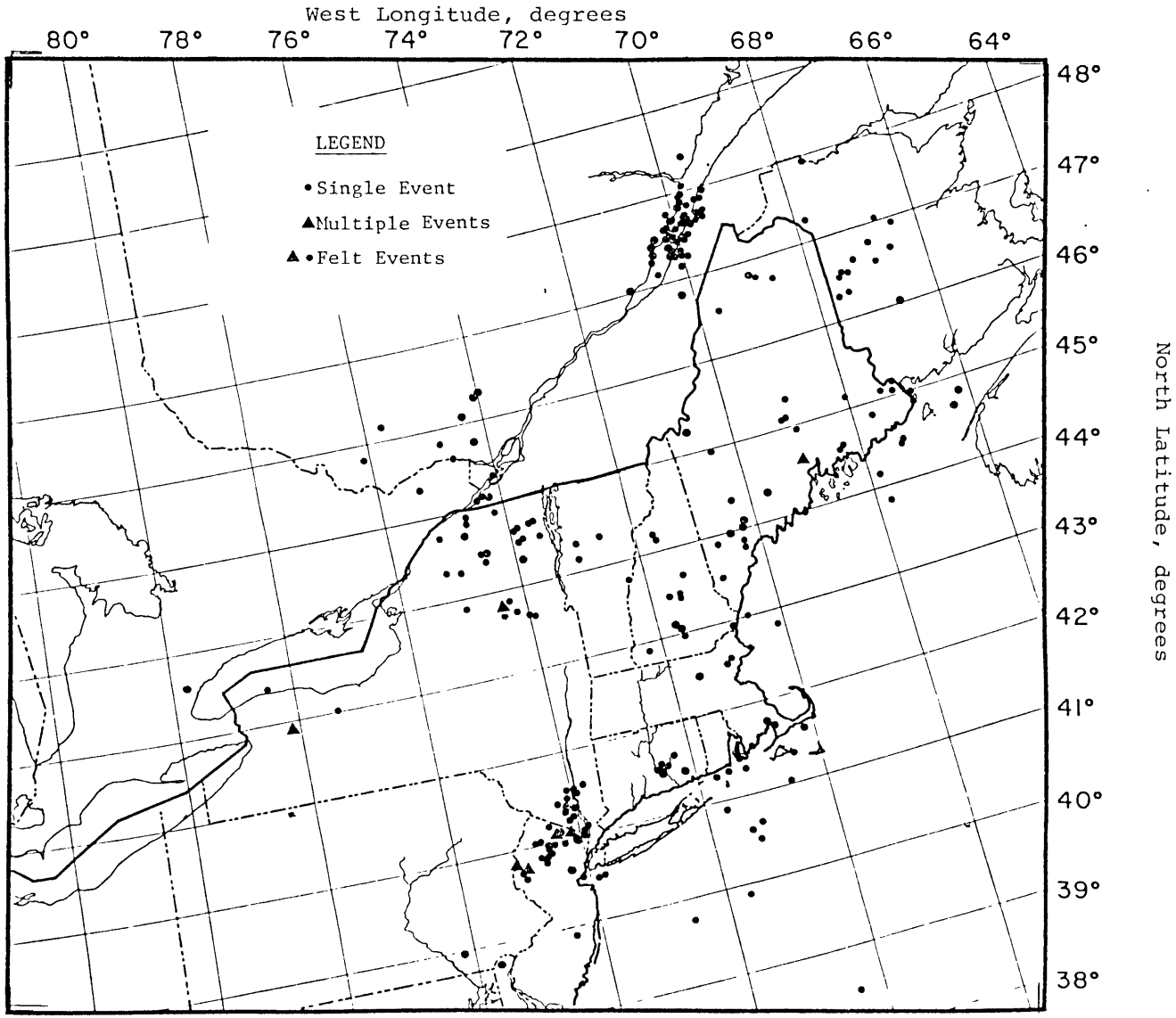
West Longitude, degrees
80°
78°
76°
74°
72°
70°
68°
66°
64°
48°
47°
46°
45°
44°
43°
42°
41°
40°
39°
38°
North Latitude, degrees
LEGEND
•Single Event
▲Multiple Events
▲•Felt Events

Figure 3.4

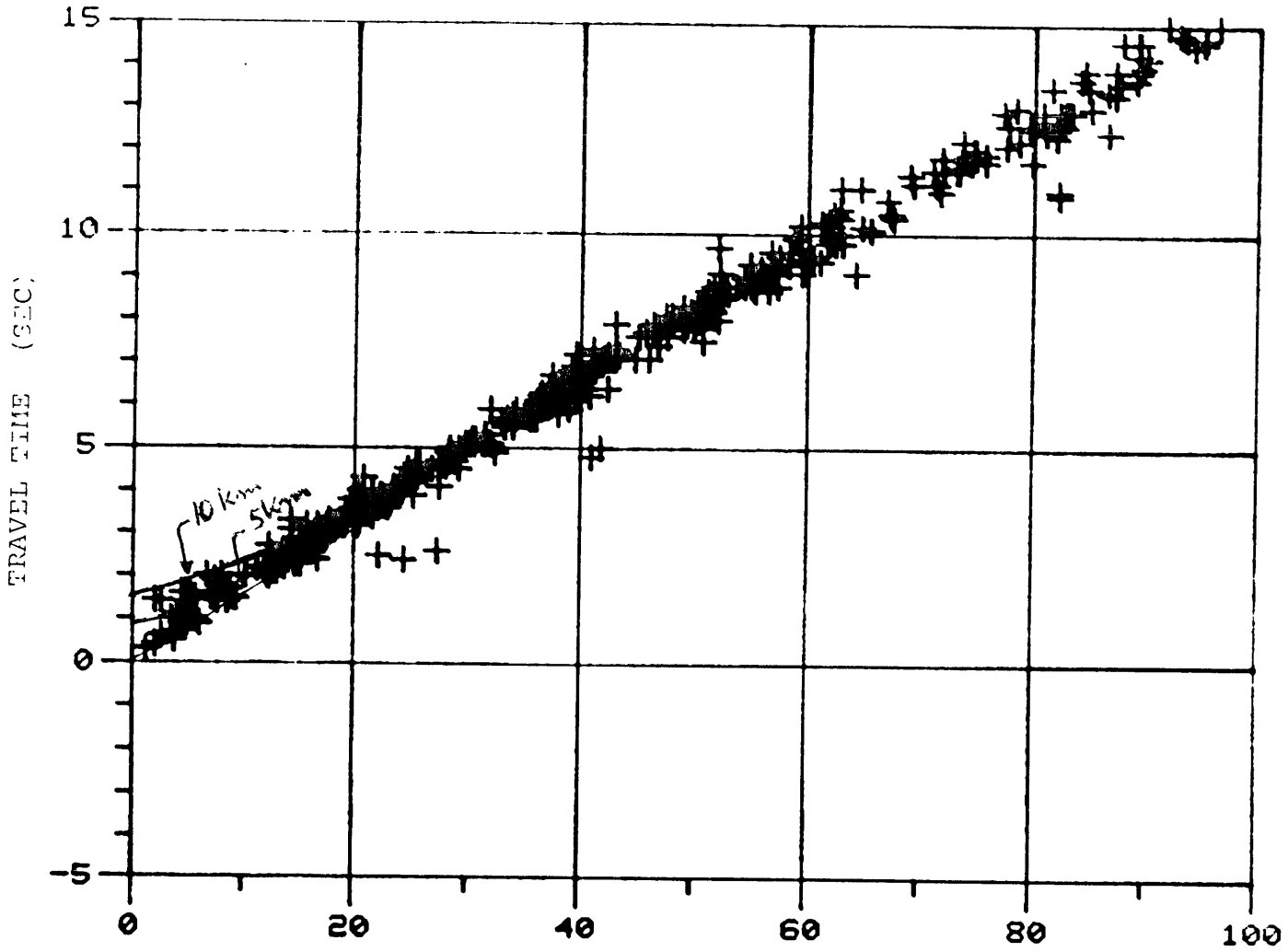

Figure 3.5a

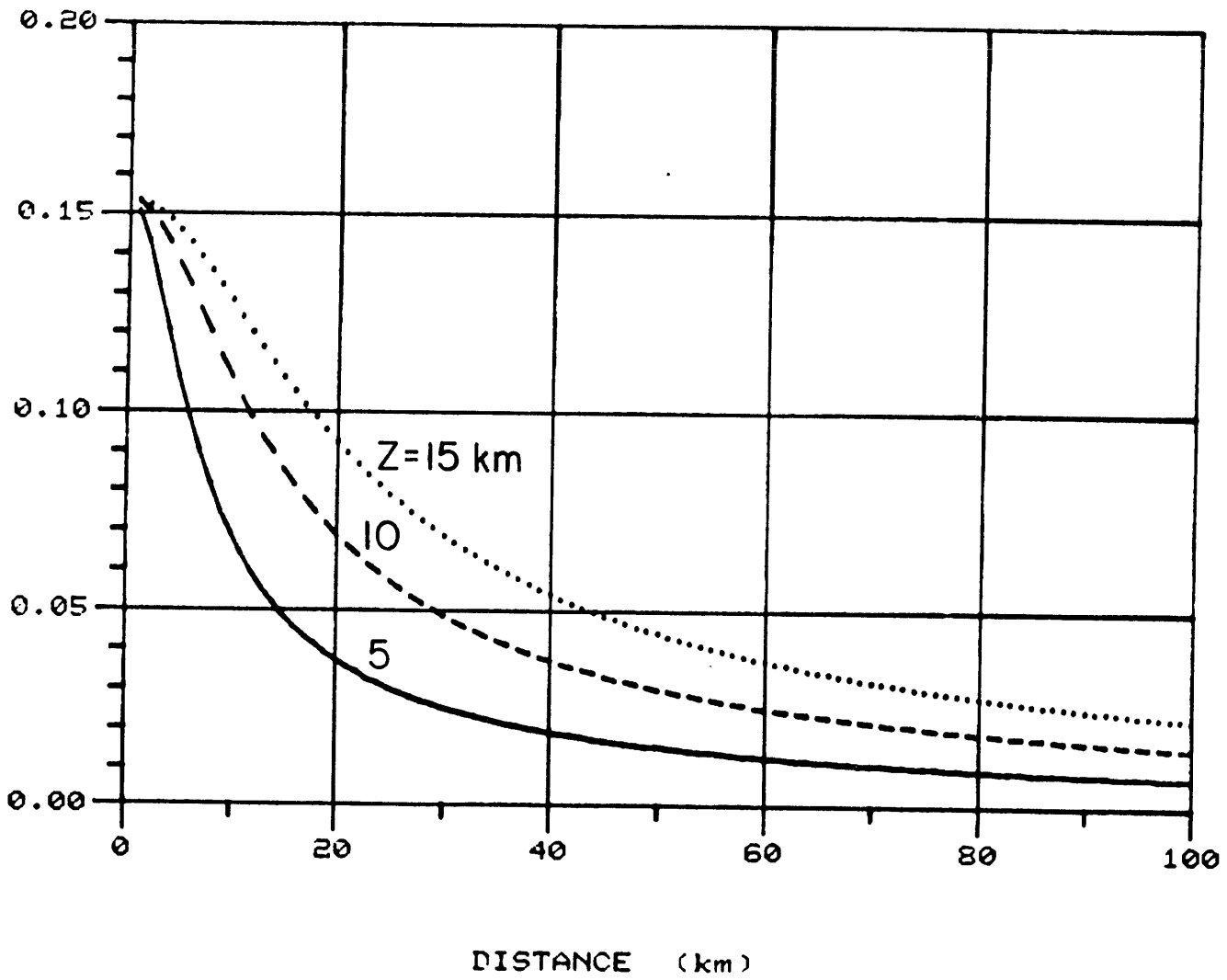

Figure 3.5b

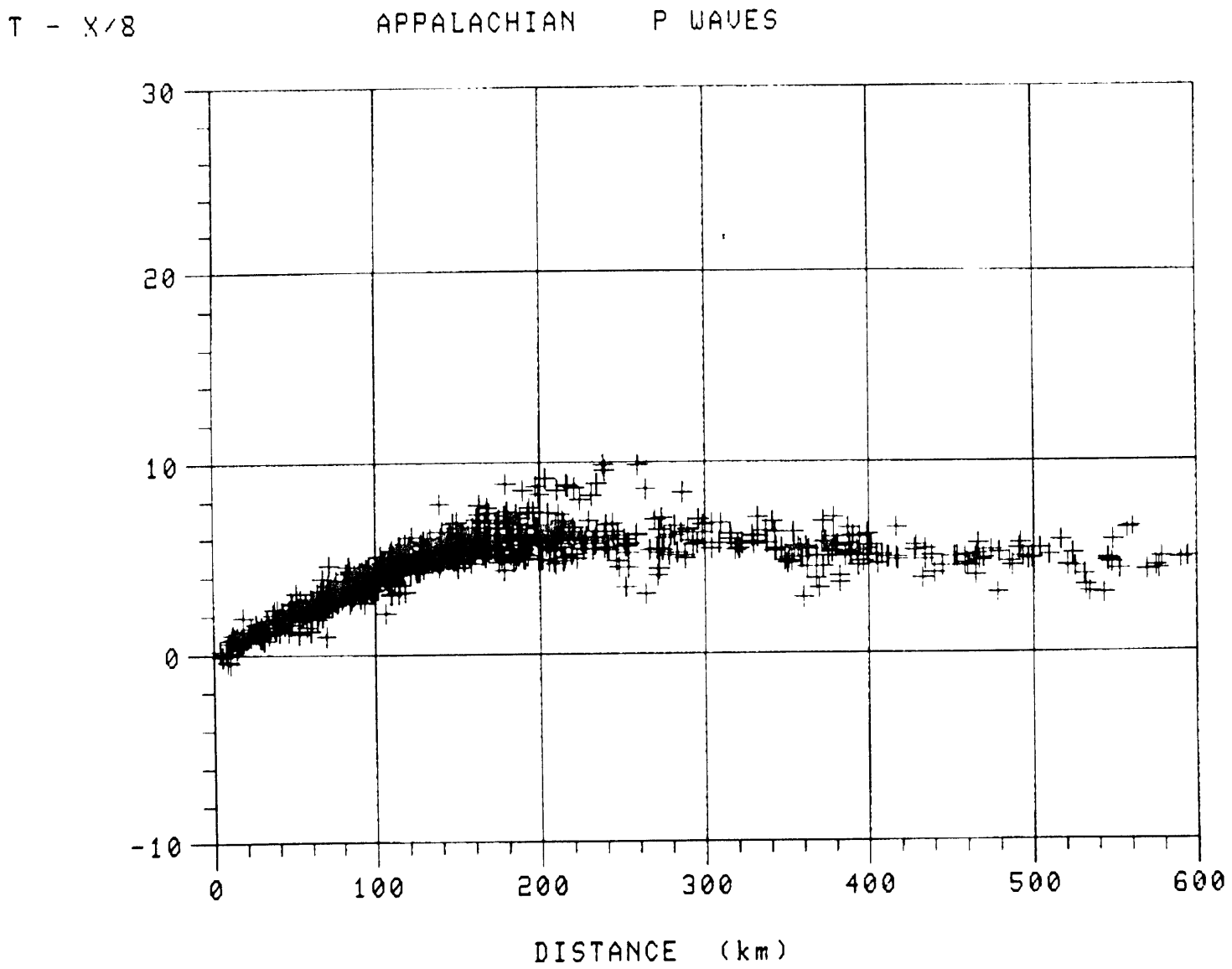
T - X/8
APPALACHIAN P WAVES
30
20
10
0
-10
0
100
200
300
400
500
600
DISTANCE (km)

Figure 3.6a

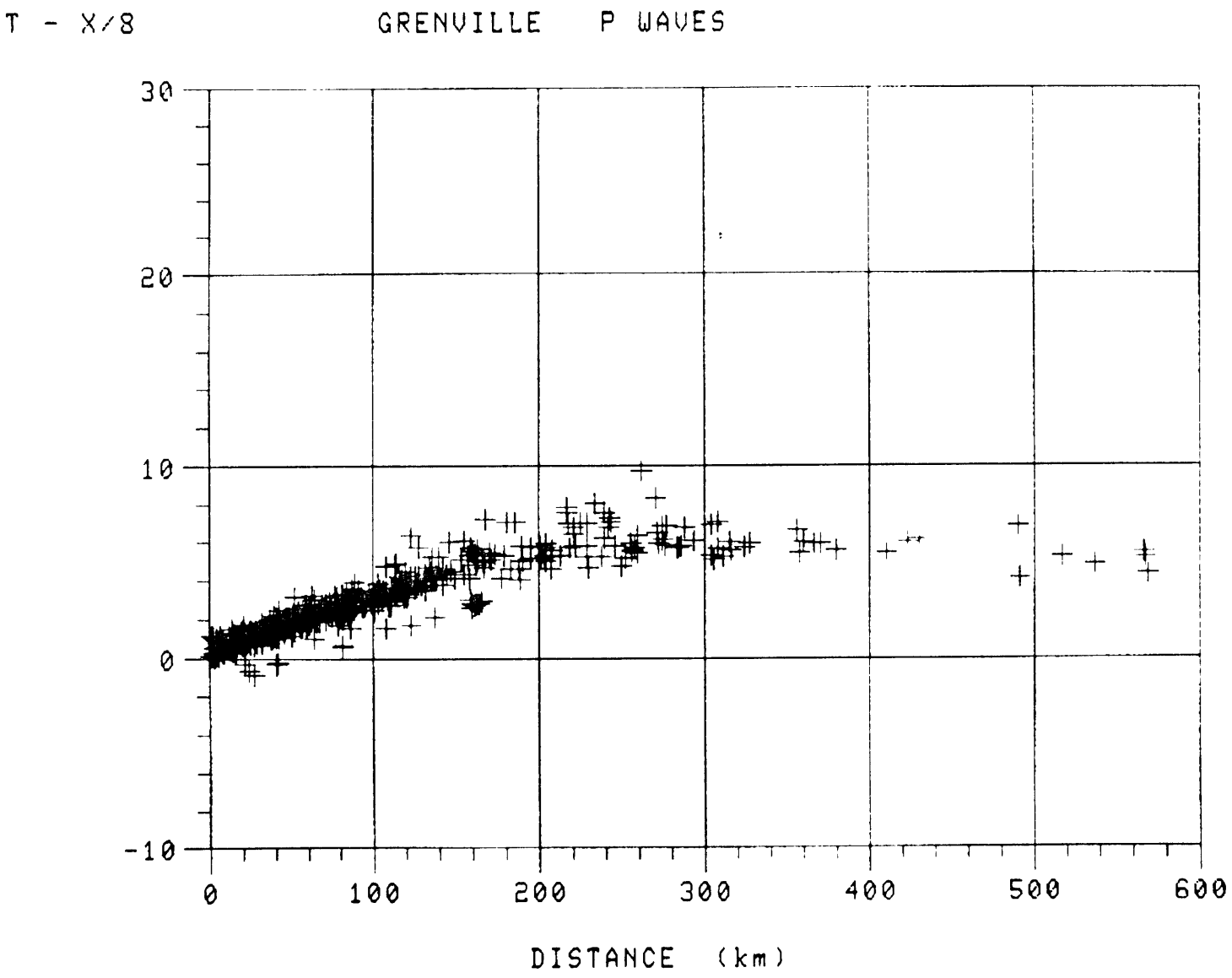
T - X/8
GRENVILLE P WAVES
30
20
10
0
-10
0
100
200
300
400
500
600
DISTANCE (km)

Figure 3.6b

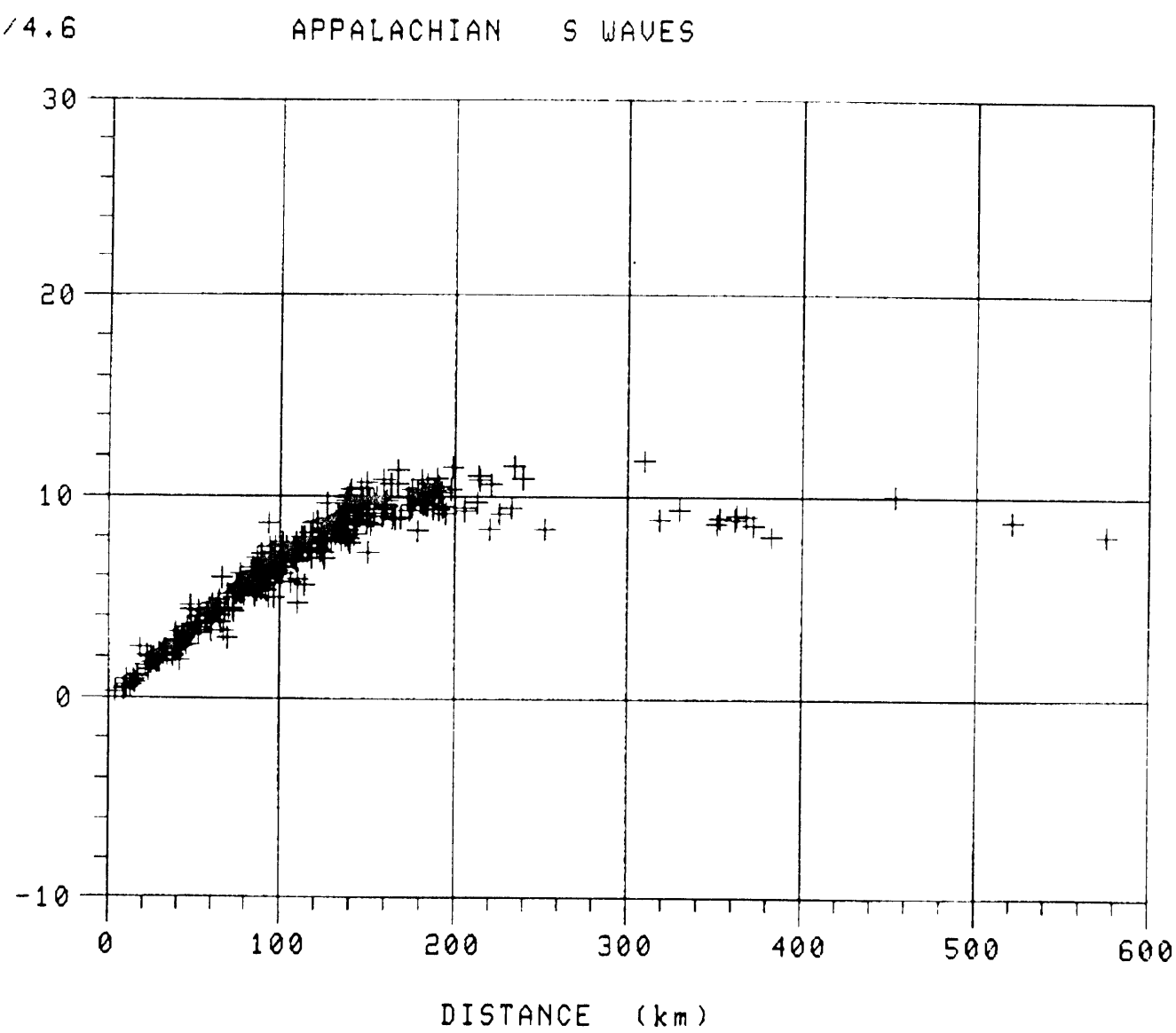
T - X/4.6
APPALACHIAN S WAVES
30
20
10
0
-10
0
100
200
300
400
500
600
DISTANCE (km)

Figure 3.6c

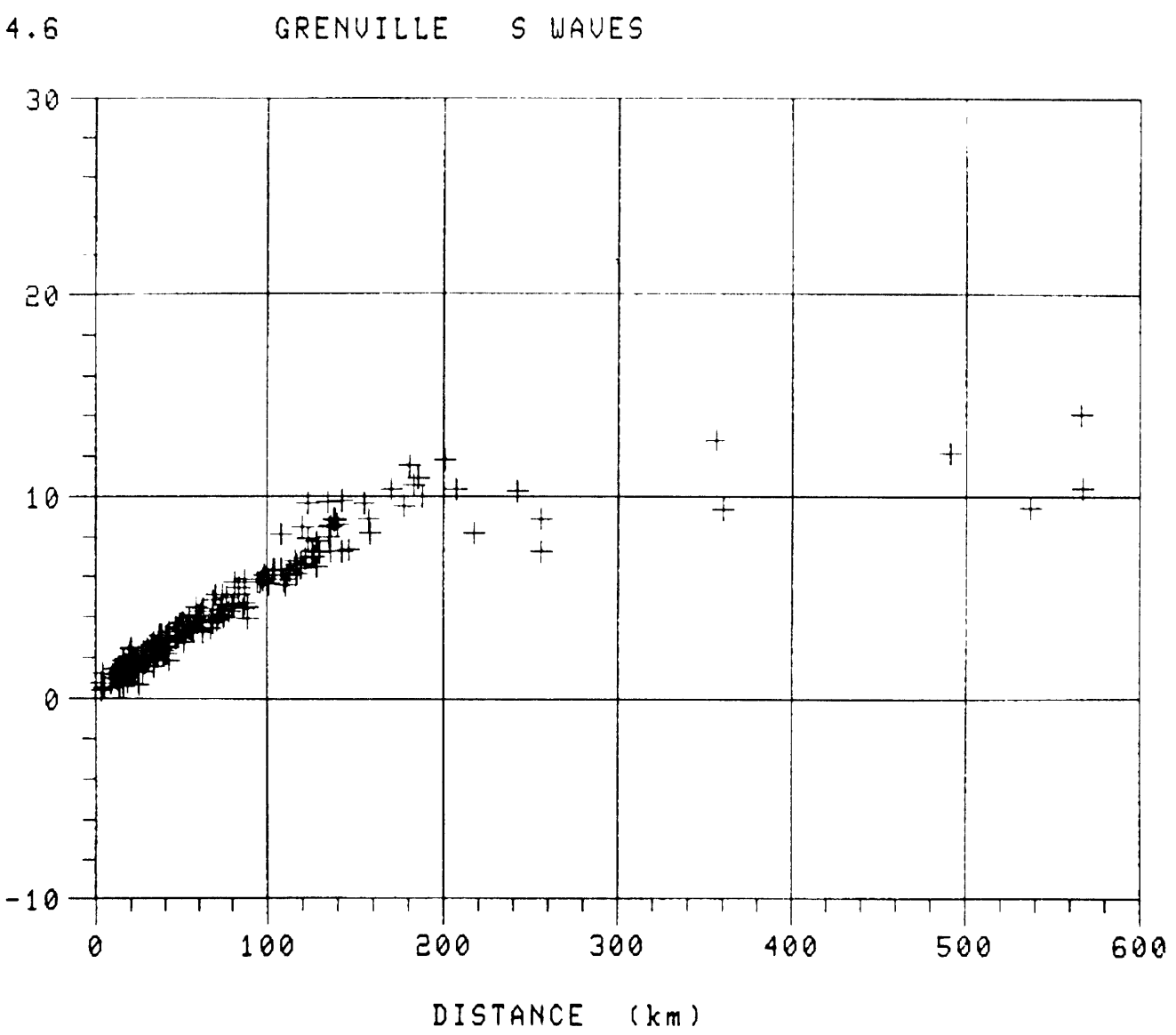
T - X/4.6
GRENVILLE S WAVES
30
20
10
0
-10
0
100
200
300
400
500
600
DISTANCE (km)

Figure 3.6d

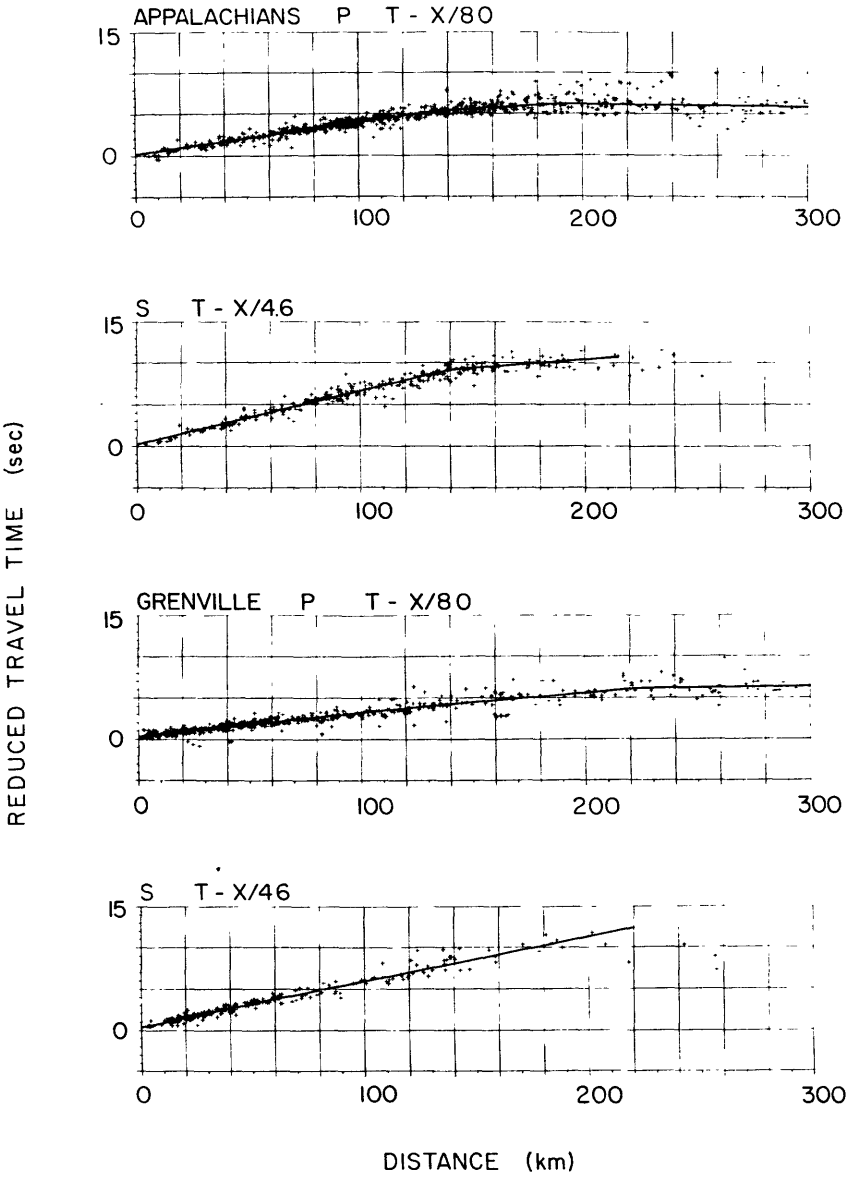
APPALACHIANS P T - X/80
S T - X/4.6
GRENVILLE P T - X/80
S T - X/46
15
0
0
100
200
300
REDUCED TRAVEL TIME (sec)
DISTANCE (km)

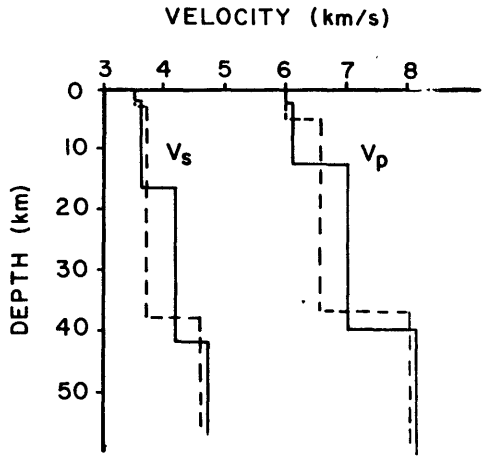
VELOCITY (km/s)
3
4
5
6
7
8
0
10
20
30
40
50
DEPTH (km)
Vs
Vp

Figure 3.7

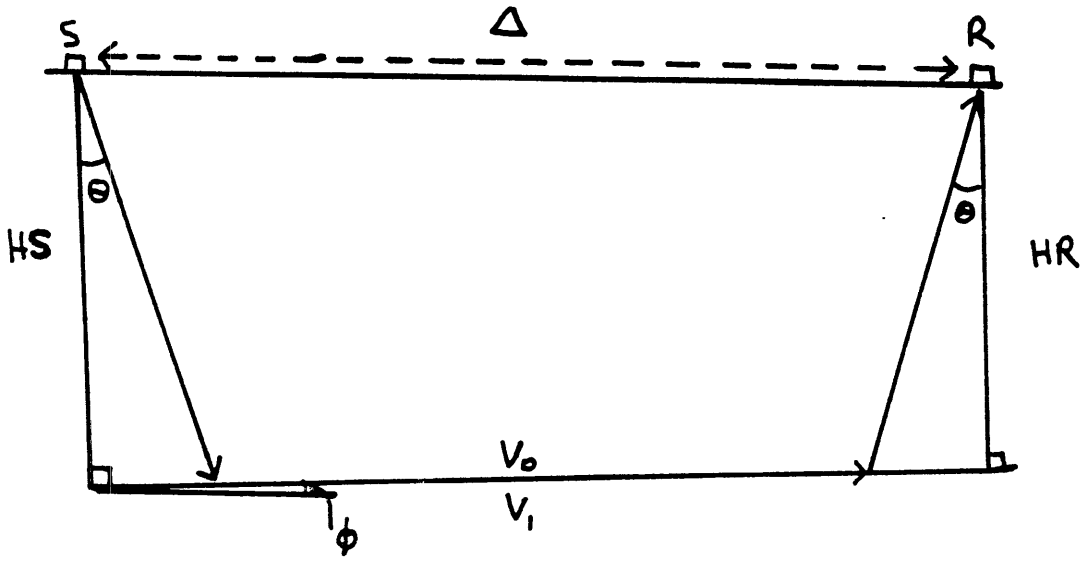

Figure 3.8

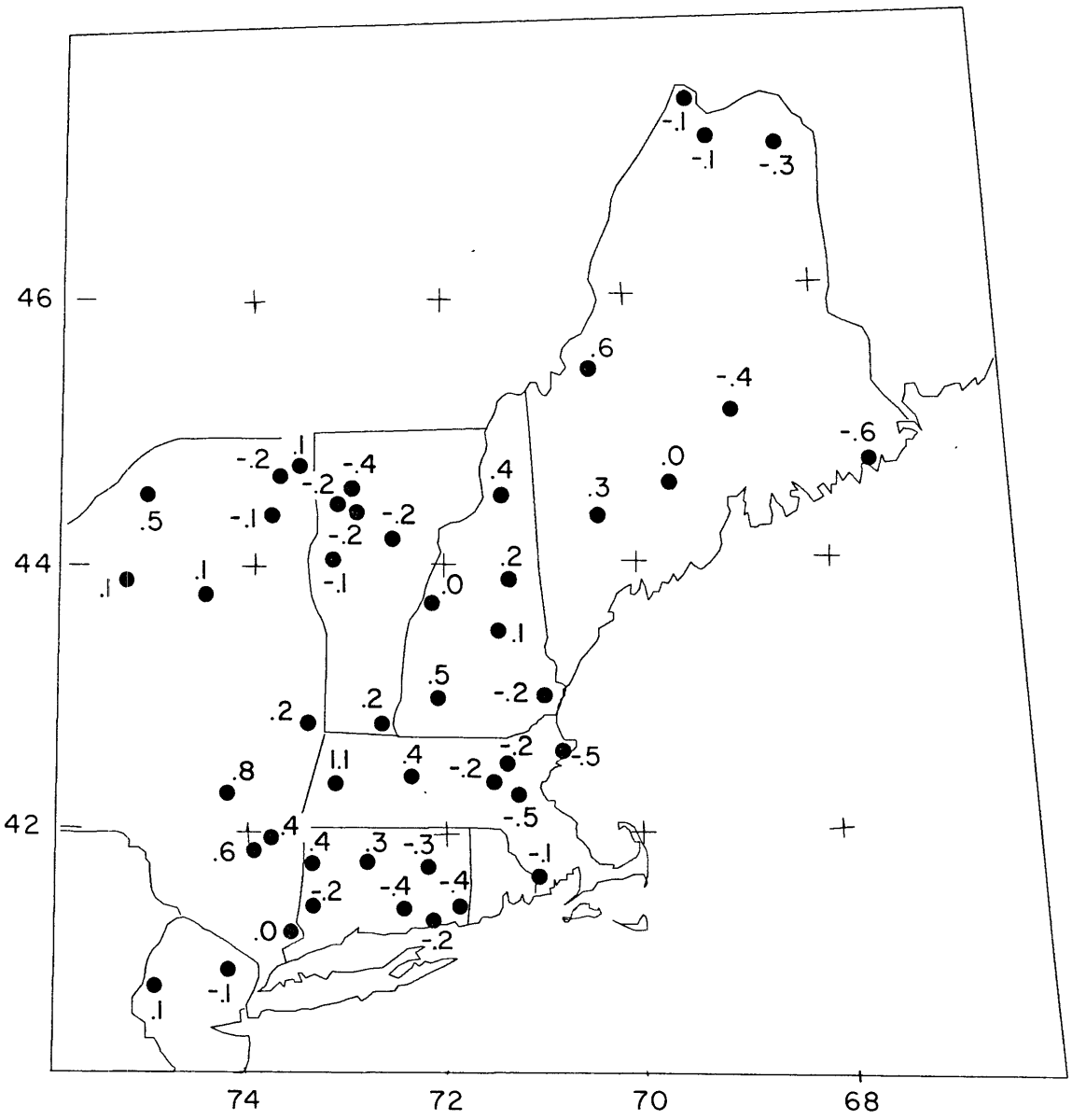
46
44
42
74
72
70
68
-.1
-.1
-.3
.6
-.4
-.6
.0
.3
.4
-.2
.1
-.4
-.2
-.2
.5
-.1
-.2
-.2
.1
.1
-.1
.0
.2
.1
.5
-.2
.2
.2
-.2
-.5
.8
1.1
.4
-.2
-.2
-.5
.6
.4
.4
.3
-.3
-.1
-.2
-.4
-.4
.0
-.2
-.1
.1

Figure 3.9

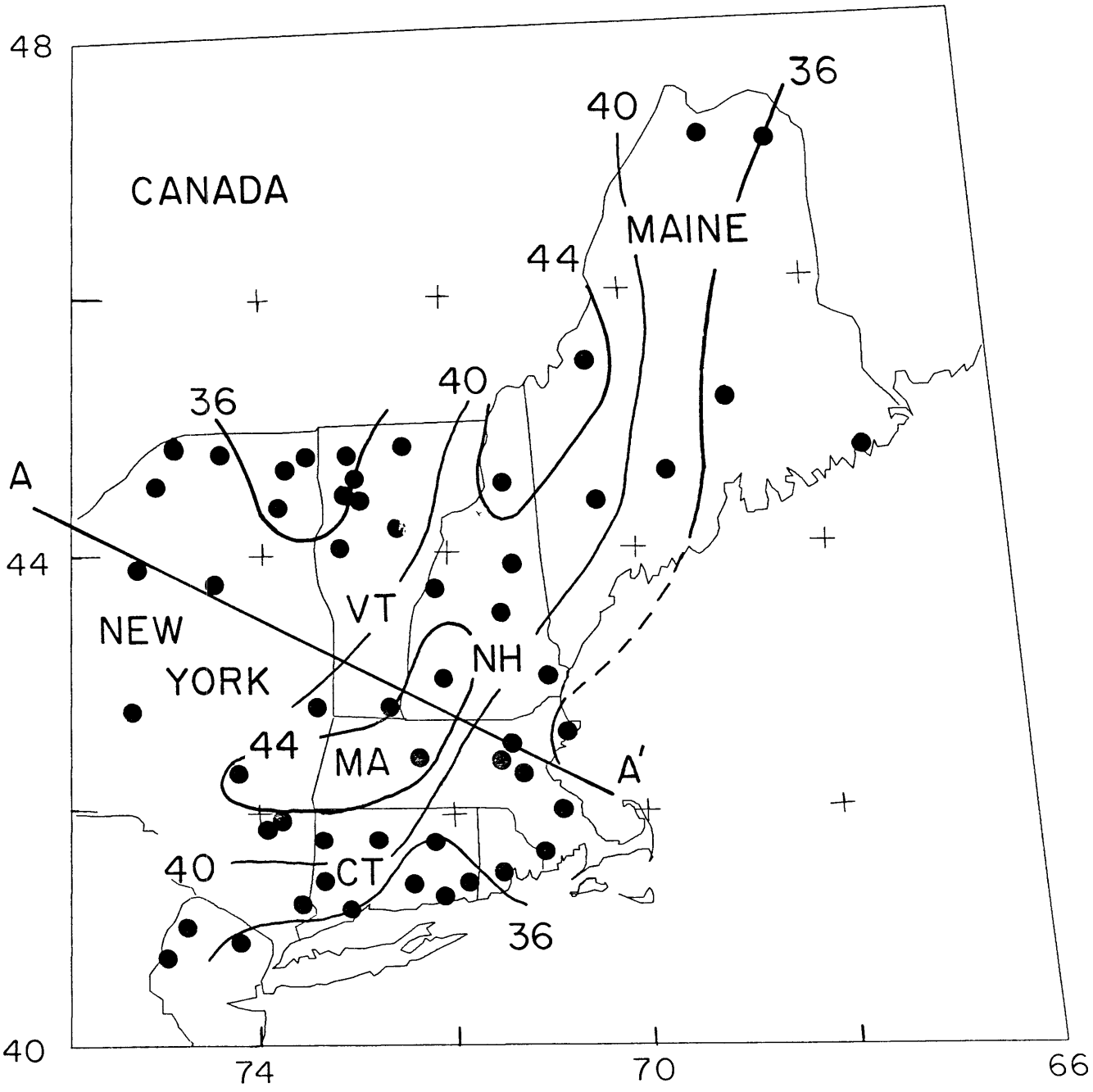
48
44
40
74
70
66
CANADA
MAINE
NEW
YORK
VT
NH
MA
CT
A
A'
36
40
44
36
40
44
40
36

Figure 3.10

Chapter 4.

STRUCTURE DERIVED FROM SURFACE WAVES

4.1 INTRODUCTION

In order to study average properties of the crust and upper mantle in the NEUS, surface wave dispersion information is collected using a variety of techniques along a number of different paths. Previous surface wave investigations in eastern North America include those by Brune and Dorman (1963) in the Canadian Shield, Dorman and Ewing (1962) in New York State, Long and Mathur (1972) in the southern Appalachians, and Mitchell and Herrmann (1979) for the eastern United States.

In this chapter we discuss the measurement and inversion of surface wave phase and group velocities in the NEUS. Because the surface wave dispersion reflects the average structure along a given path, the stations and events used are selected such that the paths are confined mainly to one tectonic region, either the Grenville or Appalachian Province. For crust and upper mantle structure, long period (15-50 sec) phase and group velocities of Rayleigh waves are computed from the windowed interstation transfer functions which are estimated using a least squares inverse filtering technique. The transfer function gives the phase

delay of the interstation medium from which the phase velocities are calculated. The multiple filtering technique is then applied to the transfer function to calculate interstation group velocities.

Rayleigh wave phase and group velocities for periods ranging from 15-40 sec are calculated in southern New England by measuring the frequency-wavenumber power spectrum across the short-period M.I.T. seismic network. The Rayleigh wave phase and group velocities are inverted simultaneously using a maximum-likelihood technique. In the last section, the shear wave velocity structure is compared between different regions.

4.2 CRUST AND UPPER MANTLE STRUCTURE FROM MEASUREMENT OF INTERSTATION PHASE AND GROUP VELOCITIES

4.2.1 DATA

In this section we describe the measurement of Rayleigh wave phase and group velocities between Canadian and WWSSN station pairs. The long-period seismograph records from St. Johns, Newfoundland (STJ); Montreal, Quebec (MNT); Ottawa, Quebec (OTT); Weston, MA (WES); and Ogdensburg, NJ (OGD) are used in this part of the analysis. Great circle paths between a variety of station pairs are chosen which sample different regions in the Appalachians and the Grenville

Province. The parameters for the 10 events used and station pairs are listed in Table 4.1 and shown in Figure 4.1. Most station pairs lie within 1 degree of the same azimuth from the source. Grenville basement is sampled between OGD-OTT and OGD-MNT using events from South America and the Carribbean (Path G). The central New England Appalachians are sampled between OTT-WES and MNT-WES using earthquakes from the Kuriles, Alaska, and the Mid-Atlantic Ridge (Path A2). Structure parallel the the tectonic fabric of the northern Appalachians is sampled between STJ-WES-OGD using earthquakes from Sicily and Crete (Path A1). For simplicity, the path parallel to the Appalachians (STJ-WES,OGD) will be called path A1; the other Appalachian path (MNT,OTT-WES) path A2; and the path in the eastern Grenville Province (MNT,OTT-OGD) path G. Most of the interstation separations are 400-500 km except for those between STJ-WES and OGD which are 1500-1900 km. As will be discussed in a later section, the station spacings are relatively small and spatial resolution is good. However because of the tradeoff between spatial and temporal resolution, the errors involved in the phase and group velocities are fairly large.

Analysis of the seismic records is performed in the frequency domain. Group velocity windows between approximately 5 km/s and 2.5 km/s were digitized from enlarged copies of photographic film at an uneven sampling rate of about 1 sample/s, interpolated using the weighted

average slope technique of Wiggins (1976) and resampled at 2 samples/s. A base-line perpendicular to the swing of the galvanometer was selected in order to prevent distortion of waveforms as described by James and Linde (1971). The digitized seismograms were 20% cosine tapered, detrended, and corrected for instrument response using the formulas of Hagiwara (1958) as corrected by Brune (1962). Examples of seismograms and their corrected amplitude and phase spectra are shown in Figure 4.2.

4.2.2 INTERSTATION TRANSFER FUNCTION USING WIENER DECONVOLUTION

Using the paths shown in Figure 4.1, we calculate interstation phase and group velocities. Group velocities are more sensitive than phase velocities to structural details such as velocity gradients. However, a suite of models can produce identical group velocity curves, and phase velocities are required to discrimminate between these.

Both phase and group velocities are measured between long period station pairs by choosing stations lying on the same azimuth from an earthquake. Typically, interstation phase velocities are measured by calculating the Fourier phase difference between station pairs. Interstation group velocities can be calculated by measuring the group arrival

times at each station either directly from the seismograms or by narrow bandpass filtering each seismogram and dividing the time difference into the station separation.

Landisman et al., (1969) suggest that the windowed cross-correlogram approximates the interstation impulse response and can be used to measure both interstation phase and group velocities. Although this is a useful technique for phase velocities, test cases performed in Appendix G show that measurement of interstation group velocities from the cross-correlogram can lead to errors of almost 10% for station separations of 500 km

A more accurate technique is to estimate the interstation transfer function using a Wiener or least squares deconvolution (see Appendix G for details).

Given two seismograms positioned along the same great circle path from a source, we want to estimate the interstation transfer function (also known as the medium impulse response or Green's function). The phase of the transfer function gives the phase delay of the system which will be used to calculate the interstation phase velocity. The shape of the transfer function in the time domain provides information on the dispersiveness of the system which will be used to estimate interstation group velocity.

The convolution of the input at station 1 which drives the system and produces the output at station 2 is given by the frequency domain representation

$$F_1(\omega) e^{i\phi_1(\omega)} F_m(\omega) e^{i\phi_m(\omega)} = F_2(\omega) e^{i\phi_2(\omega)} \qquad (4.1)$$

where the subscripts 1,2 and m refer to station 1, station 2, and the interstation medium, respectively. We wish to deconvolve the output by dividing (4.1) by the input and computing the transfer function

$$F_m(\omega)\, e^{i\phi_m(\omega)} = \frac{F_2(\omega)}{F_1(\omega)}\, e^{i(\phi_2-\phi_1)} \qquad (4.2)$$

This simple deconvolution can be very unstable, particularly in the presense of spectral holes for which frequencies the filter parameters (transfer function) will be indeterminant. Various deconvolution schemes can be used to find the filter coefficients and we have chosen a least squares or Wiener deconvolution (Wiener, 1949; Treitel and Robinson, 1966; Peacock and Treitel, 1969).

The cross-correlation function gives

$$F_1^2\, F_m\, e^{i\phi_m} = F_1 F_2\, e^{i(\phi_2-\phi_1)} \qquad (4.3)$$

which are actually the normal equations solved using Levinson recursion in the least squares deconvolution (see Appendix G). Thus, by comparison of equations 4.2 with 4.3, we see that the cross-correlogram gives the phase delay of the interstation medium but not necessarily the group delay.

4.2.3 MEASUREMENT OF INTERSTATION PHASE VELOCITIES

In this section, we discuss the measurement of interstation phase velocities. Assuming identical

instruments (or that an instrument correction has been applied) and that the focal phase, $\phi_o(\omega)$, is a constant along one azimuth, the observed Fourier phase at each station along a great circle path is

station 2:

$$^2\phi_{obs}(\omega) = \frac{\omega x_2}{c(\omega)} + \phi_o(\omega) + \phi_{in}(\omega) - \omega t_2 \pm 2\pi N$$

station 1:

$$^1\phi_{obs}(\omega) = \frac{\omega x_1}{c(\omega)} + \phi_o(\omega) + \phi_{in}(\omega) - \omega t_1 \pm 2\pi N$$

where: ti - digitizing start time at station i; xi - epicentral distance to station i; $\phi_{in}(\omega)$ - instrumental phase shift.

Subtracting gives the phase difference

$$\Delta\phi_{obs} = \frac{\omega \Delta x}{c(\omega)} - \omega \Delta t \pm 2\pi N \quad \text{where} \quad \begin{aligned} \Delta\phi &= {}^2\phi_{obs} - {}^1\phi_{obs} \\ \Delta x &= x_2 - x_1 \\ \Delta t &= t_2 - t_1 \end{aligned}$$

Rearranging terms gives the following formula for interstation phase velocity

$$c(T) = \frac{\Delta x}{\Delta t + (\Delta\phi_{obs} \pm N)T} \qquad (4.4)$$

Phase velocities were first computed by measuring the phase differences between the two stations. However, as can be seen from Figure 4.2, the phase spectrum can be very unstable, particularly at higher frequencies, and was difficult to unwrap. Because the station separation is small, the proper integer N is obvious but the phase velocities are very sensitive to small errors in the phase.

From equation 4.2, it can be seen that the phase spectrum of the interstation transfer function gives the phase delay

of the system and can be used to measure interstation phase velocities. The transfer function contains information on digitizing start times and the phase velocities are computed using

$$c(T) = \frac{\Delta x}{t_o + (\phi_{tf}(T) \pm N)T} \qquad (4.5)$$

where ϕ_{tf} is the phase of the transfer function and t0 is the first lag time.

To reduce the effect of random noise in the phase spectrum, the transfer function can be windowed where the correlation is high. The phase spectrum of the windowed transfer function is recomputed. The resulting phase spectrum is much smoother and the phase velocities are more stable. Landisman et al., (1969) suggest that the length of the windowed cross-correlogram (or transfer function in this case) be approximately five times the value of the longest period desired.

4.2.3 MEASUREMENT OF INTERSTATION GROUP VELOCITIES

Because the dispersion in the transfer function is controlled by the properties of the interstation medium, it can be used to measure interstation group velocities. Group velocities can be accurately measured using narrow band-pass filtering (multiple filtering; Dziewonski et al. (1969)). The method is particularly useful when a signal is not well dispersed such as in the vicinity of a stationary phase

where visual measurements are impossible.

The seismic signal is first detrended, tapered, padded with at least 2N zeros (where N is the number of samples), Fourier transformed, and corrected for instrument response. The signal is then narrow bandpass filtered about a center frequency ω_o . It is assumed that the bandpassed trace represents the real part of a complex waveform and the imaginary part is the Hilbert transform of the filtered signal (Oppenheim and Schafer, 1975). Depending on the dispersive characteristics of the medium, the group arrival time is approximately equal to the time of maximum amplitude of the envelope of the complex filtered signal (Cara, 1973). It should be noted that the phase velocity can also be computed from the instantaneous phase at the time of the maximum amplitude (Taner et al., 1979). This process is repeated for a series of center frequencies and the values of the envelope function are plotted as a function of frequency vs. time or group velocity.

The original signal, f(x,t), is convolved with a bandpass filter,h0(t), symmetric about a center frequency ω_o , giving a filtered trace f0(x,t). In the frequency domain, the convolution is given by

$$f_o(x,t) = \frac{1}{2\pi}\int_{-\Delta\omega}^{+\Delta\omega} F(\omega)\, H(\omega-\omega_o)\, e^{i(\omega t - kx)}\, d\omega \qquad (4.6)$$

where, x - epicentral distance, $\Delta\omega$ - half bandwidth, ω_o - center frequency, ω_c - cutoff frequency, and $\Delta\omega = |\omega_c - \omega_o|$. As discussed by Dziewonski et al. (1969), a Gaussian filter gives the optimum tradeoff between time and frequency

resolution. The spectrum of the filter is defined to be

$$H(\omega-\omega_0) = e^{-\alpha\left(\frac{\omega-\omega_0}{\omega_0}\right)^2} \qquad (4.7)$$

A constant Q filter is often used where the bandwidth, $\Delta\omega$, is proportional to the center frequency, ω_0;

$$Q \sim \frac{\Delta\omega}{\omega_0} = BAND$$

or

$$\Delta\omega = |\omega_c - \omega_0| = BAND\ \omega_0$$

Thus, the frequency cutoffs are given by

$$\omega_c = (1 \pm BAND)\omega_0$$

and the filter bandwidth increases with center frequency. On a log-period scale this gives constant resolution of group velocity because the filters have equal width. Representations of signal power as a function of frequency and time or group velocity are found by calculating the envelope function of the bandpassed signals (Oppenheim and Schafer, 1975; Taner et al., 1979). In complex waveform analysis, the bandpassed signal, fr(t), is represented as the real part of a complex function of time;

$$S(t) = f_r(t) + i f_i(t) = A(t) e^{i\phi(t)} \qquad (4.8)$$

where $A(t) = \sqrt{f_r^2(t) + f_i^2(t)}$ (4.9) =envelope function

and $\phi(t) = \tan^{-1}\left(f_i(t)/f_r(t)\right)$ (4.10) =instantaneous phase

The real and imaginary parts of s(t) are related by their Hilbert transforms. Once fi(t) is calculated from the ideal Hilbert tranform of fr(t) (by shifting the phase by 90 degrees), the envelope function of the bandpassed signal can be calculated from equation 4.9. An example of a narrow bandpassed signal and its envelope function after inverse Fourier transforming is shown in Figure 4.3.

To the first order, the maximum of the envelope of the filtered signal corresponds to the arrival time of the wave group about the center frequency (Dziewonski et al.,1972). This is derived by truncating the Taylor series expansion of $k(\omega)$ and $F(\omega)$ past the first order and inserting the expansions into equation 4.6. However, as discussed by Cara (1973) and Dziewonski et al. (1972), this approximation is not necessarily valid for frequencies showing strong dispersion or in the vicinity of a stationary phase where $\frac{d^2k}{d\omega^2}$ and $\frac{d^3k}{d\omega^3}$ are not always small. Thus, a third order expansion of $k(\omega)$ is necessary to adaquately describe most dispersion curves. Numerical experiments have shown that the errors caused by the above assumption are around 1-2% (Dziewonski et al, 1972). However, errors can be minimized if the relative bandwidth, and the damping of the Gaussian filter are selected of the basis of the first order dispersion characteristics of the region under study (Cara, 1973; Inston et al., 1971).

Many of the problems associated with the dispersiveness of the system can be reduced by computing the interstation

transfer function. As discussed in section 4.2.2, the dispersion observed on the transfer function is a function of the station separation and the properties of the interstation medium. Because the interstation separation is generally much less than the epicentral distance, the transfer function exhibits less dispersion than each of the individual stations. Thus, the systematic errors in calculated group velocities caused by the assumptions of small $\frac{d^2k}{d\omega^2}$ terms are reduced. Attempts were made to find the interstation group velocities by using the multiple filtering technique on each of the individual seismograms and taking the difference in group arrival times at each station. However, because the interstation distance is small relative to the epicentral distance, a small error in the absolute travel time resulted in large errors in group velocity. This technique also requires much more computation time than analysis of the windowed transfer function.

Figure 4.4 shows examples of contoured plots of group velocity vs. frequency derived by performing narrow bandpass filtering on the windowed transfer functions. The letters and numbers correspond to signal power in db (see description of Figure 4.4 for details). As discussed above and in section 4.2.4, the transfer function shows little dispersion over distances of 500 km and the group velocities can often be very unstable, particularly in the vicinity of spectral holes. Velocities were generally determined by

picking the maximum of the envelope function. However, in a number of cases we ignored small frequency ranges which gave unreasonable group velocities.

4.2.4 ERROR ANALYSIS

To determine whether differences in observed phase and group velocities in various regions are significant, it is necessary to identify the sources of errors and their effects on the measurements. Subsequently, it will be necessary to determine the effects of measurement error on the model derived from inversion of the dispersion curves (see section 4.4). Measurement errors result for a number of reasons, including instrument and processing errors, noise in the data, and assumptions and techniques used in calculating phase and group velocities.

Digitizing errors were checked by comparing computer generated plots with the original seismograms. As discussed in section 4.2.1, to prevent waveform distortion and systematic spectral errors, the vertical axis of the digitizing table was oriented parallel to the estimated swing of the galvanometers. Corrections were made for instrument response using the formulas of Hagiwara (1958) with the polarity correction of Brune (1962). Timing corrections for WWSSN stations are generally less than 0.1 second which is only a small fraction of the travel time for

a given phase between two stations.

Epicenter mislocation may be a small source of error related to the calculation of relative distance between two stations. Because the events used were all relatively large (Table 4.1) the ISC locations are probably accurate to within 25 km. Interstation distance is the factor used in the phase and group velocity determination, and azimuth errors caused by a tangential mislocation of 25 km at a distance of 5000 km to the nearest station will be much less than one degree. At interstation distances of 500 km an azimuth error of one degree causes a relative distance error of approximately 0.1 km resulting in velocity errors of less than 1%.

For most events used, the stations were within 1 degree of the great circle path. Although it is assumed effects of lateral refraction and multipath transmission are small, results from section 4.3 show that shorter periods (less than 20 sec) can have apparent azimuths of possibly 10 degrees from the true azimuth. These effects are difficult to correct for using a two-station technique and can cause phase or group velocities to be too high by up to .05 km/sec. However, few of the seismograms used in this study show serious effects of beating resulting from multipathing.

Signal generated noise in the form of body wave arrivals or higher mode surface waves can also contaminate the fundamental mode wavetrain. For this study, digitized windows were selected to include higher mode arrivals.

However, for most events, if higher modes were present, they showed little correlation between stations and were not evident on the filtered transfer functions.

Errors in phase velocity can be determined by estimating the errors in the phase spectrum of the transfer function. For period T, the percentage error in phase velocity caused by a phase error, $\Delta\phi$, is

$$\frac{\Delta c}{c} = \frac{\Delta\phi}{\phi} = \frac{\lambda}{2\pi\Delta x}\Delta\phi \qquad (4.11)$$

where λ is the wavelength and Δx is the interstation distance. The phase errors are related to the signal to noise ratio (Clay and Hinich, 1970) by

$$\Delta\phi \sim \frac{|N(f)|}{|S(f)|}$$

where $|N(f)|$ and $|S(f)|$ are the values for the amplitude spectra of the noise and signal for frequency f. Then the phase velocity errors for frequency f become

$$\frac{\Delta c}{c} = \frac{\lambda}{2\pi\Delta x}\frac{|N(f)|}{|S(f)|} \qquad (4.12)$$

By calculating the interstation phase velocities from the windowed transfer function, the uncorrelated noise between the two records is reduced, thus decreasing the magnitude of the errors.

In general, the smoothness of the unwrapped phase spectrum indicates the accuracy in phase determination. By comparing Figure 4.2 with Figure 4.5 it can be seen that the phase spectra of the windowed transfer functions are much more stable than that of the individual stations. For a number of events, the phase spectra were smoothed by fitting

a polynomial to the unwrapped phase. Figure 4.6 shows examples of a polynomial fit to the unwrapped phase and the calculated phase velocity. The signal to noise ratio can also be improved by increasing the number of measurements. At the expense of spatial resolution, phase velocity errors can be reduced by increasing the distance to wavelength ratio (equation 4.12). For many paths in this study, the wavelength to distance ratio varied from 1/10 to 1/2 which is quite large. However, a number of other studies have achieved phase velocity measurements accurate to 2% or better with similar wavelength to distance ratios (McEvilly, 1964; McCowan et al., 1978).

Figures 4.7 a,b,c show measured phase and group velocities for three different paths; 4.7a - between STJ and WES and OGD parallel to the trend of the Appalachians (Path A1); 4.7 b - paths between MNT, OTT, and WES which are mainly confined to the New England Appalachians (Path A2); and 4.7c - paths between OGD and MNT, OTT which sample eastern most Grenville Province (Path G). Figure 4.8 shows the phase and group velocities averaged at each period and standard deviations. Also shown in Figures 4.8 are phase and group velocities calculated from structural models (see section 4.4). Table 4.2 summarizes the phase and group velocities and standard deviations shown in Figure 4.8 and it can be seen that the phase and group velocities are usually determined to within 0.05 to 0.15 km/s (approximately 2.5 - 5%). Errors were set to 0.10 and 0.20

km/s for phase and group velocity respectively, for periods with insufficient data.

In general, the group velocity errors are slightly larger than the phase velocity errors (Table 4.2). This is consistent with the discussion by Knopoff and Chang (1977) who show under the condition of random and uncorrelated phase errors that the group velocity errors will be larger than the phase velocity errors.

As discussed in section 4.2.3, systematic errors in group velocity may arise from approximations made in the multiple filtering analysis. The group velocity errors may be correlated between neighboring periods if the samples are very close. Using a constant Q filter, the percentage error in group velocity is approximately (Der et al.,1970)

$$\frac{\Delta u}{u} = \frac{u}{\pi \Delta x Q f} \qquad (4.13)$$

which implies errors of 15% for the period range used in this study.

4.2.6 DESCRIPTION OF RAYLEIGH WAVE PHASE AND GROUP VELOCITIES

A summary of the interstation phase and group velocities, and a comparison with other dispersion curves measured in eastern North America is shown in Figures 4.8 and 4.9. As can be seen from Figure 4.8 the differences between the three paths are subtle and for many periods are not

significant under consideration of the standard errors.

The group velocities for path A1 and G are quite similar while the phase velocities along A1 are generally less than those along G. As discussed by Pilant and Knopoff (1970), a suite of different earth models can produce similar group velocity curves with different phase velocities. In contrast, paths A2 and A1 show similar phase velocity curves but the group velocities differ for periods less than about 26 seconds.

For most periods, the phase velocities along all three paths fall in between those of the Canadian Shield (Brune and Dorman, 1963) and the New York state - Pennsylvania area (Dorman and Ewing, 1962). The group velocities in all regions are similar except the velocities measured in this study show a steeper increase between periods of 20 and 35 seconds indicating greater dispersion.

Although the differences in phase and group velocities for the three paths are not large, the dispersion curves will be inverted separately in a later section to show that the models are consistent with the body wave travel time studies discussed in Chapters 3 and 5.

Addition of Love wave dispersion data theoretically can help increase the resolution of a surface wave inversion (Wiggins, 1972). However, errors in compiling Love wave velocities may be caused by the contamination of fundamental modes with higher modes and in digitizing and rotating two horizontal seismograms to the radial and transverse

directions. Thus, the errors in calculating the Love wave dispersion over the short continental paths may be larger than those involved with the Rayleigh waves. Inclusion of Love wave dispersion curves probably would not enhance the ability to discrimminate between different crustal models for this experiment.

4.3 ESTIMATION OF FREQUENCY-WAVENUMBER POWER SPECTRUM IN SOUTHEASTERN NEW ENGLAND

The interstation phase and group velocities measured in the previous section are subject to significant errors because of the relatively large wavelength to distance ratios. In this section, phase velocities of fundamental mode Rayleigh waves recorded across six short period stations in southeastern New England are used to invert for crust and upper mantle velocity structure. The phase and group velocities are measured from the frequency-wavenumber (f-k) power spectra of signals traversing the network. Because the network diameter is small relative to the wavelengths being measured, the errors in the phase velocity calculations would be large using the conventional two station technique. In contrast, because the frequency-wavenumber method used in this study is shown to be a stacking technique, the errors are reduced by $1/\sqrt{N}$ where N is the number of stations. Thus, accurate phase and

group velocity measurements are possible while maintaining good spatial resolution. Additionally, beamsteering allows for the minimization of effects caused by multipathing which are shown to be particularly severe for periods less than 20 seconds.

Early studies utilizing a time-domain wavefront correlation method were applied to surface waves propagating across Japan (Aki, 1961) and across the United States (Ewing and Press, 1959). More recently, high resolution techniques have been developed for analyzing seismic signals in frequency-wavenumber space using data from specially designed arrays such as LASA and NORSAR. Theoretical development of the application and limitations of the f-k approach are outlined by Burg (1964), Clay (1970), Lacoss et al. (1969), Linville and Laster (1966), Smith (1956), and Arnold (1978).

Applications of the f-k technique for the study of surface waves include the analysis of microseisms (Toksoz and Lacoss, 1968) and Rayleigh and Love wave multipath propagation at LASA (Capon, 1970). The method has also been successful in separating out higher modes propagating across Europe (Nolet and Panza, 1976) and the United States (Cara, 1978). Frequency-wavenumber power spectra have been used in geothermal exploration to identify the sources of seismic noise propagating from areas of hot spring activity (Liaw and McEvilly, 1979; Donze and Laster, 1979).

The technique used in this study to estimate the

frequency-wavenumber power spectra is discussed in Appendix D.

4.3.1 DATA

Two earthquakes occurring on August 23, 1978 in Costa Rica (10.05 N, 85.25 W, depth = 48 km, Ms = 7.0) and December 12, 1979 in Equador (1.584N, 79.386W, depth=33, Ms=7.9) generated surface waves in the period range of 10 to 30 seconds that were recorded very well by six stations of the Massachusetts Institute of Technology short period network (Figure 4.10). The stations are all equipted with a vertical component, 1 hz seismometer. Signals are telemetered to M.I.T. and recorded on 16mm develcorder film. For the Costa Rica event, a six minute section of each record with group velocities corresponding to fundamental mode Rayleigh waves was digitized at approximately 4 samples/sec, interpolated using the weighted average slope technique described by Wiggins (1976) and resampled at 1 sample/sec. For the Equador earthquake, an eleven minute section corresponding to a group velocity window of about 4 to 2.5 km/s was digitized for the same six M.I.T. stations used for the Costa Rica event. Filtered seismograms bandpassed between 10 and 50 seconds are shown in Figure 4.11. As can be seen from Figure 4.11, the signals are fairly coherent across the array and show some evidence of

multipathing as indicated by the "beating" observed on many of the records.

Group arrivals thought to be higher mode Rayleigh waves were also digitized. However, because of low signal to noise ratios and inadequate array response, it was not possible to separate out the higher modes. Analysis for the Costa Rica event was also complicated by P waves from an aftershock occurring 12 minutes after the main shock (mb = 5.5) which masked part of the higher mode wavetrain.

The amplitude and phase spectra for stations, uncorrected for instrument response are shown in Figure 4.11. The signals are strongly peaked at approximately .055 hz (T = 18 seconds). As can be seen from Figure 4.12, these frequencies are about 10^4 magnification units down from the peak response of each station. Although the shape of the response curves for the MIT stations are similar, the absolute magnifications are not well known. Therefore, the measured amplitude spectra for each station were normalized by dividing through by the maximum amplitude. The phase spectra were left uncorrected for instrument response because the phase correction is nearly constant for frequencies well away from the peak response (Hagiwara, 1958). The windowed seismograms were also 20% cosine tapered. Appendix D gives a detailed description of the sources of errors in the frequency-wavenumber analysis.

4.3.2 INTERPRETATION AND DISCUSSION

Using the Costa Rica earthquake, the f-k power spectra was computed using the total 6 minute signals shown in Figure 4.11 and along the beam direction of 204 degrees (measured clockwise from north) representing the azimuth between the earthquake and the array center. The power spectra is shown in Figure 4.13 where the frequency units are in hz, and wavenumber in km and power is presented in 6 decibel steps below the maximum amplitudes measured. Reasonable phase velocities were computed for frequencies below .05 hz (20 sec). However, for frequencies above .05 hz, the calculated phase velocities increased rapidly to almost 3.9 km/sec possibly indicating group arrivals coming in off-azimuth with high apparent velocities.

This was confirmed when the array was steered across a sweep of azimuths between 190 and 225 degrees. Figures 4.14 a-d, show the beamformed signal for frequencies decreasing from .0645, .0596,.0547,.0508 hz respectively (T = 15.5, 16.8, 18.3, 19.7 seconds). As can be seen from Figure 4.14, arrivals with frequencies above .05 hz come in as much as 15 degrees off azimuth which partially explains the large apparent phase velocities. For frequencies around .05 hz the arrivals are incident from an azimuth of approximately 204 degrees.

To reduce the problem of the lateral refractions, we selected a 3.3 km/sec group velocity window with a length of

3 minutes which included arrivals preceeding the first beat shown in Figure 4.11. The recomputed f-k power spectrum is shown in Figure 4.15 and the phase velocities in Figure 4.18. From Figure 4.18, it appears that the shortened group velocity window excluded much of the power arriving off-azimuth.

Lateral refraction of Rayleigh waves have been discussed by many authors including McGarr (1969), Capon (1970), and Sobel and von Seggern (1978). Identification of the discontinuities causing the lateral refractions can be a highly non-unique problem. However, from the regionalized phase velocity map for 20 second Rayleigh waves presented in Sobel and von Seggern (1978), it is possible that the multipathed arrivals recorded in New England were refracted south of the United States and propagated northwards along the continental margin.

The frequency-wavenumber power spectra on the beam direction of the 12/12/79 Equador event (191 degrees) is shown in Figure 4.16. The calculated phase velocities were very smooth but were consistently high. Beamsteering indicated that all periods were arriving from an azimuth approximately 10 degrees to the southeast of the true azimuth. Figure 4.17 shows the beamsteered power spectra for two frequencies for an azimuth range between 170-210 degrees. The seismograms from the Equador event shown in Figure 4.11 are very coherent and show little effects of multipath transmission as evidenced by the lack of

modulation. Thus, rather than using a group velocity window to elimate multipathed arrivals, the phase velocities were reduced by multiplying all periods by $\cos(10^{\circ})$. The phase velocities from both events are shown in Figure 4.18. For periods above 30 seconds, the phase velocities were still quite high. These errors may be caused by the low signal to noise ratio at these longer periods.

Group velocities were obained by differentiating the polynomial fit to the power spectra. The differentiation became unstable in both cases for periods less than about 20 seconds and greater than 32 seconds.

4.4 SIMULTANEOUS INVERSION OF RAYLEIGH WAVE PHASE AND GROUP VELOCITIES USING A MAXIMUM-LIKELIHOOD TECHNIQUE

Once the phase and group velocity curves for different paths are compiled it is necessary to interpret them in terms of earth structure. Trial and error methods can be very time consuming and give no information regarding the uniqueness (resolution) or errors in the solution. A more systematic and versatile approach is to perform a linearized inversion which minimizes the errors in a least squares sense.

Initially, an inversion routine was programmed that inverted just phase velocities. Although structures could be found that accurately reproduced observed phase velocities, they often failed to match observed group

velocities. The inversion scheme was then expanded to invert phase and group velocities simultaneously.

As discussed in section 4.2.4, observation errors differ between phase and group velocities and as a function of period. Also, calculation of phase and group velocity partial derivatives involves the evaluation of energy integrals over the thickness of a layer. Thus, it is necessary to weight the solution in both data and model space and a maximum-likelihood approach is used.

4.4.1 INFORMATION DERIVED FROM FUNDAMENTAL MODE RAYLEIGH WAVE PHASE AND GROUP VELOCITIES

In setting up the surface wave inversion, it is necessary to parameterize the problem and define what phase and group velocities of the fundamental Rayleigh mode reveal about earth structure. Inversion of phase velocities alone presents a non-unique problem because of the trade-off between certain parameters such as velocity and layer thickness. However, inversion of group velocities alone results in a more non-unique problem (Pilant and Knopoff, 1970) resulting from the derivative relationship between phase and group velocity. Because of a constant of integration, two structures generating different phase velocity curves can produce identical group velocity curves. Although phase and group velocities are not completely independent variables, they do provide slightly differing

sensitivities to different structures and can be used simultaneously to increase resolution.

Much information on the resolving power of phase and group velocities can be obtained by examining their partial derivatives. The methods used for the calculation of phase and group velocity partial derivatives is outlined in Appendix E. Der and Landisman (1972) and Knopoff and Chang (1977) give a detailed discussion of the sensitivity of phase and group velocities to various layer parameters as a function of period. For fundamental mode Rayleigh waves, both phase and group velocities are most sensitive to shear velocity for all depths, while the density is the second-most important parameter. However, for the crust, the compressional wave velocity also has a fairly significant effect on dispersion. In general, the magnitude of the phase velocity partials are smaller and smoother than those for the group velocity. Thus, it appears that for equal errors, group velocities have greater resolving power than phase velocities. With respect to shear velocity, the group velocity partials have a zero crossing while the phase velocity partials do not. This indicates that the effects of a shear velocity increase at one depth can be compensated for by a decrease at another depth with no resulting change in the group velocity curve. This further confirms that two different structures can produce the same group velocity dispersion. Numerical experiments show that, for equal errors, group velocities are more sensitive to velocity

gradients or changes in major interface depths such as the Moho (Der and Landisman, 1972; Knopoff and Chang, 1977). Under certain conditions, the group velocity errors may inherently be larger than those of the phase velocity which will degrade the resolving power of the group velocity (see section 4.2.4).

Shear wave velocity has a greater effect on phase and group velocities than density, even though the effect of density is not small (Burkhard and Jackson, 1976). However, phase and group velocity partials with respect to density have a zero-crossing indicating the trade-off with depth. Shear velocity and density are not independent variables and are coupled by the equation $\beta=\sqrt{\mu/\rho}$. Thus, including both shear velocity and density in the inversion using fundamental mode phase and group velocities does not necessarily decrease the number of degrees of freedom (Wiggins, 1972; note his definition of number of degrees of freedom is actually the number of non-zero eigenvalues, p, which is not the statistical definition , m-p, where m is the number of observations).

Compressional wave velocities have little effect on either phase or group velocities except for shallow layers. Thus, P-wave velocities can be set according to regional refraction profiles (which was done in this study) or can be adjusted to maintain a reasonable Poisson's ratio as the shear velocity is adjusted.

The phase and group velocities are inverted for shear

velocity only, while density and P-wave velocity are held fixed. The simultaneous inversion for shear velocity and density does not improve the problem because the two paramenters are not independent. P-wave velocities are known fairly well from regional travel time studies.

The effects of imprecisely known interface depths on the final solution are minimized by using a large number of thin layers. This makes adjoining layers dependent on each other and avoids a diagonal resolution matrix. The result gives an average of the actual velocity model over a depth range where the resolution in significant.

The details of the maximum-likelihood inversion scheme are given in Appendix F. The method is basically a stochastic inverse on a transformed system (Wiggins, 1972; Aki and Richards,1980) where elements of the data space are weighted according to the observation errors and the model space is uniformly dimensionalized.

In summary, simultaneous inversion of phase and group velocity improves the inversion because the group velocity may resolve certain structures better than the phase velocity. The group velocity is also useful in fixing the slope of the phase velocity curve and may provide added constraints to the inversion.

4.4.2 INVERSION RESULTS

In this section results from the inversions of the dispersion information from the three paths (A1, A2, G) are presented. It must again be emphasized that because of the relatively large errors in the phase and group velocity measurements, the differences between the dispersion curves are subtle and the models are very non-unique. However, models are calculated which are consistent with the body wave data presented in chapters 3 and 5.

Initial models for the inversion were chosen on the basis of the refraction models discussed in Chapter 3. To minimize the effect of the initial model, primary runs were made using a large number of thin (4 km) layers. In this case, if the initial guess for the crustal thickness is too great, the final velocities for the lower crust and upper mantle will be excessively high. For final runs, thicker layers were used which eliminated the false impression of velocity resolution attainable using thin layers. Models using thin layers were similar to those using thick layers except that areas showing velocity gradients which may or may not have been real were observed. Also, a better fit to the dispersion curves was attainable because the model had more parameters and greater flexibility. For the period range used, the resolution was optimal for the crust between 10-40 km, so 10 km thick layers were chosen for the crust, and 20 km layers for the mantle. Final models were chosen on the basis of resolution, model covariance, RMS fit to the dispersion and on the reliability of the solution. If the

final solution gave abnormal structures such as excessively large crustal low-velocity zones or unreasonable Sn velocities with large errors, different initial models were used or the damping of the transformed system was increased.

The measurement errors shown in Figure 4.7 and listed in Table 4.2 were calculated by taking the standard deviation of the phase velocities from the mean. The phase velocity errors were doubled to give the group velocity errors which decreased the weight of the group velocities on the final inversion. If there were only two or three data points, the errors were set at 0.20 km/s for group velocities, and 0.10 km/s for phase velocities. Because path G has little data, the standard deviations were set to 0.1 km/s for phase velocities and 0.2 km/s for group velocities for all periods.

The final shear velocity models and errors for the four paths are shown in Figure 4.19 and resolving kernals in Figure 4.20. The model errors are calculated by taking the square root of the diagonal elements of the covariance matrix. The fits to the observed phase and group velocities are shown in Figures 4.8.

The solution for path A1 converges rapidly to a model that is very consistent with the Appalachian refraction model. It is felt that this is the most reliable of the models because the path was the longest and the measured phase and group velocities were most consistent for different events. The crust is characterized by two

well-defined layers with a high velocity lower layer and is approximately 40 km thick.

The shear velocity model for the Grenville path (path G) is also characterized by a two layer crust that is approximately 35 km thick. However, the lower crust does not exhibit velocities that are as high as those found along path A1. Assuming reasonable Poissons ratios of approximately 0.25, the lower crustal compressional velocities are only about 0.1 km/s higher than the 6.6 km/s crust found from the refraction data. The two layer crust from the inversion of the Grenville dispersion data is not in agreement with the refraction results although both models have an average shear velocity of about 3.7 km/s. This may be explained by noting the location of path G which crosses part of the Taconic thrust belt. The thrust belt is a thick pile of sediments and metasediments possibly 10 km thick (Diment et al., 1972) which would probably be characterized by a thick low velocity layer overlying Grenville basement.

The calculated phase and group velocities for paths A1 and G are relatively similar even though the models are different. The model for path A1 has a slightly thicker crust with a higher velocity lower layer than the model for path G and there is a trade-off between layer thickness and velocity. This demonstrates the inability of the surface waves to discriminate between different crustal models in an older tectonic region where the velocity differences are not

great.

The dispersion curves for path A2 were more difficult to fit because phase and group velocities were inconsistent. The observed phase and group velocities appear to be too low and high, respectively, for a good fit to any reasonable model. The final model is similar to those expected from the refraction results and shows a high velocity lower crustal layer with a 40 km thick crust. There appears to be more of a velocity gradient in the lower crust for this path. Also shown in Figures 4.8 and 4.19 is a good fit the just the phase velocity curve and the corresponding model. The model is very consistent with that which would be expected across the region traversed by path A2. This area probably has the thickest crust in the entire region under study, and a 45 km thick crust generates phase velocities that fit the observed very well while maintaining a high velocity lower crustal layer.

The dispersion curves measured from the frequency-wavenumber power spectra in southeastern New England were inverted separately over a narrower band of periods than for the other paths. The results are similar to the other Appalachian paths in that they are consistent with a high velocity lower crust.

Table 4.1

Events and Stations Used in Surface Wave Analysis

Events

Date	O.T.	Lat.	Long.	M_s	Stas.	Sta. separation
8/14/69	14:19:01.6	43.1N	147.5E	6.1	MNT-WES	392.5
6/15/75	00:19:34.0	43.667N	147.801E	5.9	"	"
11/6/73	09:36:05.0	51.6N	175.4W	6.4	OTT-WES	485.9
2/27/70	07:07:58.1	50.1N	179.6W	6.0	"	"
12/9/72	06:44:40.4	15.2N	45.2W	5.7	WES-OTT	"
5/4/72	21:40:00.9	35.124N	23.612E	5.9	STJ-WES	1569.0
"	"	"	"	"	STJ-OGD	1880.0
1/15/68	02:01:04.1	37.78N	13.03E	6.1	STJ-WES	1569.0
"	"	"	"	"	STJ-OGD	1880.0
9/19/72	01:36:52.4	19.5N	70.1W	6.1	OGD-OTT	488.7
4/5/75	09:34:36.6	10.0N	69.8W	6.1	"	"
7/30/68	20:38:42.0	6.930S	80.455W	6.0	OGD-MNT	499.3

Stations

MNT	45.503N	73.623W
WES	42.385N	71.322W
OTT	45.393N	75.715W
STJ	47.57 N	52.73 W
OGD	41.067N	74.617W

Table 4.2

Mean Phase and Group Velocities and Phase Velocity Standard Errors

	Path A2			Path A1			Path G		
T	C	U	E	C	U	E	C	U	E
14	3.40	3.00	.09	3.40	3.08	.09	3.46	3.04	.10
16	3.47	3.02	.08	3.45	3.08	.09	3.54	3.04	.10
18	3.54	3.08	.06	3.52	3.08	.07	3.58	3.06	.10
20	3.60	3.14	.05	3.56	3.06	.05	3.64	3.15	.10
22	3.66	3.20	.05	3.64	3.06	.05	3.68	3.22	.10
24	3.72	3.26	.06	3.68	3.16	.05	3.74	3.26	.10
26	3.77	3.34	.06	3.74	3.26	.05	3.76	3.34	.10
28	3.82	3.42	.06	3.80	3.40	.05	3.82	3.44	.10
30	3.86	3.50	.07	3.85	3.52	.05	3.86	3.54	.10
32	3.88	3.56	.07	3.88	3.58	.05	3.92	3.60	.10
34	3.92	3.64	.08	3.92	3.64	.05	3.94	3.65	.10
36	3.95	3.68	.06	3.95	3.68	.06	3.96	3.68	.10
38	3.98	3.72	.08	3.98	3.72	.10	4.00	3.74	.10
40	3.99	3.74	.08	4.00	3.74	.10	4.02	3.76	.10
42	4.00	3.76	.08	4.02	3.75	.10	4.05	3.78	.10
44	4.00	3.78	.07	4.04	3.76	.10	4.08	3.82	.10
46	4.01	3.79	.07	4.05	3.76	.10	4.10	3.84	.10
48	4.02	3.80	.07	4.05	3.77	.10	4.12	3.84	.10
50	4.02	3.82	.07	4.06	3.78	.10	4.14	3.85	.10

Table 4.3

Final Velocity Models From Inversion of Phase and Group Velocities

Layer	Thickness (km)	Depth (km)	V_p	V_s	Density (g/cc)
		Path A1			
1	10.	0.	6.0	3.4	2.7
2	10.	10.	6.2	3.5	2.75
3	10.	20.	7.0	4.0	3.0
4	10.	30.	7.0	4.0	3.0
5	20.	40.	8.1	4.6	3.3
6	20.	60.	8.1	4.5	3.3
7	20.	80.	8.2	4.5	3.3
8		100.	8.2	4.6	3.3
		Path A2			
1	10.	0.	6.1	3.5	2.8
2	10.	10.	6.2	3.5	2.8
3	10.	20.	6.8	3.8	3.0
4	10.	30.	7.0	4.0	3.0
5	20.	40.	8.1	4.6	3.3
6	20.	60.	8.1	4.5	3.3
7	20.	80.	8.2	4.6	3.3
8		100.	8.2	4.7	3.3
		Path G			
1	5.	0.	6.0	3.5	2.7
2	10.	5.	6.0	3.5	2.7
3	10.	15.	6.6	3.8	2.8
4	10.	25.	6.8	3.8	2.85
5	20.	35.	8.1	4.5	3.3
6	20.	55.	8.1	4.5	3.3
7	20.	75.	8.2	4.7	3.3
8		95.	8.2	4.7	3.3

FIGURE CAPTIONS

Figure 4.1 Stations and events used for surface wave analysis.

Figure 4.2 Seismograms and corrected spectra for 8/14/69 and 12/9/72 events.

Figure 4.3 Narrow band-passed signals and envelope functions for frequencies of .04980 hz and .03979 hz, BAND=0.25; (a) alpha = 0. (boxcar function); (b) alpha = 20.; (c) alpha = 50.

Figure 4.4 Examples of group velocities from multiple filtering of interstation transfer function. Character a represents lowest power; 9 - highest power in dbinc increments. (a) 8/14/69 event; (b) 12/9/72 event; (c) 5/4/72 event.

Figure 4.5a Transfer functions for 8/14/69, 12/9/72, and 5/4/72 events.

Figure 4.5b Spectra of signals shown in Figure 4.5a.

Figure 4.6a Unwrapped phase spectrum and polynomial fit to spectra of three events shown in Figure 4.5b.

Figure 4.6b Interstation phase velocities calculated from smoothed phase spectrum for three events shown in Figure 4.6a.

Figure 4.7 Composite phase and group velocities for all events; (a) Path A1; (b) Path A2; (c) Path G.

Figure 4.8 Averaged phase and group velocities and standard deviations with calculated velocities from models shown in Figure 4.20. (a) Path A1; (b) Path A2; (c) Path A2 with 45 km crust; (d) Path G.

Figure 4.9 Phase and group velocities from this study compared with those of other studies in eastern North America.

Figure 4.10 MIT stations used in frequency-wavenumber analysis.

Figure 4.11 Short-period seismograms and examples of spectra from 2 events used in F-K analysis.

Seismograms are bandpassed filtered between 10 and 50 seconds. (a) 8/23/78 event; (b) 12/12/79 event.

Figure 4.12 Typical instrument response for MIT short period stations.

Figure 4.13 Frequency-wavenumber (F-K) power spectra from 8/23/78 event using total signal shown in Figure 4.11a. Beam direction is 204 degrees from north (azimuth to the event). Shading in 6db steps below maximum power is shown in the figure legend.

Figure 4.14 Beam-steered power spectrum for selected frequencies of .0508, .0547, .0596, and .0645 hz along a range of azimuths from 8/23/78 event. Actual azimuth to event is 204 degrees from array center. Same shading as in Figure 4.13.

Figure 4.15 F-K power spectra using 3.3 km/s group velocity window of three minute length along beam direction of 204 degrees. Same shading as in Figure 4.13.

Figure 4.16 F-K power spectra from 12/12/79 event using total signal shown in Figure 4.11b. Beam direction is 181 degrees (azimuth to the event). Symbol 0 corresponds to lowest power; 5 to highest in 6 db steps below maximum power.

Figure 4.17 Beam-steered power spectra for selected frequencies of .0542 hz (T = 18.5 sec) and .0332 hz (T = 30 sec) along a range of azimuths from 12/12/79 event. Actual azimuth to event is 181 degrees from array center. Same contours as in Figure 4.16.

Figure 4.18 Phase and group velocities from F-K analysis of 8/23/78 and 12/12/79 events across MIT network.

Figure 4.19 Shear velocity with depth from simultaneous inversion of phase and group velocities. Horizontal bars indicate model standard errors for each layer. See Figure 4.8 for calculated phase and group velocities from these models. (a) Path A1; (b) Path A2; (c) Path G.

Figure 4.20 Layer resolving kernels from simultaneous inversion of phase and group velocities as a

function of depth. Arrow points to position of layer. (a) Path A1; (b) Path A2; (c) Path G.

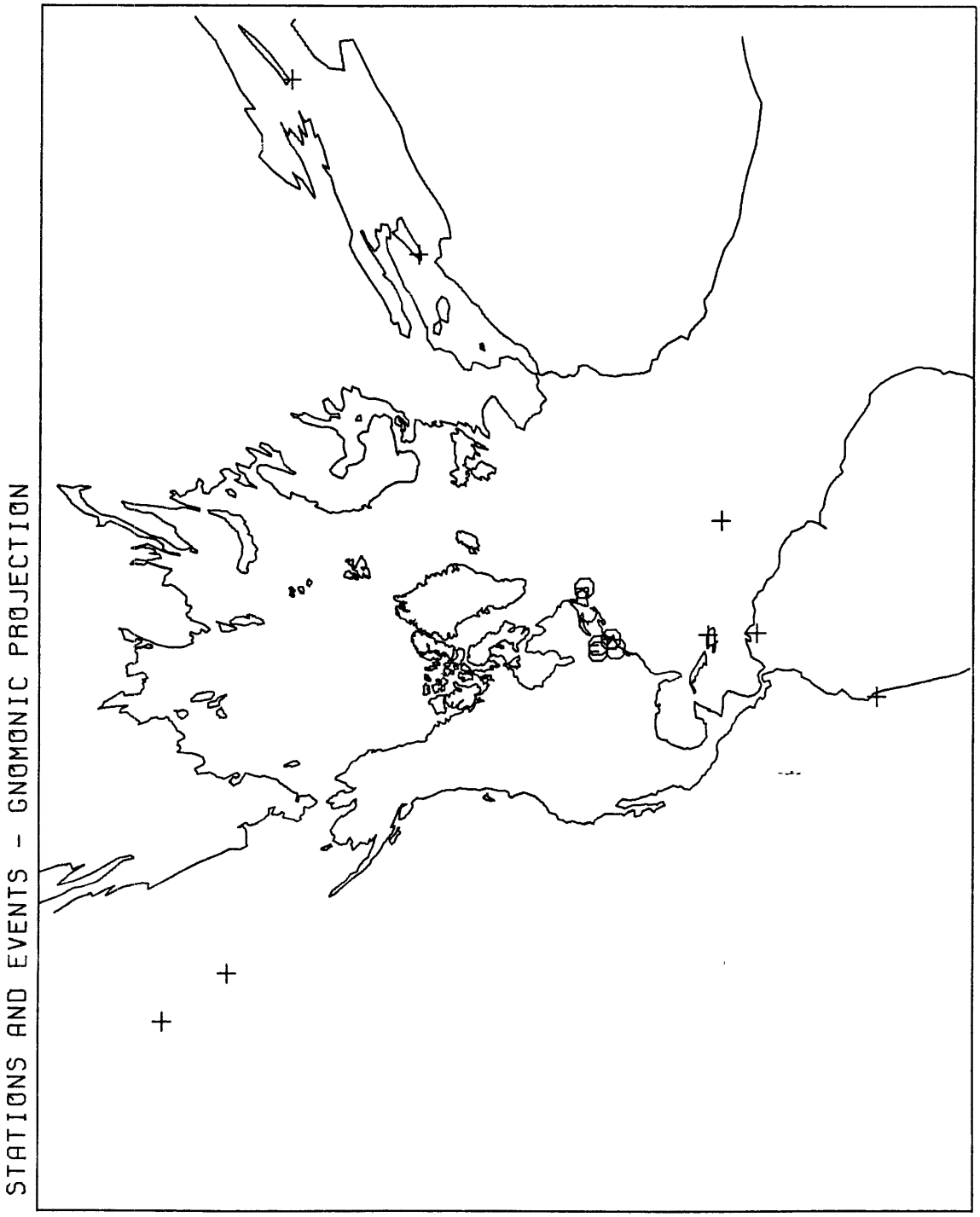

Figure 4.1

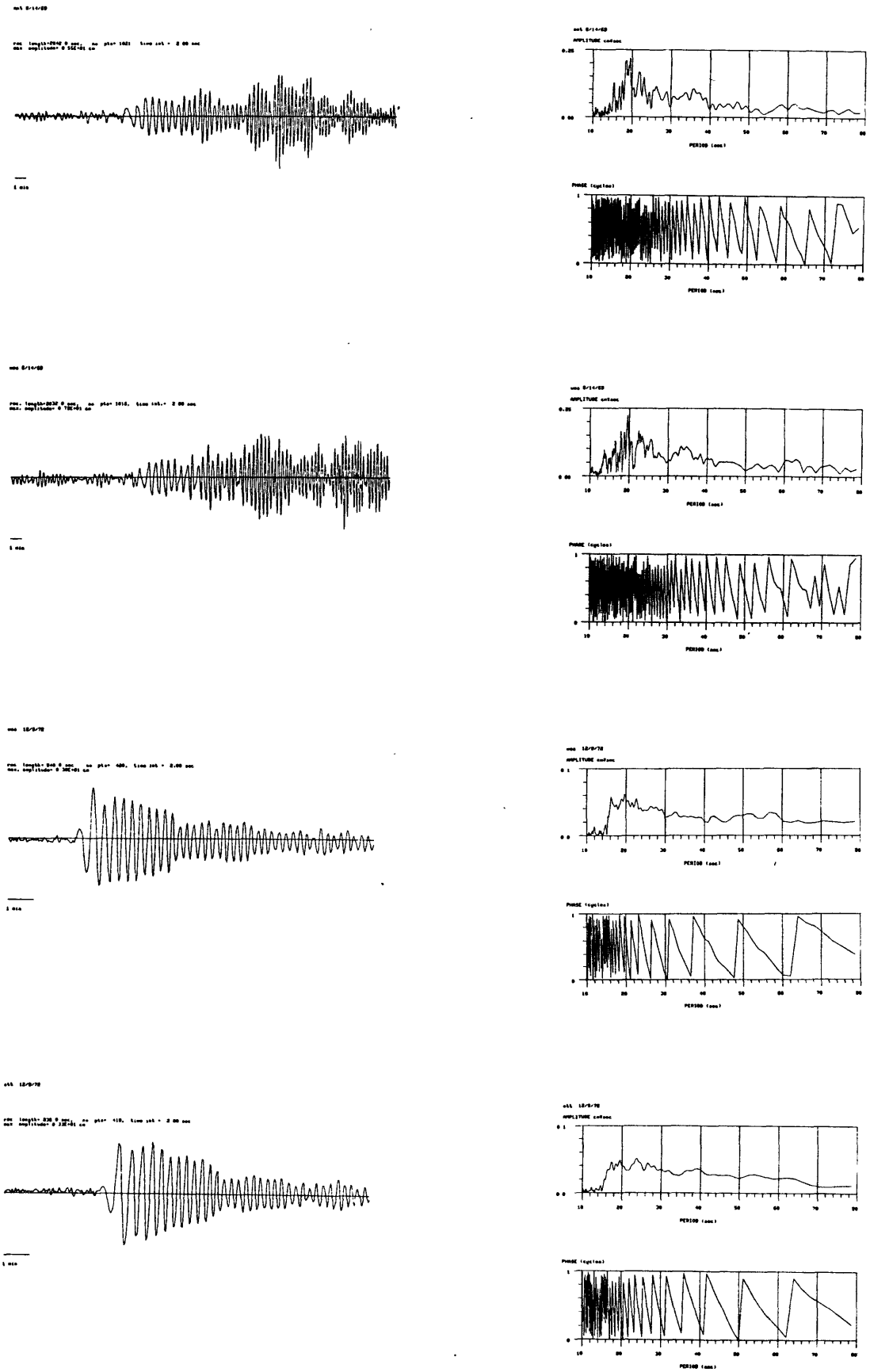

Figure 4.2

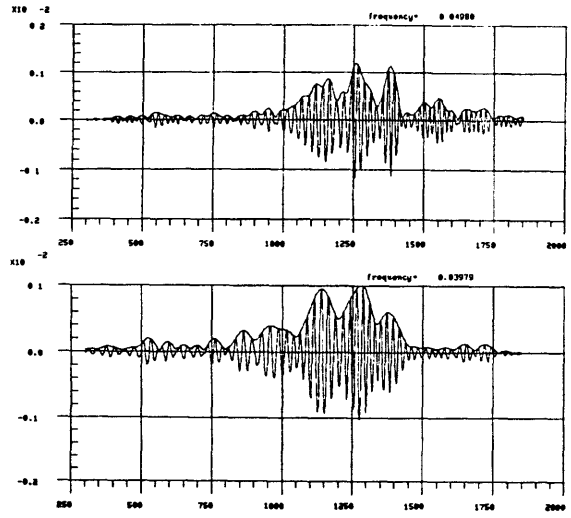

Figure 4.3a

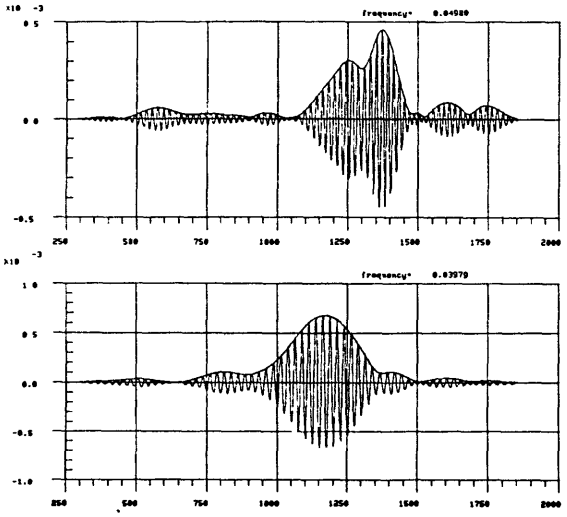

Figure 4.3b

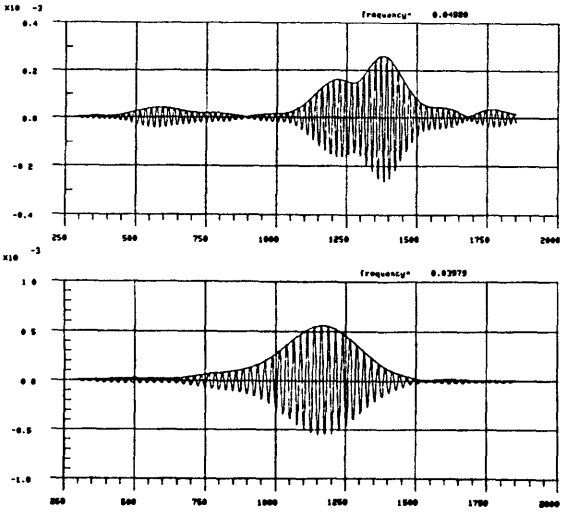

Figure 4.3c

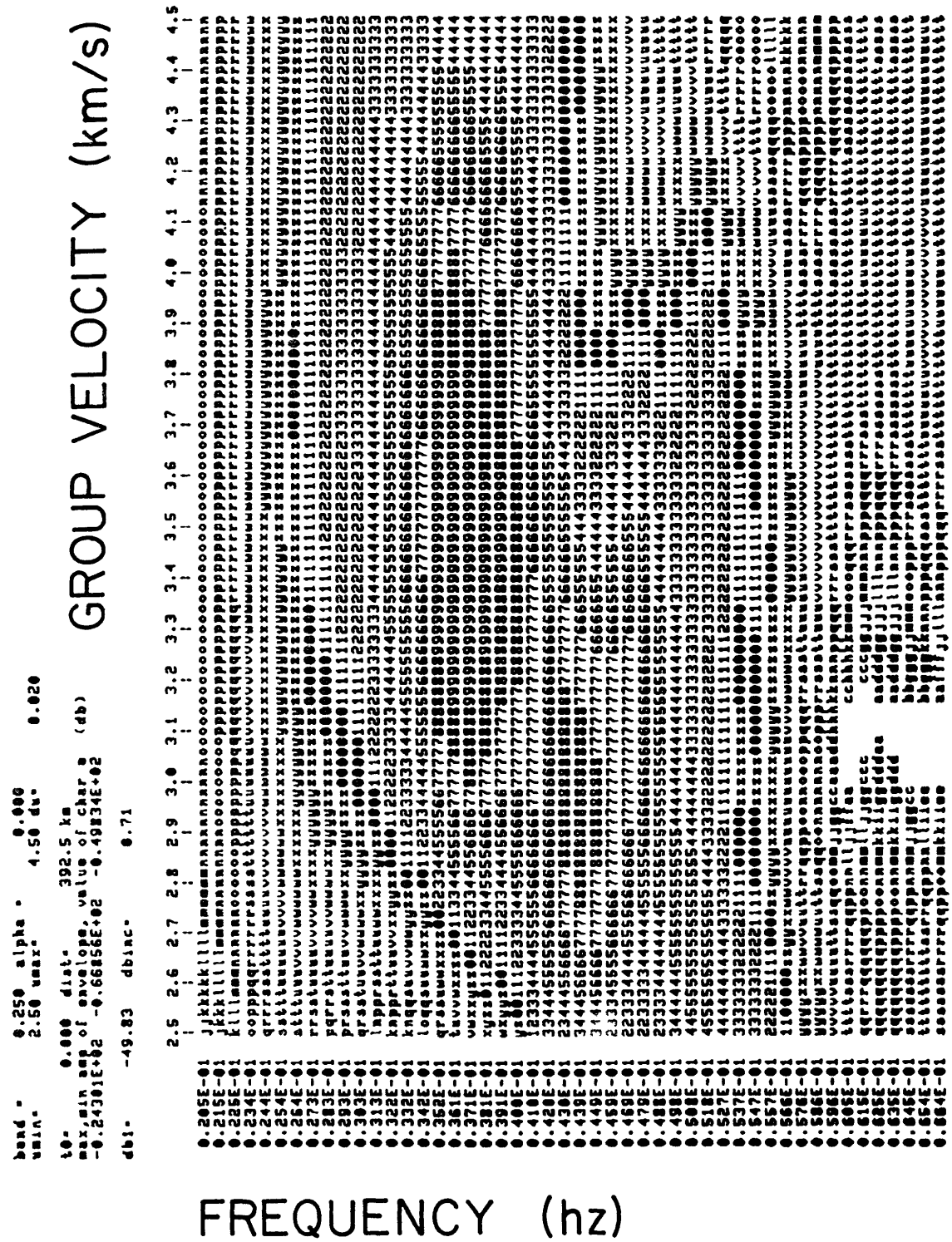

Figure 4.4a

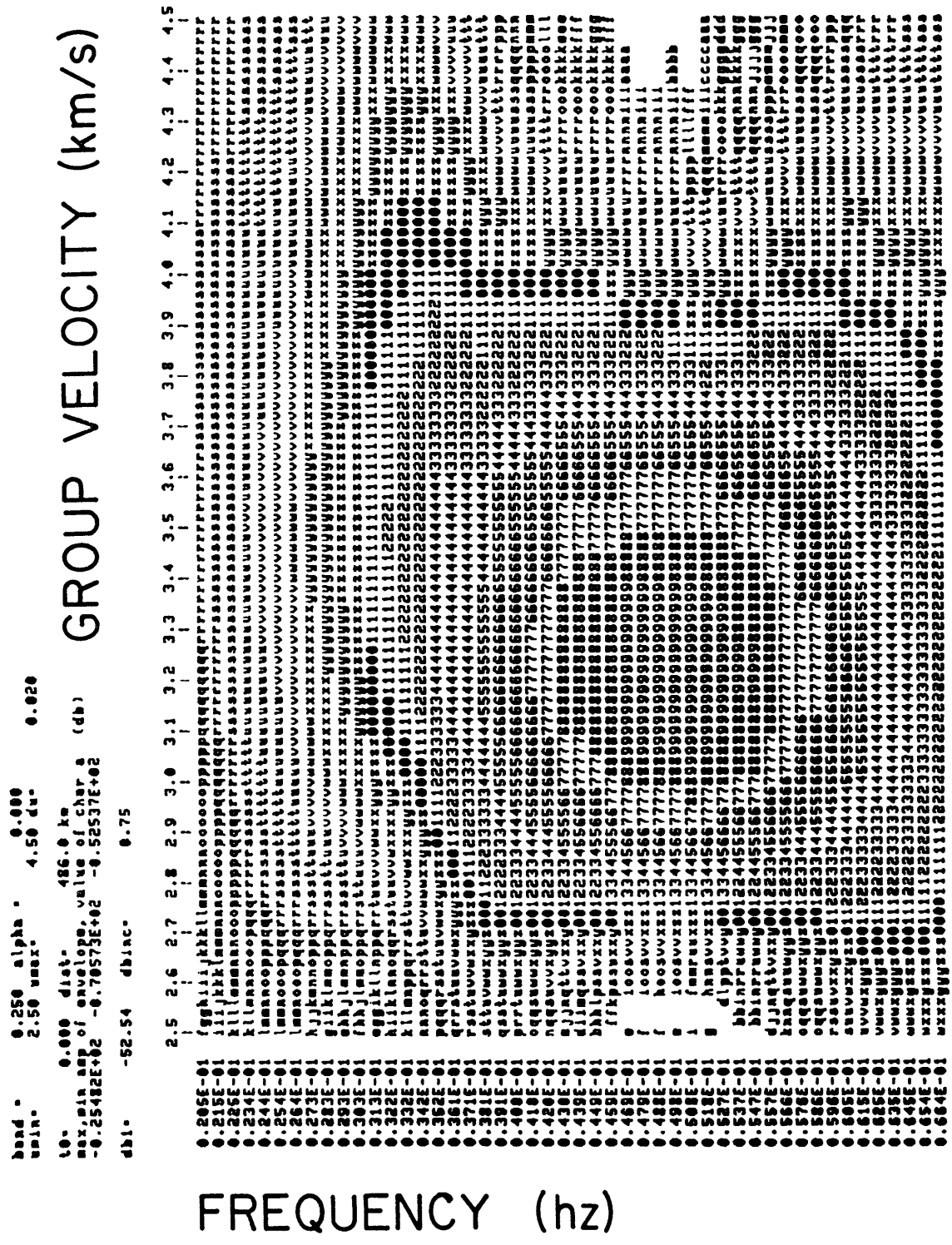

Figure 4.4b

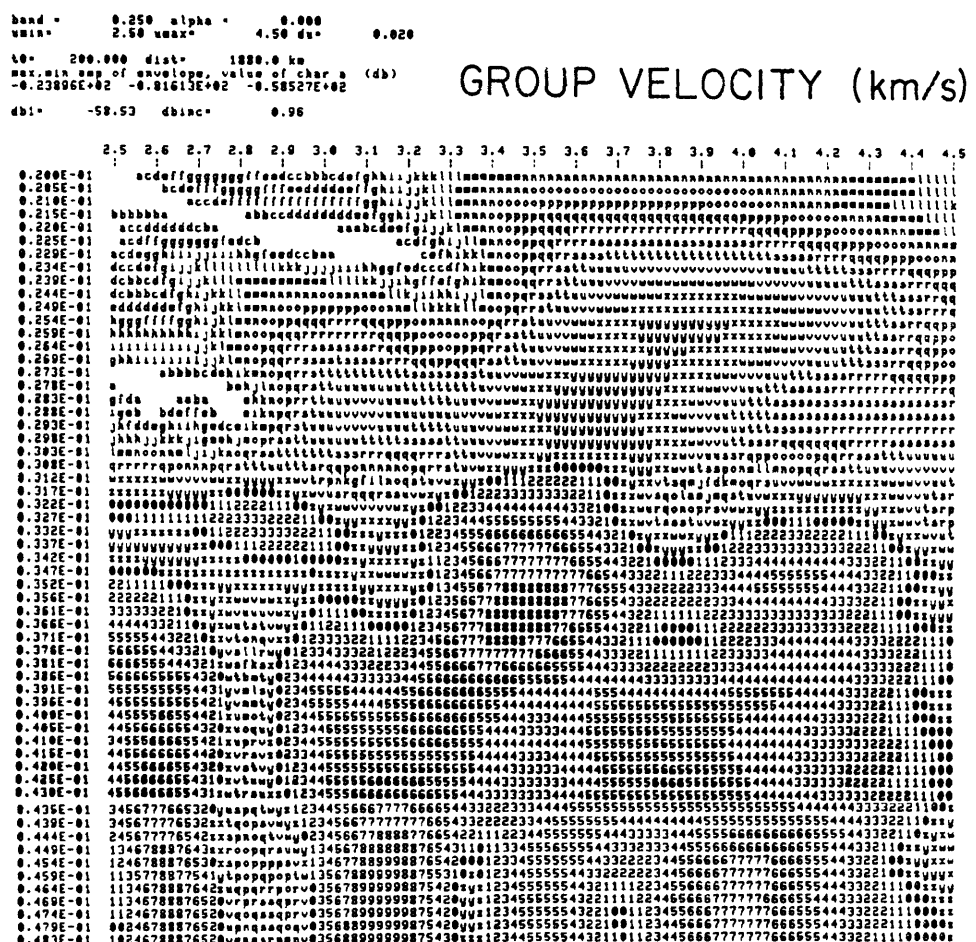
band = 0.250 alpha = 0.000
vmin= 2.50 vmax= 4.50 dv= 0.020
t0= 200.000 dist= 1880.0 km
max,min amp of envelope, value of char a (db)
-0.23896E+02 -0.81613E+02 -0.58527E+02
dbi= -58.53 dbinc= 0.96
GROUP VELOCITY (km/s)
2.5 2.6 2.7 2.8 2.9 3.0 3.1 3.2 3.3 3.4 3.5 3.6 3.7 3.8 3.9 4.0 4.1 4.2 4.3 4.4 4.5
FREQUENCY (hz)
0.200E-01
0.205E-01
0.210E-01
0.215E-01
0.220E-01
0.225E-01
0.229E-01
0.234E-01
0.239E-01
0.244E-01
0.249E-01
0.254E-01
0.259E-01
0.264E-01
0.269E-01
0.273E-01
0.278E-01
0.283E-01
0.288E-01
0.293E-01
0.298E-01
0.303E-01
0.308E-01
0.312E-01
0.317E-01
0.322E-01
0.327E-01
0.332E-01
0.337E-01
0.342E-01
0.347E-01
0.352E-01
0.356E-01
0.361E-01
0.366E-01
0.371E-01
0.376E-01
0.381E-01
0.386E-01
0.391E-01
0.396E-01
0.400E-01
0.405E-01
0.410E-01
0.415E-01
0.420E-01
0.425E-01
0.430E-01
0.435E-01
0.439E-01
0.444E-01
0.449E-01
0.454E-01
0.459E-01
0.464E-01
0.469E-01
0.474E-01
0.479E-01
0.483E-01
0.488E-01
0.493E-01
0.498E-01
0.503E-01
0.508E-01
0.513E-01
0.518E-01
0.522E-01
0.527E-01
0.532E-01
0.537E-01
0.542E-01
0.547E-01
0.552E-01
0.557E-01
0.562E-01
0.566E-01
0.571E-01
0.576E-01
0.581E-01
0.586E-01
0.591E-01
0.596E-01
0.601E-01
0.605E-01
0.610E-01
0.615E-01
0.620E-01
0.625E-01
0.630E-01
0.635E-01
0.640E-01
0.645E-01
0.649E-01
0.654E-01
0.659E-01
0.664E-01
5/4/72 STJ-OGD

Figure 4.4c

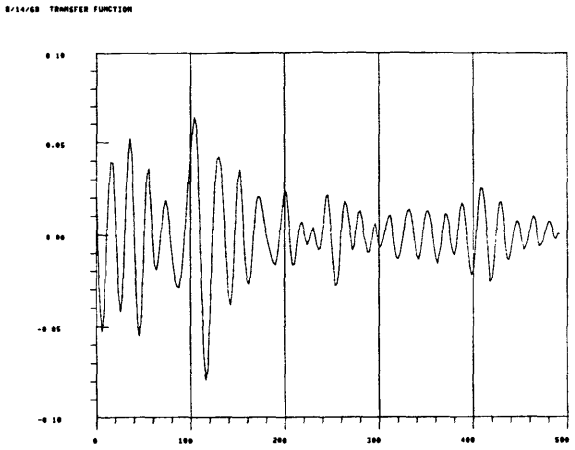
8/14/68 TRANSFER FUNCTION
0.10
0.05
0.00
-0.05
-0.10
0
100
200
300
400
500

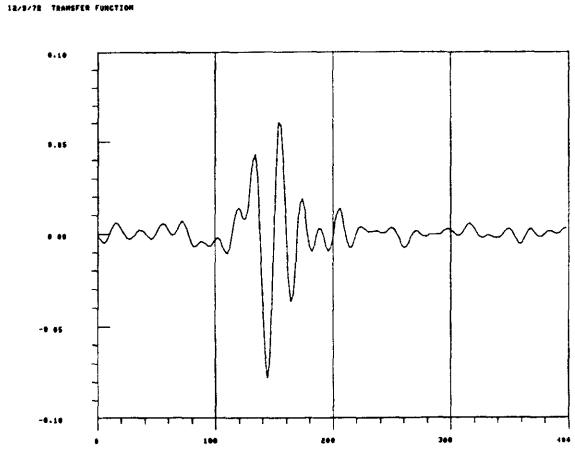
12/9/72 TRANSFER FUNCTION
0.10
0.05
0.00
-0.05
-0.10
0
100
200
300

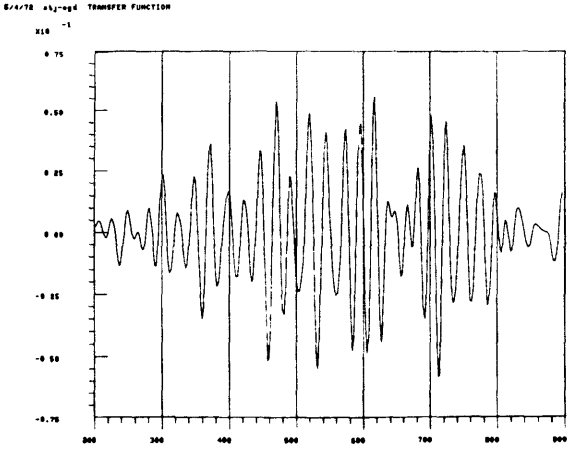
8/4/72 adj-agd TRANSFER FUNCTION
X10 -1
0.75
0.50
0.25
0.00
-0.25
-0.50
-0.75
300
400
500
600
700
800
900

Figure 4.5a

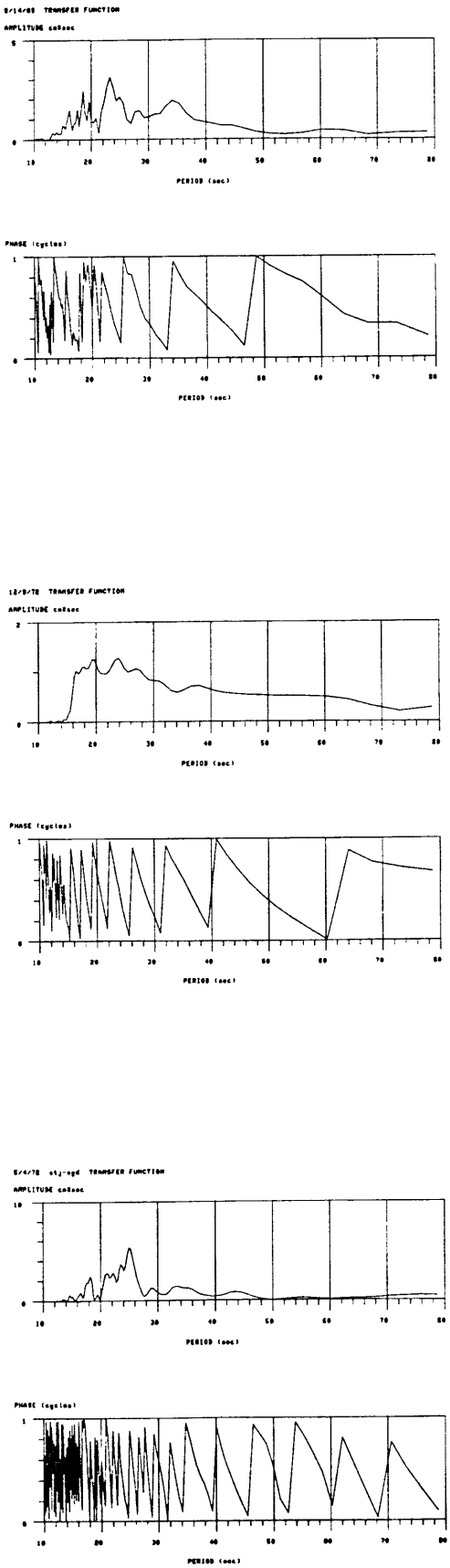
PERIOD (sec)
PERIOD (sec)
PERIOD (sec)
PERIOD (sec)
PERIOD (sec)
PERIOD (sec)

Figure 4.5b

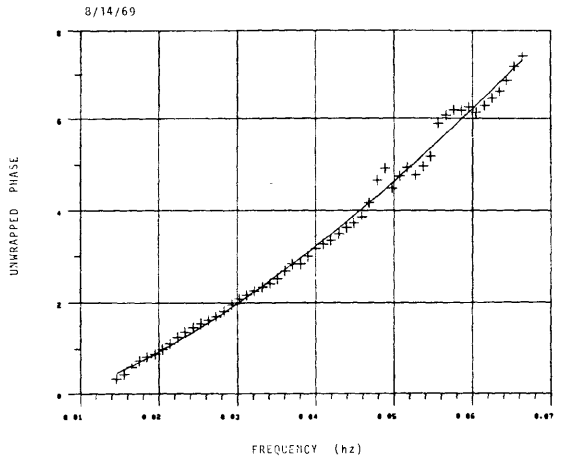
8/14/69
UNWRAPPED PHASE
FREQUENCY (hz)

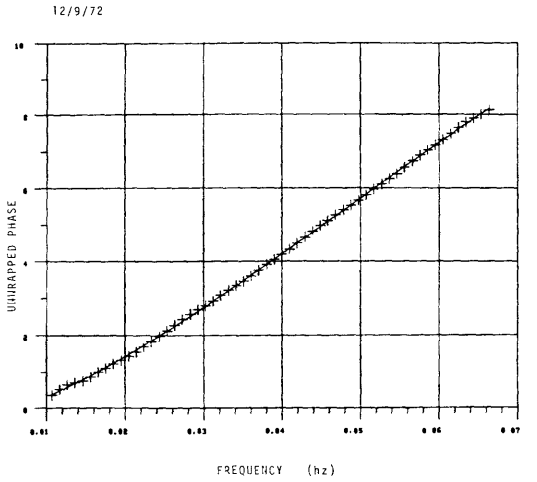
12/9/72
UNWRAPPED PHASE
FREQUENCY (hz)

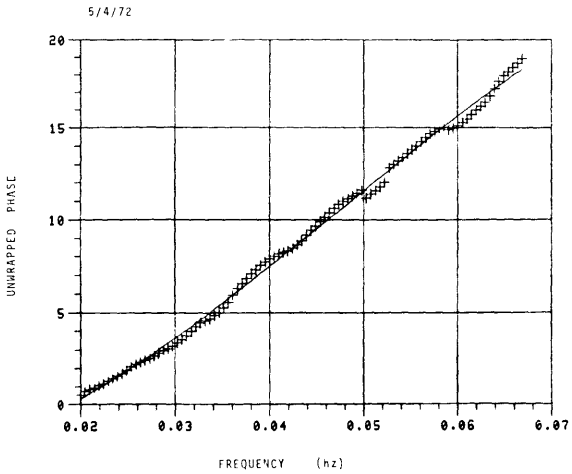
5/4/72
UNWRAPPED PHASE
20
15
10
5
0
0.02
0.03
0.04
0.05
0.06
0.07
FREQUENCY (hz)

Figure 4.6a

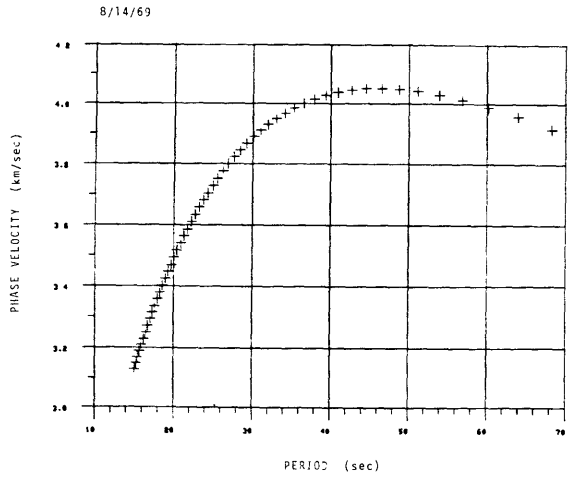
8/14/69
PHASE VELOCITY (km/sec)
PERIOD (sec)

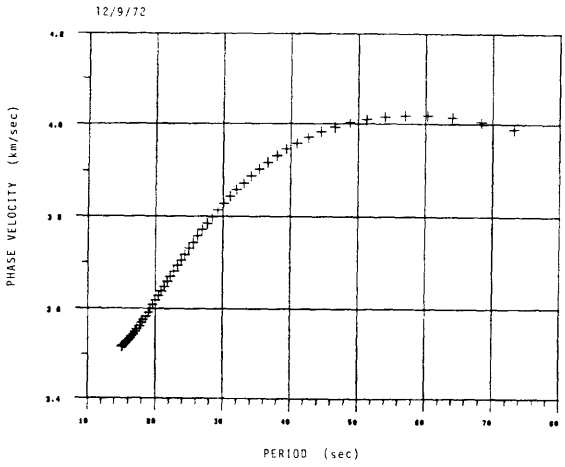
12/9/72
PHASE VELOCITY (km/sec)
PERIOD (sec)

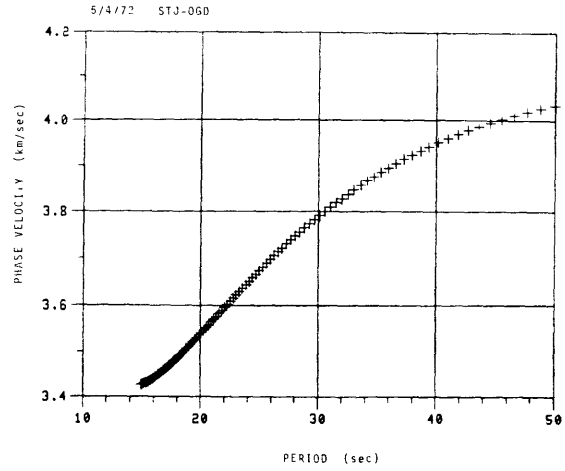
5/4/72 STJ-OGD
PHASE VELOCITY (km/sec)
4.2
4.0
3.8
3.6
3.4
10
20
30
40
50
PERIOD (sec)

Figure 4.6b

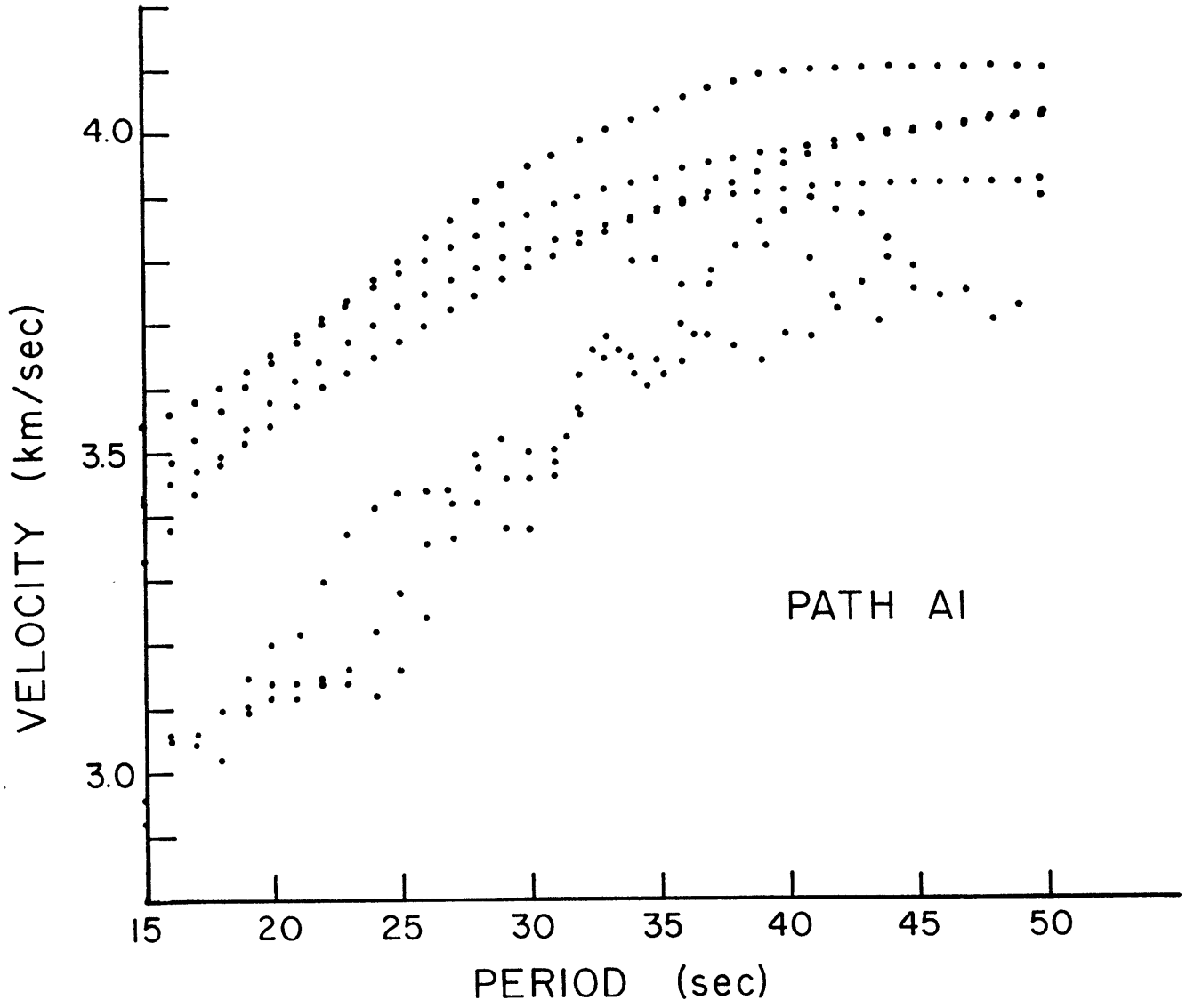
VELOCITY (km/sec)
4.0
3.5
3.0
15
20
25
30
35
40
45
50
PERIOD (sec)
PATH AI

Figure 4.7a

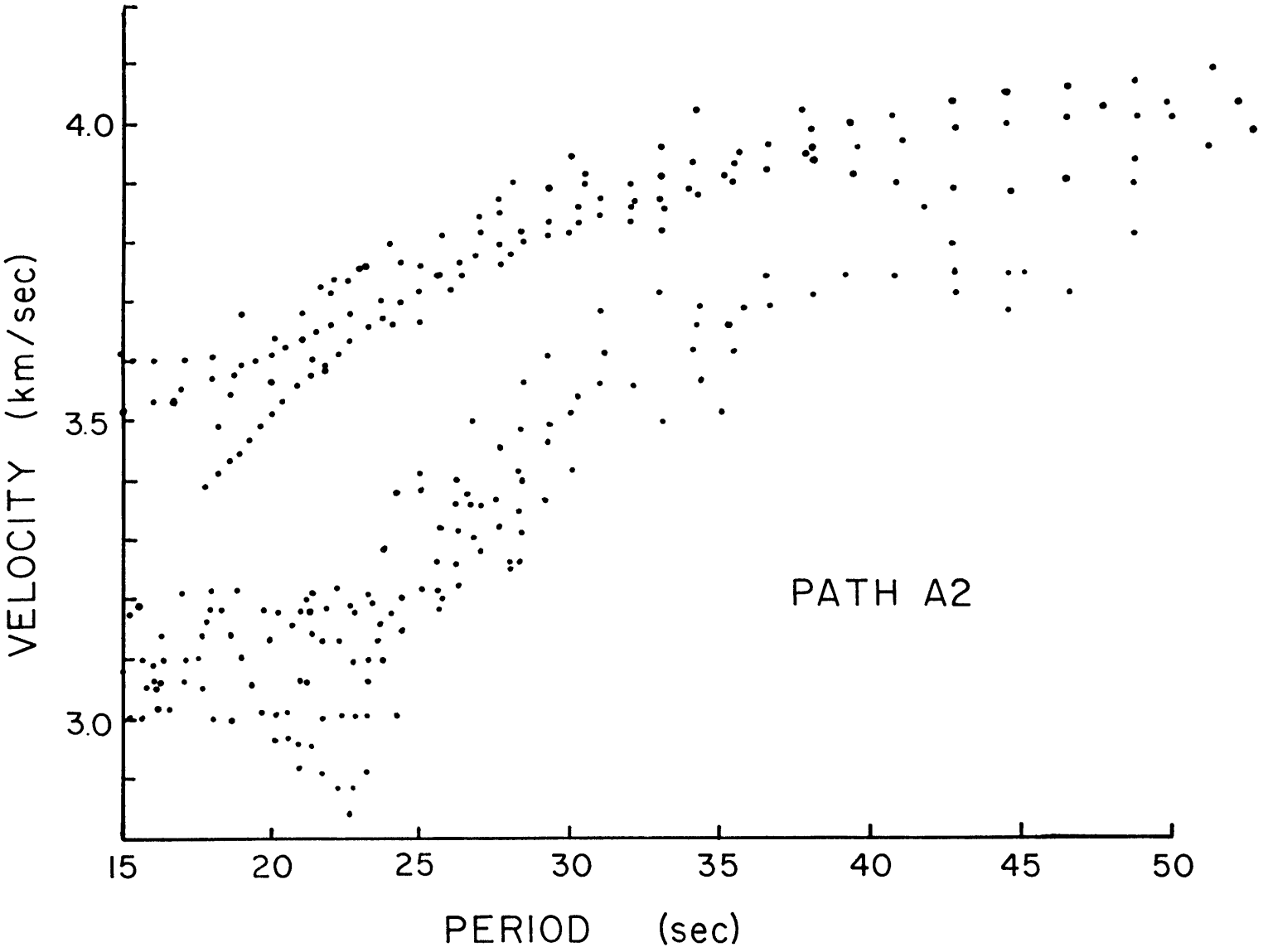
VELOCITY (km/sec)
4.0
3.5
3.0
PATH A2
15
20
25
30
35
40
45
50
PERIOD (sec)

Figure 4.7b

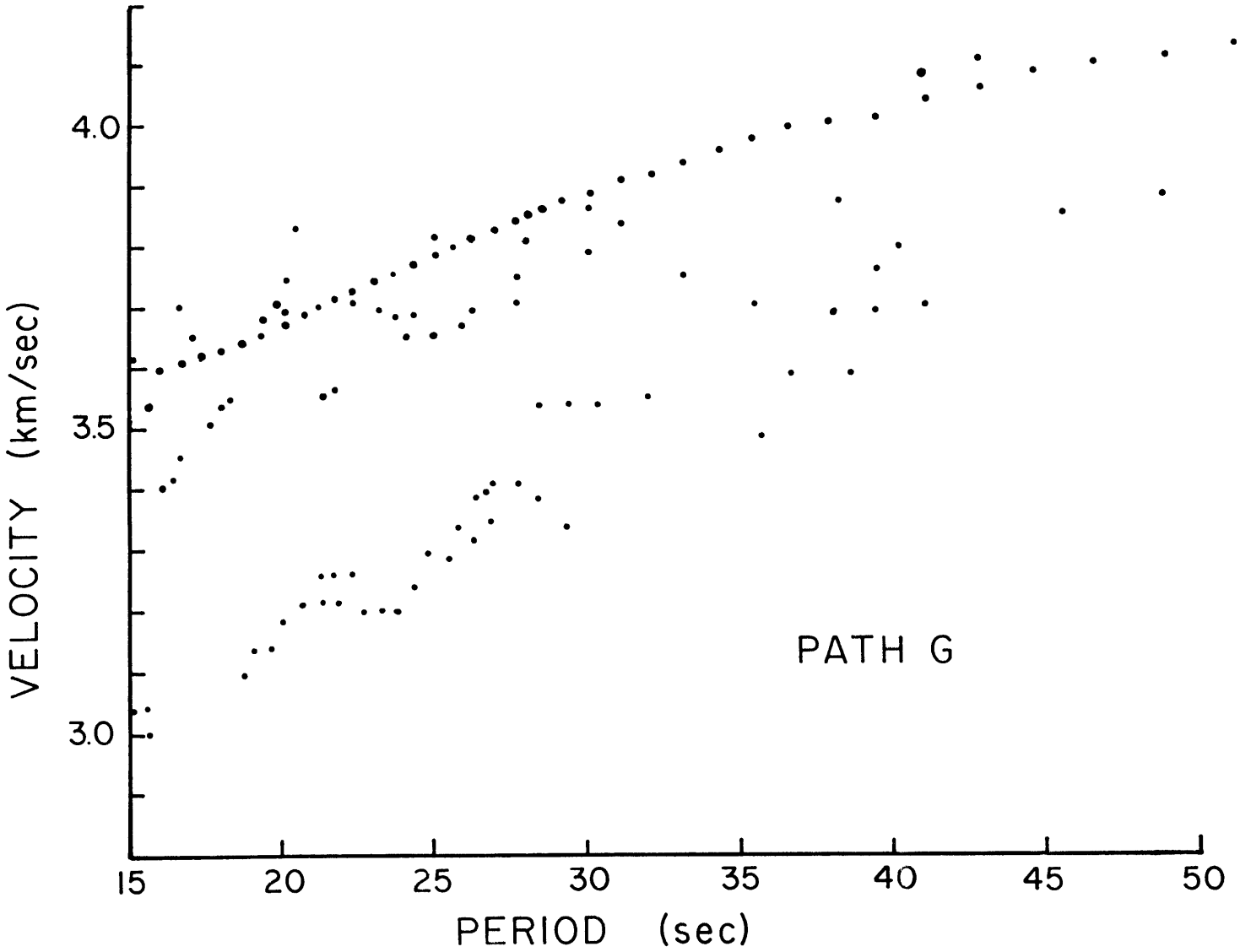

Figure 4.7c

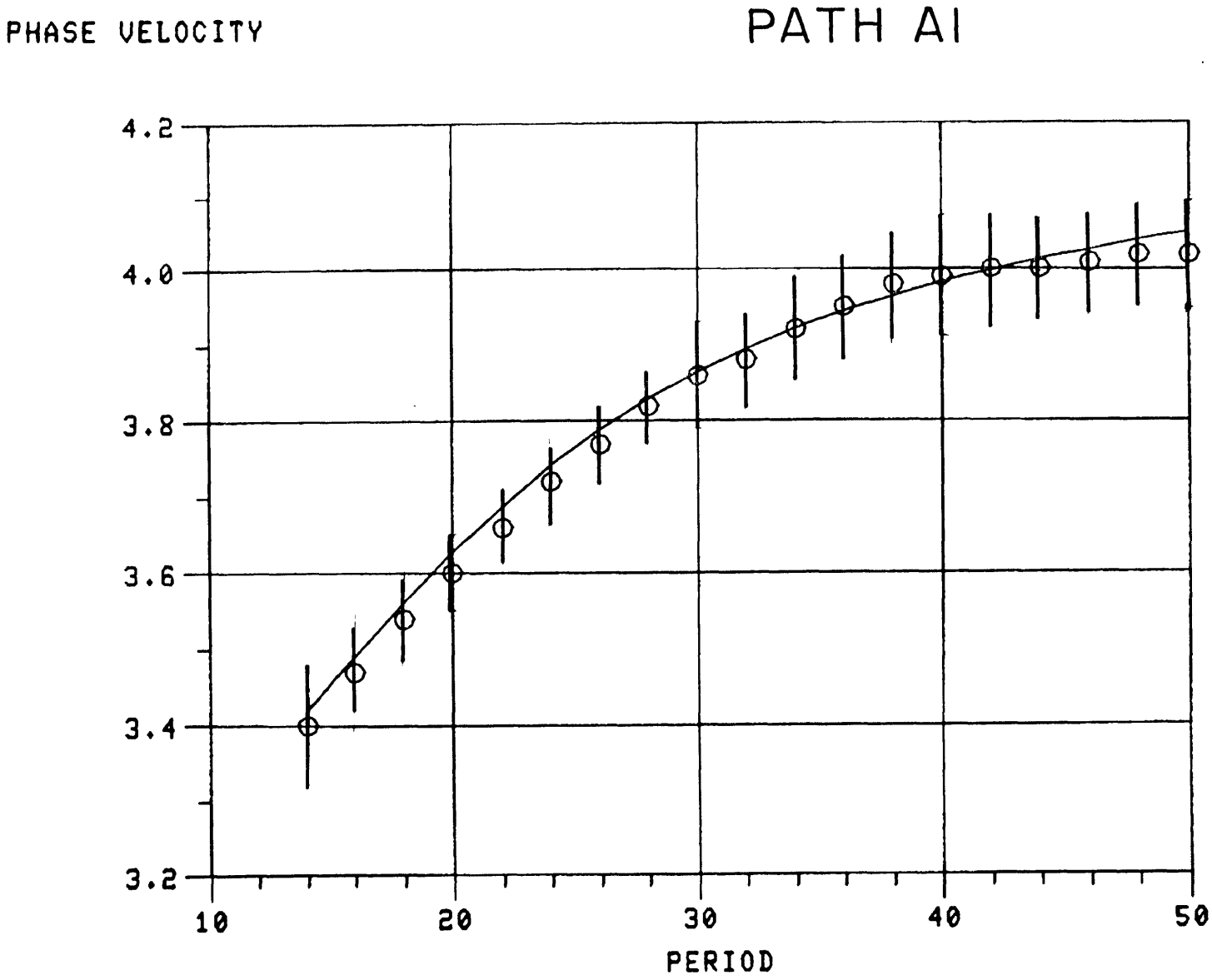

Figure 4.8a

GROUP VELOCITY

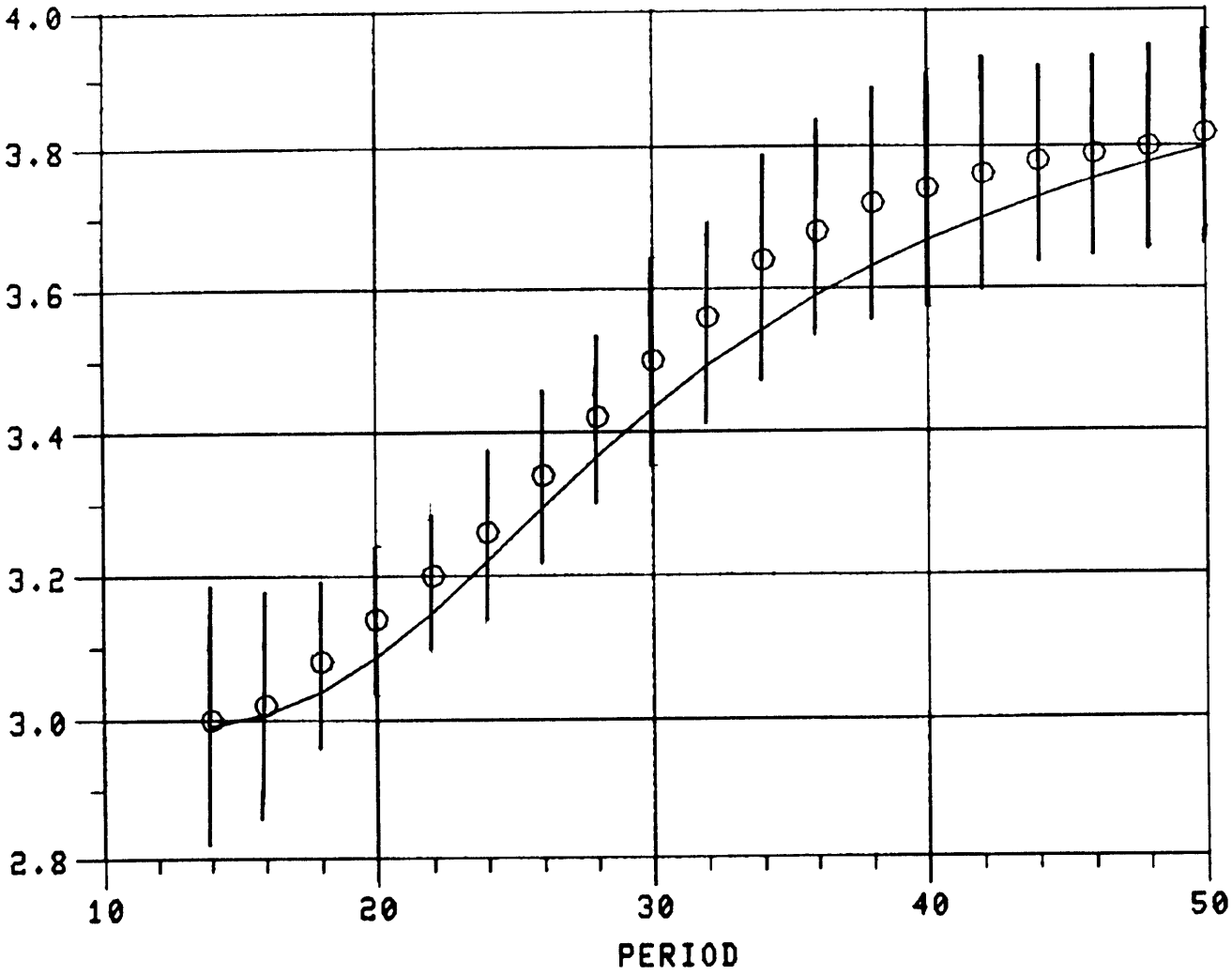

Figure 4.8a

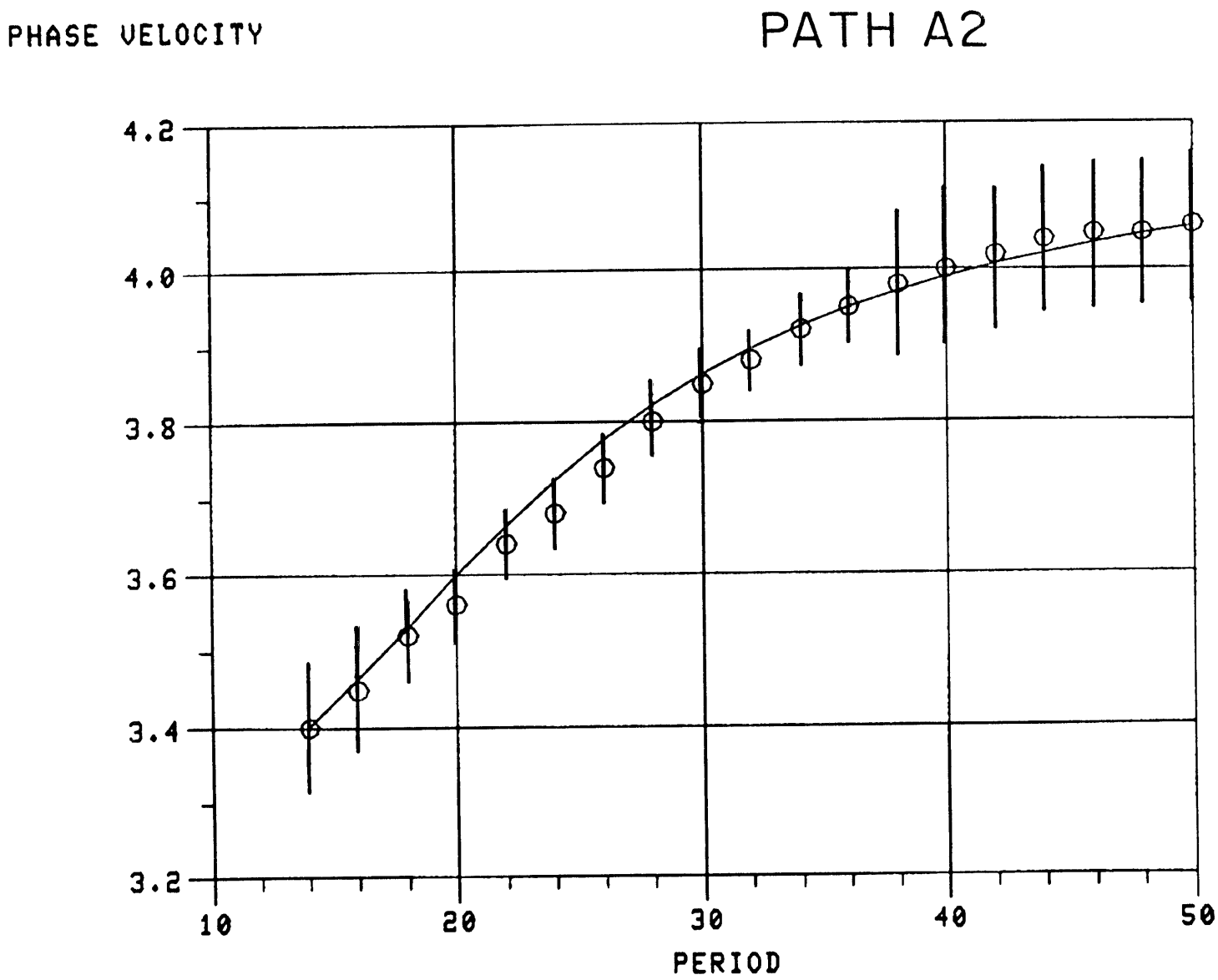

Figure 4.8b

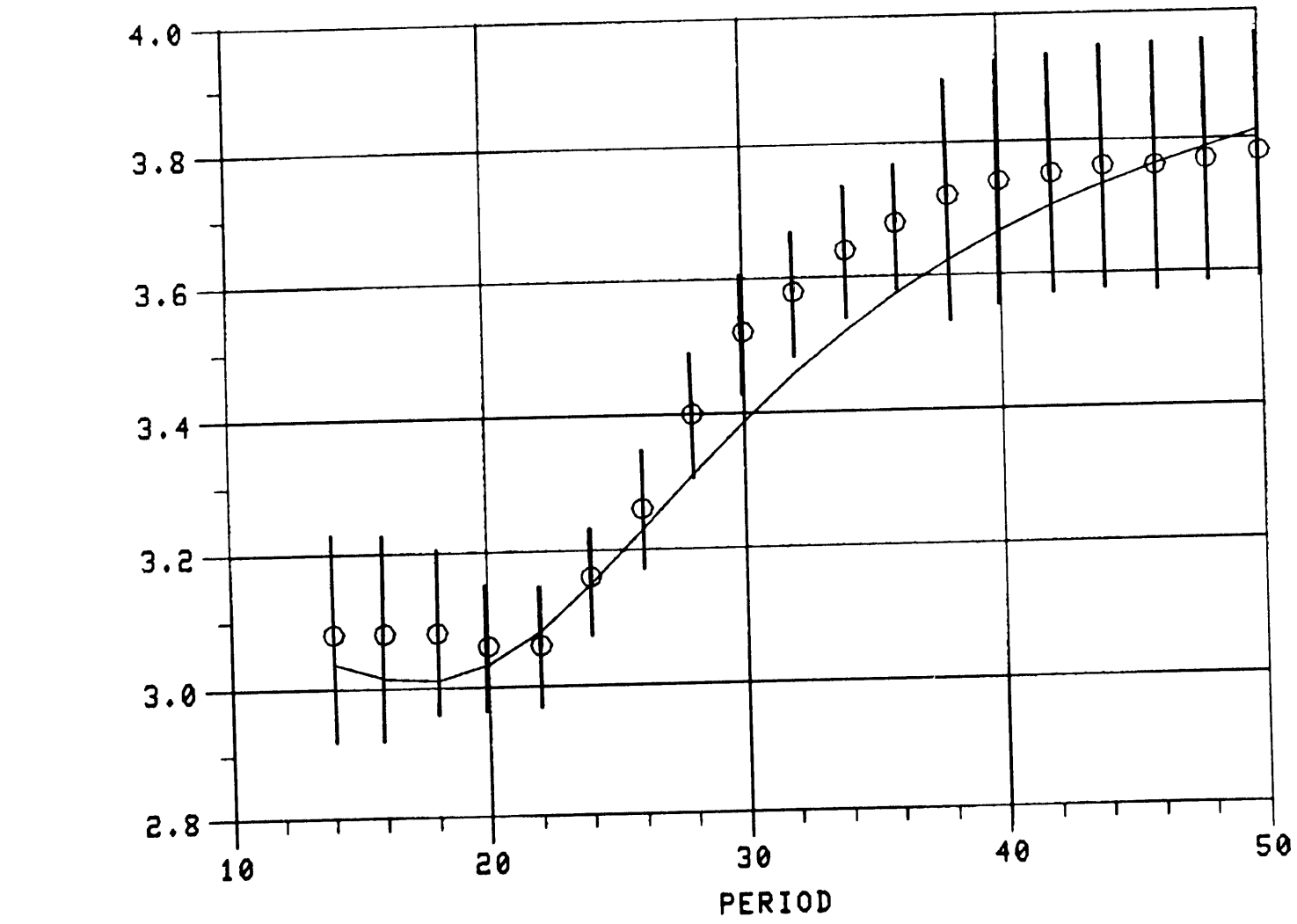

Figure 4.8b

PHASE VELOCITY

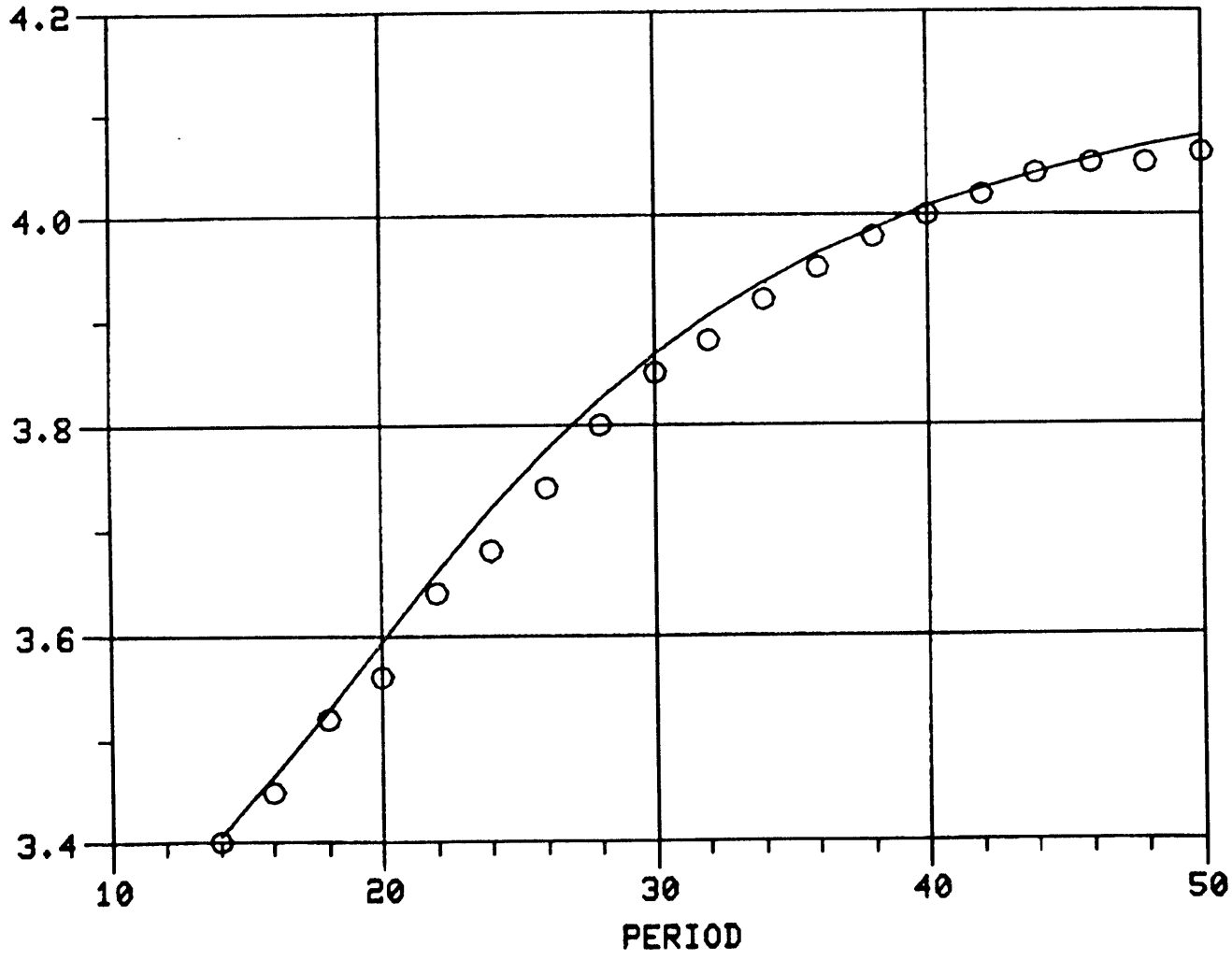

Figure 4.8c

GROUP VELOCITY

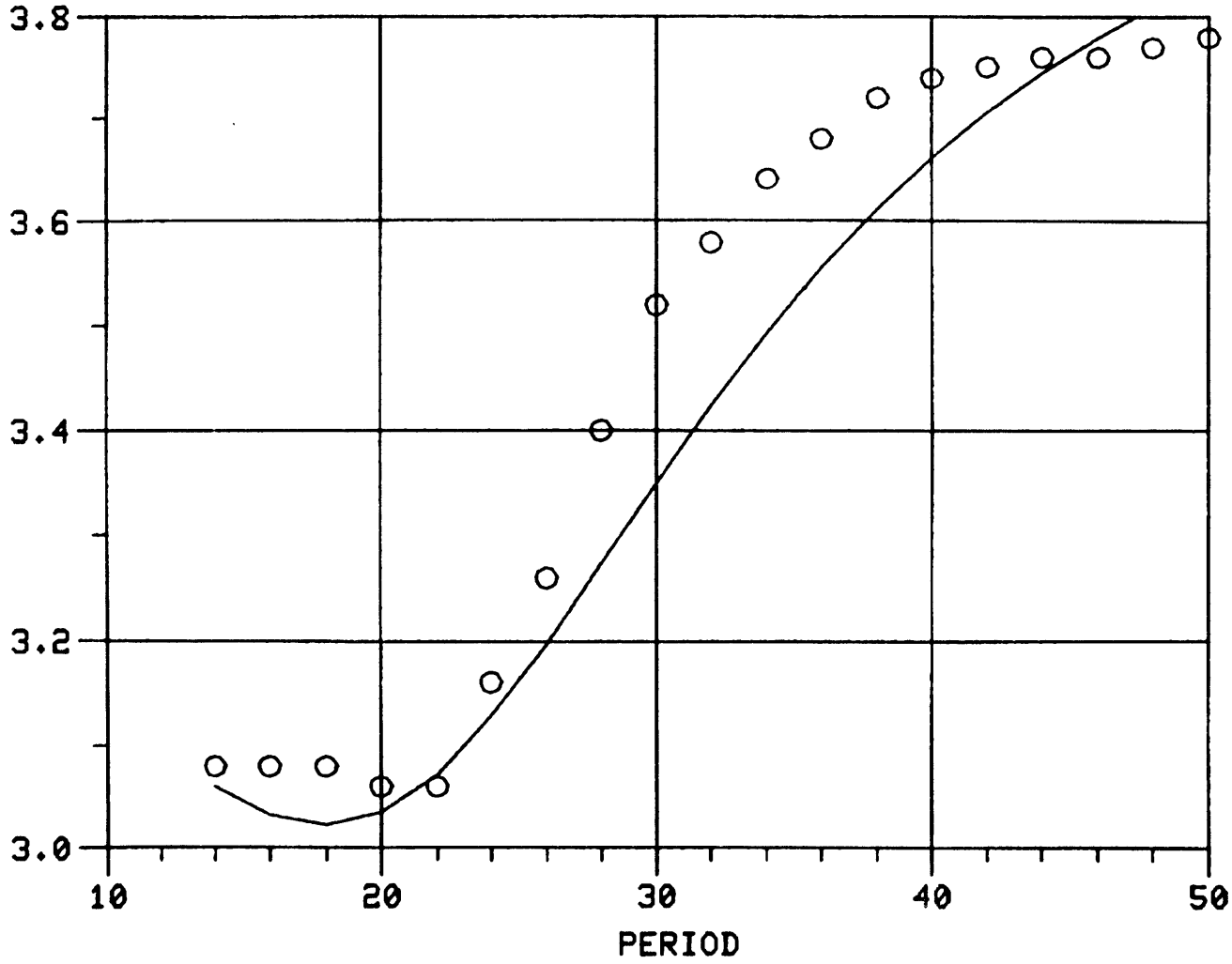

Figure 4.8c

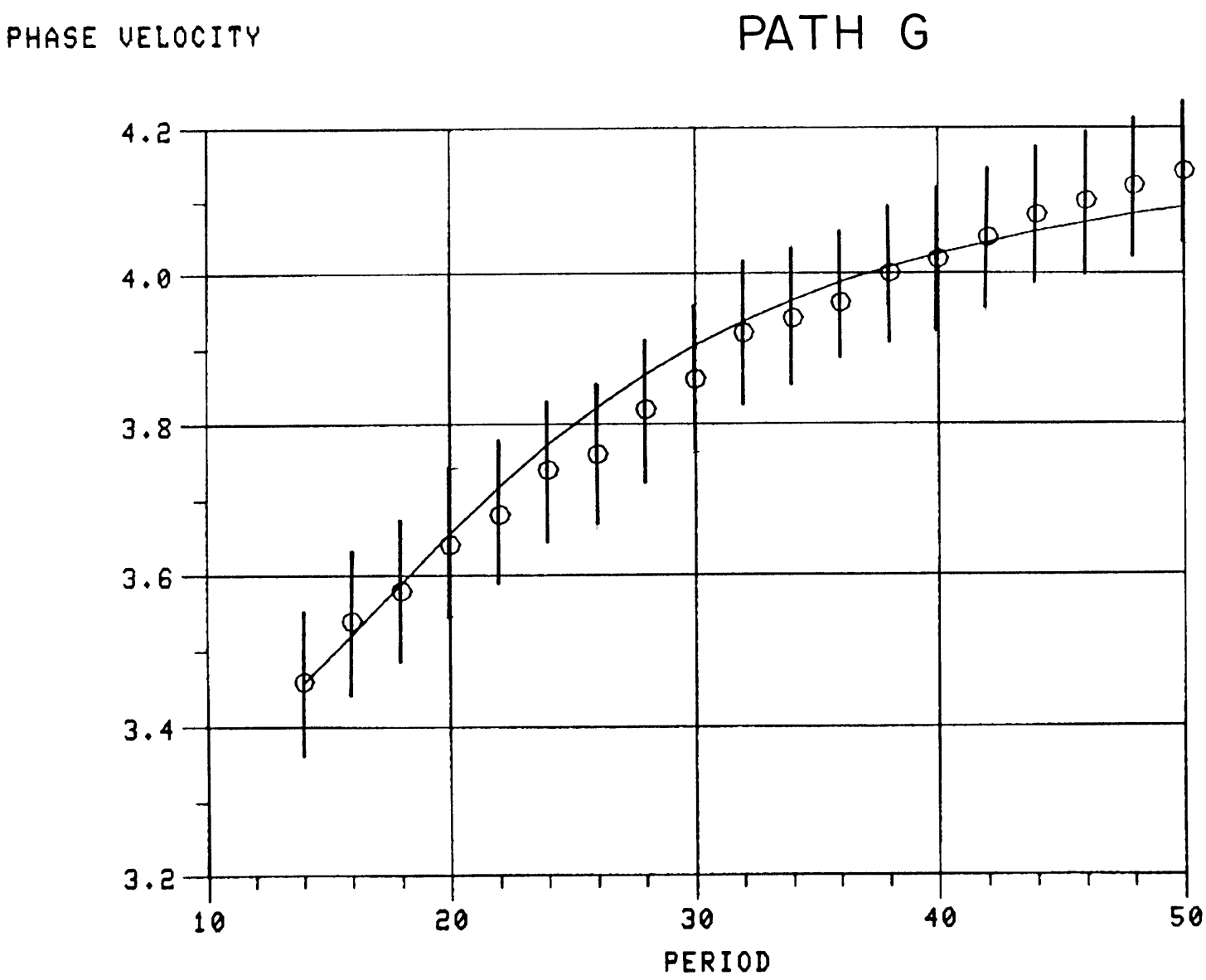

Figure 4.8d

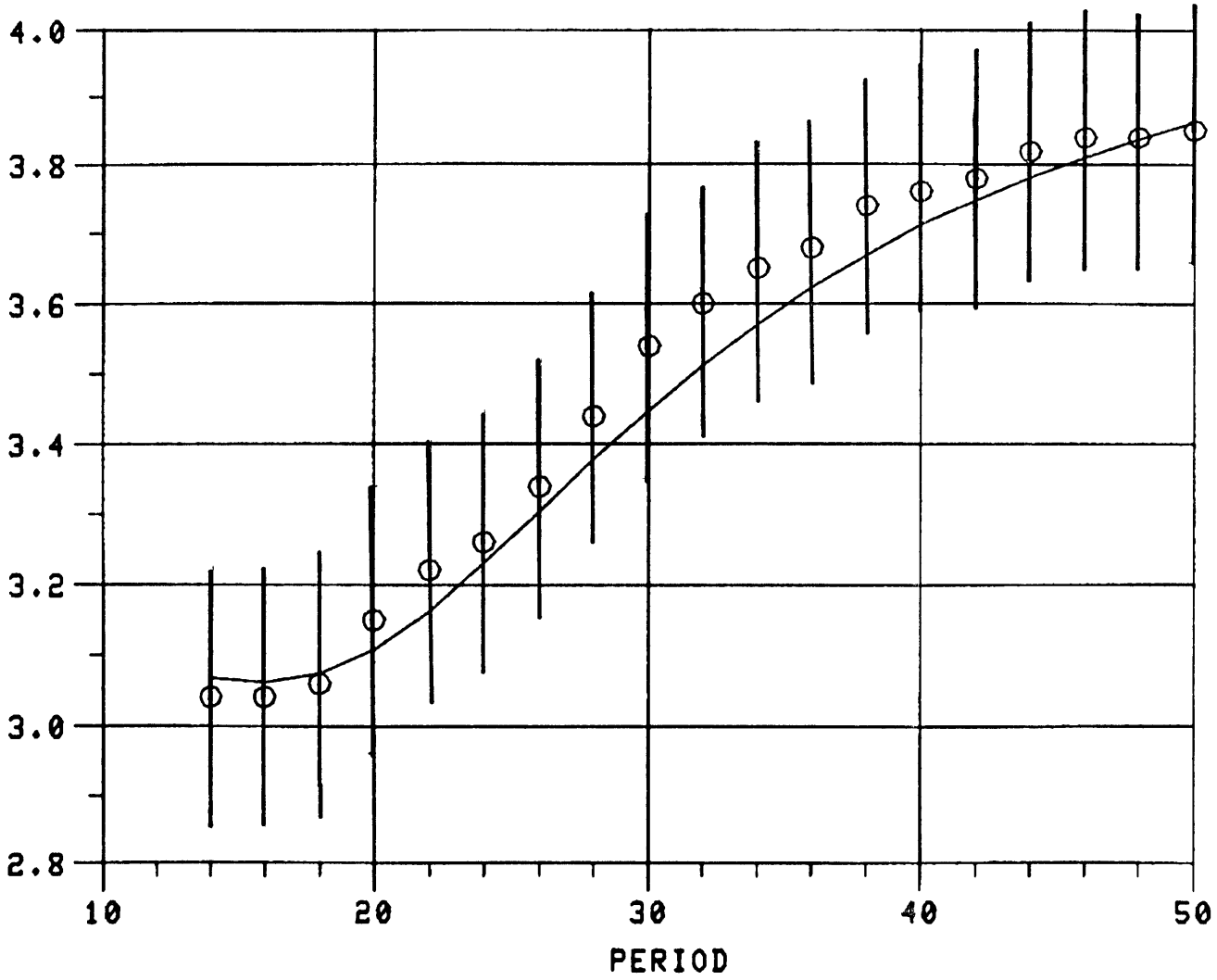

Figure 4.8d

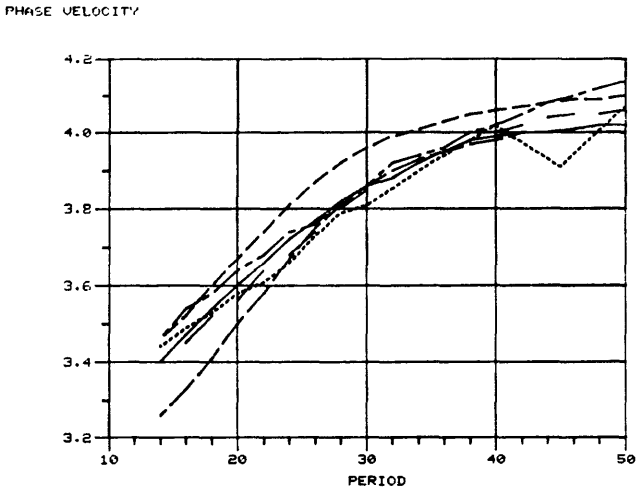

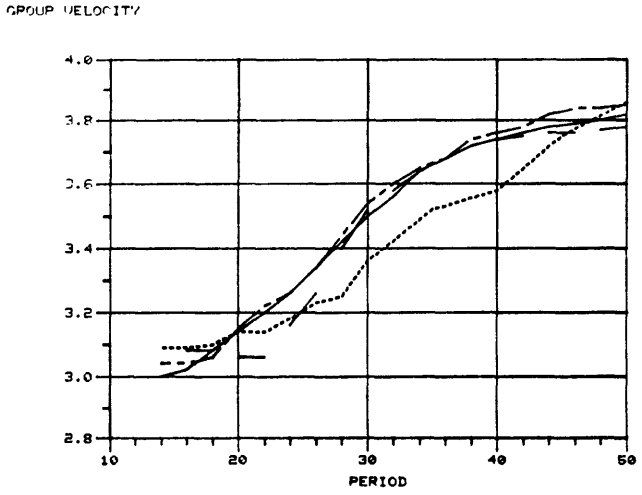

——— PATH A1

— — PATH A2

—— — PATH G

------- EUS Mitchell & Herrmann (1979)

- - - - - - CANADIAN SHIELD Brune & Dorman (1963)

—— —— N.Y.-PENN. Oliver et al. (1961)

Figure 4.9

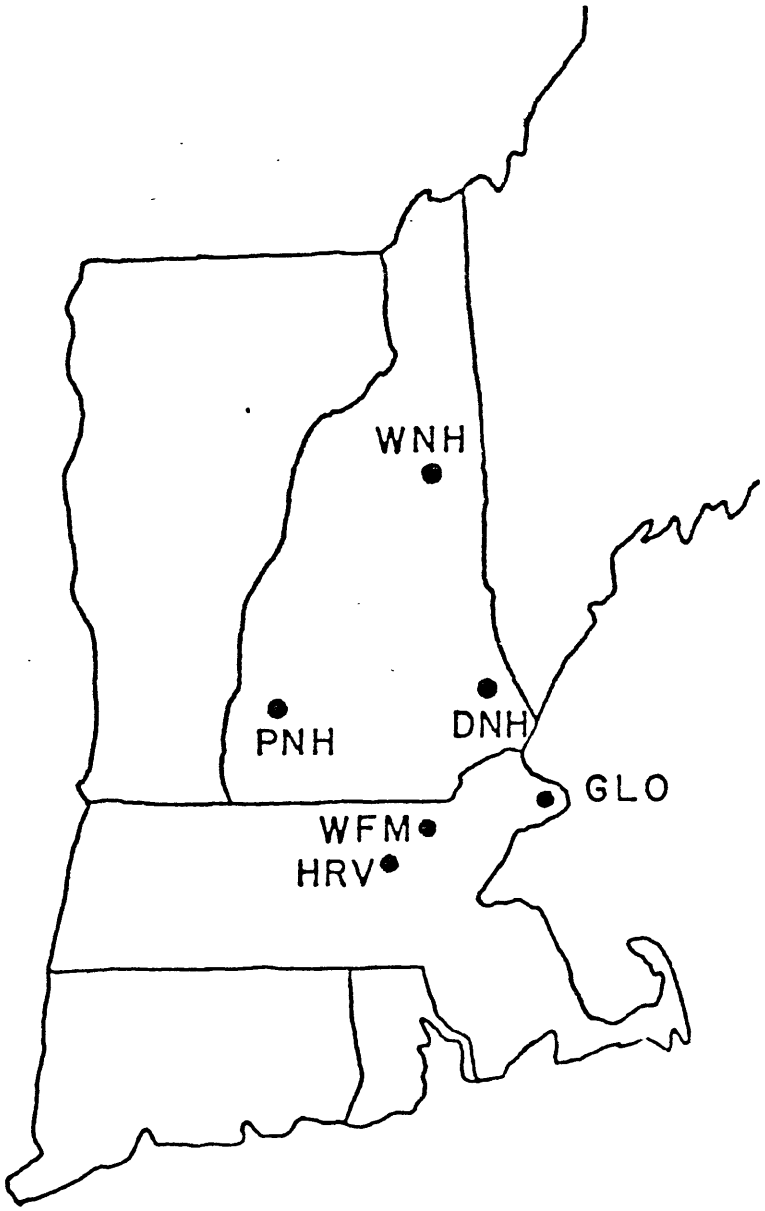

Figure 4.10

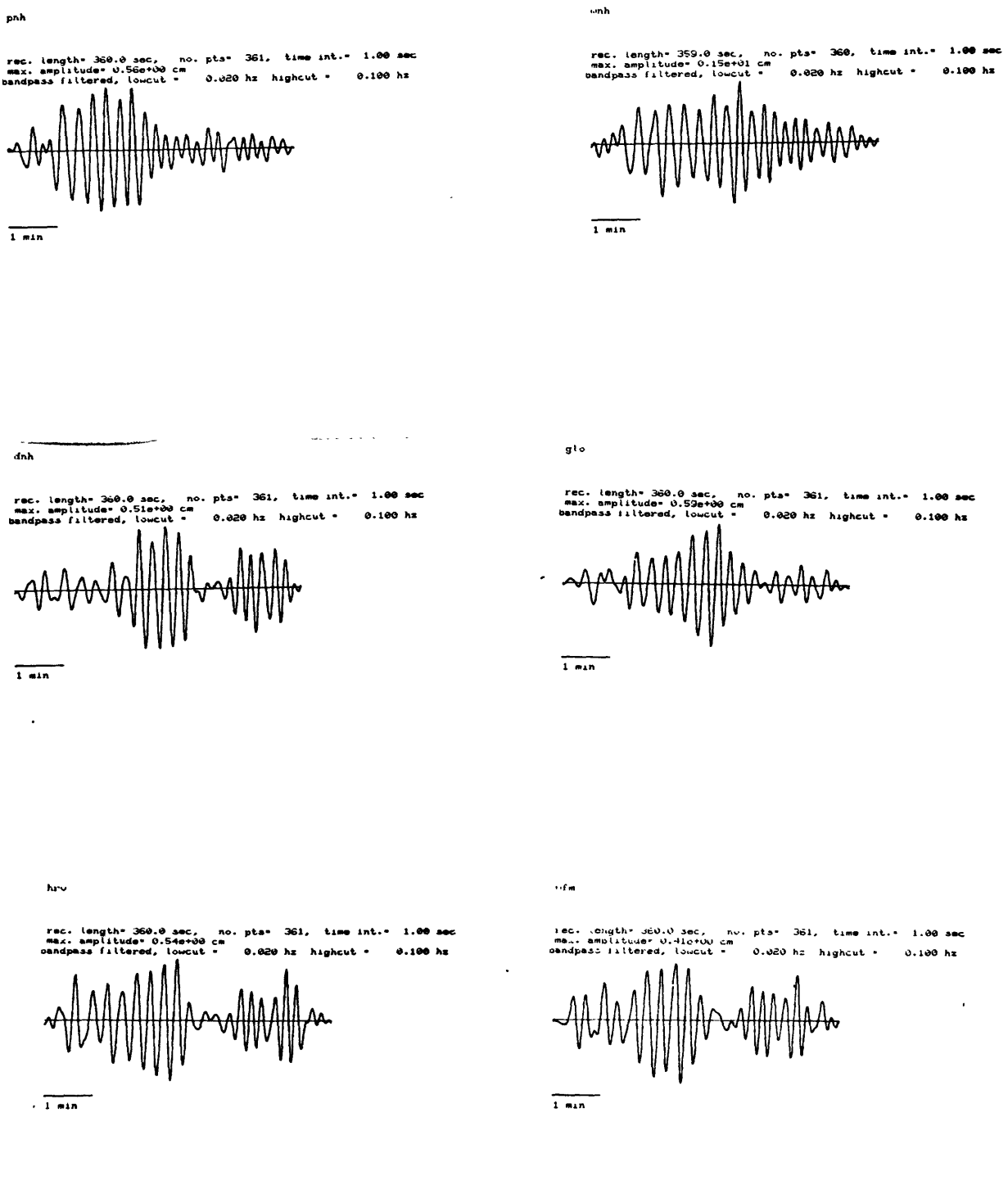
pnh
rec. length= 360.0 sec, no. pts= 361, time int.= 1.00 sec
max. amplitude= 0.56e+00 cm
bandpass filtered, lowcut = 0.020 hz highcut = 0.100 hz
1 min
unh
rec. length= 359.0 sec, no. pts= 360, time int.= 1.00 sec
max. amplitude= 0.15e+01 cm
bandpass filtered, lowcut = 0.020 hz highcut = 0.100 hz
1 min
dnh
rec. length= 360.0 sec, no. pts= 361, time int.= 1.00 sec
max. amplitude= 0.51e+00 cm
bandpass filtered, lowcut = 0.020 hz highcut = 0.100 hz
1 min
glo
rec. length= 360.0 sec, no. pts= 361, time int.= 1.00 sec
max. amplitude= 0.59e+00 cm
bandpass filtered, lowcut = 0.020 hz highcut = 0.100 hz
1 min
hnv
rec. length= 360.0 sec, no. pts= 361, time int.= 1.00 sec
max. amplitude= 0.54e+00 cm
bandpass filtered, lowcut = 0.020 hz highcut = 0.100 hz
1 min
1 min

Figure 4.11a

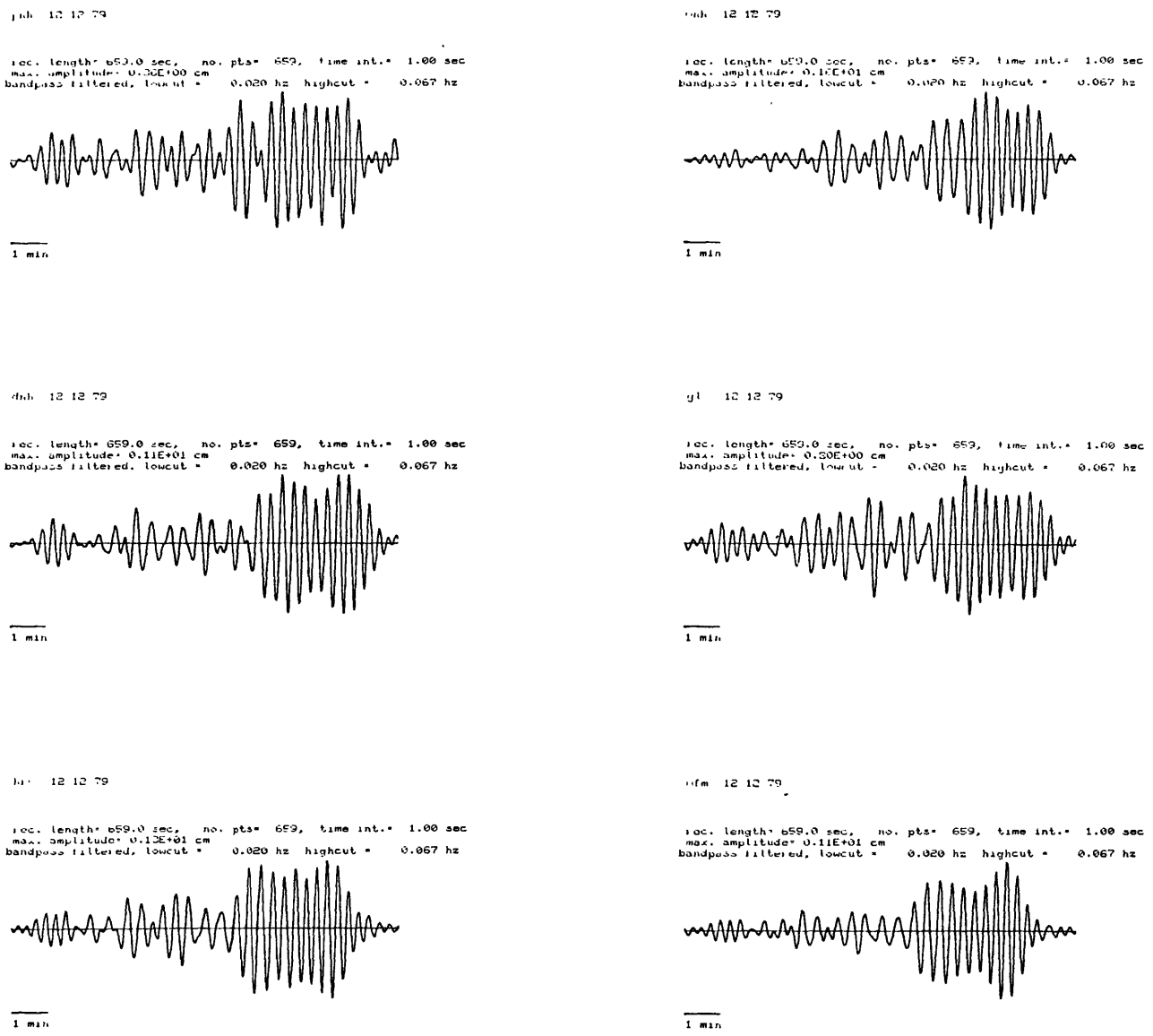
12 12 79
rec. length= 659.0 sec, no. pts= 659, time int.= 1.00 sec
max. amplitude= 0.30E+00 cm
bandpass filtered, lowcut = 0.020 hz highcut = 0.067 hz
1 min
12 12 79
rec. length= 659.0 sec, no. pts= 659, time int.= 1.00 sec
max. amplitude= 0.11E+01 cm
bandpass filtered, lowcut = 0.020 hz highcut = 0.067 hz
1 min
12 12 79
rec. length= 659.0 sec, no. pts= 659, time int.= 1.00 sec
max. amplitude= 0.30E+00 cm
bandpass filtered, lowcut = 0.020 hz highcut = 0.067 hz
1 min
12 12 79
rec. length= 659.0 sec, no. pts= 659, time int.= 1.00 sec
max. amplitude= 0.12E+01 cm
bandpass filtered, lowcut = 0.020 hz highcut = 0.067 hz
1 min
12 12 79
rec. length= 659.0 sec, no. pts= 659, time int.= 1.00 sec
max. amplitude= 0.11E+01 cm
bandpass filtered, lowcut = 0.020 hz highcut = 0.067 hz
1 min

Figure 4.11b

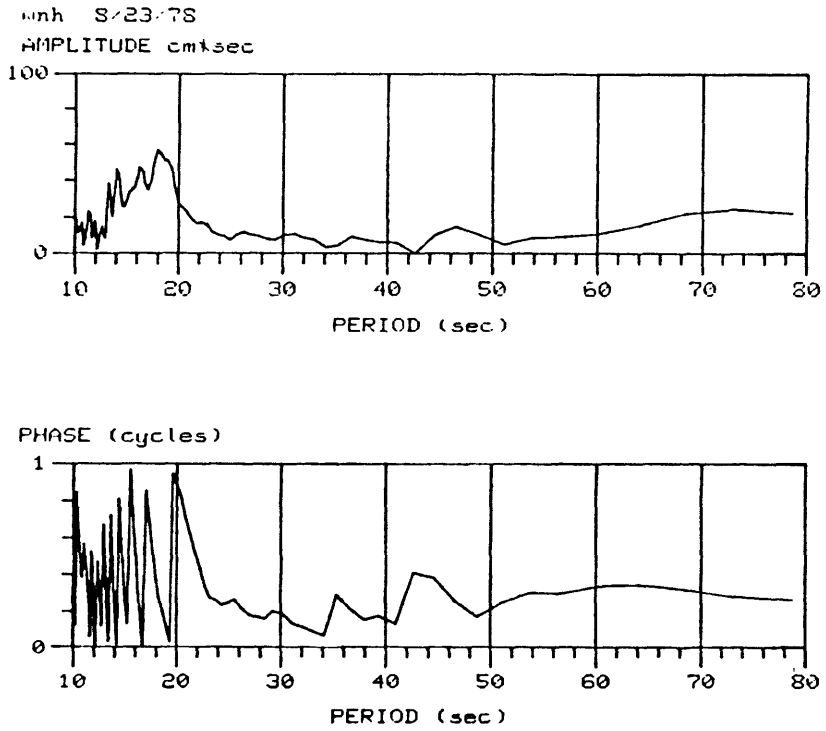
wnh S/23/78
AMPLITUDE cm/sec
100
0
10
20
30
40
50
60
70
80
PERIOD (sec)
PHASE (cycles)
1
0
10
20
30
40
50
60
70
80
PERIOD (sec)

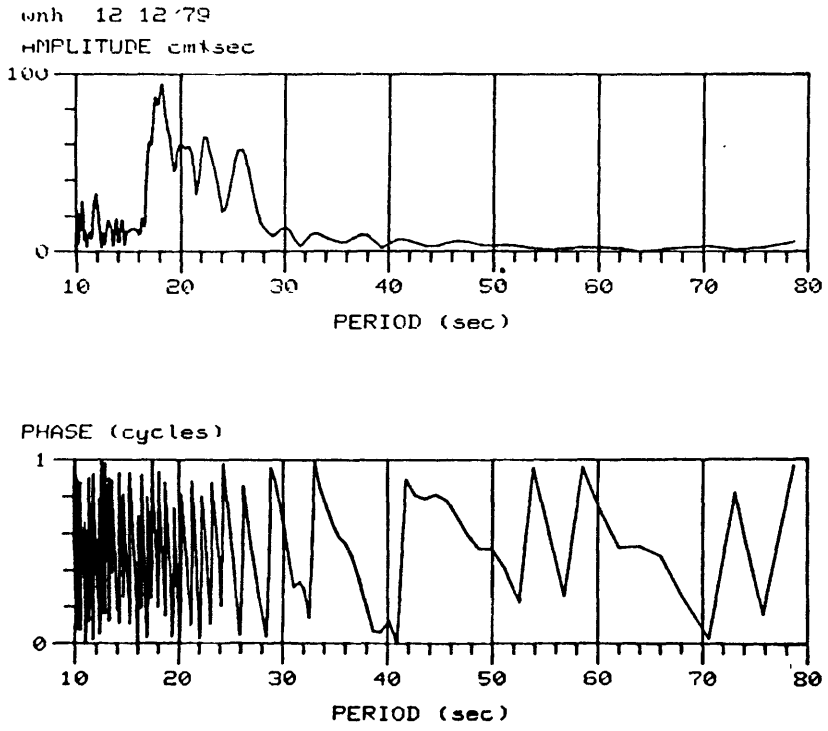
wnh 12 12/79
AMPLITUDE cm/sec
100
0
10
20
30
40
50
60
70
80
PERIOD (sec)
PHASE (cycles)
1
0
10
20
30
40
50
60
70
80
PERIOD (sec)

Figure 4.11

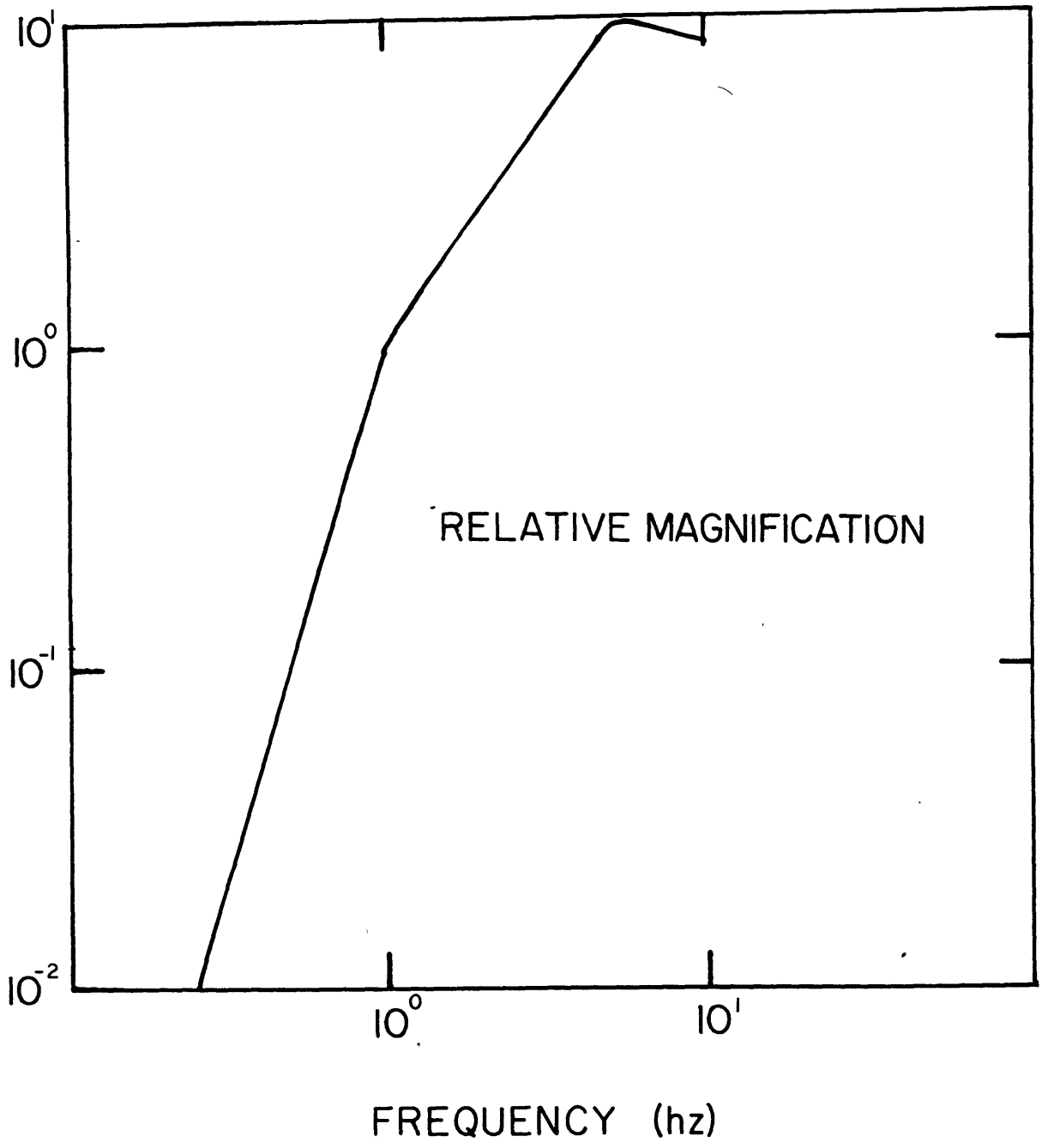
10^{1}
10^{0}
10^{-1}
10^{-2}
RELATIVE MAGNIFICATION
10^{0}
10^{1}
FREQUENCY (hz)

Figure 4.12

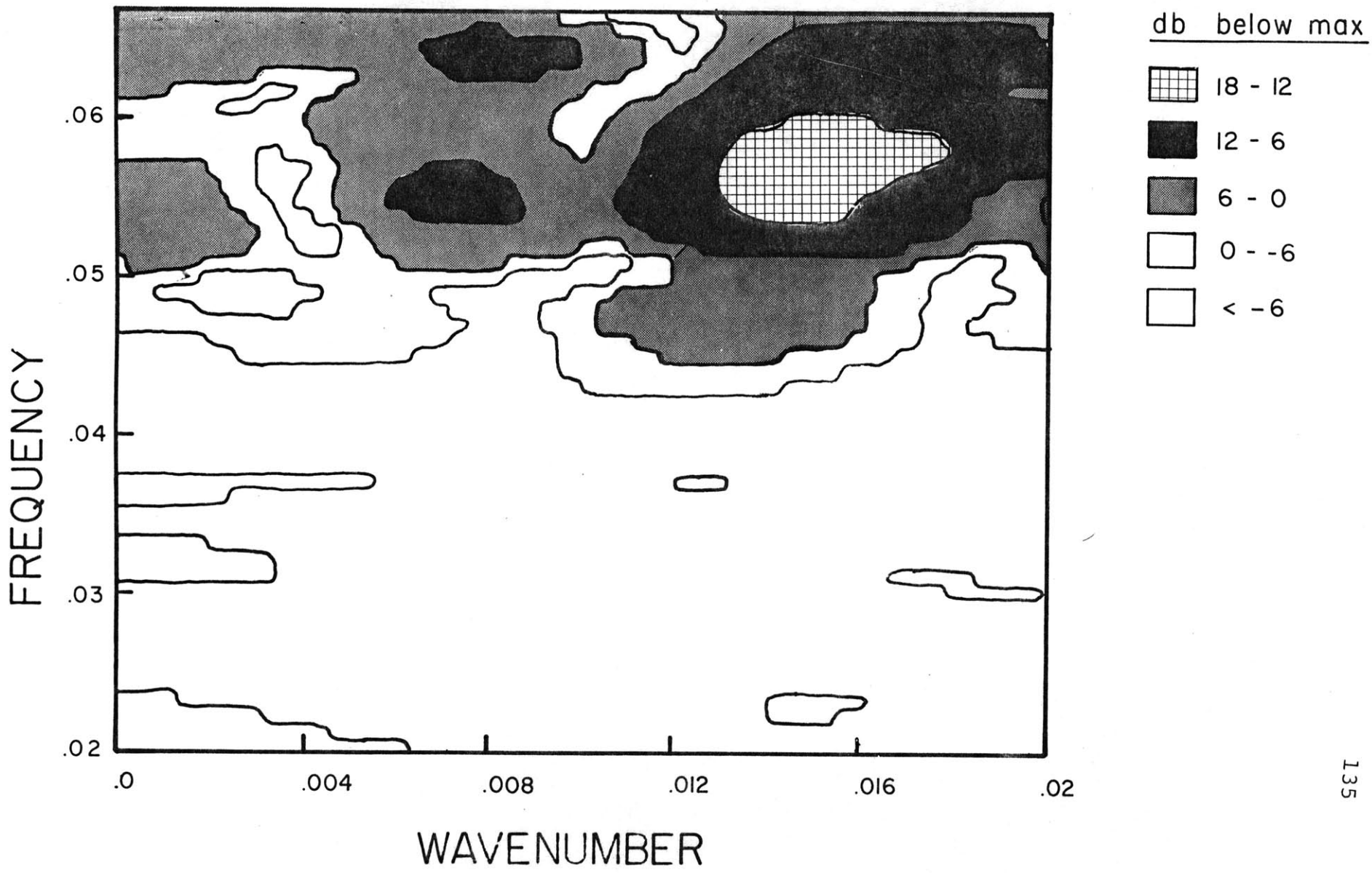
BEAM DIRECTION = 204°
db below max
18 - 12
12 - 6
6 - 0
0 - -6
< -6
FREQUENCY
.06
.05
.04
.03
.02
.0
.004
.008
.012
.016
.02
WAVENUMBER

Figure 4.13

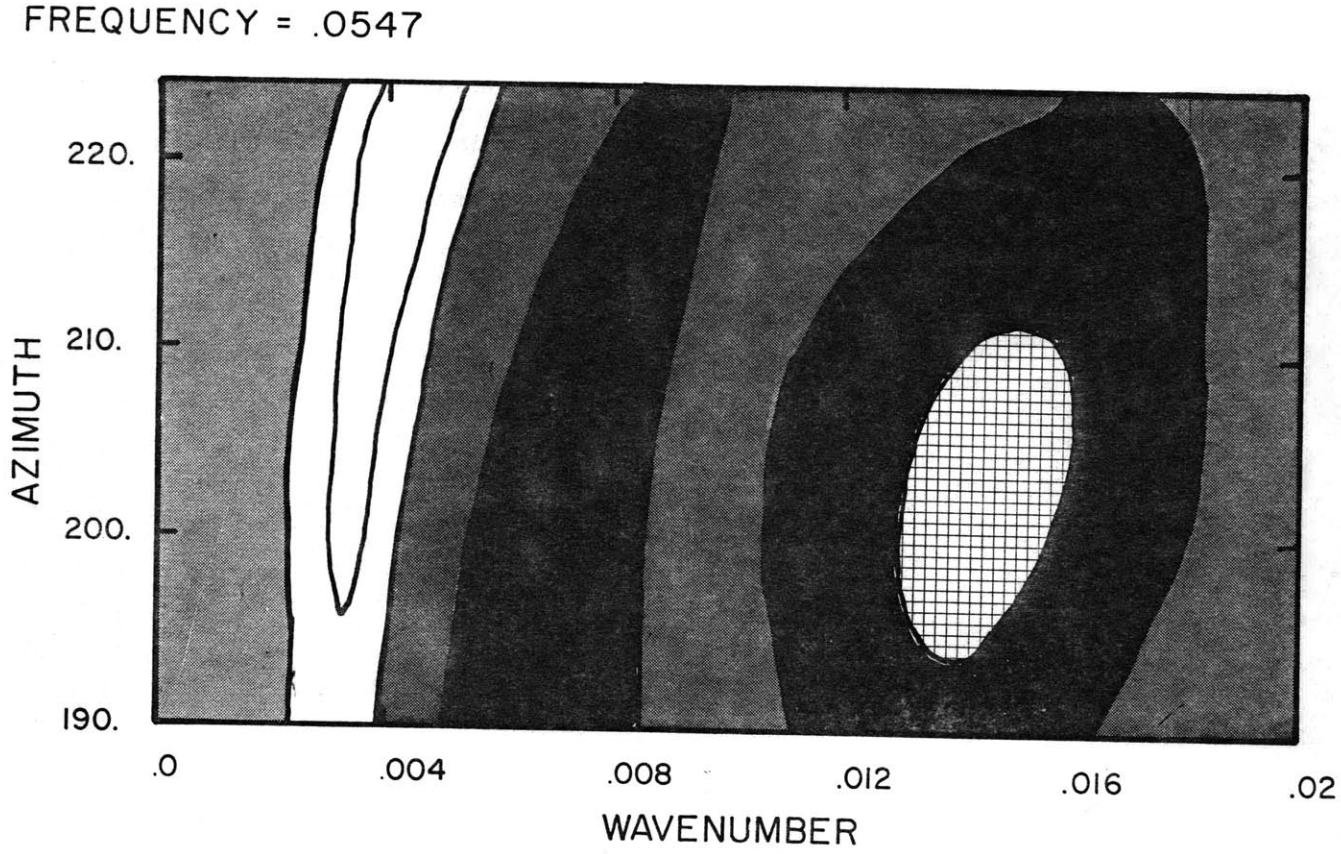
FREQUENCY = .0547
220.
210.
200.
190.
AZIMUTH
.0
.004
.008
.012
.016
.02
WAVENUMBER

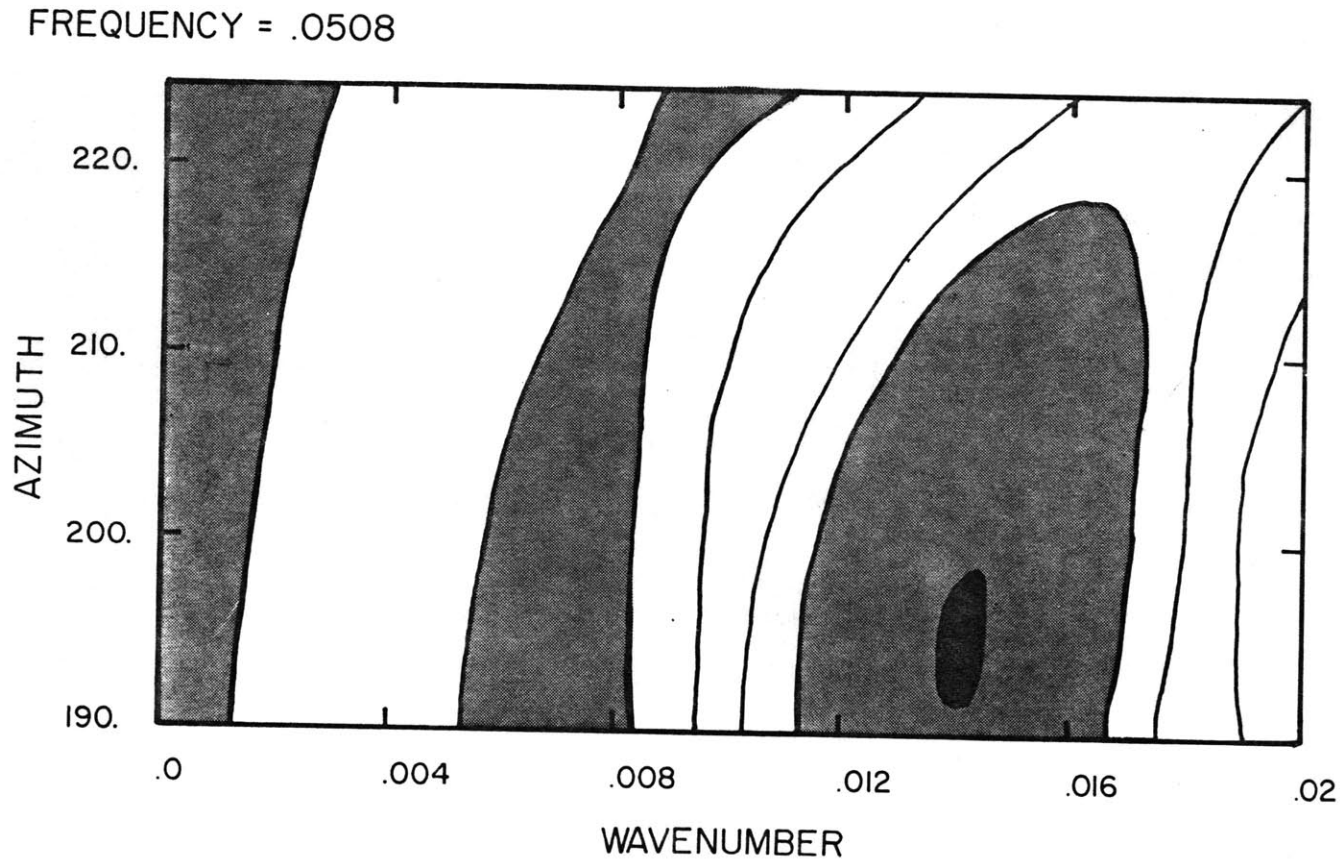
FREQUENCY = .0508
220.
210.
200.
190.
AZIMUTH
.0
.004
.008
.012
.016
.02
WAVENUMBER

Figure 4.14

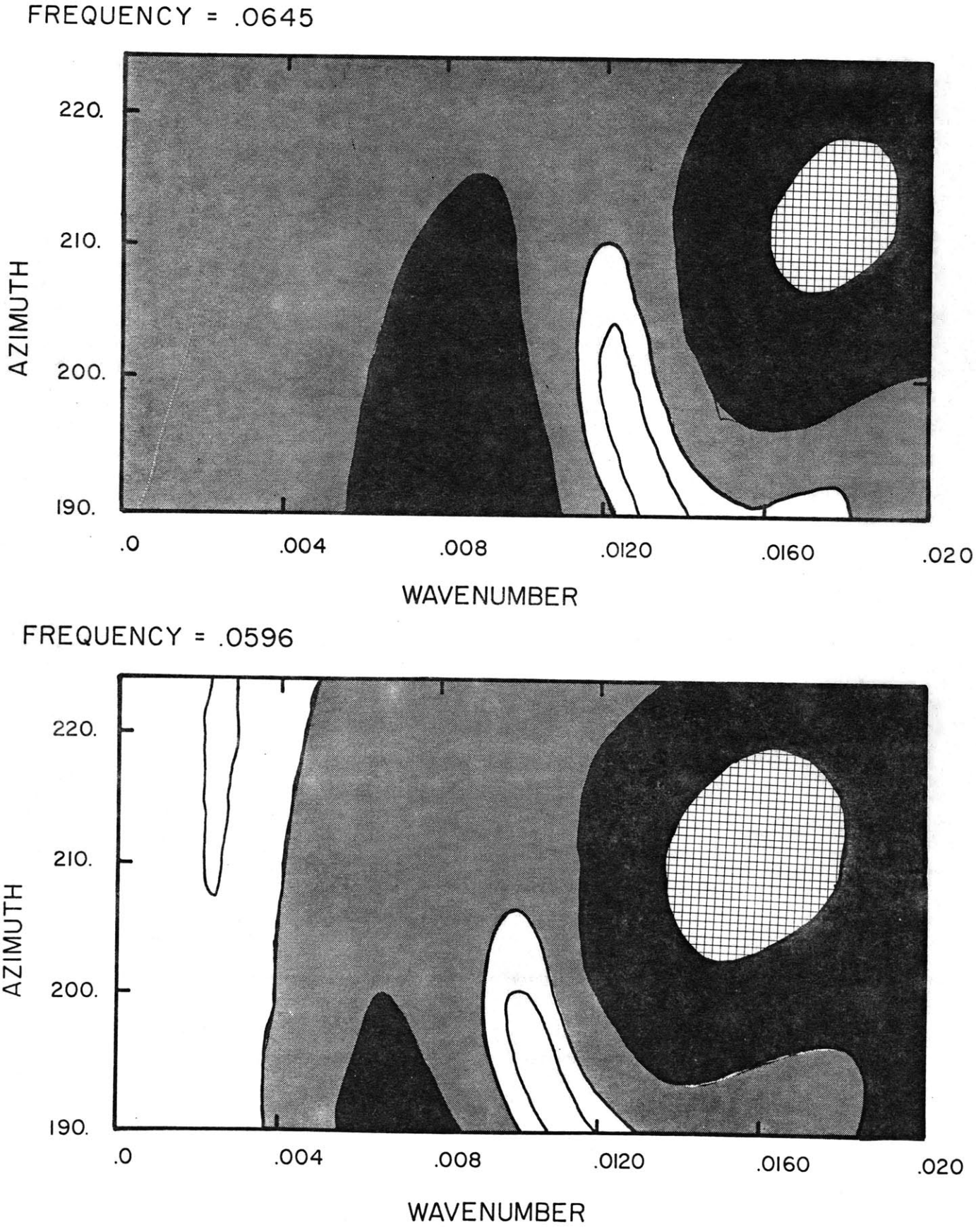
FREQUENCY = .0645
220.
210.
200.
190.
AZIMUTH
.0
.004
.008
.0120
.0160
.020
WAVENUMBER
FREQUENCY = .0596
220.
210.
200.
190.
AZIMUTH
.0
.004
.008
.0120
.0160
.020
WAVENUMBER

Figure 4.14

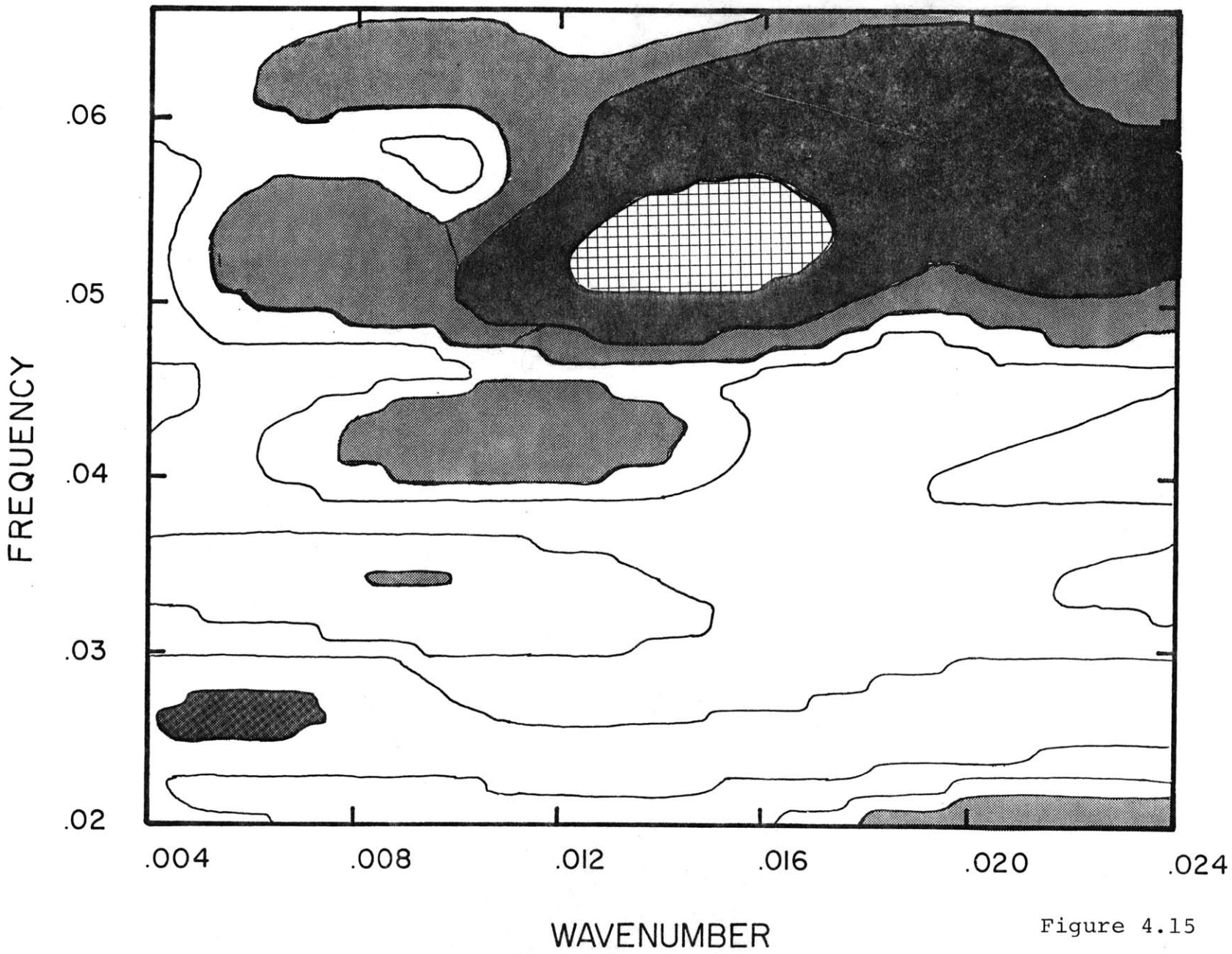
BEAM DIRECTION = 204°
FREQUENCY
.06
.05
.04
.03
.02
.004
.008
.012
.016
.020
.024
WAVENUMBER

Figure 4.15

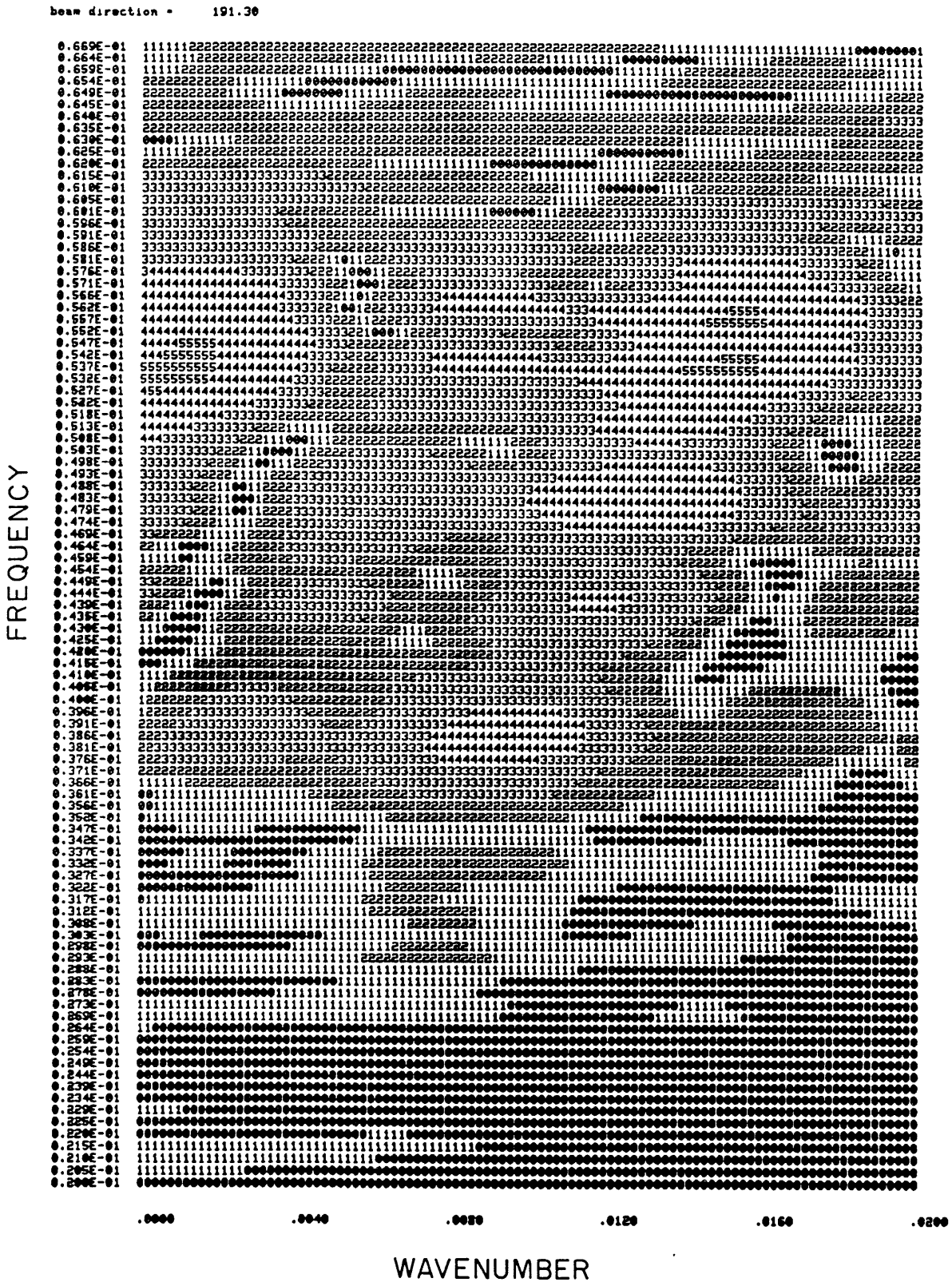
beam direction = 191.30
FREQUENCY
WAVENUMBER
.0000
.0040
.0080
.0120
.0160
.0200

Figure 4.16

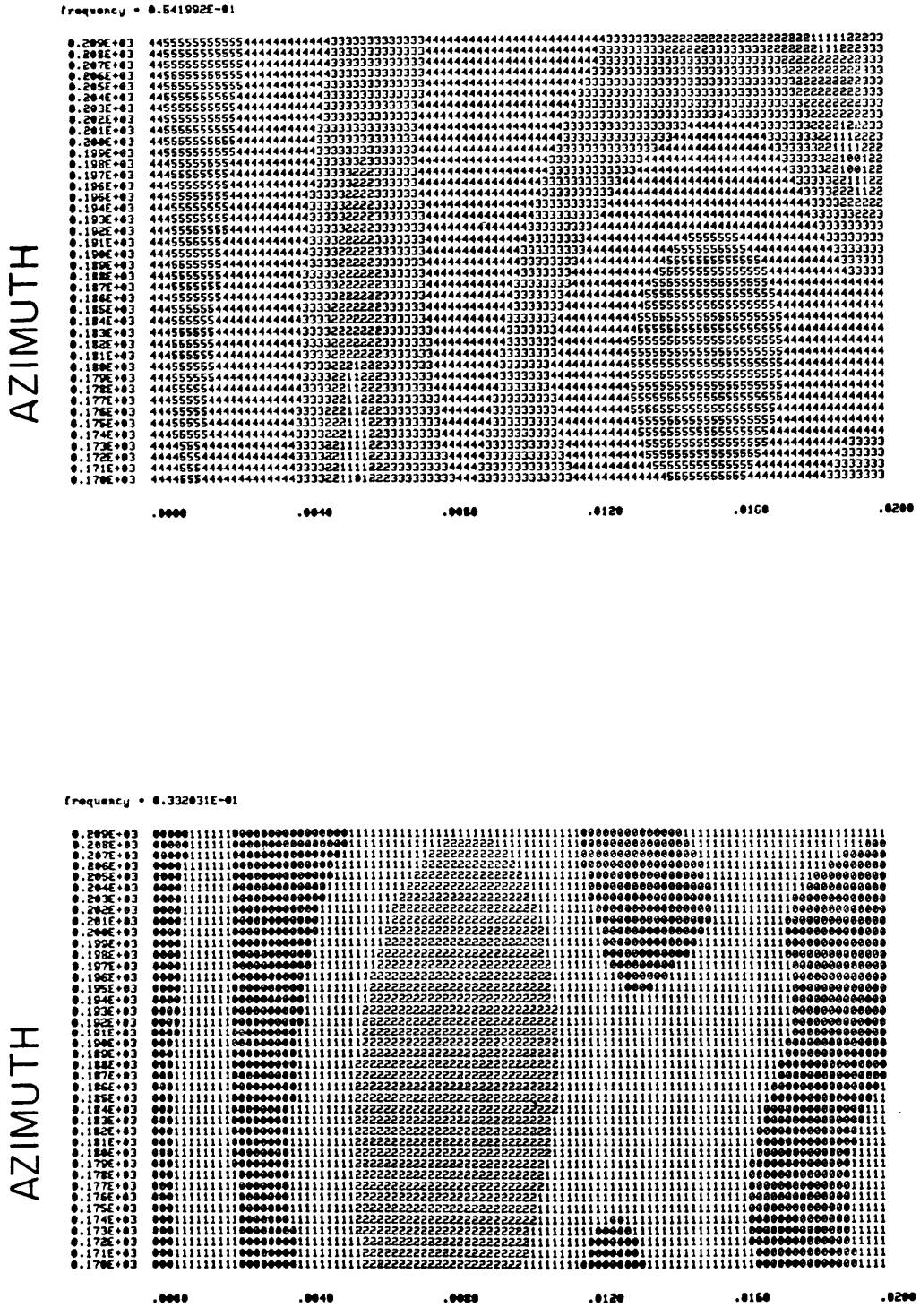
frequency = 0.541992E-01
AZIMUTH
.0000
.0040
.0080
.0120
.0160
.0200
frequency = 0.332031E-01
AZIMUTH
.0000
.0040
.0080
.0120
.0160
.0200
WAVENUMBER

Figure 4.17

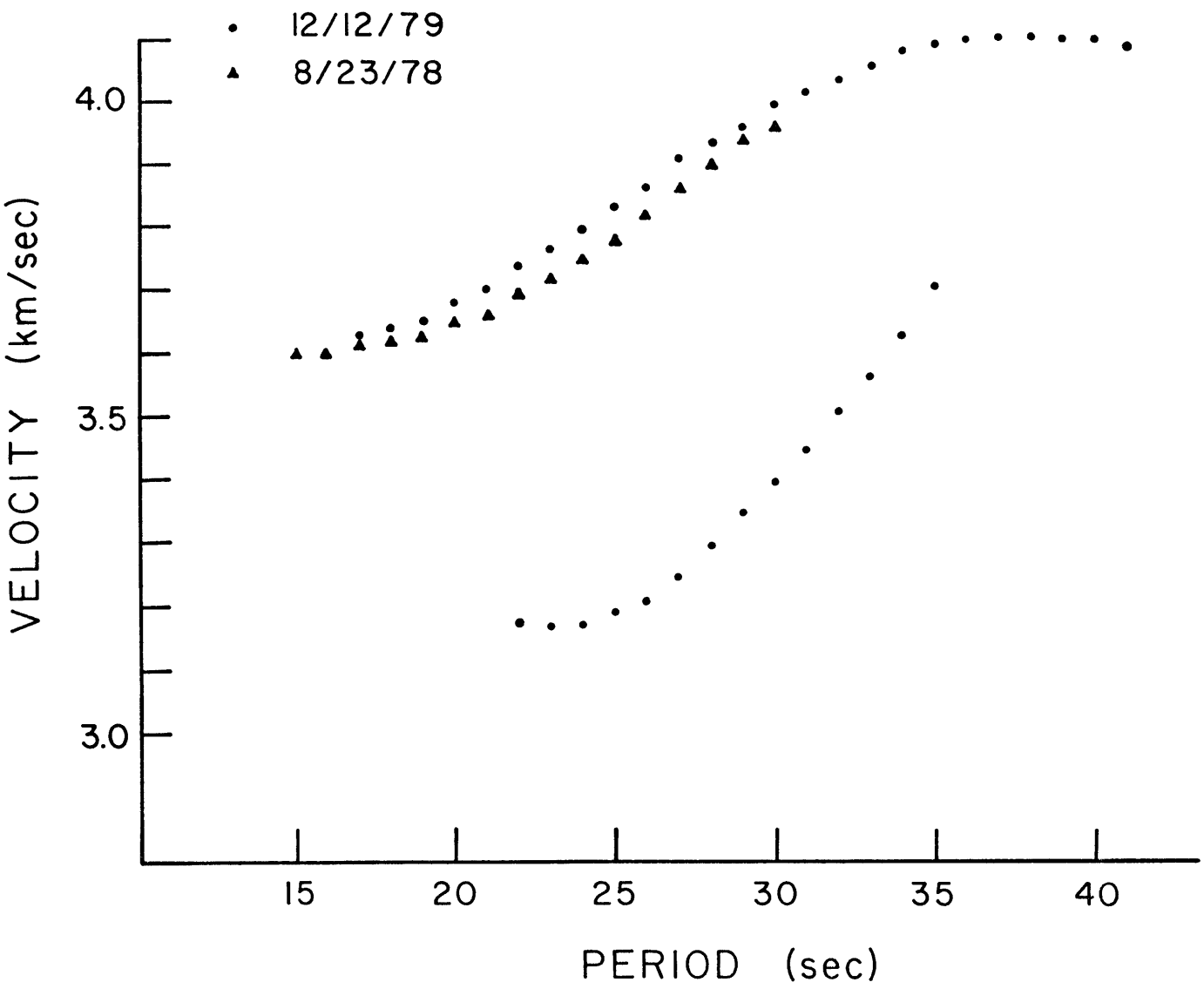
12/12/79
8/23/78
4.0
3.5
3.0
VELOCITY (km/sec)
15
20
25
30
35
40
PERIOD (sec)

Figure 4.18

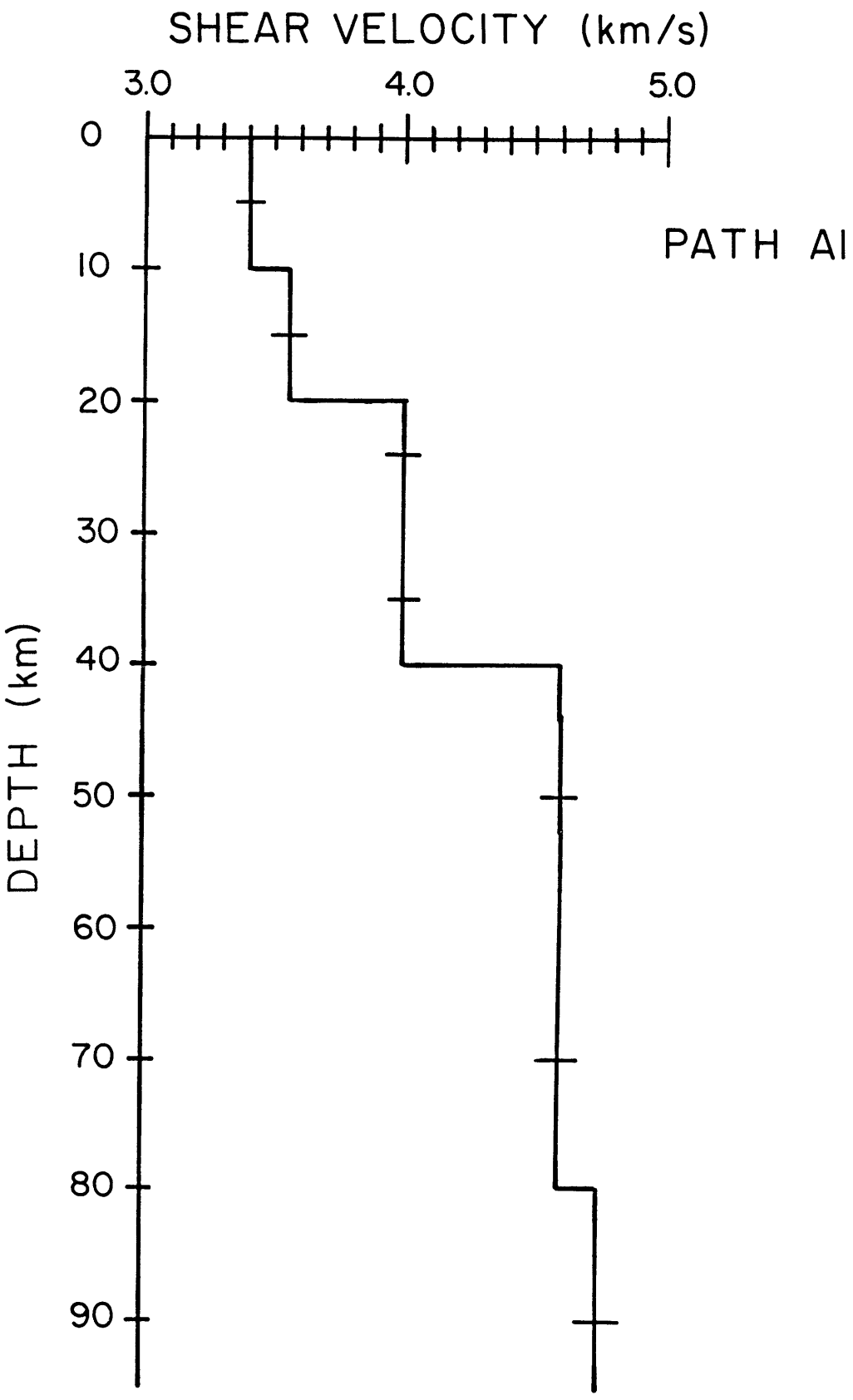
SHEAR VELOCITY (km/s)
3.0
4.0
5.0
0
10
20
30
40
50
60
70
80
90
DEPTH (km)
PATH AI

Figure 4.19a

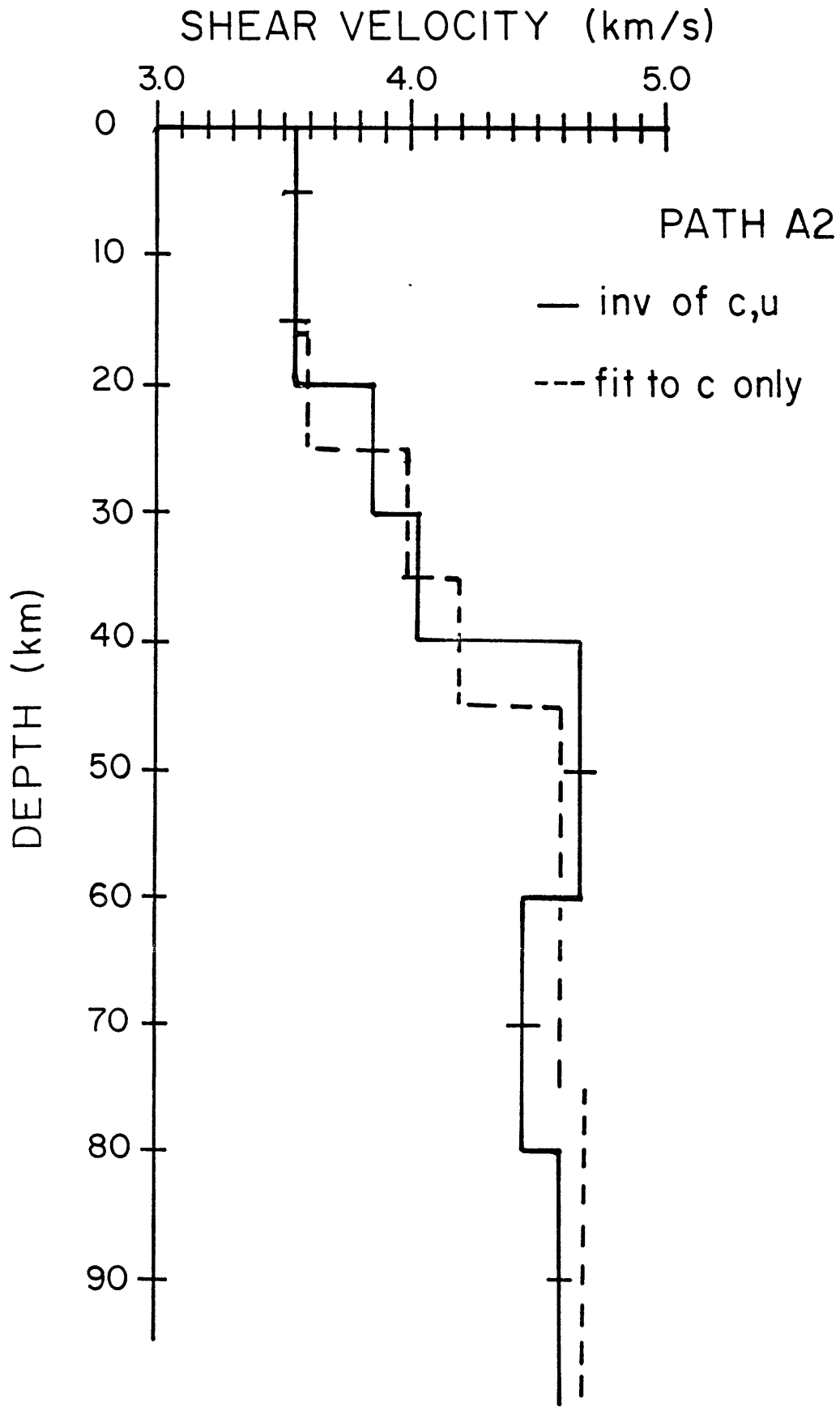
SHEAR VELOCITY (km/s)
3.0
4.0
5.0
0
10
20
30
40
50
60
70
80
90
DEPTH (km)
PATH A2
— inv of c,u
--- fit to c only

Figure 4.19b

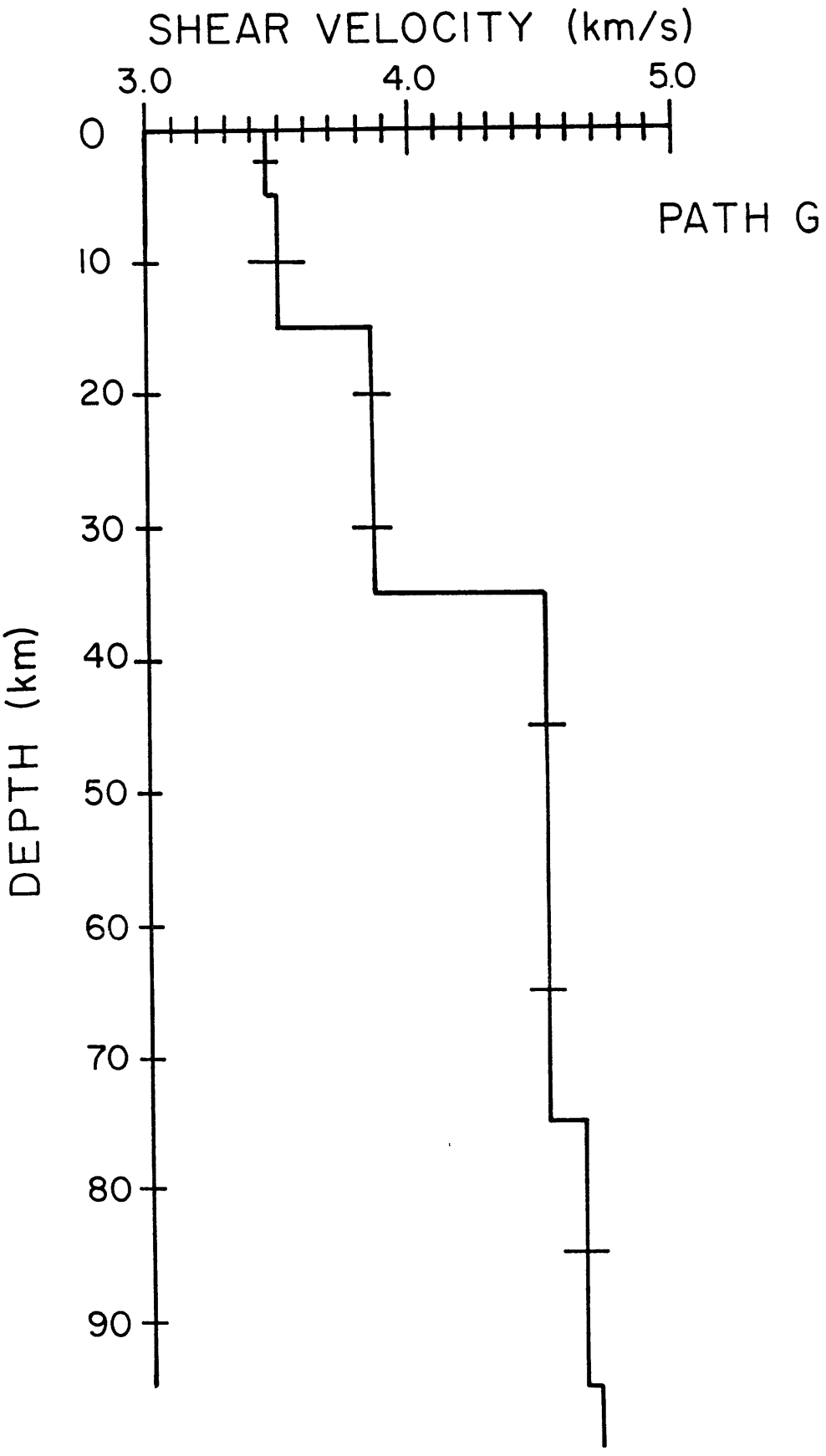
SHEAR VELOCITY (km/s)
3.0
4.0
5.0
0
10
20
30
40
50
60
70
80
90
DEPTH (km)
PATH G

Figure 4.19c

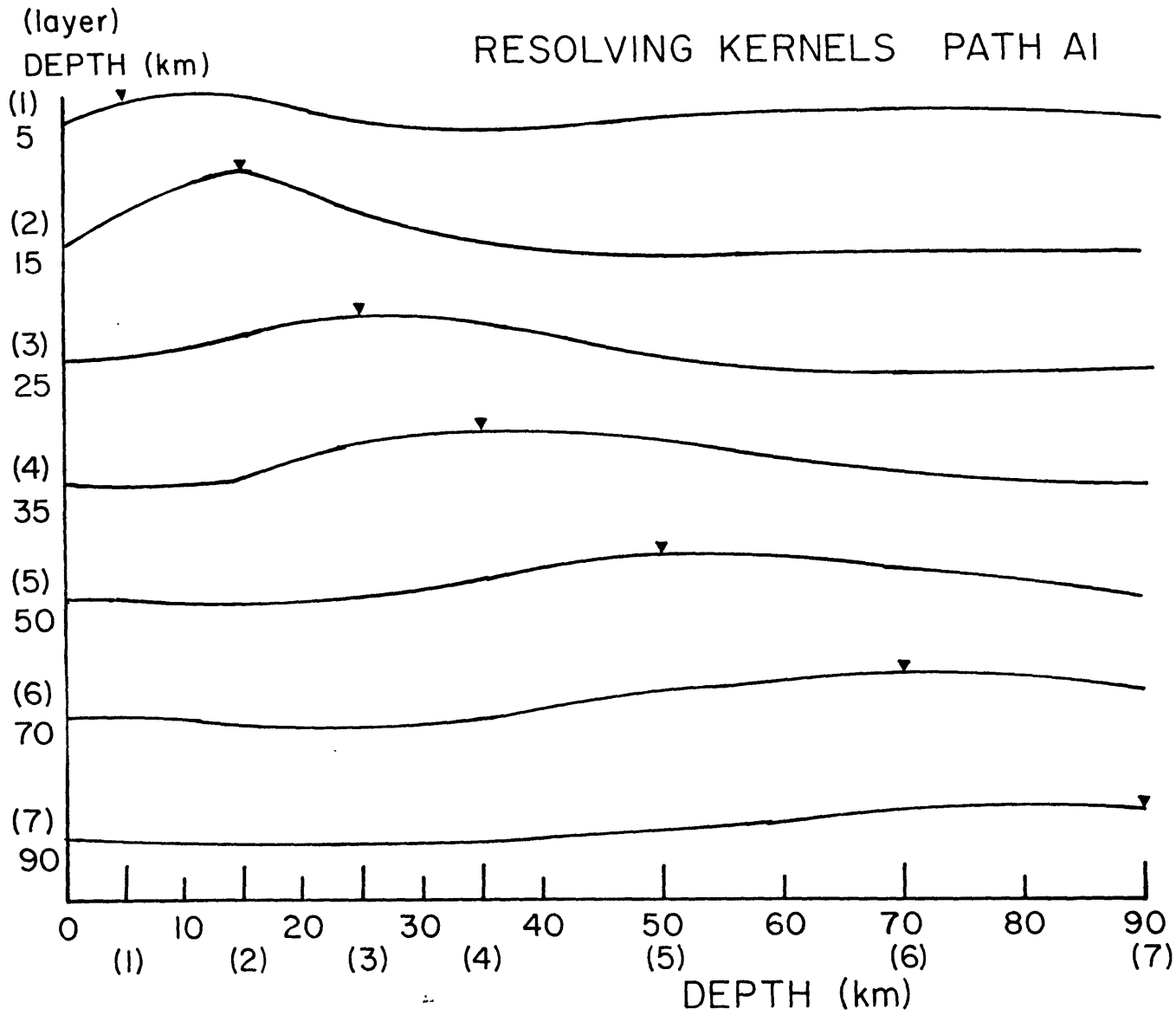
(layer)
DEPTH (km)
RESOLVING KERNELS PATH AI
(1)
5
(2)
15
(3)
25
(4)
35
(5)
50
(6)
70
(7)
90
0
10
20
30
40
50
60
70
80
90
(1)
(2)
(3)
(4)
(5)
(6)
(7)
DEPTH (km)

Figure 4.20a

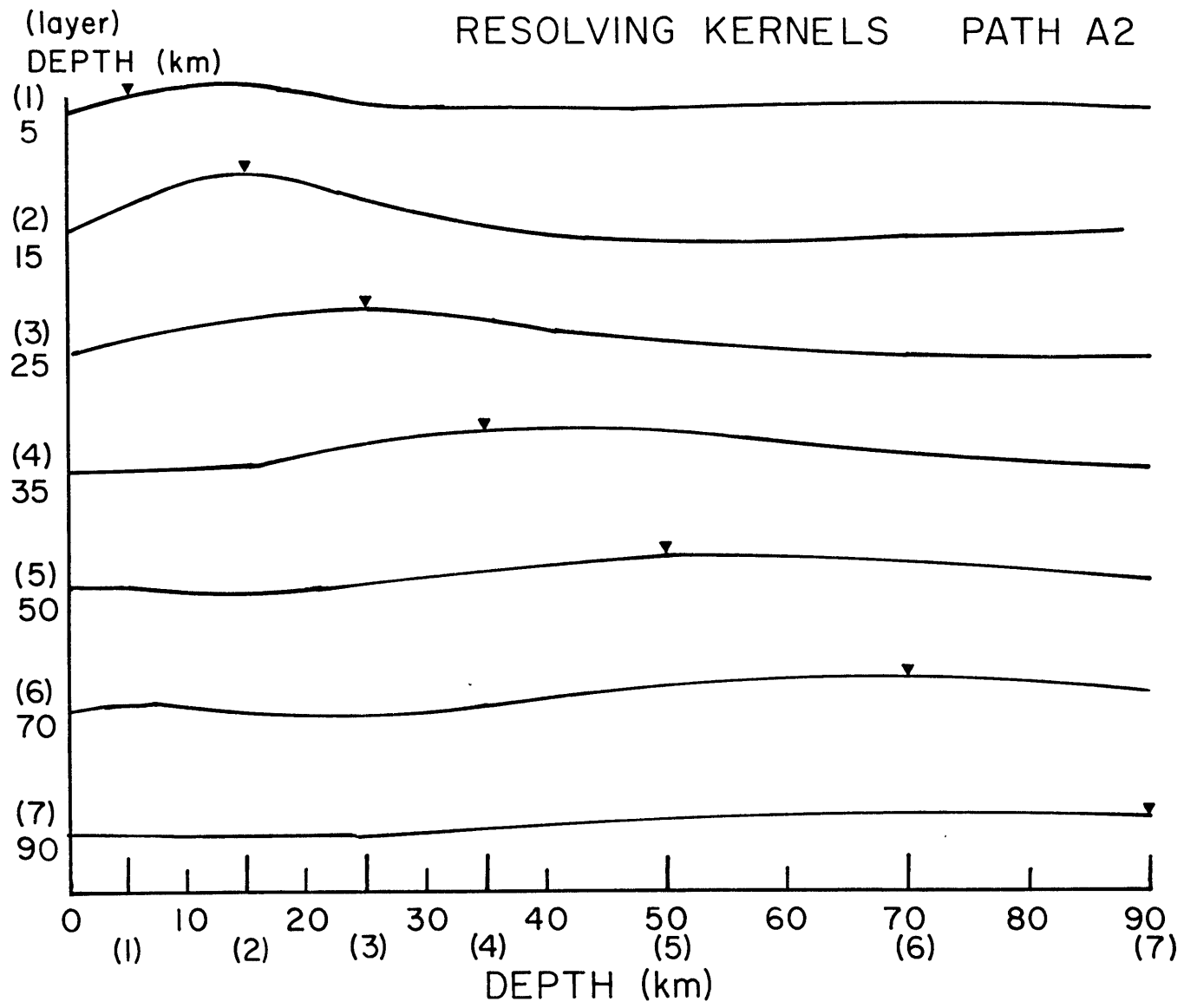
RESOLVING KERNELS PATH A2
(layer)
DEPTH (km)
(1)
5
(2)
15
(3)
25
(4)
35
(5)
50
(6)
70
(7)
90
0
10
20
30
40
50
60
70
80
90
(1)
(2)
(3)
(4)
(5)
(6)
(7)
DEPTH (km)

Figure 4.20b

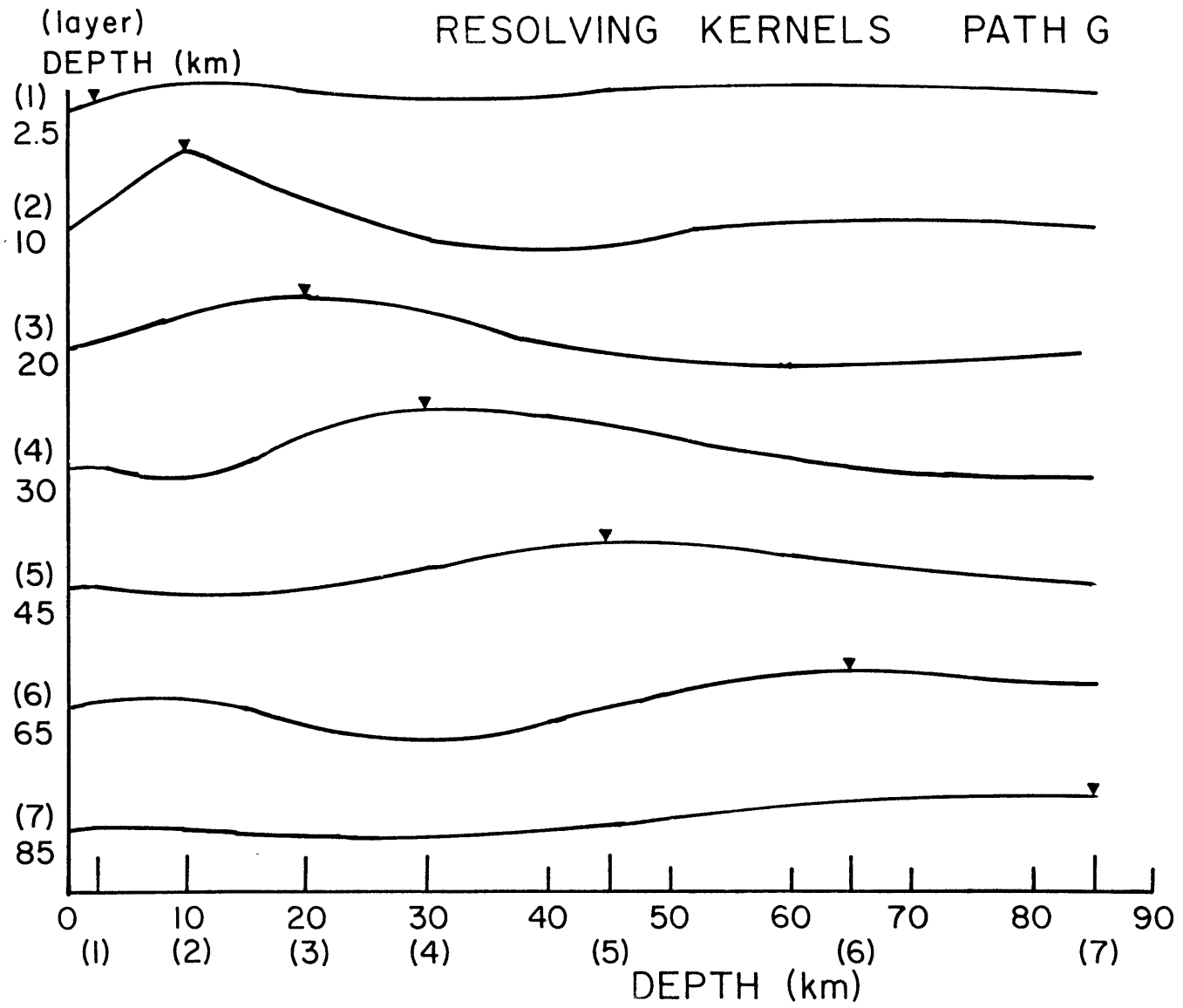
RESOLVING KERNELS PATH G
(layer)
DEPTH (km)
(1)
2.5
(2)
10
(3)
20
(4)
30
(5)
45
(6)
65
(7)
85
0
10
20
30
40
50
60
70
80
90
(1)
(2)
(3)
(4)
(5)
(6)
(7)
DEPTH (km)

Figure 4.20c

CHAPTER 5

CRUST AND UPPER MANTLE STRUCTURE FROM TELESEISMIC P WAVES

This chapter reports on the results of a study of teleseismic P wave arrival times recorded by the Northeastern Seismic Network. The inversion of teleseismic P wave travel time residuals is a commonly used method of extracting velocity information in the crust and upper mantle beneath an array. Notable studies include those in California (Bolt and Nuttli, 1966; Nuttli and Bolt, 1969; Steeples and Iyer, 1976) at LASA (Sheppard, 1966; Iyer and Healy, 1972; Greenfield and Sheppard, 1969) , in Arizona (Johnson, 1967), in Japan (Zandt, 1975; Hirahara, 1977), at NORSAR (Aki et al., 1977), in Yellowstone National Park (Iyer, 1975; Zandt, 1978), in Hawaii (Ellsworth and Koyanagi, 1977)in New Madrid (Mitchell et al., 1977), in the southeastern United States (Volz, 1979), and beneath the Tarbela Array (Menke, 1977).

Many of the earlier studies consisted of determination of residual patterns and development of qualitative models to explain the observed trends. Recent models have utilized the techniques developed by Aki et al. (1977) , for mapping the three-dimensional structure beneath an array. The comprehensive analysis of the three-dimensional inversion method will not be discussed in this chapter because the

details are covered in Aki et al., (1977), Zandt (1978), and Ellsworth (1977).

To date, very little seismological work pertaining to crust and upper mantle structure has been done in the northeastern United States. Leet (1941), Linehan (1962), and Katz (1955) published refraction results using a small permanent array combined with some portable stations. More recently some refraction work has been reported by Chiburis and Graham (1978) and Aggarwal in Schnerk et al. (1976). Other relevant studies include a surface wave analysis in New York (Dorman and Ewing, 1962), analysis of teleseismic PP residuals beneath Newfoundland (Stewart, 1978) , and a study of teleseismic P-wave residuals across the eastern United States and Canada (Fletcher et al., 1978). In Chapter 3 we discussed the crustal models derived from interpretation of regional travel time data.

In this chapter, a three-dimensional inversion of teleseismic P-wave residuals is presented using data collected from the Northeastern Seismic Network. The model is interpreted in conjuction with other geophysical and geological observations in an attempt to learn about the crust and upper mantle structure beneath two adjacent ancient orogenic belts, the Grenville and Appalachian Provinces. An effort is also made to interpret the models in light of, and to place constraints on a plate tectonics origin for both orogenic belts.

5.1 TRAVEL TIME RESIDUALS

Teleseismic P-wave arrival times were collected from 50 stations which are part of the Northeastern Seismic Network (Figure 5.1). The stations were installed and are operated by research groups at Boston College (Weston Observatory), Lamont-Doherty Geological Observatory, and Massachusetts Institute of Technology. Station distribution is fairly uniform, although there are areas with large station spacing. Not all of the stations were in operation for the duration of this study. Because the network was not in full operation until February, 1976, events used in this study covered a time range between February, 1976, and December, 1977. Most stations are equipped with vertical component, short period 1 or 2 hz geophones. Signals are telemetered to central recording sites (located at each of the above institutions) and recorded on develocorder film.

The relative arrival times of teleseismic P-waves were read from enlarged copies of 16mm develocorder film. In general, strong scattering in the frequency bandwidth of the incident P waves is not observed as indicated by the coherency of the first few cycles across the network. The signals from each of the stations were visually correlated using an overlay of representative waveforms. Relative arrival measurements were taken from a prominent peak or trough early in the signal, and readings were taken to the nearest 0.1 second. A misidentification of the peak or

trough would cause a residual error of 0.5 to 1.0 seconds which is readily apparent once the residuals are calculated.

1822 arrival times from 68 events were read from stations of the northeast network. The epicentral distances ranged between 25 and 95 degrees and azimuths were mainly from the northeast (from Eurasia), south and southwest (Central and South America), and the northwest (Aleutians, Kuriles), (Figure 5.2).

Elevation corrections were applied to the data and travel times were reduced to a datum elevation at sea level. Absolute P-wave residuals were calculated using Herrin travel-time tables and are defined to be

$$R_{ij}^{H} = T_{ij}^{obs} - T_{ij}^{H} \qquad (5.1)$$

where R_{ij}^{H} is the absolute residual with respect to Herrin tables for station i , event j; T_{ij}^{obs} is the observed travel time using event locations and origin times from PDE bulletins; T_{ij}^{H} is the theoretical travel time through a Herrin earth. The residuals were further reduced by calculating relative residuals with respect to a mean residual computed for each event;

$$\bar{R}_{ij} = R_{ij}^{H} - \frac{1}{N}\sum_{i=1}^{N} R_{ij}^{H} \qquad (5.2)$$

where N is the number of stations reporting P arrivals for event j.

Using the above relationships, positive residuals represent late arrivals where the incident rays have been

slowed in the crust or upper mantle beneath the network. It should be noted that no significant differences were observed in the values of the relative residuals when Jeffreys-Bullen travel time tables were used instead of Herrin Tables. An error in the reported origin time or a source correction term will affect all stations similarly and will drop out when relative residuals are computed. The effects of the structure at the source, heterogeneities encountered along the major portion of the travel path, and structural variations beneath the array are major causes of the absolute residuals. Intuitively, the cone of rays from a teleseismic source to different stations in the network will sample nearly identical travel paths until they diverge into the upper mantle and crust beneath the array. Thus, it is reasonable to assume that the computed average residuals contain information regarding this common travel path up to the point where the rays diverge significantly. By subtracting off the average residual, effects caused by mislocation errors or heterogeneities encountered along the common path are greatly reduced.

The above approximations which are reasonable when network aperture is small become progressively less valid as the network aperture is increased. If the apparent network aperture is large enough, the curvature (second derivative) of the travel time curve becomes significant. The problems involved in the analysis of relative P-wave residuals have been discussed by Engdahl et al. (1977). Using data from

Alaskan-Aleutian stations, Engdahl concluded that the primary source of observed variations in relative residuals was from local structure beneath the network. For station separations comparable to the maximum diameter of the Northeastern U.S. Network (600 km), scatter in relative residuals from epicenter mislocations, source structure, earth models, etc. were at most 0.2 seconds, which is little more than our reading accuracy. Analysis of relative residuals recorded in the northeastern U.S. supports these conclusions. We found no systematic differences in relative residuals from various depths in the same epicentral regions where it is presumed rays would encounter different source structures.

Two additional sources of error remain to be discussed. Because of down-time for some stations, and of other stations that became operational during the period of this study, slightly different station subsets are available for each earthquake, and the mean residual subtracted off from a given source region may vary for different events. However, this problem is greatly reduced by the large number of stations (typically 25-35) used to calculate the mean residual for each earthquake. The other problem results from the fact that each subnetwork records on a different time base. Each subnetwork operates a temperature compensated crystal oscillator clock and timing corrections are generally less than 20 ms/day. To assure accuracy, tests were made by comparing signals from a common station

recorded on more than on subnetwork. The analysis of travel time residuals was carried out using relative residuals. The distribution of average relative residuals, $\bar{R}$, for each station is shown in Figure 5.3. The relative residuals as a function of azimuth and incidence angle show significant variations across the network (Figure 5.4). These trends suggest the presence of large scale lateral heterogeneities in the crust and upper mantle, and considerable effort is required to separate the factors causing the observed patterns.

Average relative residuals for each station were calculated with ten or more readings from well-distributed azimuths. Large positive residuals (late arrivals) occur throughout central and northern New Hampshire, southern Maine and eastern Vermont. As was observed by Fletcher et al. (1978) these contrast sharply with large negative residuals in western Vermont, northern New York, southeastern New York, and southwestern Connecticut. Shallow, localized structural differences should result in rapidly varying trends between adjacent stations. However, the slowly varying distribution of residuals suggests that the observed variations are probably due to deep, regional structures such as differences in crustal thickness and upper mantle velocity.

As a first step we compare the residuals with surface geologic and other geophysical data. Figure 5.5 illustrates the relationship between average relative station residuals,

$\bar{R}$, and the regional Bouguer gravity taken from each station site (Kane et al. (1972), Simmons, (1964), and Diment et al. (1972)). Because the long wavelength ($\sim$100km) regional gravity anomalies probably reflect variations in Moho topography, (Simmons, 1964), the correlation between gravity and average residuals suggests that for many stations, the average residuals depend partly on crustal thickness variations. It is also interesting to note the dependence of average residuals on the age of the basement beneath each station. The two sets of symbols in the figure correspond to the inferred age of the basement for each station site. Stations in New York and New Jersey are located above Precambrian (> 1.0 b.y.) Grenville basement, while most New England stations are atop younger (< 1.0 b.y.) Paleozoic basement of the Appalachian Province (the central mobile belt, and eastern belt described earlier). Clearly, the stations within the older Grenville Province see early arrivals relative to those in the younger Appalachian Province. However, because of the relationship between Bouguer gravity anomalies and station elevation it is difficult to attribute this separation totally to crustal thickness variations (Figure 5.6). In isostatically compensated regions, crustal thickness should be correlated with surface elevations (Woolard, 1959; Tseng, 1975). Figure 5.6 illustrates that there is a poor correlation between gravity and elevation and more importantly there is no obvious separation between the two regions. To explain

the behavior of both Figures 5.5 and 5.6 it is necessary to invoke velocity changes in addition to any possible variations in crustal thickness. This idea is supported by refraction profiles constructed in the northeastern U.S. Although little detailed refraction work has been done in this region, existing studies and results cited in Chapter 3 indicate slightly higher average crustal velocities in the Grenville Province, as opposed to the Appalachian Province. Table 3.5 shows refraction models collected from regional travel times in the NEUS. Comparison of the refraction models indicates that the crust beneath this part of the Appalachian Province is on the average slightly thicker and slower, and it is possible to account for almost half of the approximately 0.5 second difference in relative residuals between the two regions.

The dependence of average relative residuals on crustal properties is also supported by the results of the time-term analysis which indicates a positive correlation between Pn residuals and teleseismic P-wave residuals (Chapter 3). The relative Pn and teleseismic P wave residuals are compared in Figure 5.7a. Also shown in Figure 5.7a is a line representing the theoretical relationship between the two sets of residuals assuming total crustal effects. By assuming a simple crustal model, we compare Pn time terms with teleseismic "time terms" from a shallow focus event, 50 degrees away (Figure 5.7b). From Figure 5.7b, we define the crustal thickness h=35 km; crustal velocity Vc = 6.4 km/s;

upper mantle velocity Vm = 8.1 km/s, and the apparent velocity of the teleseismic P wave is calculated to be Va = 14.7 km/s. The incidence angle for the refracted wave is ic = 52 degrees and for the teleseismic P wave i_t = 26 degrees. If the variations in residuals across the network are caused by differences in crustal thickness, Δh, then the resulting difference in travel time for the refracted wave through the crust is given by

$$\Delta T_{P_n} = \frac{\Delta h \cos i_c}{V_c} \qquad (5.3)$$

Similarly for the teleseismic P wave

$$\Delta T_{P_T} = \frac{\Delta h \cos i_t}{V_c} \qquad (5.4)$$

The ratio of (5.3) to (5.4) gives the slope of the relationship to be expected

$$\frac{\Delta T_{P_n}}{\Delta T_{P_T}} = \frac{\cos i_c}{\cos i_t} = \frac{\sqrt{1-(V_c/V_m)^2}}{\sqrt{1-(V_c/V_a)^2}} \qquad (5.5)$$

For the parameters given above, the slope will equal 0.7. Because the Δ T values represent the time it takes for the wavefronts to move vertically upward through the crust, the two set of residuals should show a positive correlation. Because of the differences in incidence angles, if the mean teleseismic P wave residuals are a result of variations in crustal thickness, the trend of the Pn vs. Pt residuals shown in Figure 5.7 should have a slope less than one. Although there is a fairly good correlation between the two

sets of the residuals, there is a large amount of scatter about the line which they should cluster about if the variations in teleseismic P-wave residuals are due to crustal thickness differences. To the first order, it appears that the distribution of average teleseismic P wave residuals is affected by crustal thickness or velocity effects. However, these observations cannot fully explain Figures 5.5 and 5.6 and, as indicated by three-dimensional models presented in the next section, structural differences between the two regions extend into the upper mantle.

In addition to distinct patterns in the distribution of average residuals across the network, most stations show a strong dependence in residuals with azimuth and incidence angle. Polar plots of relative residuals as a function of azimuth and incidence angle for many northeastern stations are shown in Figure 5.4. Moving from south to north we see a number of interesting residual trends. In Connecticut, for arrivals from the northeast, the residuals become increasingly less positive (arrive earlier) as the incidence angle decreases until in southwest Connecticut and northern New Jersey residuals are largely negative. Rapidly varying structure is observed to the south which will be reflected in the three-dimensional models presented in the next section. In Massachusetts, arrivals are late to the northwest and small to the south and northeast while New Hampshire and southern Maine observe late arrivals from all azimuths. Negative residuals are observed in the Grenville

Province across most of New York, particularly in the northern regions, where large negative residuals are observed from the northwest.

The residual patterns indicate that between the Grenville and Appalachian orogenic belts, structural differences exist in the crust, and into the upper mantle. It appears that a large region of relatively low velocities occurs in the upper mantle beneath central New England and that velocities become increasingly higher beneath the older Grenville Province to the west. From Figure 5.3 it is evident that most stations in close proximity to one another show a similar distribution in residual values implying that lateral variations are not a near surface effect. Since the incidence angles are small for the teleseismic P-waves (15 - 30 degrees), lateral variations in crustal velocities cannot account for the observed effects. For example, teleseismic rays of equal slowness and incident from opposite azimuths, enter the crust with a maximum separation of 50 km. Azimuthal variations of one second and greater would require unreasonably large lateral velocity differences.

The possibility of a dipping Moho as a cause of azimuthal variations in residuals was investigated. To the first order in the dip, α , the maximum differential travel time for a teleseismic ray approaching from opposite azimuths perpendicular to the strike of a dipping layer is given by

$$T = 2hp\left(1 - \frac{\cos\theta}{V_m^2\sqrt{\eta^2 - p^2}}\right)\alpha \qquad (5.6)$$

where h is the depth to the interface beneath a given station; α is the dip of the interface; $\theta = \sin^{-1}(pV_m$ represents the incident angle at the interface; and $\eta_c = 1/V_c$ (Taylor, 1977). Substitution into equation 5.6 implies that unreasonably large regional dips of the Moho (20 - 30 degrees) are required to satisfy the observations. Thus, it is reasonable to assume that laterally varying structures in the upper mantle beneath the network are required to explain the pronounced residual versus azimuth and incident angle variations.

5.2 THREE-DIMENSIONAL INVERSION

Qualitative description of residual patterns as in the previous section is a useful but inadequate means of estimating the structual disturbances an incident ray encounters beneath the network. In this section we present results from a three-dimensional inversion of the teleseismic travel time data following the techniques illustrated by Aki et al. (1977). The initial model used in the inversion consists of a plane-layered medium where each layer is sub-divided into a series of right rectangular blocks. Using relative teleseismic P wave residuals, individual slowness perturbations $\left(\frac{\delta v}{v}\right)$ are computed for each block relative to a layer average. Aki et al. (1977) has shown that for the ith station and jth event, relative

residuals (with respect to a mean) can be represented by

$$r_{ij} = \sum_{k=1}^{a} T'_{ijk} D_{ijk} \qquad (5.7)$$

where $T'_{ijk} = T_{ijk} - \frac{1}{N} \sum_{k=1}^{N} T_{ijk}$, reduced travel times

T_{ijk} - travel time through kth block

D_{ijk} - $-\left(\frac{\delta v}{v}\right)_k$, percent perturbation in slowness relative to the layer average ($\frac{1}{v_k}$)

N - number of observations for event j

a - number of layers

In matrix form $$\underline{r} = A\underline{m} \qquad (5.8)$$

where

$\underline{r}$ - n-length vector containing relative residuals

$\underline{m}$ - k-length vector containing unknown velocity perturbations

A - n x k symmetric matrix with reduced travel times

Solution of the system (5.8) by classical least squares fails because there exist two sources of non-uniqueness. The first source can be caused by insufficient data and results in vertical "coupling" of inadequately sampled blocks in separate layers which share a common ray path. The other source of non-uniqueness is inherent to the formulation of the problem and results from the removal of the average residual from the data. This implies that within a given layer, the velocity perturbations are determinant only to within a constant and no information regarding absolute velocities is attained. Thus, the system (5.8) is solved by using a damped least squares technique where a positive constant is added to the diagonal elements of A^TA which reduces the effect of zero-eigenvalues on the generalized inverse solution. The solution to (5.8) is given by

$$\hat{\underline{m}} = (A^TA + \theta^2 I)^{-1} A^T \underline{r} \qquad (5.9)$$

where θ^2 is the damping parameter and I is the identity matrix. The resolution and covariance matrices are, respectively

$$R = (A^TA + \theta^2 I)^{-1} A^TA \qquad (5.10)$$

$$C = s^2(A^TA + \theta^2 I)^{-1} R \qquad (5.11)$$

where s^2 is the estimate of the data variance, σ_d^2 . Because addition of the damping parameter has the effect of

reducing the number of degrees of freedom, the trade-off between resolution and standard-error should be examined in order to select a proper choice for θ^2. For this study we chose $\theta^2 = 0.1$ (sec/%).

Selection of the initial model geometry requires experimentation with different configurations in order to derive a well-resolved solution with small standard errors. The blocksize depends on the station distribution, and the number of observations. Because it is desirable to have a minimum of ten rays sample each block, we chose our blocks to be one degree on a side. The inversion should be carried to a depth of at least one array diameter which we selected to be 500 km. As suggested by Ellsworth (1977), a suitable height to width ratio is 1.5:1 which we found to be satisfactory. Experimentation with displaced layers (in an effort to decouple blocks) and rotated coordinate systems showed little, if any, improvement on the final model.

The initial model used for the ray tracing was a layered spherical model with constant velocities in each layer. Velocity differences of up to 10% do not substantially alter the sampling of the blocks. We averaged velocities from a Herrin earth model to derive the layer velocities (Table 5.1).

The velocity perturbations and the number of observations for blocks in each layer of the final model are shown in Figure 5.8 and listed in Table 5.2 with the diagonal elements of the resolution matrix. In these figures,

negative velocity perturbations represent relatively lower velocities. We only included blocks which were sampled by a minimum of ten rays which mainly eliminated the outermost elements.

Modeling of the crust is probably one of the most crucial results we wish to obtain. Unfortunately, because of small incidence angles, most rays pass through the crustal block and the block lying directly underneath. This makes in difficult to decouple the effects of the two superposed blocks. Resolution could be improved if the thickness of the surface layer were increased. However, the surface blocks would then contain a large and important velocity discontinuity (the Moho) and information regarding crustal structure would be lost.

Problems may also arise because of the uneven station distribution. If rectangular prisms are used to model the crust, a number of stations located in areas with potentially different structures may be included within the same element. To remedy this problem we compute velocity perturbations for each individual station rather than for a given block configuartion. It was found that using this approach had little effect on the upper mantle layers and it facilitated a means to compute a three-dimensional crustal thickness model which is described below.

Although resolution is poor and standard errors are large, the velocity perturbations show a good correlation with the average station residuals (Figure 5.9). This further

supports previous conclusions that the average station residuals are mainly dependent on crustal structure, and may reflect crustal thicknesses and velocity variations. Iyer and Healy (1972) successfully used a general relationship to model crustal thickness at LASA from the distribution of average station residuals. They made the assumption of a homogeneous crust beneath the array which may be a reasonable assumption for a first order crustal model in the particular region they were modeling. However, in the previous section, we concluded that the two orogenic belts in the northeastern U.S. show regional differences in average crustal velocities and thicknesses. This implies that we must account for lateral velocity variations in order to use the average residuals for crustal thickness. Combination of the velocity perturbations with the average station residuals allows us to construct a crustal thickness model. Although there is a trade-off between crustal thickness and lateral velocity differences we feel that the method is justified because independent geophysical data suggests the dependence of average station residuals on crustal thickness and lateral velocity variations. However, effects of the upper mantle may leak into the model in certain regions through both the average residual and velocity perturbation terms.

We assumed that the velocity perturbations, $\frac{\delta V}{V}$, represent differences from an average crustal velocity, Vc . It should be stressed that any information regarding

absolute velocities in the three dimensional inversion is lost and the technique we are using is therefore an approximation and represents only a first order crustal model. The average crustal velocity, Vi, beneath each station i is then

$$V_i \sim V_c\left(\left(\frac{\delta V}{V}\right)_i / 100\right) + V_c \qquad (5.12)$$

and the crustal thickness is

$$h_i \sim v_i \bar{R}_i + h_o$$

where h0 is some average crustal thickness to be varied. We chose Vc = 6.5 km/s and h0 = 38 km and calculated the crustal thickness and average crustal velocity maps shown in Figure 5.10. Overall, the crust beneath the Appalachian Province appears to be 3 km thicker than that of the Grenville. Average crustal velocities differ very little but may be slightly lower in many parts of the Appalachians. There is a region of greater crustal thickness beneath eastern Vermont, New Hampshire, and southern Maine. In western Vermont, and western Connecticut there are high thickness gradients where the crust thins to the west. These features are located just to the east of the Taconic thrust belt and in western Vermont, the gradients show an impressive correlation with the serpentinite belt. Slight crustal thinning is obseved in eastern Massachusetts, and it is not clear if this represents a trend which may continue eastward towards the outer edge of the continental margin.

Alternatively, it may represent the contact between the central orogenic belt and the eastern belt described earlier. The average crustal thickness of 36 km in northern New York agrees very well with refraction models of Katz (1955) and those of Aggarwal in Schnerk et al. (1976).

The upper mantle (layer 2) between 35 and 200 km (Figure 5.8b) depth is characterized by a northeast trending region of low velocities beneath Massachusetts, New Hampshire and southern Maine. The trend of this zone has an interesting parallel with the "grain" of the Appalachian surface structure. The velocities appear to increase to the west and northwest beneath the Precambrian Grenville Province. This suggests that structural differences between the two orogenic belts extends into the upper mantle. The resolution in the upper mantle layer increases markedly relative to that of the crustal elements. Because the block configuration in layer 2 is better suited for sampling incident waves, each element, particularly the central elements, observe a good cross-fire of rays. Resolution degrades somewhat towards the outer edges of the model because the number of obsevations decreases, and the azimuths are limited to a small sector. The overall resolution and standard errors are best for this particular layer.

In layer 3 (200 - 350 km) the region of lower velocities is shifted west and northwest and is found beneath Vermont and central Maine. There is still some evidence of higher

velocities in the western-most blocks in the model.

The deepest layer (layer 4; 350 - 500 km) shows little resemblance to the overlying layers. The overall trends appear to be of shorter wavelength and, not surprisingly, there is little, if any distinction between the two geologic provinces observed at the surface.

The results shown in Figure 5.8 are highly model dependent and the block configuration used would be inadequate to describe the case where lateral differences did not extend below a depth significantly shallower than 200 km. Because of the relatively sparse network geometry, addition of more layers or smaller blocks would seriously degrade resolution. However, qualitative analysis of the variation of residuals with incidence angle between stations as shown in Figure 5.4 suggests that major differences in lateral structure extend to depths of at least 150 km.

In summary, we have presented geophysical data which suggests that structural differences between two juxtaposed orogenic belts exist to depths of 200 km and greater. This indicates that major collisional episodes have very long lasting deep-seated effects as well as large areal extents. Crustal thickness and velocity variations are correlative with many surficial geologic and tectonic features. The Paleozoic Appalachian Province appears to have a slightly thicker crust with lower average velocities than the Precambrian Grenville Province. The higher average velocities associated with the Grenville Province are

evident to depths of 200 km particularly beneath the Adirondack dome. A relatively low velocity anomaly extending to depths of at least 200 km and dipping to the northwest shows a spatial correlation with the Bronson Hill - Boundary Mountains Anticlinorium.

Table 5.1

Initial Layered Velocity Model For Three-Dimensional Inversion

Layer No.	Velocity(km/s)	Thickness(km)	Block Length
1	6.4	35.0	(see text)
2	8.2	165.0	1°
3	8.6	150.0	1°
4	9.2	150.0	1°

Table 5.2

Diagonal Elements of Resolution Matrix for 3-D Inversion

Layer 2

0.0	0.0	0.0	0.0	0.54	0.73	0.60	0.0
0.0	0.0	0.0	0.0	0.0	0.81	0.48	0.0
0.64	0.82	0.85	0.45	0.57	0.75	0.68	0.0
0.77	0.91	0.93	0.89	0.85	0.82	0.76	0.0
0.81	0.91	0.92	0.92	0.89	0.33	0.42	0.0
0.76	0.82	0.92	0.94 x	0.90	0.0	0.0	0.0
0.78	0.92	0.94	0.93	0.84	0.0	0.0	0.0
0.79	0.87	0.91	0.86	0.23	0.0	0.0	0.0
0.0	0.0	0.0	0.0	0.0	0.0	0.0	0.0

Layer 3

0.0	0.0	0.0	0.0	0.0	0.42	0.60	0.32	0.0	0.0
0.0	0.0	0.0	0.0	0.25	0.42	0.61	0.57	0.0	0.0
0.0	0.39	0.25	0.43	0.0	0.52	0.69	0.54	0.0	0.0
0.44	0.72	0.81	0.85	0.79	0.75	0.80	0.68	0.54	0.0
0.33	0.67	0.80	0.86	0.86	0.80	0.77	0.39	0.0	0.0
0.33	0.69	0.85	0.90	0.90	0.88	0.79	0.60	0.30	0.0
0.32	0.82	0.91	0.92	0.91 x	0.85	0.49	0.62	0.0	0.0
0.64	0.80	0.85	0.86	0.88	0.78	0.43	0.0	0.0	0.0
0.0	0.70	0.82	0.87	0.88	0.79	0.52	0.0	0.0	0.0
0.28	0.69	0.83	0.86	0.81	0.20	0.0	0.0	0.0	0.0
0.0	0.54	0.48	0.0	0.0	0.0	0.0	0.0	0.0	0.0

Table 5.2 (continued)

Layer 4

0.0	0.0	0.0	0.28	0.27	0.52	0.60	0.69	0.44	0.0
0.0	0.0	0.42	0.55	0.44	0.51	0.0	0.0	0.35	0.0
0.50	0.74	0.79	0.74	0.75	0.70	0.67	0.66	0.52	0.36
0.66	0.69	0.79	0.87	0.86	0.76	0.77	0.43	0.43	0.0
0.62	0.72	0.81	0.86	0.86	0.85	0.85	0.0	0.37	0.0
0.33	0.79	0.89	0.88	0.88	0.89	0.86	0.52	0.25	0.0
0.76	0.85	0.89	0.91	0.89	0.87	0.74	0.64	0.33	0.31
0.72	0.85	0.88	0.89	0.87	0.80	0.79	0.67	0.0	0.0
0.55	0.77	0.87	0.87	0.87	0.85	0.57	0.52	0.29	0.0
0.58	0.70	0.86	0.89	0.91	0.85	0.73	0.33	0.0	0.0
0.47	0.73	0.86	0.88	0.87	0.65	0.38	0.0	0.0	0.0
0.45	0.72	0.83	0.85	0.79	0.52	0.23	0.0	0.0	0.0

x

FIGURE CAPTIONS

Figure 5.1 Seismograph stations used for three-dimensional inversion of teleseismic P wave residuals. Labeled stations correspond to those referred to in the text or shown in Figure 5.4.

Figure 5.2 Epicenters of earthquakes and explosions used as P wave sources.

Figure 5.3 Map of average relative travel time residuals in seconds for seismograph stations in northeastern United States.

Figure 5.4 Station focal sphere projection plots. Relative residuals plotted as a function of azimuth to the source and incidence angle.

Figure 5.5 Mean relative teleseismic travel time residual in seconds relative to Bouguer gravity for northeastern United States stations. Open circles correspond to stations located in the Grenville Province above Precambrian basement. Solid circles correspond to stations mainly in the Appalachian Province located above Paleozoic basement.

Figure 5.6 Bouguer gravity relative to station elevation for northeastern United States stations.

Figure 5.7a Relative Pn residuals from time term analysis versus relative teleseismic P wave residuals. Solid line indicates theoretical fit assuming total crustal effects (not a least squares fit; see text).

Figure 5.7b Terminology used in deriving theoretical line shown in Figure 5.7a.

Figure 5.8a Percent velocity variations for crust and upper mantle layer 1 beneath northeastern United States. Numbers in parentheses correspond to the number of observations in each element used in the inversion.

Figure 5.8b Same as Figure 5.8a for layer 2; 35-200 km.

Figure 5.8c Same as Figure 5.8a for layer 3; 200-350 km.

Figure 5.8d Same as Figure 5.8a for layer 4; 350-500 km.

Figure 5.9 Percent velocity variations for the crustal layer plotted against mean relative travel time residual for the northeastern United States seismic stations.

Figure 5.10a Lateral average velocity (kilometers per second).

Figure 5.10b Crustal thickness variations in kilometers across the northeastern United States.

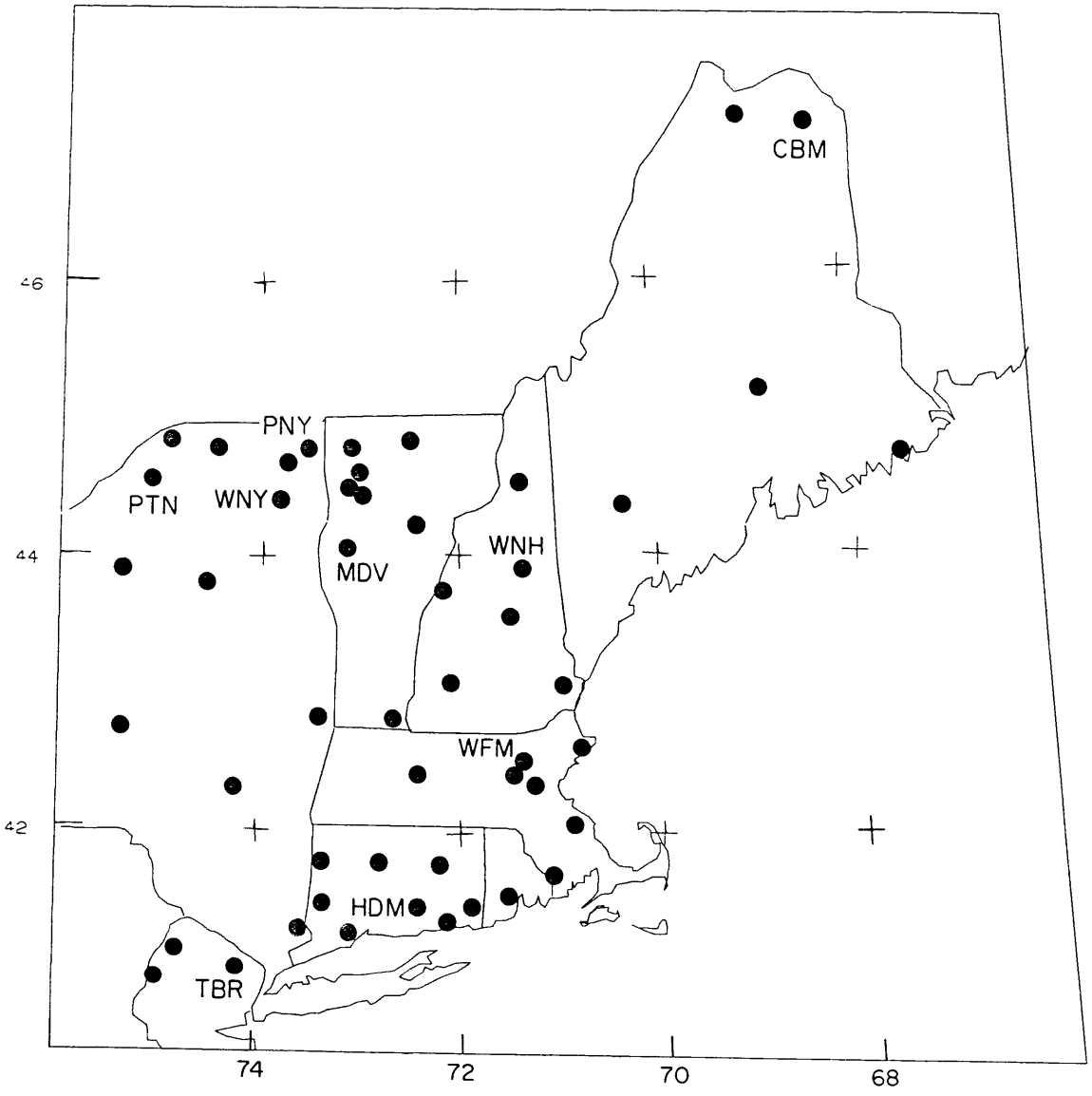

Figure 5.1

Figure 5.2

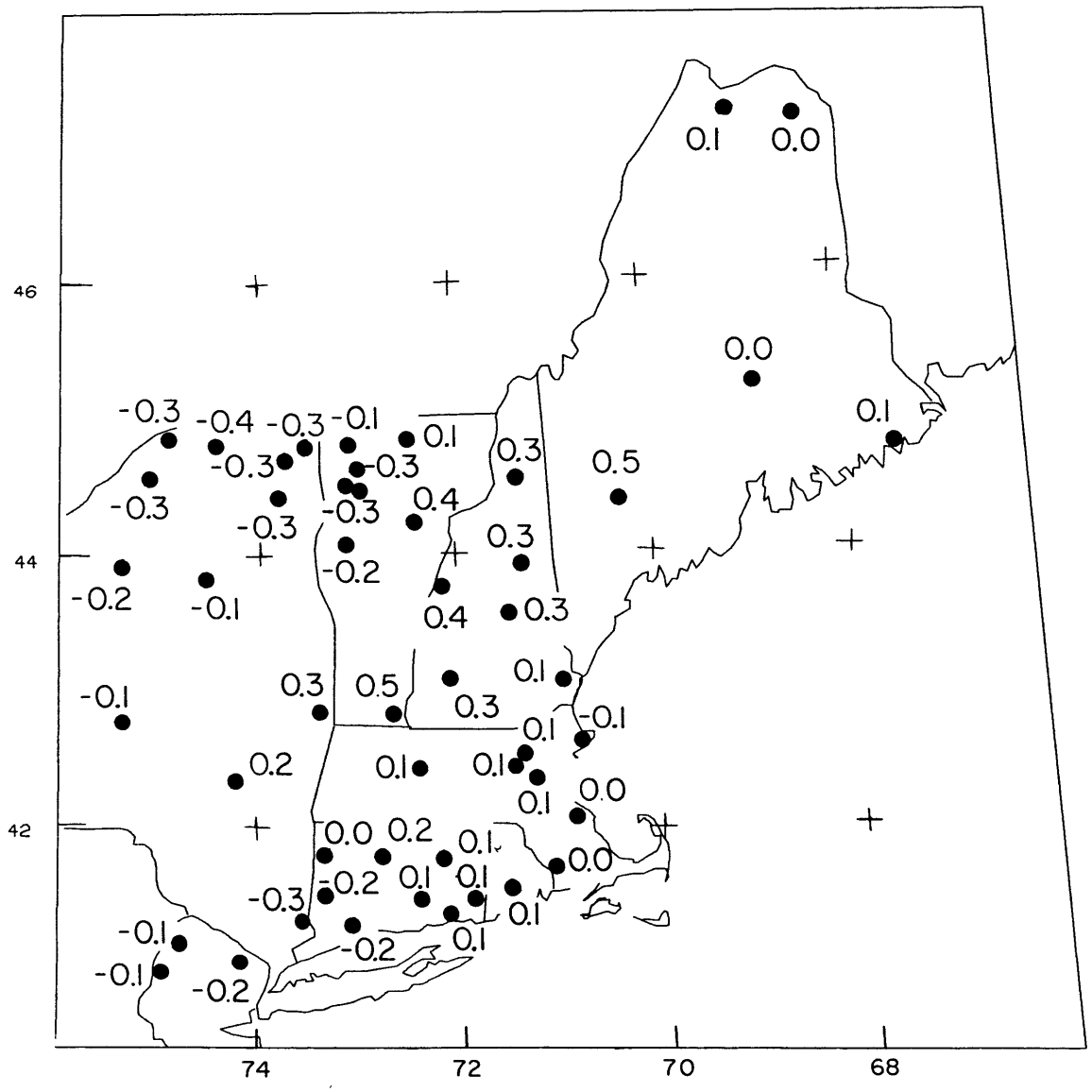
46
44
42
74
72
70
68
0.1
0.0
0.0
0.1
-0.3
-0.4
-0.3
-0.1
0.1
-0.3
-0.3
0.3
0.5
-0.3
-0.3
0.4
-0.3
-0.3
0.3
-0.2
-0.2
-0.1
0.4
0.3
0.1
0.3
0.5
0.3
-0.1
0.1
-0.1
0.2
0.1
0.1
0.1
0.0
0.0
0.2
0.1
0.0
-0.2
0.1
0.1
-0.3
0.1
-0.2
0.1
-0.1
-0.1
-0.2

Figure 5.3

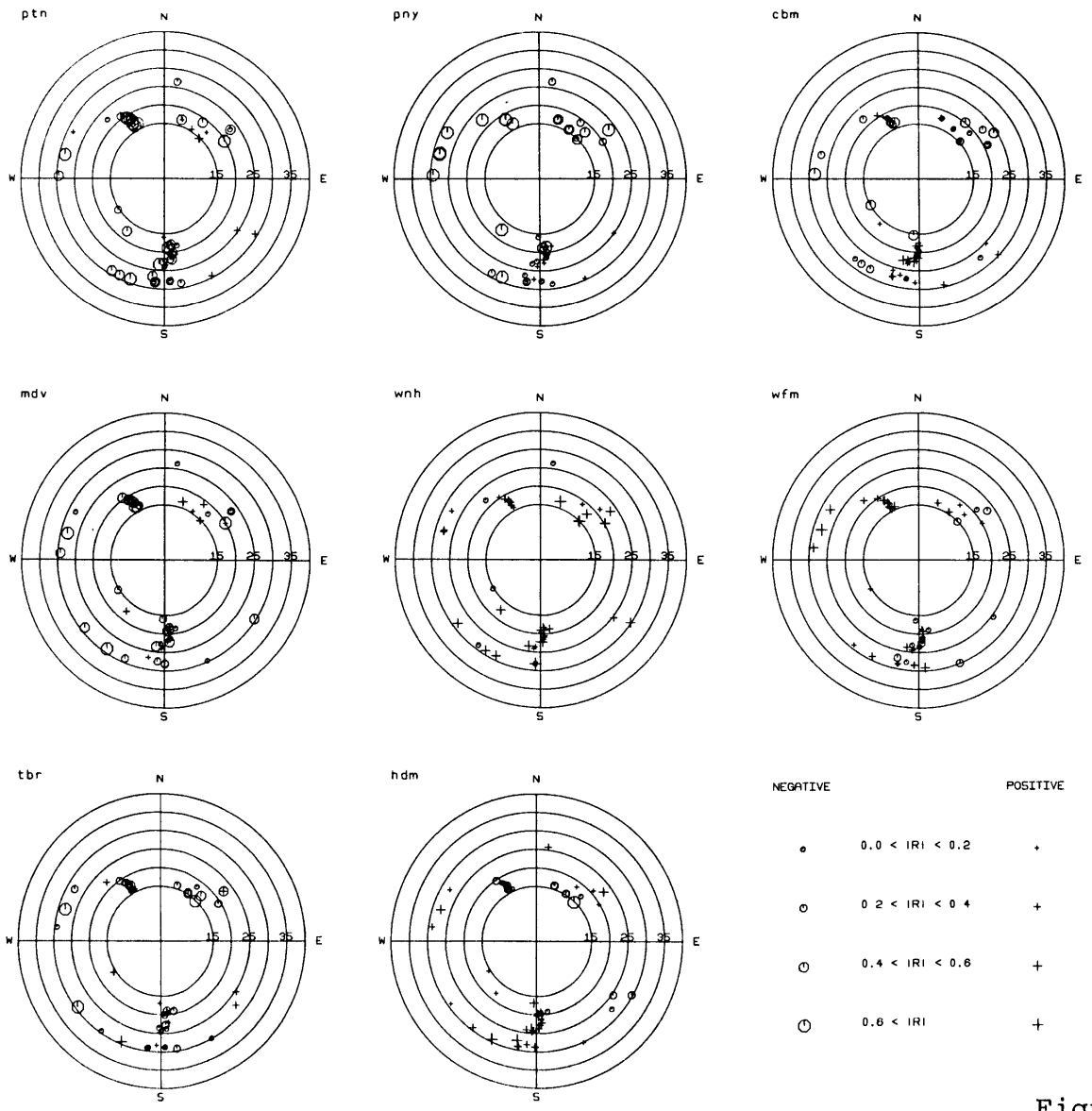
ptn
pny
cbm
mdv
wnh
wfm
tbr
hdm
N
S
E
W
15
25
35
NEGATIVE
POSITIVE
0.0 < IRI < 0.2
0.2 < IRI < 0.4
0.4 < IRI < 0.6
0.6 < IRI

Figure 5.4

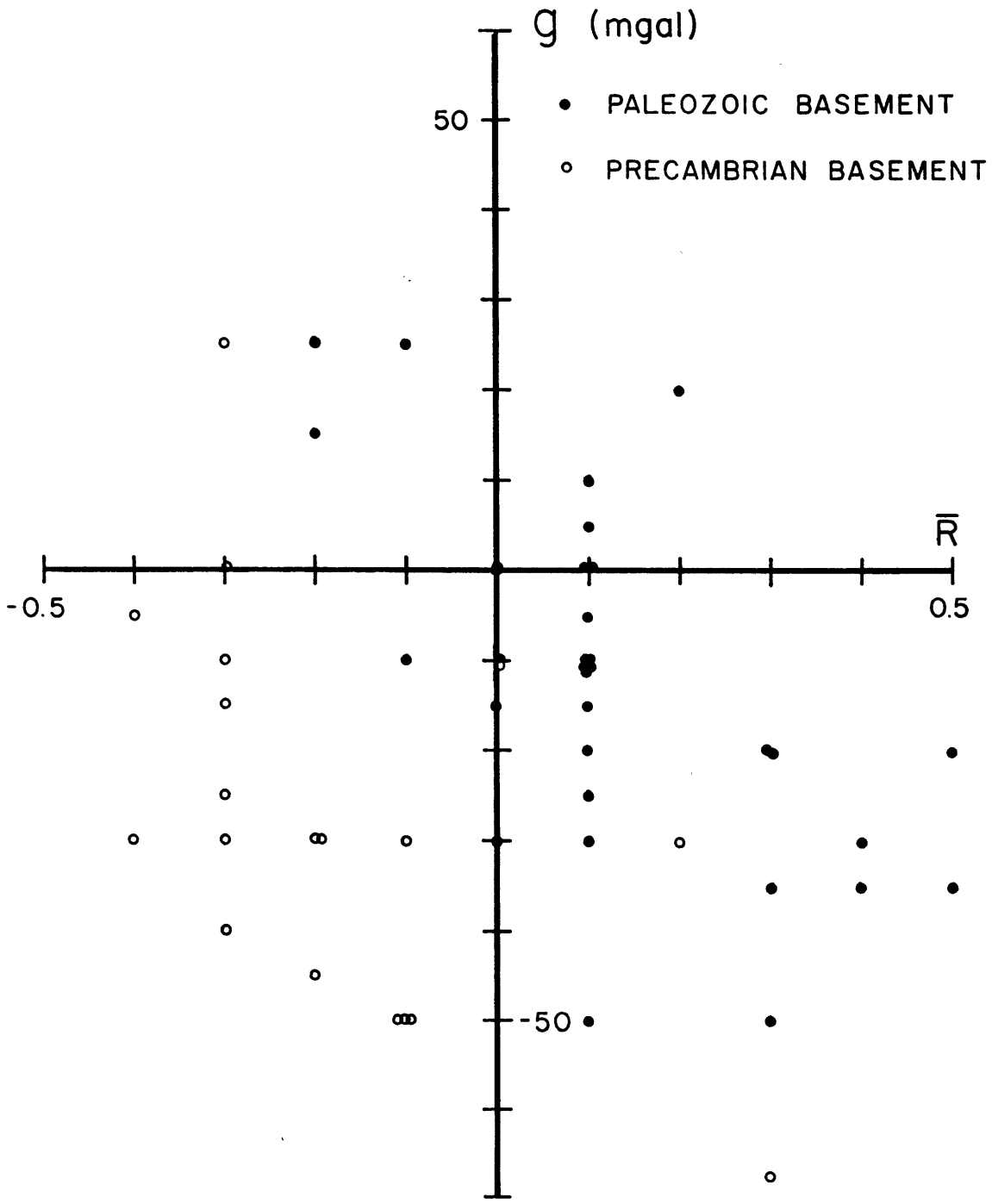
g (mgal)
PALEOZOIC BASEMENT
PRECAMBRIAN BASEMENT
50
-50
-0.5
0.5
R̄

Figure 5.5

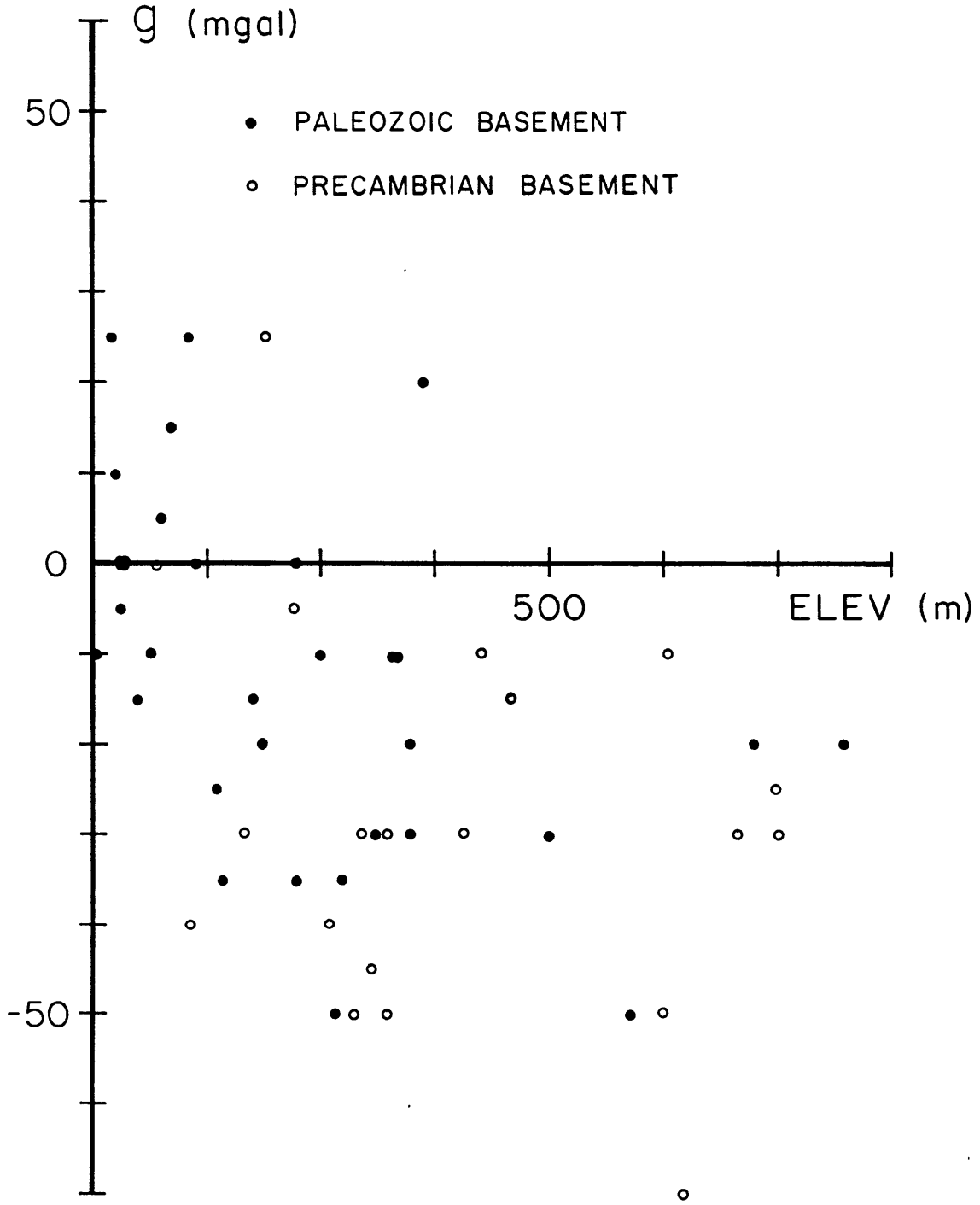
g (mgal)
50
0
-50
PALEOZOIC BASEMENT
PRECAMBRIAN BASEMENT
500
ELEV (m)

Figure 5.6

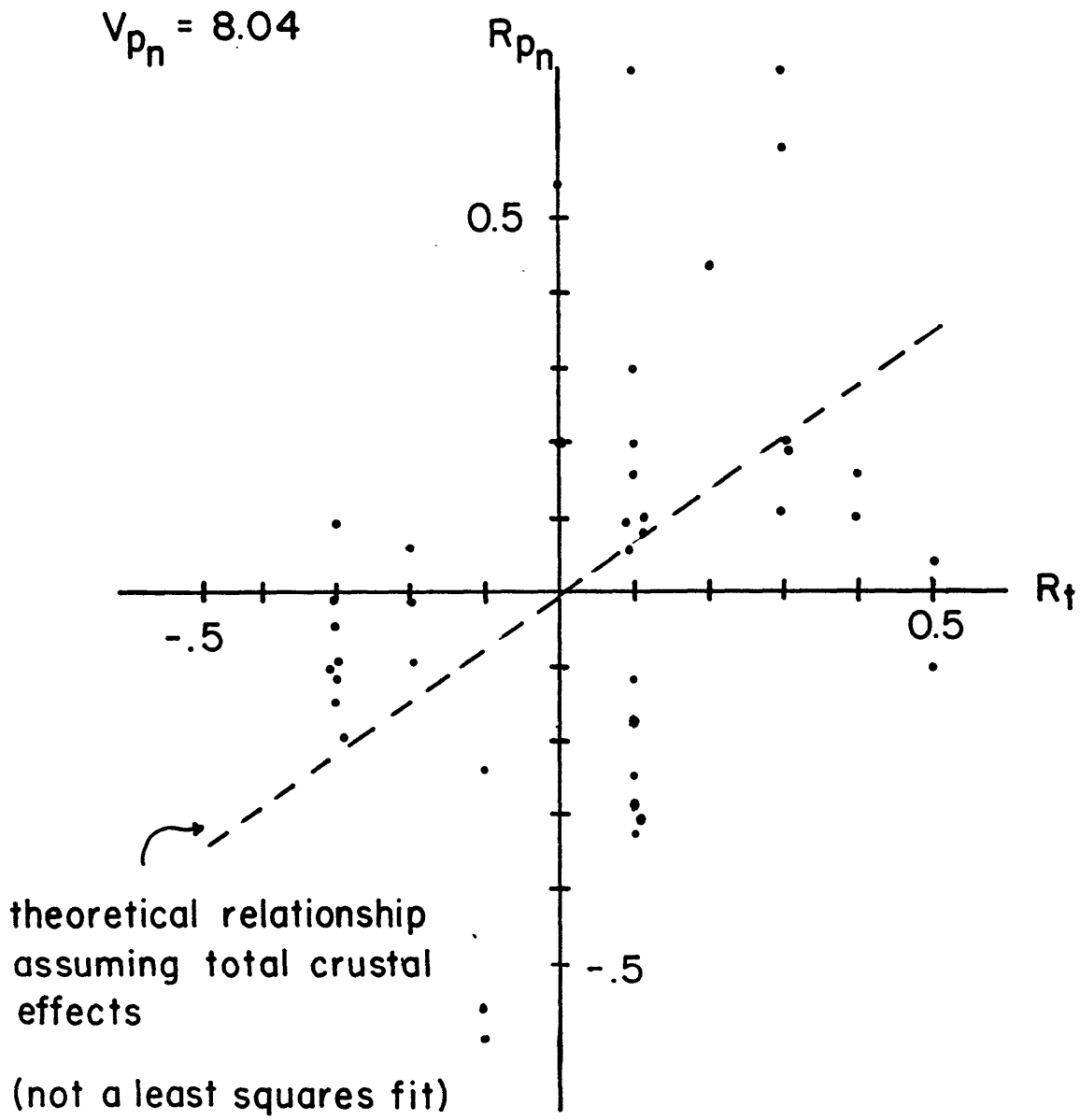
V_{p_n} = 8.04
R_{p_n}
0.5
-.5
0.5
R_t
-.5
theoretical relationship
assuming total crustal
effects
(not a least squares fit)

Figure 5.7a

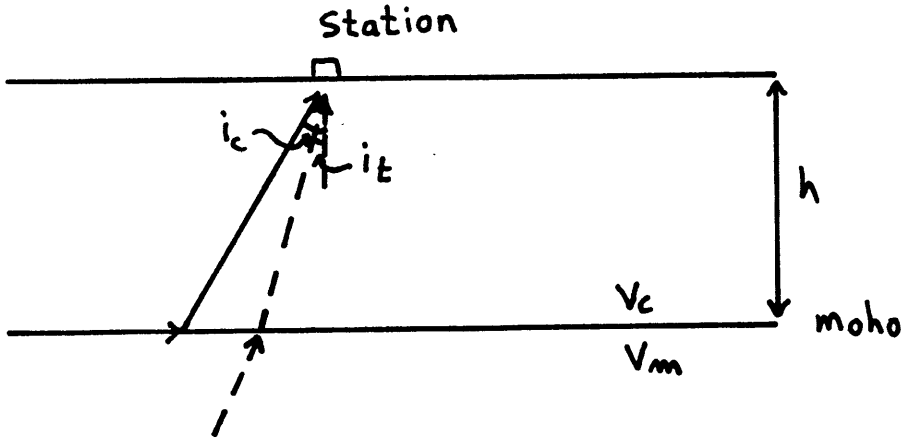

Figure 5.7b

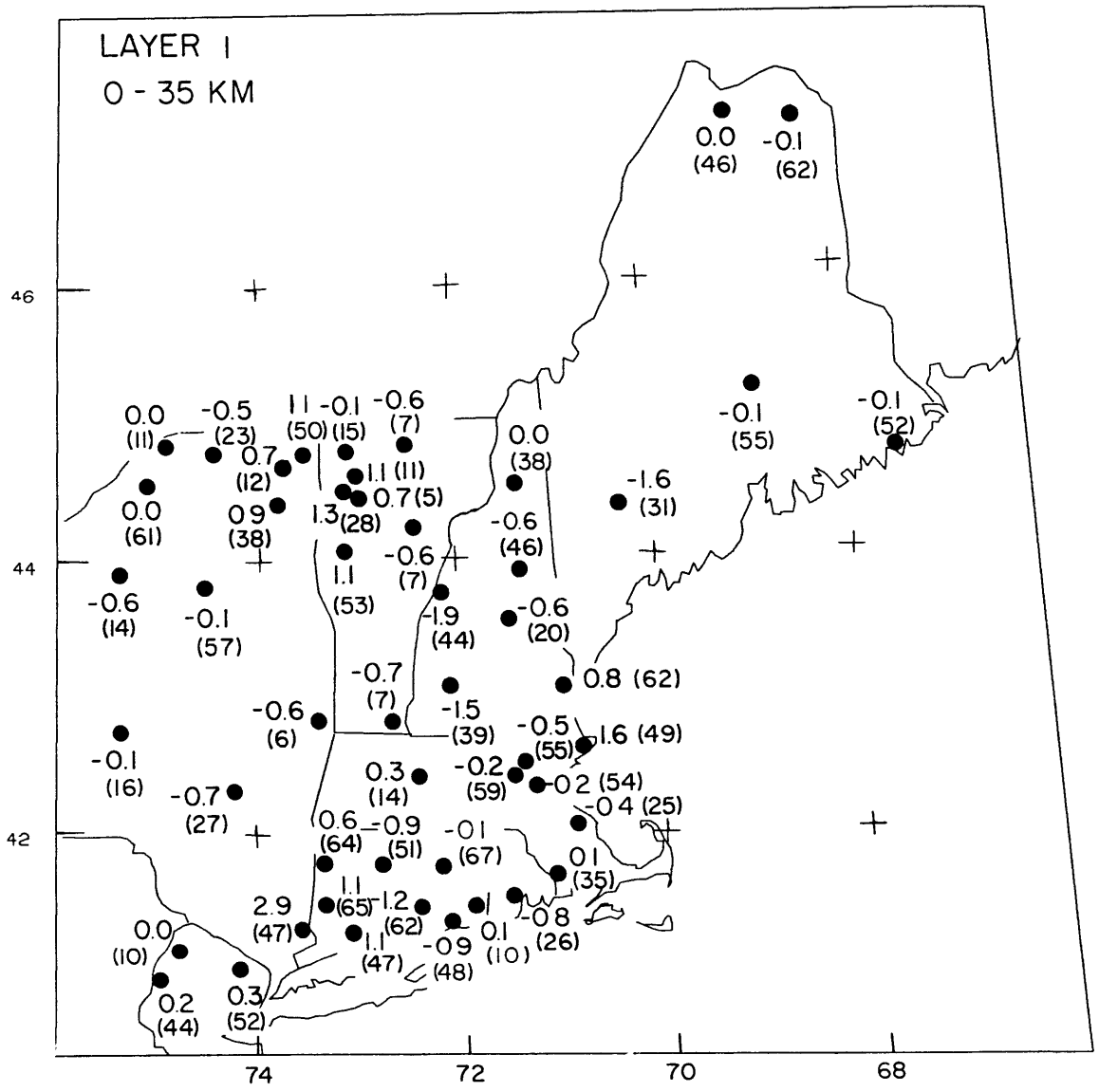
LAYER 1
0 - 35 KM
46
44
42
74
72
70
68
0.0 (46)
-0.1 (62)
-0.1 (55)
-0.1 (52)
0.0 (38)
-1.6 (31)
-0.6 (46)
0.0 (11)
-0.5 (23)
1.1 (50)
-0.1 (15)
-0.6 (7)
0.7 (12)
1.1 (11)
0.7 (5)
0.0 (61)
0.9 (38)
1.3 (28)
-0.6 (7)
1.1 (53)
-0.6 (14)
-0.1 (57)
-1.9 (44)
-0.6 (20)
-0.7 (7)
0.8 (62)
-0.6 (6)
-1.5 (39)
-0.5 (55)
1.6 (49)
-0.1 (16)
0.3 (14)
-0.2 (59)
-0.2 (54)
-0.7 (27)
-0.4 (25)
0.6 (64)
-0.9 (51)
-0.1 (67)
0.1 (35)
1.1 (65)
2.9 (47)
1.2 (62)
0.1
-0.8 (26)
0.0 (10)
1.1 (47)
-0.9 (48)
0.1 (10)
0.2 (44)
0.3 (52)

Figure 5.8a

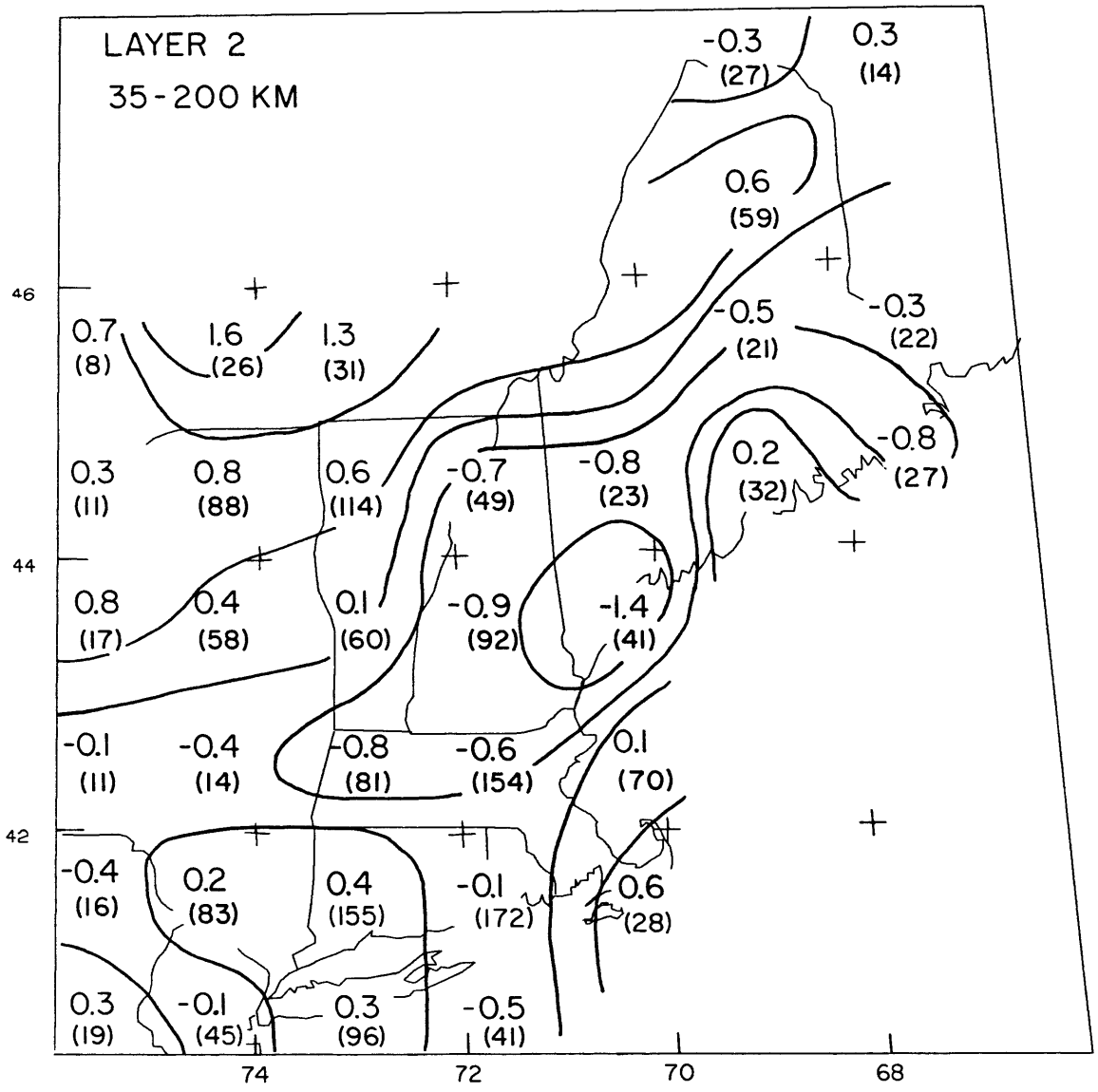
LAYER 2
35-200 KM
-0.3
(27)
0.3
(14)
0.6
(59)
-0.5
(21)
-0.3
(22)
0.7
(8)
1.6
(26)
1.3
(31)
0.3
(11)
0.8
(88)
0.6
(114)
-0.7
(49)
-0.8
(23)
0.2
(32)
-0.8
(27)
0.8
(17)
0.4
(58)
0.1
(60)
-0.9
(92)
-1.4
(41)
-0.1
(11)
-0.4
(14)
-0.8
(81)
-0.6
(154)
0.1
(70)
-0.4
(16)
0.2
(83)
0.4
(155)
-0.1
(172)
0.6
(28)
0.3
(19)
-0.1
(45)
0.3
(96)
-0.5
(41)
46
44
42
74
72
70
68

Figure 5.8b

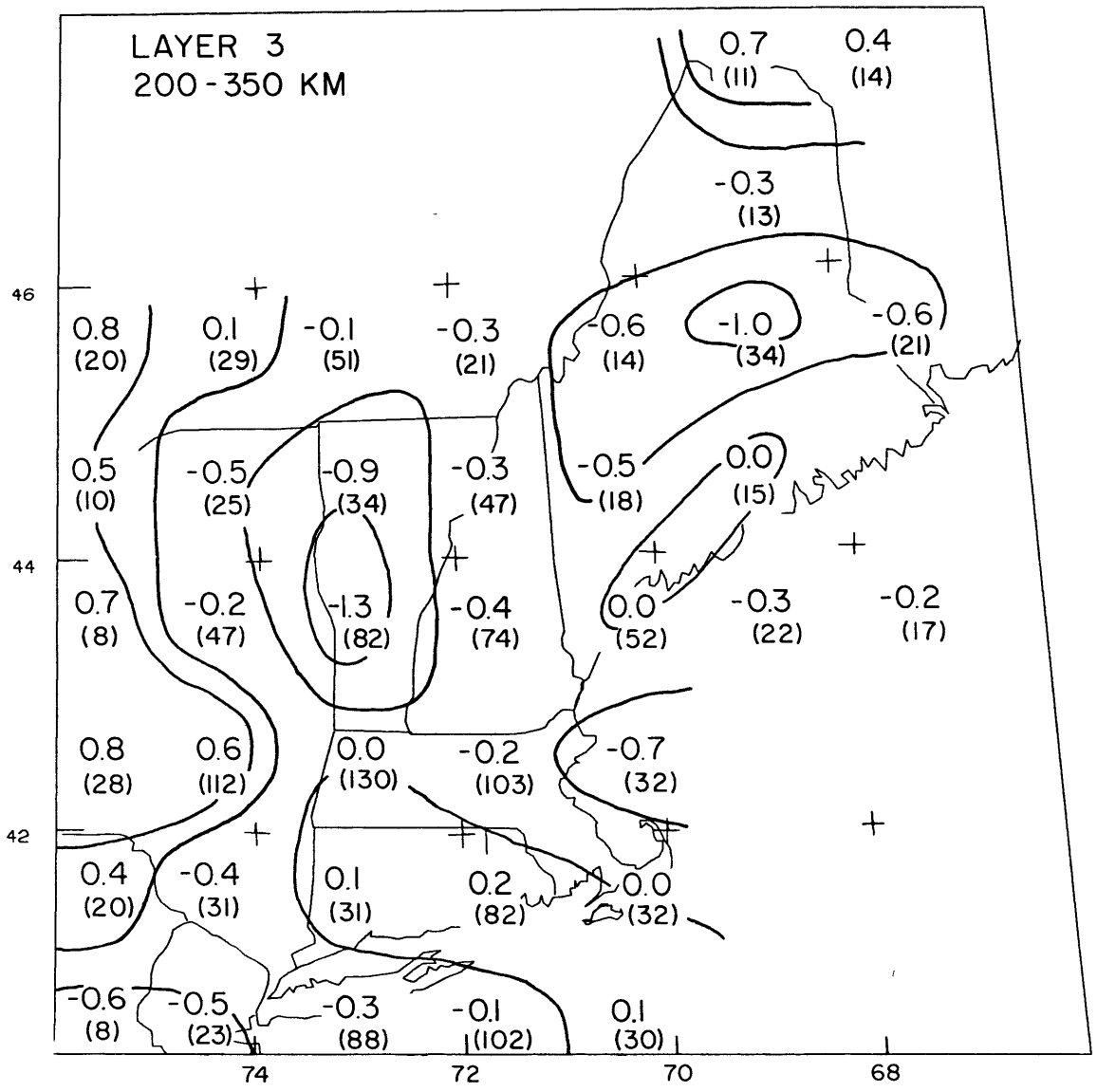
LAYER 3
200-350 KM
0.7 (11)
0.4 (14)
-0.3 (13)
0.8 (20)
0.1 (29)
-0.1 (51)
-0.3 (21)
-0.6 (14)
-1.0 (34)
-0.6 (21)
0.5 (10)
-0.5 (25)
-0.9 (34)
-0.3 (47)
-0.5 (18)
0.0 (15)
0.7 (8)
-0.2 (47)
-1.3 (82)
-0.4 (74)
0.0 (52)
-0.3 (22)
-0.2 (17)
0.8 (28)
0.6 (112)
0.0 (130)
-0.2 (103)
-0.7 (32)
0.4 (20)
-0.4 (31)
0.1 (31)
0.2 (82)
0.0 (32)
-0.6 (8)
-0.5 (23)
-0.3 (88)
-0.1 (102)
0.1 (30)
46
44
42
74
72
70
68

Figure 5.8c

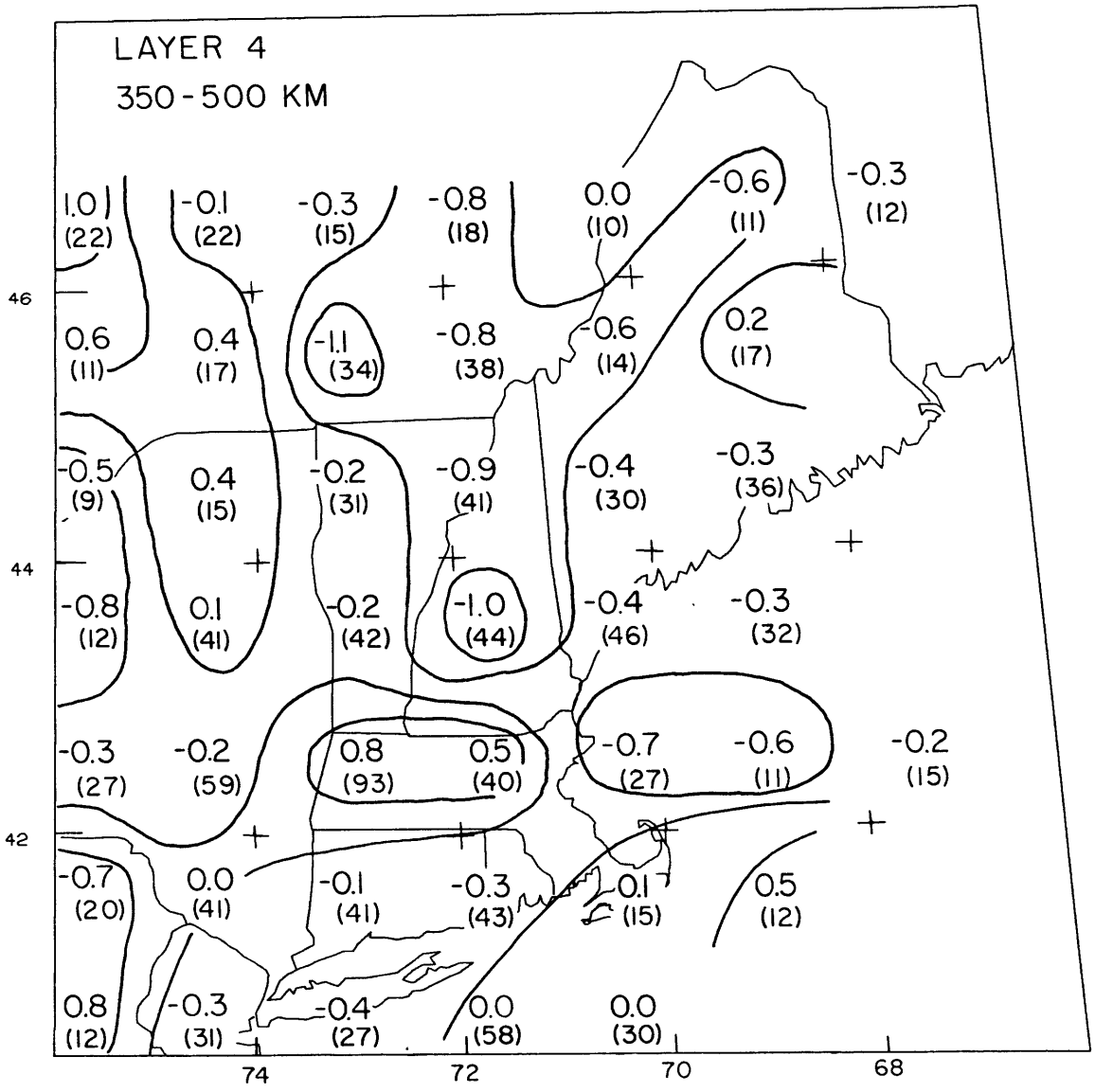
LAYER 4
350-500 KM
1.0 (22)
-0.1 (22)
-0.3 (15)
-0.8 (18)
0.0 (10)
-0.6 (11)
-0.3 (12)
0.6 (11)
0.4 (17)
-1.1 (34)
-0.8 (38)
-0.6 (14)
0.2 (17)
-0.5 (9)
0.4 (15)
-0.2 (31)
-0.9 (41)
-0.4 (30)
-0.3 (36)
-0.8 (12)
0.1 (41)
-0.2 (42)
-1.0 (44)
-0.4 (46)
-0.3 (32)
-0.3 (27)
-0.2 (59)
0.8 (93)
0.5 (40)
-0.7 (27)
-0.6 (11)
-0.2 (15)
-0.7 (20)
0.0 (41)
-0.1 (41)
-0.3 (43)
0.1 (15)
0.5 (12)
0.8 (12)
-0.3 (31)
-0.4 (27)
0.0 (58)
0.0 (30)
46
44
42
74
72
70
68

Figure 5.8d

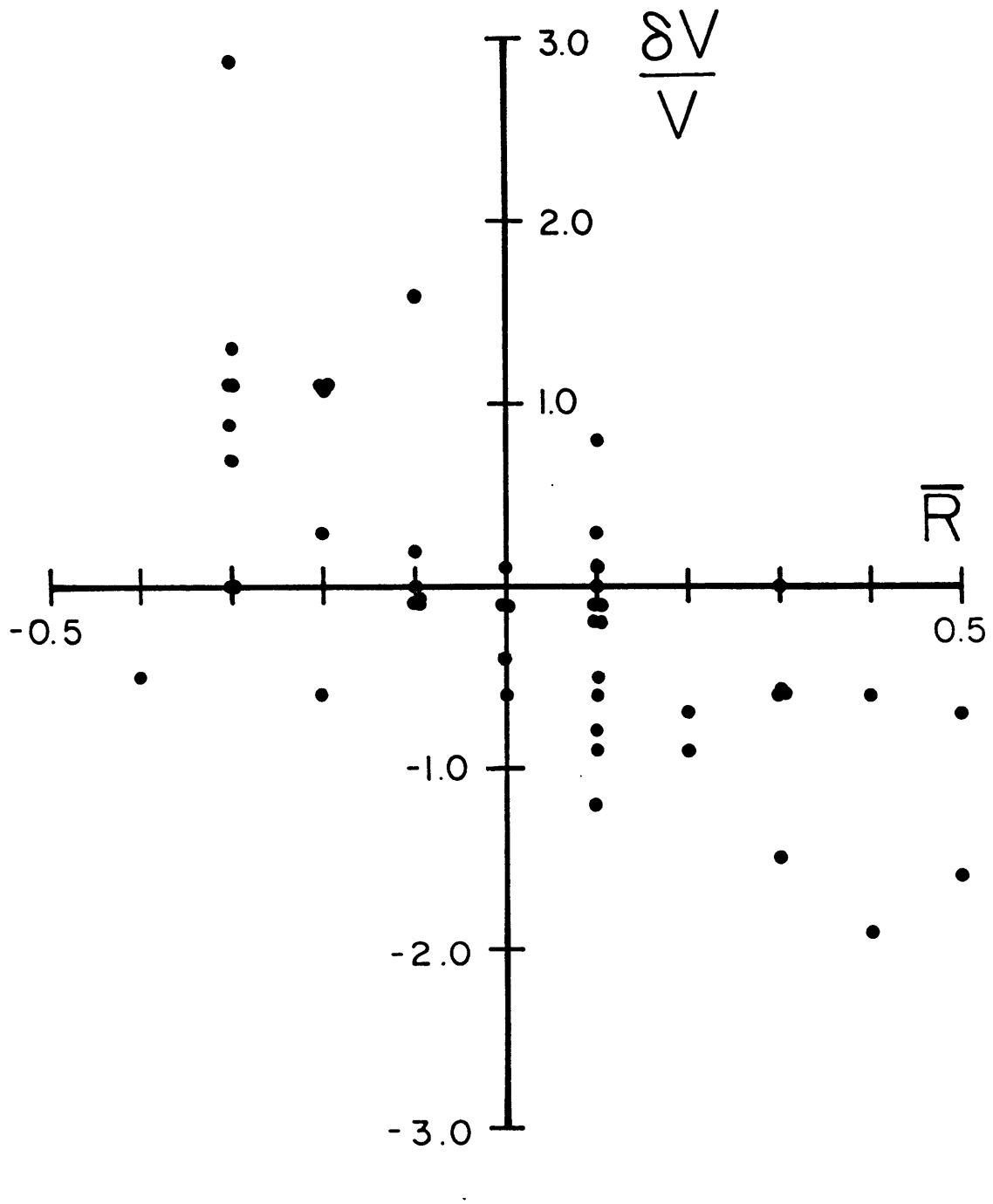

Figure 5.9

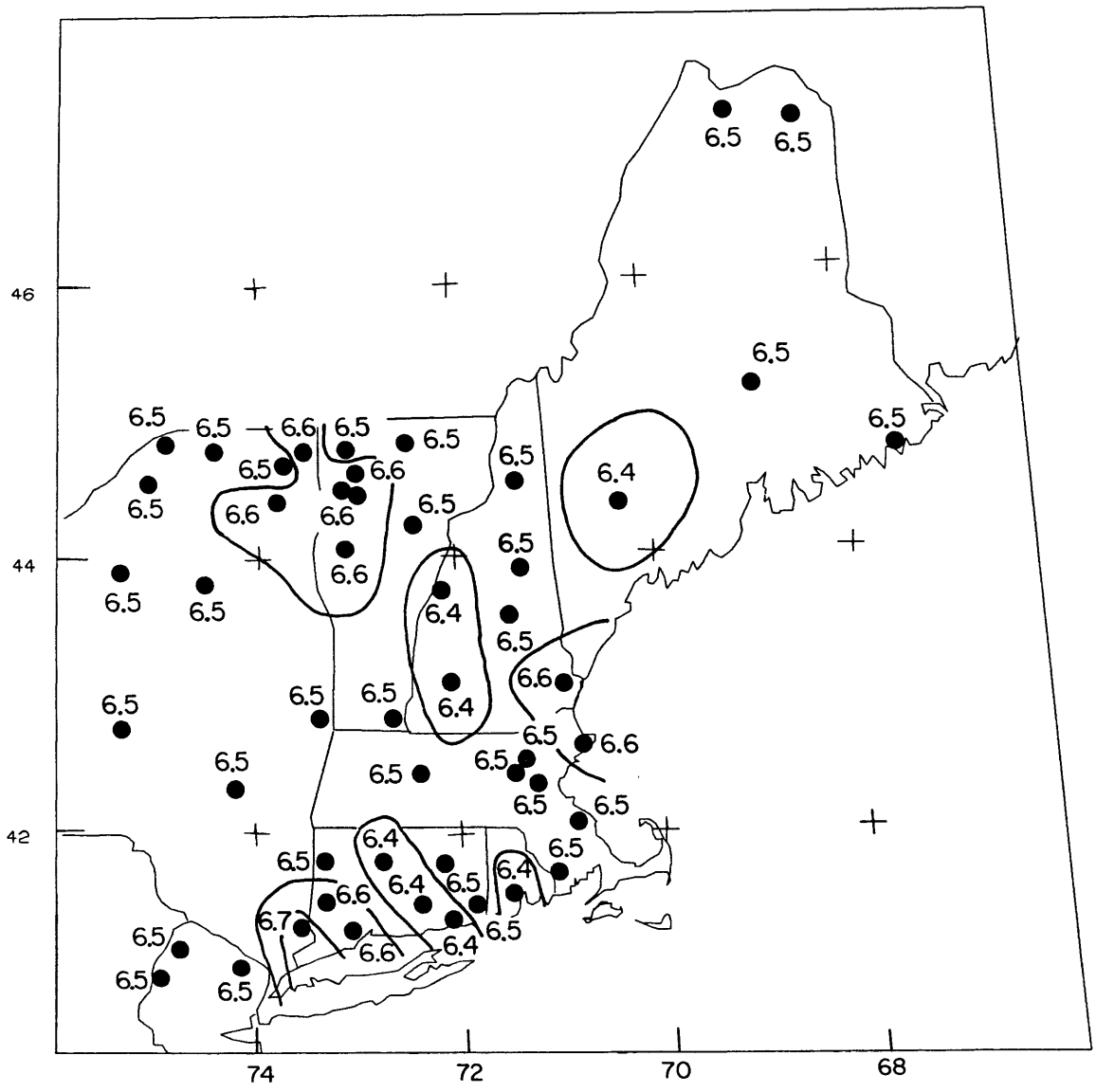

Figure 5.10a

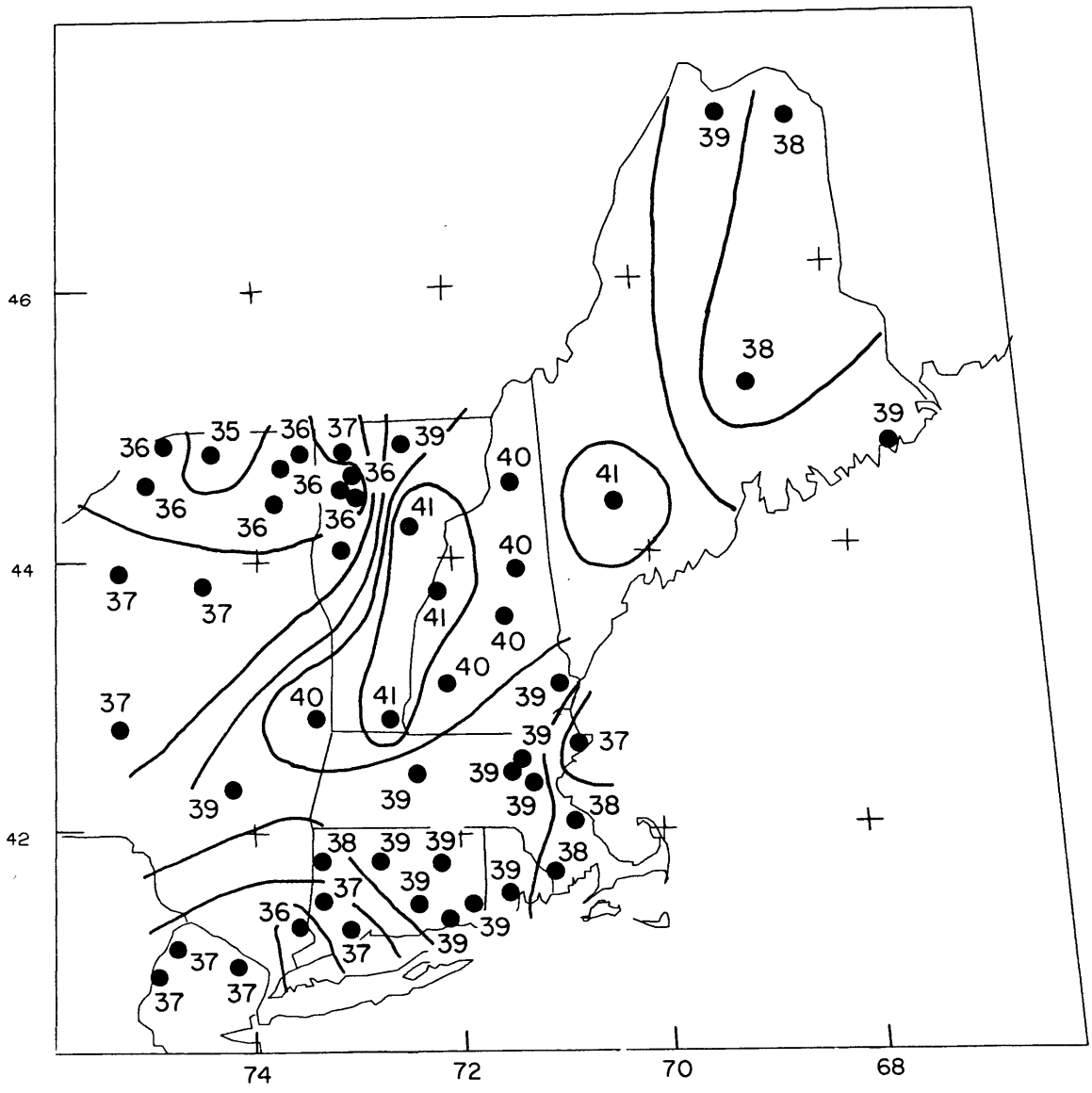
46
44
42
74
72
70
68
39
38
38
39
36
35
36
37
39
36
36
36
36
36
41
40
41
40
37
37
41
40
40
37
40
41
39
39
37
39
39
39
38
39
38
39
39
39
37
36
39
37
37
37
37

Figure 5.10b

CHAPTER 6

VARIATIONS OF CRUST AND UPPER MANTLE STRUCTURE IN THE APPALACHIAN OROGENIC BELT: IMPLICATIONS FOR TECTONIC EVOLUTION

In the previous chapters we have synthesized body wave data from measured blasts and regional and teleseismic earthquakes with surface wave dispersion measurements. Although the variations in regional structure are subtle (which is not unexpected in an ancient orogenic belt), the structural models derived using different measurement techniques are relatively self-consistent and provide some important constraints on the tectonic evolution of the northern Appalachians. In this chapter, we will first review the basic results of previous chapters and then, by combining our results with other geologic and geophysical information, we will contrast the structure of the New England Appalachians with the Grenville Province and with the southern Appalachians. Finally, the results will be interpreted in a plate tectonic framework and simple, first order plate tectonic models will be presented which satisfy geological and geophysical constraints.

6.1 SUMMARY OF RESULTS PRESENTED IN PREVIOUS CHAPTERS

Figure 6.1 summarizes the features observed in the previous chapters. The Appalachians are characterized by a two-layer, 40 km thick crust with a relatively high velocity lower crustal layer. To the west in the Grenville Province, the crust thins by a few kilometers and appears to be very homogeneous except in the vicinity of the Taconic thrust belt. This contrast in crustal structure between the Appalachians and the Grenville Province occurs across the north-northeast trending serpentinite belt. To the east, there also appears to be a contrast in crustal structure between the central orogenic belt of the Appalachians and the eastern block (Avalonia) described in Chapter 2. Because of the proximity to the coastline, this difference in structure (which may occur across the Clinton-Newbury - Bloody Bluff fault zone in eastern Massachusetts) is poorly defined.

To depths of about 200 km, the upper mantle velocities beneath the Grenville Province are about 2% higher than those beneath the Appalachians.

Specific observations are outlined below in greater detail.

1. Regional travel times recorded across the NEUS seismic network indicate that
   a. The northern Appalachians are characterized by a well-defined two layer crust, with a relatively high velocity lower layer. The upper crustal layer,

approximately 15 km thick with P and S velocities of 6.1 and 3.6 km/s, respectively, overlies a high velocity lower crust with P and S velocities of 7.0 and 4.1 km/s. The average crustal thickness is approximately 40 km.

b. The crust of the Grenville Province is vertically homogeneous with nearly constant P and S velocities of 6.6 and 3.7 km/s, respectively, and an average crustal thickness of 37 km.

c. Pn velociities are 8.0 km/s for the Grenville and 8.1 km/s for the Appalachians.

d. A time term analysis of the Pn branch defines a region of thick or low-velocity crust trending northeast across eastern New York, western Massachusetts, southeast Vermont, central New Hampshire, and central Maine. Crustal thinning, or higher velocities are observed in northeastern New York and northwest Vermont and also along much of the coastline.

2. Analysis of Rayleigh wave phase and group velocities in the region yields structural models that are relatively consistent with those described above.

a. For a path along the strike of the Appalachians, a 40 km thick crust with upper layer S velocities of about 3.6 km/s overlies a relatively high velocity lower layer with S velocities around 3.9 - 4.1 km/s.

b. A second path, mainly in the Appalachians (path A2) is characterized by a 40 to 45 km thick crust. The upper

crustal layer (approximately 20 km thick) has S velocities of about 3.5-3.6 km/s and overlies a lower crust of relatively high velocity (3.9-4.0 km/s). In contrast to the other Appalachian path (path A1), the lower crust is characterized by more of a positive velocity gradient with depth.

c. The Grenville path (path G) appears to have a thinner 35 km crust with a slightly lower velocity lower-crust relative to the Appalachian paths. In contrast to the travel time models which show a homogeneous crust, a two layer crust is necessary to fit the observed phase and group velocities. However, part of the surface wave path crosses the Taconic thrust sheet in eastern New York where a two layer crust in not unexpected.

d. Phase and group velocities calculated from the frequency-wavenumber power spectra in southeastern New England appear to be relatively high which implies that the high velocity lower crustal layer is probably well-developed.

3. Analysis of teleseismic P-wave residuals delineates structures which correlate well with surface geology and is useful for studying lateral variations in structure.

a. Structures down to at least 200 km can be correlated with surficial geologic and tectonic features.

b. The Grenville upper mantle is characterized by velocities that are approximately 2% higher than those

beneath the Appalachians. These velocities are maximum beneath the Adirondack dome.

c. A relatively low velocity anomaly dips to the northwest beneath the central mobile belt of the Appalachians and shows a spatial correlation with the Bronson Hill - Boundary Mountains Anticlinorium in New Hampshire and Maine.

d. Crustal features are relatively consistent with those derived from the time term analysis, and the Appalachian crust appears to be slightly thicker than the Grenville.

e. Rapid crustal thinning or high velocities in the crust occur in northwestern Vermont and southeastern Connecticut.

f. Thick crust is observed over the Taconic thrusts in east-central New York and western Massachusetts.

g. There is some evidence that the crust becomes thinner along the coastline.

6.2 CONTRASTS BETWEEN GRENVILLE AND APPALACHIAN PROVINCES IN THE NEUS

One of the most significant results of this study is the pronounced difference in crustal structure between the Precambrian Grenville Province and the Paleozoic Appalachian Province. The observed differences in crustal structure

between the two orogenic belts are probably the result in variations of petrology, chemistry, water content, temperature, and tectonic evolution. These factors will be examined in this section.

6.2.1 COMPOSITIONAL DIFFERENCES

Recent summaries of geophysical, geological, and geochemical information suggest that beneath the sedimentary layer, the upper crust is composed mainly of schists and gneisses of the amphibolite facies which grade downward into migmatites and finally basic and intermediate granulites in the lower crust (Smithson, 1977). Because seismic velocities increase rapidly from amphibolite to granulite facies rocks, the depth of the Conrad discontinuity may mark the location of this change in metamorphic grade (Fountain, 1976). Numerous crustal layers characterized by low velocities, high and low velocity gradients, etc., have been observed and/or postulated using deep seismic sounding techniques (cf. Mueller, 1977; Giese, 1976) and will not be reviewed here. Electrical measurements in the northeastern United States suggest the presence of a highly conductive lower crust in the Adirondack Mountains in New York State (Connerney et al., 1979), while a resistive lower crust underlies a slightly conductive 15 km thick upper crust in New England (Kasameyer, 1974). The slightly conductive 15

km thick upper layer in New England correlates well with the 15 km thick, upper layer observed in this study and probably corresponds to metamorphosed eugeoclinal rocks of the major synclinoria. This implies that the observed differences in velocity and conductivity of the lower crust between the two belts may be the result of a hydrated lower crust beneath the Grenville Province. Although the rocks of the lower crust may be chemically similar, a hornblende-granulite petrology beneath the Grenville would yield lower velocities than a pyroxene-granulite beneath the Appalachians (Christensen and Fountain, 1975).

The existence of a low velocity lower crust beneath the Grenville Province is also supported by the study of the Sp phase across eastern Canada by Jordan and Frazer (1975), who found evidence for a lower crustal layer with a very high Poisson's ratio of 0.33. Because we only acquired travel times of first arrivals, it was not possible for us to positively identify a low velocity zone. We found shear velocity models with low velocity crustal layers that could fit the observed surface wave dispersion curves. However, these models were eliminated because the resolution was inadequate and the model errors too large to positively identify a low velocity layer. Using the P and S wave velocity models derived from regional travel times, the Poisson's ratio of the lower crust beneath the Grenville is 0.27 which is slightly higher than the value of 0.24 found beneath the Appalachians.

The values of Poisson's ratio and shear velocity for the Grenville and Appalachian Provinces are shown on Figure 6.2 (modified from Jordan and Frazer, 1975) which is a plot of Poisson's ratio versus shear velocity at 10 kbar for a number of rocks that may exist in the lower crust. Rocks that may be classified as amphibole granulites (Christensen and Fountain, 1975) and pyroxene granulites (or gabbroic granulites; Manghani et al., 1974) are also shown on the graph (note that these velocities are not corrected for temperature). From Figure 6.2, it can be seen that the observed lower crustal velocities may be explained by an amphibole granulite beneath the Grenville Province and a pyroxene granulite beneath the Appalachians. Interestingly, the Grenville point on Figure 6.2 plots in the vicinity of gneiss and anorthosite. The Grenville Province is characterized by a number of large anorthosite intrusive bodies. Dewey and Burke (1973) suggest the Grenville Province is a deeply eroded zone of basement reactivation similar to a Tibetan plateau. Partial melting of a dioritic lower crust during the Grenville Orogeny may have resulted in potassic granitic melts which rose to higher crustal levels leaving an anorthositic refractory residue.

The above interpretation of hydrous versus anhydrous mineral phases beneath the Grenville and Appalachian Provinces is also consistent with the observed resistivity models. However, the cause for the observed differences in water content is unknown.

Temperature differences may affect the velocities observed in the lower crust. However, at temperatures and pressures representative of the lower crust in older geologic belts (Blackwell, 1976), the effect of temperature on seismic velocities is small relative to pressure (Christensen, 1979). Christensen (1979) concluded that critical thermal gradients resulting in low velocity layers can be reached at temperatures and pressures representative of the upper and middle crust in shield areas. This is particularly apparent for coarse grained rocks with euhedral crystals such as granites, amphib olites, anorthosites, and granulites which have grain boundaries that open at higher temperatures. However, at greater pressures, the grain boundary cracks remain closed even at elevated temperatures and it is more difficult to reach critical thermal gradients in the lower crust. As will be discussed in the next section, temperature differences may also be important in the upper mantle and may account for the observed P-wave delays.

6.2.2 CONTRASTS IN TECTONIC EVOLUTION

The rocks of the Grenville and Appalachian Provinces may show contrasts in their chemistry and petrology that are caused by differences in their tectonic evolution. In this section, causes for the observed crust and upper mantle

differences between the two provinces will be discussed and related to their orogenic history.

The northern Appalachians have a high velocity lower crustal layer relative to the Grenville Province which appears to have a vertically homogeneous crust. Combining this observation with resistivity models suggests that the differences may be due to variations in rock conductivity caused by hydrous mineral phases. However, compositional changes may also be important. As was noted from Figure 6.2, rocks of the lower crust in the Grenville Province may be very similar to those found on the surface. Geochemical models suggest that some members of the White Mountain Plutonic series in central New Hampshire were formed by reaction of fractionated mantle derived alkali basalt with metamorphosed tholeiitic (oceanic) basalt at the base of the crust (Loiselle, 1978). At temperatures and pressures representative of the lower crust, a tholeiitic basalt will alter to a garnet or pyroxene granulite (Green and Ringwood, 1972).

From Figure 6.1, the upper 15 km layer in the northern Appalachians probably corresponds to rocks which have been subjected to a high degree of compression and crustal shortening during the Taconic and Acadian orogenies. The rocks of the Appalachian belt probably were associated with a cycle of oceanic opening and closure. It is therefore possible that the chemistry of the lower crust was strongly affected by tectonic interaction of these sediments with the

underlying basement during orogeny. Thus, involvement of ocean floor within the Appalachians would account for the higher velocities found in the lower crust relative to the predominantly ensialic crust of the Grenville Province.

The homogeneous character of the crust in this portion of the Grenville Province is consistent with the hypothesis that the crust underwent substantial reactivation, thickened, and became vertically uniform during the Grenville orogeny (Dewey and Burke, 1973). Subsequent to the thickening, the crust was eroded to relatively deep levels, as evidenced by the surface exposure of granulite terrains (Putman and Sullivan, 1979).

Based on data teleseismic P-wave residuals and Pn residuals, it appears that the transition zone between the Grenville and Appalachian Province in the NEUS occurs in the vicinity of the Precambrian uplifts and the serpentinite belt (Figure 6.1). This north-northeast trending belt may mark the suture zone between the two orogenic belts. At many locations along this postulated suture, particularly in northwest Vermont, there are geological and geophysical features such as high crustal velocities, a linear gravity high, a serpentinite belt, Precambrian uplifts, and the Taconic thrusts which show many similarities to the Ivera zone in northern Italy (Giese and Prodehl, 1976; Fountain, 1976).

There is also the possibility of a second suture located in the eastern section of the study area. This feature is

marked by the Clinton-Newbury - Bloody Bluff fault zone (CN - BB F.Z.) in eastern Massachusetts (see Figure 6.1, and Chapter 2) and other structures such as the Norumbega fault zone in eastern Maine (Loiselle and Ayuso, 1979). In eastern Massachusetts, the CN - BB F.Z. separates rocks that are probably correlative with Avalon rocks from those of the central mobile belt. The northwest-dipping fault zone is also well-marked by such features as the offset of metamorphic isograds, a strong magnetic signature, and a mylonite zone that is up to 1.5 km thick. A pronounced gravity anomaly is also associated with the fault zone (Taylor et al., 1980), and the Bouguer gravity is relatively high over the eastern basement (Figure 2.2a). Loiselle and Ayuso (1980), present evidence suggesting that post-Acadian strike slip faulting along the Norumbega fault has juxtaposed plutonic rocks of differing geochemistry, texture, and mode of emplacement.

The deep crustal structure of the eastern block appears to differ from that of the central belt. Refraction models, Pn and teleseismic P-wave residuals indicate that the crust of the eastern block is probably thinner than that of the central belt and may be missing a high velocity lower crustal layer.

Although there are a few localities along the CN - BB F.Z. where mafics and ultramafics are exposed that resemble highly altered ophiolites (P. Osberg, personal communication, 1980), the paucity of ophiolites along this

zone is problematical. As discussed by Dewey (1977), zones of intense suturing undergo the most uplift and subsequent erosion and may exhibit the most cryptic suture of ophiolite. In general, the ophiolites are thrust in the late stages of orogeny and occupy high structural levels. Thus, a deeply eroded suture zone may be observed as a narrow high-strain or thrust zone with little evidence of any ophiolites. For example, few ophioite bodies are observed along the eastern portion of the Indus suture of the Himalayas where the collision appears to have been more intense (LeFort, 1975). Additionally, the CN - BB F.Z. may have become a transform fault in late Paleozoic time (Skehan, 1968; Ballard and Uchupi, 1975) which may have obliterated any evidence of ophiolites.

Alternatively, the suture may be located further west and the CN - BB F.Z. may have had a history similar to the Main Central Thrust or the Boundary Fault of the Himalayas. This hypothesis is supported by recent paleomagnetic results which suggest that Lower Devonian volcanics from north-central Maine have paleopoles closer to Avalonia than to North America (Brown, 1980). Even in this case, however, the suture remains cryptic and numerous other tectonic problems are encountered.

Irrelevant of its mode of emplacement, the eastern block has undergone a significantly different orogenic history than that of the central belt, and differences in deep crustal structure across the CN - BB F.Z. are not

unexpected.

Three dimensional inversion of travel time data illustrates that structures down to perhaps 200 km and greater can be correlated with surface geology. This has the important implication that major orogenic belts have effects that reach will into the lithosphere which are stable for extended periods of time, perhaps as long as 1 billion years. The lateral variations in seismic properties of the crust and upper mantle beneath the northeastern United States are very small relative to those observed over similar distances in active tectonic regions such as central Asia or the western United States. Poupinet (1979) showed that absolute P-residuals are a linear function of the square root of age inside stable continental plates. This indicates that the crust and upper mantle become increasingly more uniform with age during evolution toward a state of equilibrium.

In addition to the regional differences existing between the two structural provinces in the northeastern U.S., we see smaller scale features that are related to specific segments of each orogenic belt and to the intervening suture zone. As discussed previously, the Taconite belt, the eastward-lying Precambrian uplifts (The Berkshire Highlands and Green Mountains), and serpentinite belt are Lower Ordovician structures that may be related to the closure of an inner-arc basin and to a continent-island arc collision. This region is not only a site of large scale geologic

deformation but it is also characterized by geophysical anomalies such as apparent crustal thinning, high crustal velocities, and large positive Bouguer gravity anomalies (Figure 2.2a). It is possible that these effects are related to deep-seated thrusts emplaced near the end of the Taconic orogeny which carried oceanic crust and upper mantle material to higher levels within the crust. This material would have high velocities and densities relative to the surrounding eugeoclinal lithologies and would provide a model consistent with the observed geophysical anomalies. There are at least two objections to this model. The first is that higher crustal velocities are obseved just to the west of the Taconic thrust belt at stations PNY and WNY. Secondly, we see that geophysical anomalies are not observed along the entire Taconide belt. A similar pattern is observed on the map showing station time terms (Figure 3.9). This gap in the zone of high crustal thickness and velocity gradients, east of and parallel to the thrust belt in southwestern Vermont and western Massachusetts, is located in the vicinity of the Taconic klippen and a regional northeast trending gravity low extends from southeastern New York into this zone (Figure 2.2a). This region of low velocities and/or thick crust may be related to the thick pile of thrusts of the Taconic klippen.

As pointed out by Fletcher et al. (1978), the anomalous residuals beneath PNY may be related to buried mafic or ultramafic bodies whose presence is indicated by local

gravity highs (anomaly 22 of Simmons, 1964). However, it is readily apparent that all of the stations in northern New York record very early arrivals from the northwest. This implies the existence of regional, deep-seated effects extending to the northwest beneath the Adirondack dome and is supported by the three dimensional inversion (Figure 5.8). Interestingly, the large negative residuals from the northwest are not observed at stations farther south, which suggests that the zone of relatively high upper mantle velocities is controlled by a structure unique to the Adirondacks. It has been postulated that the Adirondacks and associated Grenville basement represent deeper levels of an ancient "Tibetan Plateau" characterized by crustal thickening and shortening behind a continental collision zone (Dewey and Burke, 1973; Toksoz and Bird, 1977). It is not clear when the Adirondack dome was elevated, and the cause of relatively high velocities found in the upper mantle beneath the region remains problematical. If the Grenville belt does represent an analog of a Tibetan Plateau, and crustal thicknesses presently average 36 km, then possibly another 15 km of crust has been eroded away since the Late Precambrian. Rocks presently exposed in the southern Adirondacks appear to have been subjected to temperature and pressure conditions found at approximately 20 km depth (Putman and Sullivan, 1979; McLelland and Isachsen, 1980). This implies that the presently exposed surface geologic features of the Adirondacks represent

lithologies deformed, metamorphosed, and intruded at great crustal depths.

Another prominent feature in the crustal model is the apparent crustal thickening beneath central New Hampshire and southern Maine. Topographically, these are the regions of highest elevations in New England and are therefore isostatically compensated highland areas. The Lower Devonian Acadian orogeny had a severe impact on the structure as evidenced by high grade metamorphism, intrusion of granitic plutons, and large scale westward recumbent folding of many of these plutons (Naylor, 1968). Many lines of evidence suggest the uplift of a significant mountain belt. Early Devonian miogeoclinal sediments in eastern New York are overlain by a thick clastic Middle Devonian sequence of the Catskill Delta - a thick clastic wedge derived from the uplifted landmass in central New England (Rodgers, 1970). The crustal thinning towards central and northern Maine is correlated with the drop-off in the grade of metamorphism (Thompson, 1968). This implies that the continental collision of the Acadian orogeny was particularly severe in southeastern and central New England, and we would expect to see greater crustal thicknesses in these regions.

In eastern Massachusetts we again see an apparent crustal thinning over much of the eastern belt described in an earlier section. These contours conform very well with the position of the middle Paleozoic thrust belt and the abrupt

falloff to the southeast in metamorphic isograds from sillimanite to chlorite (Thompson, 1968).

The low velocity anomalies in the upper mantle (35 - 200 km) beneath Massachusetts, New Hampshire, and southcentral Maine strike northeast parallel to the structural grain of the Appalachian orogenic belt. There is some evidence that this feature dips to the northwest to depths greater than 200 km. Because of the geometry of the initial model, the vertical extent of this structure is only constrained to lie somewhere between 200 and 350 km. It is interesting to note the spatial correlation of this low velocity trend with the Bronson Hill - Boundary Mountains Anticlinorium. As discussed previously, these structures probably occupy the sites of a complex series of island arc sequences last active in the Early Devonian time prior to the Acadian orogeny. If it is true that subduction last occurred east-southeast of the Bronson Hill in a west-northwest direction, we may expect to observe some anomalous feature at these depths.

Assuming that a subducted oceanic slab can produce such a long-term anomaly, the existence of velocities that are lower than the surrounding mantle material is surprising, yet not necessarily inconsistent with its possible thermal evolution. Thermal models of downgoing oceanic lithosphere (Toksoz et al., 1973) illustrate that in the early stages of subduction, the slab is cold and dense relative to its surroundings to a depth of at least 600 km. At

approximately 100 m.y. from the cessation of subduction, the slab reaches thermal equilibrium. Thermal models suggest that beyond about 100 m.y. the subducted oceanic lithosphere starts to heat up relative to the surroundings (Toksoz et al., 1971). The anomaly is not necessarily thermally induced and other explanations related to the compositional changes of the descending lithosphere may be constructed. If we assume the velocity anomalies are produced by temperature changes, and take the temperature coefficient of velocity for dunite, a 1% velocity decrease corresponds to a temperature increase of about 100 - 200 degrees C. These observations are consistent with preliminary unpublished heat flow measurements in central New England corrected for radioactivity which show regions of highest heat flow in central and southeastern New Hampshire relative to northern New Hampshire and southeastern Massachusetts (Jaupart, pers. comm.). Geomagnetic data from the northeastern United States suggests a 200 degree C temperature anomaly in the lower crust beneath central New Hampshire and southern Maine (Bailey et al., 1978).

Alternatively, the oceanic lithosphere may have been totally subducted resulting in lower velocity material filling the vacated Benioff zone. This interpretation is consistent with observations of relatively low velocities dipping westward beneath the Great Valley in central California (Cockerham and Ellsworth, 1979). In this case, the oceanic slab would not have had sufficient time to heat

up (5 m.y. at most) and if still present, would probably result in higher rather than lower velocities.

It is also interesting to note that similar trends in teleseismic PP residuals are observed beneath Newfoundland (Stewart, 1978). Newfoundland is a northward extension of the Appalachian orogenic belt and it is not inconsistent that the crust and upper mantle structures appear to be similar to our observations in New England.

6.3 CONTRASTS BETWEEN NORTHERN AND SOUTHERN APPALACHIANS

Recent COCORP seismic reflection profiling in the southern Appalachians indicates that the platform rocks overlying the Grenville basement can be traced beneath the Blue Ridge and continue at least 150 km to the east (Cook et al., 1979). Because the northern and southern Appalachians show many contrasts in structural style and tectonic history, it may not be possible to extrapolate the COCORP results to the northern Appalachians (north of about 41 degrees latitude).

The tectonic history of the southern Appalachians is reviewed by Hatcher (1978) and Cook et al. (1979) and shown in Figure 6.3 (from Cook et al., 1979). As will be seen in the next section, the tectonic evolution of the northern and southern Appalachians is very similar up through the Acadian orogeny. However, the southern Appalachians have an

additional orogenic episode (the Alleghenian orogeny; Figure 6.3f) which resulted in the westward thrusting of the Blue Ridge, Inner Piedmont, and Carolina Slate Belt. In the northern Appalachians, the Alleghenian orogeny was only felt in southeastern New England and by strike slip faulting further north. It has been suggested that the Alleghenian deformational belt truncates the Appalachian-Caledonian belt in southern Connecticut and Rhode Island and is correlative with the Hercynian belt in central Europe (Dewey and Kidd, 1974). The extensive crustal shortening of the late Paleozoic Alleghenian marginal fold and thrust belt is confined mainly to the southern Appalachians. Slices of relatively unmetamorphosed carbonates are found to the east of the Blue Ridge in the Brevard zone and the Grandfather Mountain window (Cook et al., 1979). The ultramafics found in the southern Appalachians are diffuse and are irregularly distributed throughout the Piedmont zone indicating their involvment in the numerous thrusts of the allochthonous crystalline belt (Misra and Keller, 1978). In contrast, the ultramafics of the northern Appalachians form a narrow north-northeast trending belt and lower Paleozoic platform rocks are not found east of the Precambrian outliers in the northern Appalachians (Figure 6.1).

The COCORP results indicate that the suture between proto-Africa and North America is located at least 150 km to the east of the Blue Ridge. However, by combining gravity and geologic information, Diment et al. (1972) suggested

that the suture (which would actually separate North America from Avalonia) cuts across southern New England and trends north-northeast up the coast of New England (boundary EF in Figure 6.4). In the southern Appalachians, boundary EF (in Figure 6.4) is actually on a thin-skinned allochthonous belt. Reconstruction of the westward-directed thrusts may allign the two segments of boundary EF.

Seismic refraction data also suggests differences in crustal structure between the northern and southern Appalachians. The structure to the west of the Blue Ridge in the southern Appalachians (Table 3.5) is similar to that west of the Precambrian outliers in the northern Appalachians. Both regions are missing a high velocity lower crustal layer and are composed of the homogeneous Grenville basement. However, to the east of the Precambrian outliers, the southern Appalachians continue to show a relatively homogeneous, low velocity crust in marked contrast to the two-layer crust of the northern Appalachians. These similarities in crustal structure across the Blue Ridge are consistent with the interpretation that the crystalline rocks of the Blue Ridge, Inner Piedmont, and the Carolina slate belt are allochthonous and overlie Grenville basement. The contrasts in crustal structure across the serpentinites in the northern Appalachians suggest that they are located in the vicinity of the suture separating the Grenville from the Appalachian Province.

Observation and 3-D inversion of teleseismic P-wave residuals in the southeastern United States delineates a zone of relatively low velocities (approximately 1-2%) parallel to the trend of the Appalachians and dipping vertically or to the southeast under the Piedmont (Volz, 1979).

6.4 TECTONIC EVOLUTION OF THE NORTHERN APPALACHIANS

A possible scenario for the evolution of the northern Appalachians will be outlined in this section. Figure 6.4 shows cross-sections (taken approximately across line AA' in Figure 6.1) illustrating the possible tectonic evolution. Table 6.1 lists major orogenic episodes in the Appalachians and the maximum manifestation in the area of influence (from Rodgers, 1970). It must be emphasized that this is an over-simplified first order model, based on often poorly defined, conflicting geology. However, many of the large scale features are correlative with observed velocity anomalies described in previous section.

The oldest rocks in the study area are exposed in the Adirondacks and the Precambrian outliers of the Green Mountains, Berkshires, and Hudson Highlands. On the basis of petrological and structural arguments Dewey and Burke (1973) suggested that the Adirondacks represent deep erosional levels of part of an ancient Tibetan-type plateau formed

behind a continental collision zone during the Grenville orogeny (~ 1,100 m.y.). Doming in the southern Adirondacks may be due to intersection of regional fold structures affecting Precambrian rocks (McLelland and Isachsen, 1980). Since the late Precambrian, the Adirondacks have apparently remained a regional high, as suggested by the onlap of Paleozoic sediments (Rodgers, 1970).

It is currently thought that a continental rifting stage initiated approximately 820 m.y. ago leading to the formation of the Iapetus Ocean (proto-Atlantic) (Rankin, 1976). The late Precambrian and Cambrian geology of the western belt is characterized by the establishment of an Atlantic-type, stable continental margin (Figure 6.5a).

Late Precambrian lithologies on the eastern belt also indicate a rifting stage with the development of an active continental margin (Kennedy, 1976). Geochemical, paleomagnetic, and paleontological evidence suggests that the western and eastern belts were located on opposite sides of the Iapetus Ocean (Strong et al., 1974; McKerrow and Cocks, 1976; Kent and Opdyke, 1978).

Early or Mid-Ordovician through Permian times are characterized by the episodic closing of the Iapetus Ocean (Figure 6.5b). The BHA was a site of major volcanic activity in this time period as evidenced by the presence of thick volcanic sequences. The curvature of the BHA (convex to the northwest) and the asymmetrical distribution of volcanics (Osberg, 1978) in the central mobile belt suggest

an eastward dipping Benioff zone existed at this time. However, in a later section we will present evidence for a reversal of the polarity of subduction following the Taconic orogeny. Major deformation occurring in Middle and Late Ordovician time marked the climax of the Taconic orogeny which affected rocks within and west of the BHA (Figure 6.5c). The Taconic klippe were thrust at this time and late phase deep seated thrusts involved the Grenville basement resulting in the emplacement of the Precambrian massifs (Ratcliffe, 1975). The linear belt of ultramafics found to the east of the massifs were emplaced at the time, and probably represent highly altered, Cambrian to Lower Ordovician (Chidester, 1968) obducted oceanic crust of the Iapetus Ocean or of a marginal sea behind the volcanic arcs of the central mobile belt. The sequence of tectonic and metamorphic events is indicative of effects caused by long-term heating, increased ductility and basement reactivation resulting from induced convection above subducted lithosphere. This effect is observed in continent-continent convergence zones (Toksoz and Bird, 1977) as well as on active continental margins involving only subductive oceanic lithosphere and arc-continent collisions (Burchfiel and Davis, 1975).

Evidence based on styles of deformation and metamorphism indicates that the Taconic orogeny in New England probably was an episode of arc-continent collision. Numerous island arc segments and inner-arc basins now located within the

central mobile belt were probably involved in the deformation. Although a major unconformity was formed in the CVS at this time, the lack of any major unconformity and Ordovician deformation in the MS (Moench and Zartman, 1976) indicates that oceanic terrain continued to separate continental crust of the eastern belt from North America. However, the amount and type of volcanism in the central mobile belt following the Taconic orogeny indicate that closure of the Iapetus was nearly complete. It may have been the close approach of the eastern belt and possibly the attempted subduction of an oceanic ridge which caused the island arcs to converge onto North America. Delong et al. (1978) suggest that the middle Ordovician was a period of ridge subduction in central Newfoundland.

The Silurian to Early Devonian time was a period of relative quiescence and erosion of the Taconic highlands (Boucot, 1968). In the Early Devonian era there is evidence of increased tectonic activity as indicated by the deposition of vast thicknesses of turbidite sequences across the major synclinoria (Littleton Formation of New Hampshire) and renewed volcanism along arcs in the central mobile belt (Figure 6.5d). This episode of major deformation is called the Acadian orogeny and appears to have spanned a period of approximately 30 m.y. (Naylor, 1971) which is similar to the duration of the main collisional stages of the Himalayas (Toksoz and Bird, 1977).

The Acadian orogeny (Figure 6.5e) is typified by the

following overlapping sequence of events: 1) high grade metamorphism in southeastern New England, 2) intrusion of granitic plutons, 3) large scale westward recumbent folding of many of the plutons, and 4) brittle deformation and development of large thrust belts. These styles of deformation show many parallels with those documented in other continental convergence zones (Dewey, 1977). The period of metamorphism, intrusion, and ductile deformation are deep crustal processes characteristic of a major thermal event associated with initial heating of the crust from below resulting from asthenospheric convection prior to collision and post-collisional radioactive heat generation (Toksoz and Bird, 1977). The binary granites of the New Hampshire Plutonic Series (dated around 360 m.y.; Naylor, 1975) are indicative of extensive crustal heating and partial fusion of crustal sediments and are similar to those found throughout much of the Himalayas (Bird, 1976).

Three major events following the Acadian orogeny are recorded in New England. Alleghenian deformation in Pennsylvanian to Permian times strongly affected rocks in southeastern New England. The Allegheny orogeny probably represents the final closure of the Iapetus Ocean by the collision of Africa with North America. It has been suggested (Dewey and Kidd, 1974) that the Alleghenian deformational belt truncates the Appalachian-Caledonian belt in southern Connecticut and Rhode Island and is correlative with the Hercynian belt in central Europe. Strike slip

faulting in the northern Appalachians may have been important in the late Paleozoic (Rodgers, 1970; Arthand and Matte, 1977; Ballard and Uchupi, 1975) although the sense of motion is not well defined.

In Late Triassic time large rift-valley graben systems were developed along the trend of the Appalachians. These grabens were filled with thick accumulations of non-marine red beds. The rifting was accompanied by the fissure eruption of basaltic lavas and the intrusion of numerous diabase dikes, sills and stocks. This period of time represents the initial opening of the modern Atlantic Ocean. The most recent major tectonic activity in New England was the emplacement of the White Mountain Magma Series, intruded over a 100 m.y. interval from Jurassic to Cretaceous time (Chapman, 1976).

The northeastern U.S. is presently an intraplate region adjacent to a stable continental margin, characterized by relatively low-level, diffuse seismicity. It is not clear at this time what structures control seismicity patterns. The region within and possibly east of the Grenville Province is characterized by a northeast trending maximum compressive stress and some earthquakes appear to be controlled by reactivated Paleozoic faults (Sbar and Sykes, 1977).

In New England, the stress pattern appears to be more complex, with local stress concentrations controlling the distribution and mcechanism of earthquakes (Pulli and

Graham, 1979).

Orogenic Movements in the Appalachian Region

Orogenic episode and approximate date	*Known area of influence*	*Maximum manifestation*
Appalachian movements		
Palisades Late Triassic (Carnian-Norian) 190—200 m.y.	Belt along central axis of already completed mountain chain	Fault troughs, broad warping, basaltic lava, dike swarm
Alleghany Pennsylvanian and/or Permian (Westphalian and later) 230—260 m.y.	West side of central and southern Appalachians, southeast side of northern Appalachians, perhaps also in Carolina Piedmont	Strong folding, also middle-grade metamorphism and granite intrusion at least in southern New England
Early Ouachita Mid-Mississippian through early Pennsylvanian (Visean to early Westphalian)	Only in southernmost Appalachians in central Alabama	Clastic wedge, also possibly broad east-west structures that influenced later deformation
Acadian Devonian, mainly Middle but episodic into Mississippian (Emsian-Eifelian) 360—400 m.y.	Whole of northern Appalachians, except along northwest edge; as far southwest as Pennsylvania	Medium- to high-grade metamorphism, granite intrusion
Salinic Late Silurian (Ludlow)	Local on northwest side of northern Appalachians	Mild angular unconformity, minor clastic wedge
Taconic Middle (and Late) Ordovician (Caradoc, locally probably older) 450—500 m.y.	General on northwest side of northern Appalachians, local elsewhere; an early phase in Carolinas and Virginia, perhaps general in Piedmont province	Strong angular unconformity, gravity slides (?), at least low-grade metamorphism, granodioritic and ultramafic intrusion
Penobscot Early Ordovician or older (Arenig or older)	Local on northwest side of northern Appalachians	Strong angular unconformity, slaty cleavage, possibly some intrusion
Avalonian Latest Precambrian	Southeastern Newfoundland, Cape Breton Island, southern New Brunswick; probably also central and southern Appalachians (Florida?)	Probably some deformation, uplift of sources of coarse arkosic debris, gravity slides(?)
Late Precambrian about 580 m.y.	Southeastern Newfoundland, Cape Breton Island, southern New Brunswick; perhaps eastern Massachusetts	Mostly low-grade metamorphism, granitic intrusion
Grenville (pre-Appalachian) movements Late Precambrian 800—1100 m.y.	Eastern North America including western part of Appalachian region	High-grade metamorphism, granitic and other intrusion

FIGURE CAPTIONS

Figure 6.1 Generalized geologic map of the northeastern United States (King, 1969) and schematic structural cross-section along profile AA'. Key to abbreviations: T - Taconic thrust belt; GM - Green Mountains; CVS - Connecticut Valley Synclinorium; BHA - Bronson Hill Anticlinorium; MS - Merrimac Synclinorium; CN-BB - Clinton-Newbury - Bloody Bluff fault zone.

Figure 6.2 A plot of Poisson's ratio versus shear velocity at 10 kbar for a number of rocks that are possible constituents of the lower crust. Ranges of Poisson's ratio versus shear velocity for amphibole granulites from Christensen and Fountain (1975) and gabbroic granulites from Manghnani et al. (1974). Symbol A corresponds to Poisson's ratio and shear velocity for Appalachians and G for Grenville using regional travel times in this study. Figure modified from Jordan and Frazer (1975).

Figure 6.3 Schematic illustration of plate tectonic model for evolution of southern Appalachians from Cook et al. (1979).

Figure 6.4 Some tectonic features of eastern North America. Line EF represents line across which there are marked differences in Bouguer gravity (Diment et al., 1972).

Figure 6.5 Schematic illustration of plate tectonic model for evolution of New England Appalachians.

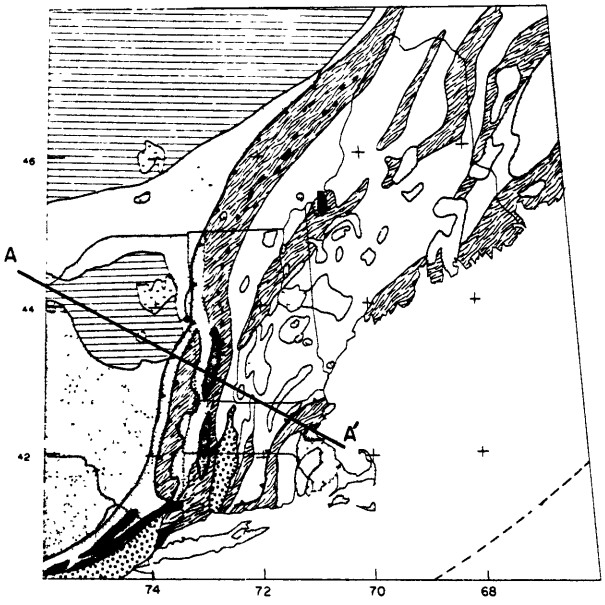

EXPLANATION

Thrust fault, barbs on upper block

Normal fault, hachures on downthrown side

STRATIFIED ROCKS

- Cenozoic glacial deposits
- Triassic red beds
- Carboniferous
- Silurian - Devonian eugeoclinal rocks
- Cambrian - Ordovician foreland rocks
- Cambrian - Ordovician deformed miogeoclinal rocks
- Cambrian - Ordovician eugeoclinal rocks
- Precambrian rocks of the eastern block
- Precambrian uplifts, Grenville basement
- Precambrian Grenville basement

IGNEOUS ROCKS

- Mesozoic White Mountain Plutonic Series
- Devonian New Hampshire Plutonic Series
- Cambrian - Ordovician serpentinites, ultramafics
- Precambrian anorthosites

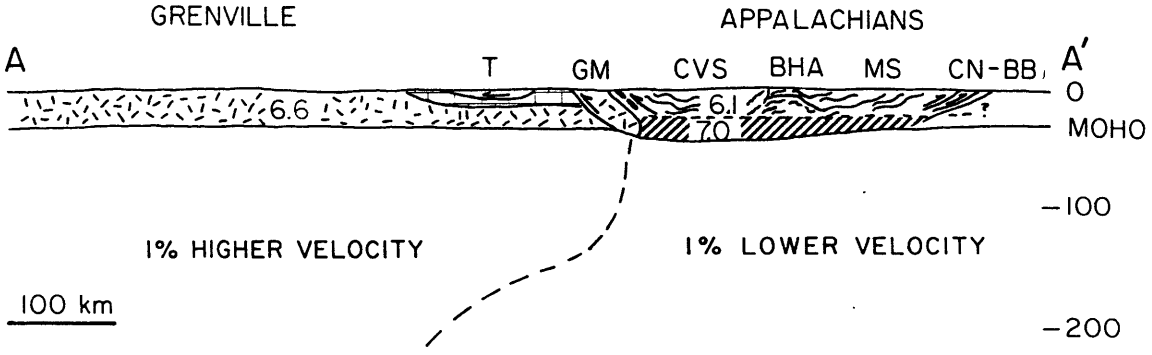

Figure 6.1

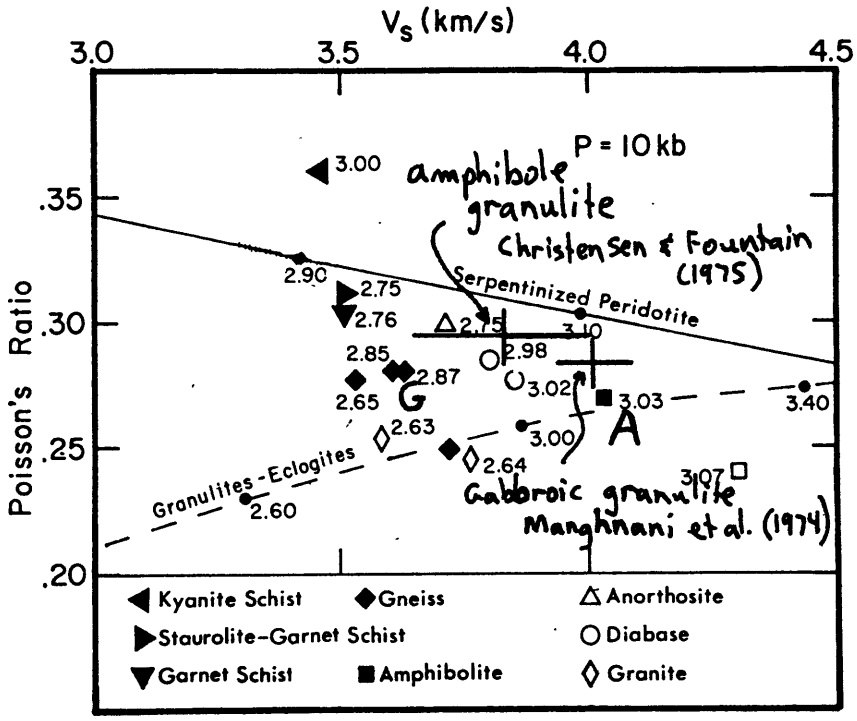
V_S (km/s)
3.0
3.5
4.0
4.5
Poisson's Ratio
.35
.30
.25
.20
P = 10 kb
3.00
amphibole granulite
Christensen & Fountain (1975)
Serpentinized Peridotite
2.90
2.75
2.76
2.85
2.87
2.65
G
2.98
3.10
3.02
3.03
3.40
A
2.63
3.00
2.64
3.07
Gabbroic granulite
Manghnani et al. (1974)
Granulites-Eclogites
2.60
Kyanite Schist
Gneiss
Anorthosite
Staurolite-Garnet Schist
Diabase
Garnet Schist
Amphibolite
Granite

Figure 6.2

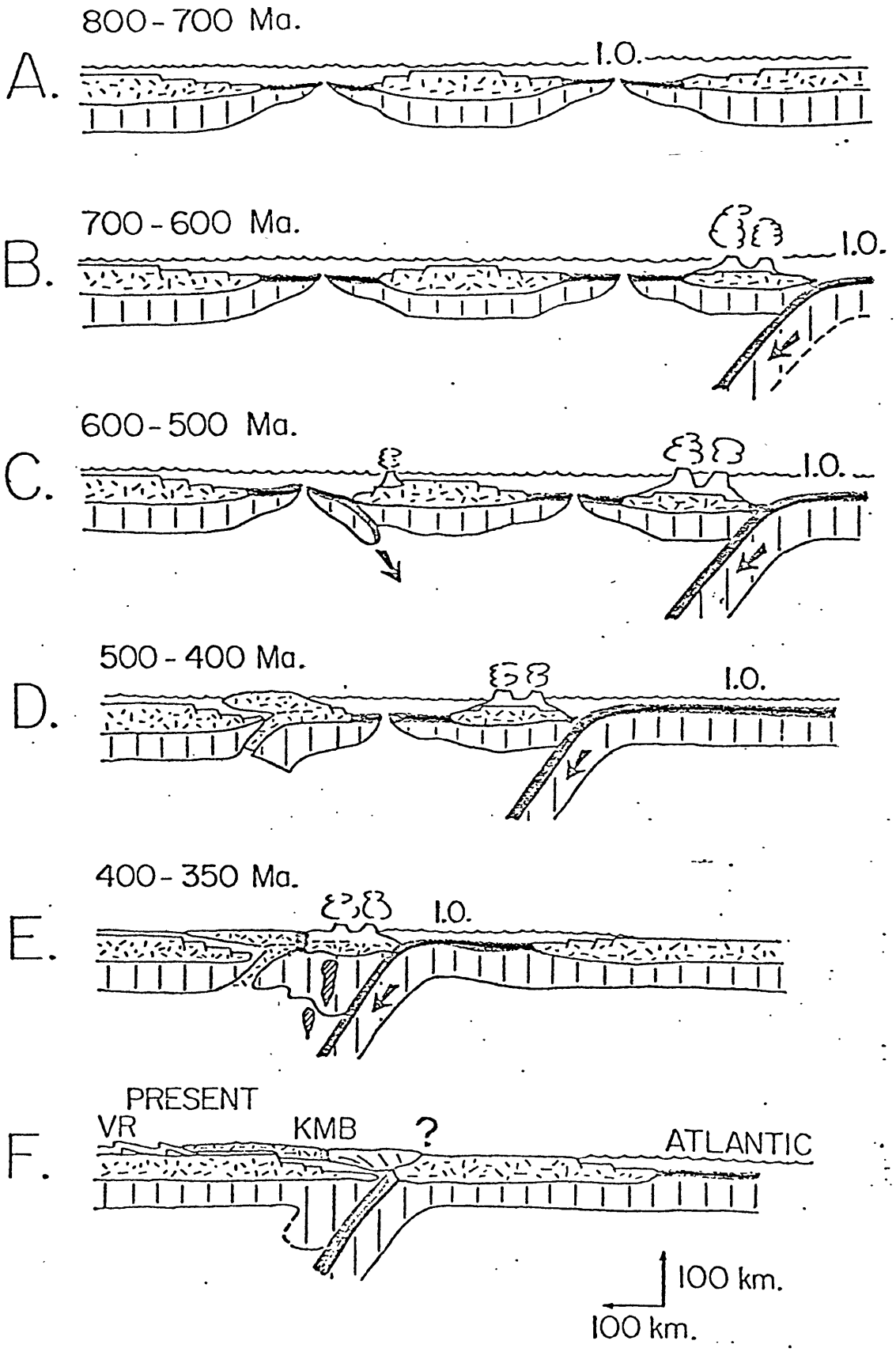
800 - 700 Ma.
A.
I.O.
700 - 600 Ma.
B.
I.O.
600 - 500 Ma.
C.
I.O.
500 - 400 Ma.
D.
I.O.
400 - 350 Ma.
E.
I.O.
PRESENT
VR
KMB
?
ATLANTIC
F.
100 km.
100 km.

Figure 6.3

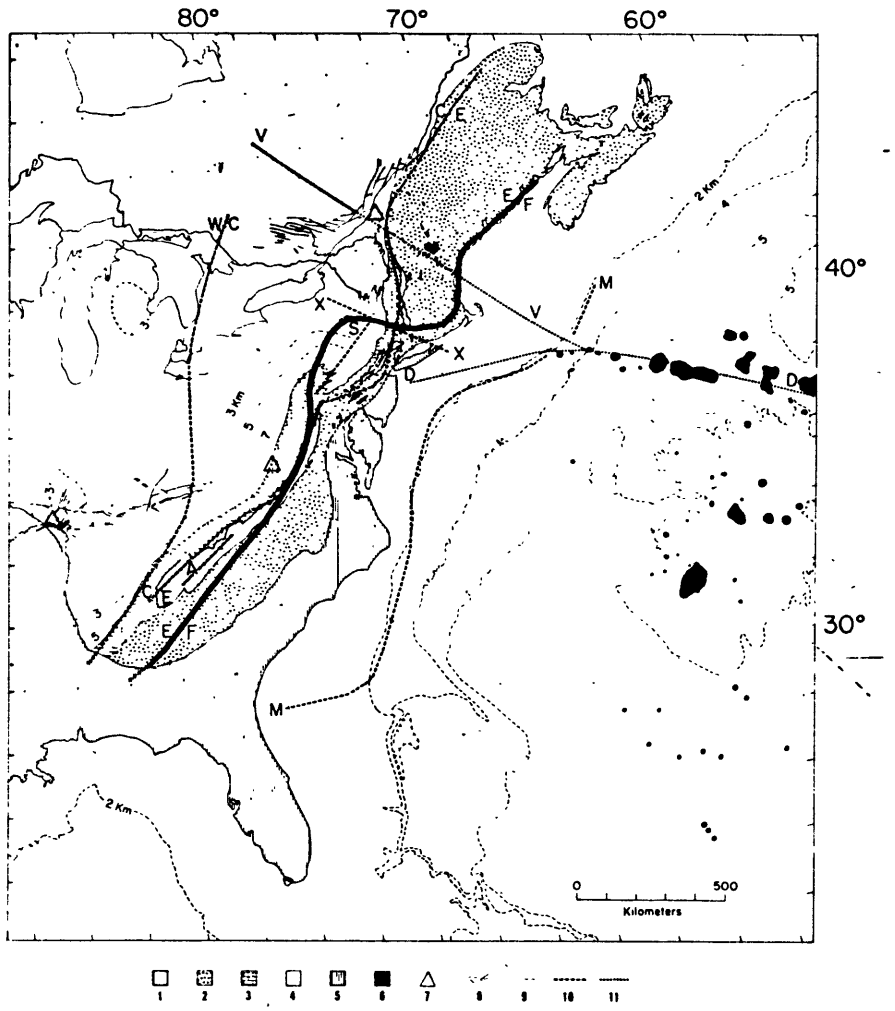

. Some tectonic features of eastern North America. Geologic features generalized from King (1969). (1) Precambrian rocks. (2) Paleozoic metasediments, metavolcanics, and plutonic rocks of core of the Appalachians. (3) Miogeosynclinal rocks. (4) Paleozoic platform deposits. (5) Cretaceous and later deposits of the coastal plane and Mississippi embayment. (6) On the land, post Paleozoic alkaline intrusive rocks; in the oceans, seamounts. (7) Areas of unusual concentrations of small alkaline Cretaceous and early Tertiary intrusions. (8) Fault systems in the platform deposits. (9) Depth contours: in ocean areas depth of water, in continental areas depth to Precambrian basement. (10) Province boundaries as discussed in text and line *M* which is the trace of the magnetic high that closely follows the continental margin except in the south where it changes form and turns inland (from Taylor et al., 1968). This magnetic high is continuous except at the intersection with the Kelvin seamount chain. (11) Cross-trending structural trends discussed in text.

Figure 6.4

EOCAMBRIAN - EARLY ORDOVICIAN

EARLY - MIDDLE ORDOVICIAN

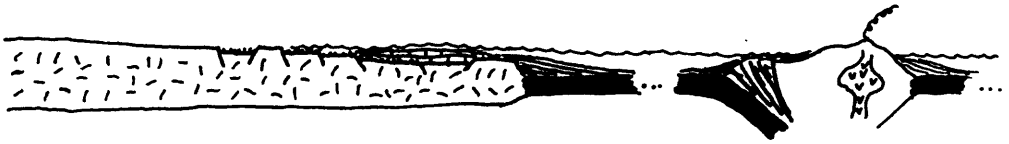

MIDDLE ORDOVICIAN TACONIC OROGENY

SILURIAN - EARLY DEVONIAN

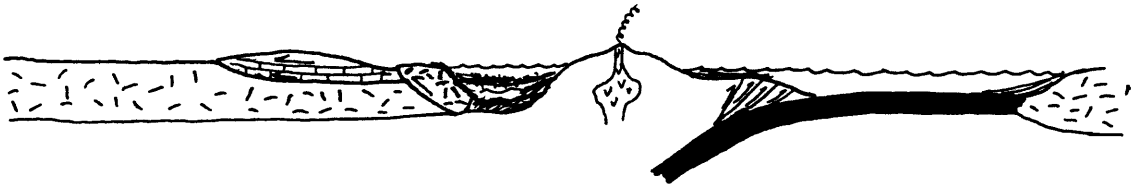

MIDDLE DEVONIAN ACADIAN OROGENY

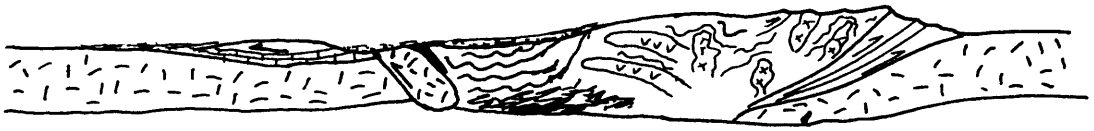

Figure 6.5

REFERENCES

Aki, K., Crustal structure in Japan from the phase velocity of Rayleigh waves, Bull. Eq. Res. Inst.,39,255-283,1961.

Aki, K., A. Christoffersson, and E.S.Husebye, Determination of the three-dimensional seismic structure of the lithosphere, J. Geophys. Res.,82,277-296,1977.

Aki, K. and W.H.K. Lee, Determination of three-dimensional velocity anomalies under a seismic array using first P arrival times from local earthquakes 1. A homogeneous initial model, J. Geophys. Res.,81, 4381-4399,1976.

Aki, K. and P.Richards, Methods of Quantitative Seismology, Freeman, 1980.

Anderson, K.R., Automatic processing of local earthquake data, unpublished Ph.D thesis, Massachusetts Institute of Technology, 1978.

Alvord, D.C., K.Bell, M. Pease, and P. Barosh, The areomagnetic expression of bedrock geology between the Clinton-Newbury and Bloody Bluff fault zones, northeastern Massachusetts, J. Res. U.S. Geol. Surv., 4, 601-604, 1976.

Arnold, M.E., Effect of hydrophone arrays on offshore Texas seismic signals, Geophysics, 43, 1083-1098, 1978.

Arthand, F. and P. Matte, Late Paleozoic strike-slip faulting in southern Europe and northern Africa: Result of a right-lateral shear zone between the Appalachians and the Urals, Geol. Soc. Am. Bull., 88, 1305-1320, 1977.

Bailey, R.C., R.N. Edwards, G.D.Garland, and J.P. Greenhouse, Geomagnetic sounding of eastern North America and the White Mountain heat flow anomaly, Geophys. J.R. Astr. Soc., SS, 499-502, 1978.

Ballard, R.D. and E. Uchupi, Triassic rift structure in Gulf of Maine, Am. Assoc. Pet. Geol. Bull., 59, 1041-1072, 1975.

Bath, M., An analysis of the time term method in refraction seismology, Tectonophys., 51, 155-169, 1978.

Berry, M.J. and K. Fuchs, crustal structure of the superior and Grenville Provinces of the northeastern Canadian Shield, Bull. Seism. Soc. Am., 63, 1393-1432, 1973.

Berry, M.J. and G.F. West, An interpretation of the first-arrival data of the Lake Superior experiment by the time-term method, Bull. Seism. Soc. Am., 56, 141-171, 1966.

Bevington, P.R., Data Reduction and Error Analysis for the Physical Sciences, McGraw-Hill, New York, 336pp., 1969.

Bird, G.P., Thermal and mechanical evolution of continental convergence zones: Zagros and Himalayas, unpublished Ph.D. Thesis, Massachusetts Institute of Technology, 1976.

Brown, L., Paleomagnetic results from northern Maine and the western limit of "Avalon" in the mid Paleozoic, (abstract), in abstracts with programs, Geol. Soc. Am.,12,26,1980.

Brune, J.N., Correction of initial phase measurements for the southeast Alaska earthquake of July 10, 1958, and for certain nuclear explosions, J. Geophys. Res., 67, 3643-3644, 1962.

Bird, J.M., and J.F. Dewey, Lithosphere plate-continental margin tectonics and the evolution of the Appalachian orogen, Geol. Soc. America Bull., 81, 1031-1060, 1970.

Blackwell, D.D., The thermal structure of the continental crust, AGU Mono. 14, 169-184, 1971.

Bollinger, G.A., M.C. Chapman, and T.P. Moore, Central Virginia Regional Seismic Network: Crustal velocity structure in central and southwestern Virginia, NUREG CR-1217, 187pp.,1980.

Bolt, B.A., and O.W. Nuttli, P wave residuals as a function of Azimuth, J. Geophys. Res., 71, 5977-5985, 1966.

Boucot, A.J., Silurian and Devonian of the northern Appalachians, in Studies of Appalachian Geology-Northern and Maritime, E. Zen, ed., Interscience, New York, 83-94, 1968.

Brune, J. and J. Dorman, Seismic waves and earth structure in the Canadian shield, Bull. Seism. Soc. Am., 53, 167-210, 1963.

Burchfiel, B.C., and G.A. Davis, Nature and controls of Cordilleran orogenesis, western United States: extensions of an earlier synthesis, American J. of Sc., 275-A, 363-396, 1975.

Burg, J.P., Three-dimensional filtering with an array of seismometers, Geophys., 29, 693-713, 1964.

Burkhard, N.R., and D.D. Jackson, Density and surface wave inversion, Geophys. Res. Lett., 3, 637-638, 1976.

Capon, J., Analysis of Rayleigh-wave multipath propagation at LASA, Bull. Seism. Soc. Am., 60, 1701-1731, 1970.

Cara, M., Filtering of dispersed wavetrains, Geophys. J.R. astr. Soc., 33, 65-80, 1973.

Cara, M., Regional variations of higher Rayleigh-mode phase velocities: a spatial-filtering method, Geophys. J.R. astr. soc., 54, 439-460, 1978.

Chapman, C.A. Structural evolution of the White Mountain Magma series, GSA mem 146, 281-300, 1976.

Chiburis, E.F., R.O. Ahner, and T. Graham, Northeastern U.S. Seismic Network, Bulls. 1-12, 1975-1979.

Chiburis, E.F., and T. Graham, Seismic networks in New England (abstract), Bull. 10, p.36, Northeast. Sect., Geol. Soc. of Amer., Boston, MA, 1978.

Chidester, A.H., Evolution of the ultramafic complexes of northwest New England, in studies of Appalachian Geology - Northern and Maritime, E. Zen, ed., Interscience, New York, 343-354, 1968.

Christensen, N.I., Compressional wave velocities in rocks at high temperatures and pressures, critical thermal gradients, and crustal low-velocity zones, J. Geophys. Res., 84, 6849-6857, 1979.

Christensen, N.I. and D.M. Fountain, Constitution of the lower continental crust based on experimental studies of seismic velocities in granite, Geol. Soc. Am. Bull., 86, 227-236, 1975.

Claerbout, J.F., Fundamentals of Geophysical Data Processing, McGraw-Hill, Inc., 274pp, 1976.

Clay, C.S., and M.J. Hinich, Use of a two-dimensional array to receive an unknown signal in a dispersive waveguide, J. Acoust. Soc. Am.,47, 431-440, 1970.

Cockerham, R. and W. Ellsworth, Three-dimensional large scale mantle structure in central California, (abstract), Trans. Am. Geophys. Un., 60, 875, 1979.

Connerney, J.E.P., T. Nekut, and A.F. Kuckes, Deep crustal electrical conductivity in the Adirondacks, (abstract), Trans. Am Geop. Un., 60, 242, 1979.

Cook, F.A., D.S. Albough, L.D. Brown, S. Kaufman, J.E. Oliver, R.D. Hatcher, Thin-skinned tectonics in the crystalline southern Appalachians; COCORP seismic-reflection profiling of the Blue Ridge and Piedmont, Geol., 7, 563-567, 1979.

Delong, S.E., P.J. Fox, and F.W. McDowell, Subduction of the Kula Ridge at the Aleution Trench, Geol. Soc. Amer. Bull., 89, 83-95, 1978.

Dainty, A.M., C.E. Keen, M.J. Keen, and J.E. Blanchard, Review of geophysical evidence on crust and upper mantle structure on the eastern seaboard of Canada, AGU Mono. 10, Washington D.C., 349-369, 1966.

Der, Z., R. Masse, and M. Landisman, Effects of observational errors on the resolution of surface waves at intermediate distances, J. Geop. Res., 75, 3399-3409, 1970.

Der, Z.A., and M. Landisman, Theory for errors, resolution, and separation of unknown variables in inverse problems, with application to the mantle and the crust in southern Africa and Scandinavia, Geophys. J.R. astr. soc., 27, 137-178, 1972.

Dewey, J.F., Suture zone complexities: a review,Tectonophysics, 40, 53-67, 1977.

Dewey, J.F. and K.C.A. Burke, Tibetan, Variscan, and Precambrian basement reactivation: products of continental collision, J. Geol., 81, 683-692, 1973.

Dewey, J.F., and W.S. Kidd, Continental collisions in the Appalachian Caledonian Orogenic belt. Variations related to complete and incomplete suturing, Geology, 2, 543-5461, 1974.

Diment, W.H., T.C. Urban, and F.A. Revetta, Some geophysical anomalies in the eastern United States: in the Nature of the Solid Earth, Robertson, E., ed., McGraw Hill, New York, p.544-574, 1972.

Dobrin, M.B., Introduction to Geophysical Prospecting, McGraw Hill, New York, 630pp, 1976.

Dorman, J. and M. Ewing, Numerical inversion of seismic surface wave dispersion data and crust-mantle structure in the New York- Pennsylvania area, J. Geophys. Res., 67, 5227-5241, 1962.

Douze, E.J. and S.J. Laster, Seismic array noise studies at Roosevelt Hot Springs, Utah geothermal area, Geophys., 44, 1570-1583, 1979.

Dziewonski, A., S. Bloch, and M. Landisman, A technique for the analysis of transient seismic signals, Bull. Seism. Soc. Am., 59, 427-444, 1969.

Dziewonski, A., J. Mills, and S. Bloch, Residual dispersion measurement - a new method of surface-wave analysis, Bull. Seism. Soc. Am., 62, 129-139, 1972.

Ellsworth, W.L., Three-dimensional structure of the crust and mantle beneath the island of Hawaii, unpublished Ph.D. thesis, Massachusetts Institute of Technology, 1977.

Ellsworth, W.L. and R.Y. Koyomagi, Three-dimensional crust and mantle structure of Kilauea Volcano, Hawaii, J. Geophys. Res., 82, 5379-5394, 1977.

Engdahl, E.R., J.G. Sindorf, and R.A. Eppley, Interpretation of relative teleseismic P wave residuals, J. Geophys. Res., 82, 5671-5682, 1977.

Ewing, M. and F. Press, Determination of crustal structure from phase velocity of Rayleigh waves, Part 3, the United States, Bull. Geol. Soc. Am., 70, 229-234, 1959.

Fletcher, J.B., M.L. Sbar, and L.R. Sykes, Seismic trends and travel-time residuals in eastern North America and their tectonic implications, Geol. Soc. Amer. Bull., 89, 1656-1676, 1978.

Ford, W.T. and J.H. Hearne, Least-squares inverse filtering, Geophys., 31, 917-926, 1966.

Forsyth, D.W. and F. Press, Geophysical tests of petrological models of the spreading lithosphere, J. Geophys. Res., 76, 7963-7979, 1971.

Fountain, D.M., The Ivrea-Verbano and Strona-Ceneri Zones, northern Italy: a cross-section of the continental crust - New evidence from seismic velocities of rock samples, Tectonophys., 33, 145-165, 1976.

Franklin, J.N., Well-posed stochastic extensions of ill-posed linear problems, J. Math. Anal. Appl., 31, 682-716, 1970.

Giese, P. and C. Prodehl, Main features of crustal structure in the Alps, in Explosion Seismology in Central Europe - Data and Results, P. Giese, C. Prodehl, and A. Stein, eds., Springer, New York, 347-375, 1976.

Giese, P., Models of crustal structure and main wave groups, in Explosion Seismology in Central Europe - Data and

Results, P. Giese, C. Prodehl, and A. Stein, eds., Springer, New York, 196-200, 1976.

Graham, T. and E.F. Chiburis, Fault plane solutions and the state of stress in New England, submitted to Earthquake Notes, 1980.

Green, D.H. and A.E. Ringwood, A comparison of recent experimental data on the gabbro-garnet granlite-eclogite transition, J. Geol., 80, 277-288,1972.

Greenfield, R.J. and R.M. Sheppard, The Moho depth variations under the LASA and their effect on dT/dD measurements, Bull. Seism. Soc. Am., 59, 409-420, 1969.

Hagiwara, T., A note on the theory of the electromagnetic seismograph, Bull. Eq. Res. Inst., 36, 139-161, 1958.

Haskell, N.A., The dispersion of surface waves on multilayered media, Bull. Seism. Soc. Am., 43, 17-34, 1953.

Hatcher, R.D., Tectonics of the western Piedmont and Blue Ridge, southern Appalachians: review and speculation, Am. J. Sci., 278, 276-304, 1978.

Hirahara, K., A large-scale three-dimensional seismic structure under the Japan Islands and the Sea of Japan, J. Phys. Earth, 25, 393-417, 1977.

Inston, H.H., P.D. Marshall, and C. Blamey, Optimization of filter bandwidth in spectral analysis of wavetrains, Geophys. J. R. astr. soc., 23, 243-250, 1971.

Iyer, H.M. and J.H. Healy, Teleseismic residuals at the LASA-USGS extended array and their interpretation in terms of crust and upper mantle structure, J. Geophys. Res., 77, 1503-1527, 1972.

Iyer, H.M., Anomalous delays of teleseismic P waves in Yellowstone National Park, Nature, 253, 425-427, 1974.

Jackson, D.D., Interpretation of inaccurate, insufficient and inconsistent data, Geophys. J. R. astr. soc., 28, 97-109, 1972.

James, D.E., and A.T. Linde, A source of major error in the digital analysis of world wide standard station seismograms, Bull. Seism. Soc. Am., 61, 723-728, 1971.

James, D.E., T.J. Smith, and J.S. Steinhart, Crustal Structure of the Middle Atlantic States, J. Geophys.

Res., 73, 1983-2007, 1968.

Jaupart, C., Heat flow and heat generation in New England, unpublished manuscript, 1979.

Johnson, L.R., Array measurements of P velocities in the upper mantle, J. Geophys. Res., 72, 6309-6324, 1967.

Jordan, T.H. and L.N. Frazer, Crustal and upper mantle structure from Sp phases, J. Geophys. Res., 80, 1504-1518, 1975.

Kane, M.F., M.J. Yellin, K.G. Bell, and I. Zietz, Gravity and magnetic evidence of lithology and structure in the Gulf of Maine Region, U.S. Geol. Survey Prof. Paper, 726-B, 22pp.

Kane, M.F., G. Simmons, W. Diment, M. Fitzpatrick, W. Joyner, R. Bromery, Bouguer gravity and generalized geologic map of New England and adjoining areas, U.S. Geol. Surv. Geophys. Inv. Map GP-839, 1972.

Kasameyer, P.W., Low-frequency magnetotelluric survey of New England, unpublished Ph.D. thesis, Massachusetts Institute of Technology, 1974.

Katz, S., Seismic study of crustal structure in Pennsylvania and New York, Bull. Seism. Soc. Am., 45, 303-325, 1955.

Kent, D.V. and N.D. Opdyke, Paleomagnetism of the Devonian Catskill red beds: evidence for motion of the coastal New England-Canadian Maritime region relative to cratonic North America, J. Geophy. Res., 83, 1441-1450, 1978.

Kennedy, M.J., Southeastern margin of the Northeastern Appalachians: late Precambrian orogeny on a continental margin, Geol. Soc. America Bull., 87, 1317-1325, 1976.

King, P.B., Tectonic map of North America, scale 1:5,000,000, U.S. Geol. Surv., Washington, D.C., 1969.

Knopoff, L. and F.S. Chang, The inversion of surface wave dispersion data with random errors, J. Geophys., 43, 299-309, 1977.

Lacoss, R.T., E.J. Kelley, and M.N. Toksoz, Estimation of seismic noise structure using arrays, Geophys., 34, 21-38, 1969.

Lancsoz, C., Linear Differential Operators, D. Van Nostrand, London, 564pp, 1961.

Landisman, M., A. Dziewonski, and Y. Sato, Recent improvements in the analysis of surface wave observations, Geophys. J. R. astr. Soc., 17, 369-403, 1969.

Leet, D., Trial travel times for northeastern America, Bull. Seism. Soc. Am., 31, 325-334, 1941.

LeFort, P., Himalayas: The collided range. Present knowledge of the continental arc, Am. J. Sci., 275-A, 1-44, 1975.

Liaw, A.L. and T.V. McEvilly, Microseisms in geothermal exploration - studies in Grass Valley, Nevada, Geophys., 44, 1097-1115, 1979.

Lineham, D., New England seismic network, Semiann. Tech. Rep. V, Air Force Geophysics Lab., Bedford, MA, 1962.

Linville, A.F. and S.J. Laster, Numerical experiments in the estimation of frequency-wavenumber spectra of seismic events using linear arrays, Bull. Seism. Soc. Am., 56, 1337-1355, 1966.

Loiselle, M., Geochemistry and petrogenesis of the Belknap Mountains Complex and Plinz Range, White Mountain Series, New Hampshire, unpublished Ph.D. thesis, Massachusetts Institute of Technology, 1978.

Loiselle, M.C., and R.A. Ayuso, Geochemical characteristics of granitoids across the Merrimack Synclinorium eastern and central Maine, in The Caledonides in the U.S.A., I.A.C.P., Blacksburg, VA, 117-121, 1979.

Long, L.T., The Carolina slate belt - evidence of a continental rift zone, Geol., 7, 180-184, 1979.

Long, T.L., and U.P. Mathur, Southern Appalachian crustal structure from the dispersion of Rayleigh waves and refraction data, Eq. notes, 43:1, 31-39, 1972.

Manghnani, M.H., R. Ramananantoandro, and S.P. Clark, Compressional and shear wave velocities in granulite facies rocks and eclogites to 10 kbar, J. Geophys. Res., 79, 5427-5446, 1974.

McCollom, R.L. and R.S. Crosson, An array study of upper mantle velocity in Washington State, Bull. Seism. Soc. Am., 65, 467-482, 1975.

McCowan, D.W., P. Glover, and S.S. Alexander, A crust and upper mantle model for Novaya Zemlya from Rayleigh-wave dispersion data, Bull. Seism. Soc. Am., 68, 1651-1662, 1978.

McEvilly, T.V., Central U.S. crust - upper mantle structure from Love and Rayleigh wave phase velocity inversion, Bull. Seism. Soc. Am., 54, 1997-2015, 1964.

McKerrow, W.S., and L.R.M. Cocks, The location of the Iapetus Ocean suture in Newfoundland, Can. J. Earth Sci., 14, 488-495, 1977.

McLelland, J. and Y. Isachsen, Structural synthesis of the southern and central Adirondacks: A model for the Adirondacks as a whole and plate-tectonics interpretations, Geol. Soc. Am. Bull., 91, 68-72 and 208-292, 1980.

Menke, W.H., Lateral inhomogeneitres in P velocity under the Tarbela Array of the Lesser Himalayas of Pakistan, Bull. Seism. Soc. Am., 67, 725-734, 1977.

Misra, K.C. and F.B. Keller, Ultramafic bodies in the southern Appalachians: A review, Am. J. Sci., 278, 389-418, 1978.

Mitchell, B.J., C.C. Cheng, and W. Stauder, A three-dimensional velocity model of the lithosphere beneath the New Madrid seismic zone, Bull. Seism. Soc. Am., 67, 1061-1074, 1977.

Mitchell, B.J. and B.M. Hashim, Seismic velocity determinations in the New Madrid seismic zone: a new method using local earthquakes, Bull. Seism. Soc. Am., 67, 413-424, 1977.

Mitchell, B.J., and R.B. Herrmann, Shear velocity structure in the eastern United States from the inversion of surface-wave group and phase velocities, Bull. Seism. Soc. Am., 69, 1133-1148, 1979.

Moench, R.H., and R.E. Zartman, Chronology and styles of multiple deformation, plutonism, and polymetamorphism in the Merrimack Synclinorum of western Maine, Geol. Soc. of America, Mem 146, 203-238, 1976.

Mueller, S., A new model of the continental crust, in The Earth's Crust, AGU mono. 20, J.G. Heacock ed., AGU, Washington, D.C., 289-317, 1977.

Nakamura, Y. and B.F. Howell, Maine seismic experiment frequency spectra of refraction arrivals and the nature of the Mohorovicic discontinuity, Bull. Seism. Soc. Am., 54, 9-18, 1964.

Naylor, R.S., Origin and regional relationships of the core-rocks of the Oliverion domes, in Studies of Appalachian Geology - Northern and Maritime, E. Zen,

ed., Interscience, New York, 231-239, 1968.

Naylor, R.S., Acadian Orogeny: an abrupt and brief event, Science, 172: 558-560, 1971.

Naylor, R.S., Age Provinces in the Northern Appalachians, Ann. Rev. Earth and Planetary Sci., 3, 387-400, 1975.

Nelson, A.E., Structural elements and deformational history of rocks in eastern Massachusetts, Geol. Soc. America Bull., 87, 1377-1383, 1976.

Nolet, G., and G.F. Panza, Array analysis of seismic surface waves: limits and possibilities, Pure Appl. Geophys., 114, 775-790, 1976.

Nuttli, O.W., and, B.A. Bolt, P wave residuals as a function of azimuth, J. Geophys. Res., 74, pp.6594-6602, 1969.

Oppenheim, A.V., and R.W. Schafer, Digital Signal Processing, Prentice- Hall, New Jersey, 585pp., 1975.

Osberg, P.H., Synthesis of the geology of the northeastern Appalachians, U.S.A., IGCP Project 27, Geol. Surv. Com. Pap., 78-13, 137-147, 1978.

Pilant, W.L. and L. Knopoff, Inversion of Phase and group slowness dispersion, J. Geophys. Res., 75, 2135-2136,1970.

Poupinet, G., On the relation between P wave travel time residuals and the age of continental plates, Earth Planet. Sci. Lett., 43, 149-161, 1979.

Pulli, J.J., and T. Graham, The earthquake mechanism in New England (abstract), Earthquake Notes, 49, 86, 1979.

Putman, G.W. and J.W. Sullivan, Granitic pegmatites as estimators of crustal pressures - A test in the eastern Adirondacks, New York, Geol., 7, 549-553, 1979.

Ratcliffe, N.M., Cross section of the Berkshire massif at 42 N.: Profile of a basement reactivation zone, in N.E.I.G.C. Guidebook for field trips in western Massachusetts, northern Connecticut and adjacent areas of New York, N.M. Ratcliffe, ed., 1975.

Rankin, D.W., Volcanism related to tectonism in the Piscataquis volcanic belt, an island arc of Early Devonian age in north-central Maine, in Studies of Appalachian Geology - Northern and Maritime, E. Zen, ed., Interscience, New York, 355-369, 1968.

Rankin, D.W., Appalachian salients and recesses: Late Precambrian continental breakup and the opening of the Iapetus Ocean, J. Geop. Res., 81, 5605-55619, 1976.

Rodgers, J., The Tectonics of the Appalachians, Wiley - Interscience, N.Y., 271pp., 1970.

Rodi, W.L., P. Glover, T.M.C. Li, and S.S. Alexander, A fast, accurate method for computing group-velocity partial derivatives for Rayleigh and Love modes, Bull. Seism. Soc. Am., 65, 1105-1114, 1975.

Peacock, K.L., and S. Treitel, Predictive deconvolution: theory and practice, Geophys., 34, 155-169, 1969.

Sbar, M.L. and L.B. Sykes, Seismicity and lithospheric stress in New York and adjacent areas, J. Geop. Res., 82, 5771-5786, 1977.

Scheiddegger, A.E. and P.L. Willmore, The use of a least squares method for the interpretation of data from seismic surveys, Geophys., 22, pp.9-22, 1957.

Schnerk, R., Y.P. Aggarwal, M. Golisono, and F. England, Reg. Seism. Bull. of the Lamont-Doherty Network, Lamont-Doherty Geological Observatory, Palisades, N.Y., 1976.

Senturia, S.D., and B.D. Wedlock, Electronic Circuits and Applications, John Wiley and Sons, 623pp., 1975.

Sheppard, R.M., Values of LASA time station residuals, velocity and azimuth errors, Lincoln Lab tech note, 90p., 1967.

Simmons, G., Gravity survey and geological interpretation,northern New York, Geol. Soc. Am. Bull., 75, 81-98, 1964.

Skehan, J.W., Fracture tectonics of southeastern New England as illustrated by the Wachusett-Marlborough Tunnel, Studies in Appalachian Geology: Northern and Maritime: New York, Interscience Publs., 281-290, 1968.

Smith, M.E., Noise analysis and multiple seismometer theory, Geophys., 11, 337-360, 1956.

Smithson, S.B., A model for lower continental crust, Earth planet. Sci. Lett., 35, 134-144, 1977.

Steeples, D.W. and H.M. Iyer, Low-velocity zone under Long Valley as determined from teleseismic events, J. Geophys. Res., 81, 849-860, 1976.

Steinberg, D.I., Computational Matrix Algebra, McGraw-Hill, New York, 280pp., 1974.

Steinhart, J.S., and R.P. Meyer, Explosion Studies of Continental Structure, Carnegie Inst. of Washington, Publ. 622, Wash., D.C., 409pp., 1961.

Steinhart, J.S., R. Green, T. Asada, B.A. Rodriguez, L.T. Aldrich, and M.A. Tuve, Seismic studies: Carnegie Inst. Washington Year Book 61, 1961-1962, 221-234, 1962.

Stewart, I.C.F., Teleseismic reflections and the Newfoundland lithosphere, Can. J. of Earth Sci., 15, 175-180, 1978.

Strong, D.F., Dickson, W.L., O'Driscoll, L.F., Kean, B.F., and R.K. Stevens, Geochemical evidence for an east-dipping Appalachian subduction zone in Newfoundland: Nature, 248, 37-39, 1974.

Takenchi, H., J. Dorman, and M. Saito, Partial derivatives of surface wave phase velocity with respect to physical parameter changes within the earth, J. Geophys. Res., 69, 3429-3441, 1964.

Taner, M.T., F. Koehler, and R.E. Sheriff, Complex seismic trace analysis, Geophys., 44, 1041-1063, 1979.

Taylor, S.R., New England crust and upper mantle structure derived from teleseismic and local P-wave data, unpublished manuscript, 1977.

Taylor, S.R. and M.N. Toksoz, Three-dimensional crust and upper mantle structure of the northeastern United States, J. Geophys. Res., 84, 7627-7644, 1979a.

Taylor, S.R. and M.N. Toksoz, Frequency-wave number power spectra of fundamental mode Rayleigh waves across southeastern New England, Eastern sect. SSA, 51st meeting (abs.), 1979b.

Taylor, S.R., G. Simmons, and P. Barosh, A gravity survey of the Clinton-Newbury and Bloody Bluff fault zones in eastern Massachusetts, (abstract), in abstracts with programs, Geol. Soc. Am., 12, 86, 1980.

Thompson, M., Paleozoic regional metamorphism in New England and adjacent areas, in Studies in Appalachian geology: Northern and Maritime: E. Zen, ed., Interscience, N.Y., 319-326, 1968.

Toksoz, M.N. and R.T. Lacoss, Microseisms: Mode structure and sources, Science, 159,1 872-873, 1968.

Toksoz, M.N. and P. Bird, Modelling of temperatures in continental convergence zones, Tectonophysics, 41, 181-193, 1977.

Toksoz, M.N., N.H. Sleep, A.T. Smith, Evolution of the downgoing lithosphere and the mechnisms of deep focus earthquakes, Geophys. J.R. astr. soc., 35, 285-310, 1973.

Treitel, S. and E.A. Robinson, The design of high resolution digital filters, IEEE Trans. Geoscience Electronics, 4, 25-38, 1966.

Tseng, J., Gravity compensation of the Mohorovicic discontinuity and the basic model of crustal structure, Acta Geophysica Sinica, 16, 1-5, 1973.

Volz, W.R., Travel time perturbations in the crust and upper mantle in the southeast, unpublished masters thesis, Georgia Institute of Technology, 198pp., 1979.

Warren, D.J., Transcontinental geophysical survey (35 -39 N) seismic refraction profiles of the crust and upper mantle from 74 to 87 W longitude, Misc. Geol. Inv. Map I-535-D, U.S.G.S., Washington D.C., 1968.

Weston Geophysical Research, Inc., Areomagnetic map of southeastern New England and the western Gulf of Maine, Pl. 2c-1, 1976.

Weiner, N., Time Series, M.I.T. Press, Cambridge, MA, 163pp., 1949.

Wiggins, R.A., The generalized linear inverse problem: implication of surface waves and free oscillations for earth structure, Rev. Geophys. and Sp. Phys., 10, 251-285, 1972.

Wiggins, R.A., Interpolation of digitized curves, Bull. Seism. Soc. Am., 66, 2077-2081, 1976.

Willmore, P.L. and A.M. Bancroft, The time term approach to refraction seismology, Geophys. J., 3, 419-432, 1960.

Woollard, G.P., Crustal structure from gravity and seismic measurements, J. Geophys. Res., 64, 1521-1544, 1959.

Wu, F.T. and R.P. Allen, dT/dD measurements at Weston observatory, USA, Geophys. J.R. astr. Soc., 26, 537-543, 1972.

Zandt, G., Study of three-dimensional heterogeneity beneath seismic arrays in central California and Yellowstone, Wyoming, unpublished Massachusetts Institute of

Technology Ph.D. thesis, 1978.

Zandt, G., Three-dimensional seismic velocity anomalies in the crust and upper mantle under southwest Japan, (abstract), Trans. Am. Geop. Un., 56, 394, 1975.

Zarrow, L., Naylor, R.S., and F.A. Frey, Precambrian age of the Lynn Volcanics at Pine Hill in the Middlesex Fells Reservation, North Boston Quandrangle, Massachusetts, (abstract), N.E. Geol. Soc. of America, 10, 91, 1978.

Zen, E-An, The Taconide Zone and the Taconic Orogeny in the western part of the northern Appalachian Orogen, Geol. Soc. Am. S.P. 135, 1972.

Zietz, I. and E. Zen, Northern Appalachians, Geotimes, 18, 24-28, 1973.

APPENDIX A

GENERALIZED AND STOCHASTIC INVERSION

In this appendix, the generalized and stochastic inverse for a linearized system are briefly reviewed (see Lancsoz, 1961; Aki and Richards, 1980; and Wiggins, 1972 for details). In Appendix F, the problem for the simultaneous inversion of fundamental mode Rayleigh wave phase and group velocities using a maximum-likelihood method is formulated.

Given a set of experimentally observed phase and group velocity data, theoretical phase and group velocities are calculated using the propagator matrix method of Haskell (1953) and the variational principle described in Appendix E. Assuming the surface wave velocities, v, are not rapidly varying and the perturbations to the initial model are small, the problem can be linearized by expanding in a Taylor series about the initial model to the first order

$$\Delta V_i = \sum_{k=1}^{n} \frac{\partial V_i}{\partial p_k} \Delta p_k \qquad \begin{array}{ll} i = 1,\dots,m & \text{- period index} \\ j = 1,\dots,l & \text{- layer index} \\ k = 1,\dots,n & \text{- parameter index} \end{array} \qquad (1)$$

where

$\Delta V_i = V_i^{obs} - V_i^{th}$ difference between observed and theoretical velocity at period i

p_j - parameter for layer j

Δp_j - parameter correction for layer j

Equations 1 can be re-written in matrix form

$$\begin{bmatrix} \Delta V_1 \\ \Delta V_2 \\ \vdots \\ \Delta V_m \end{bmatrix} = \begin{bmatrix} \frac{\partial V_1}{\partial p_1} & \frac{\partial V_1}{\partial p_2} & \cdots & \frac{\partial V_1}{\partial p_n} \\ \vdots & & & \\ \frac{\partial V_m}{\partial p_1} & & \cdots & \frac{\partial V_m}{\partial p_n} \end{bmatrix} \begin{bmatrix} \Delta p_1 \\ \Delta p_2 \\ \vdots \\ \Delta p_n \end{bmatrix} \qquad (2)$$

or

$$\underline{b} = A\underline{x} \qquad (3)$$

Following the generalized inverse technique of Lancsoz (1961), the matrix A in equation 3 is decomposed into

$$A = U\Lambda V^T \qquad (4)$$

where U- contains n eigenvectors $\underline{u}_i$ of length m from the data space

Λ - diagonal matrix with n eigenvalues

V - contains n eigenvectors $\underline{v}_i$ of length n from model space

The matrices U and V satisfy the relationships

$$AA^T U = U\Lambda^2 \qquad (5a)$$

$$A^T AV = V\Lambda^2 \qquad (5b)$$

The matrices U and V are coupled through the p non-zero eigenvalues by

$$\begin{aligned} A\,u_p &= u_p \Lambda_p \\ A^T v_p &= v_p \Lambda_p \end{aligned} \qquad (6)$$

where Λ_p is a diagonal matrix containing only non-zero eigenvalues. The eigenvectors associated with (n-p) zero eigenvalues in U and V become independent

$$\begin{aligned} A^T u_0 &= 0 \\ A\,v_0 &= 0 \end{aligned} \qquad (7)$$

In the presence of zero eigenvalues, U and V are semi-orthogonal and

$$u_p^T u_p = v_p^T v_p = I_{p\times p}$$

But because the non-zero eigenvalues may not span either or both the data or model spaces, $U_p U_p^T$ and $V_p V_p^T$ are not guaranteed to equal the m-dimensional or n-dimensional identity matrices, respectively. Equations 6 and 7 can be written as

$$AV = A\left[V_p V_o\right] = \left[u_p u_o\right]\begin{bmatrix}\Lambda_p & 0\\ 0 & 0\end{bmatrix} \qquad (8)$$

and since $VV^T = I$

$$A = \left[u_p u_o\right]\begin{bmatrix}\Lambda_p & 0\\ 0 & 0\end{bmatrix}\begin{bmatrix}V_p^T\\ V_o^T\end{bmatrix} = U_p \Lambda_p V_p^T \qquad (9)$$

The generalized inverse operator is given by

$$A_g^{-1} = V_p \Lambda_p^{-1} U_p^T \qquad (10)$$

As discussed by Lancsoz (1961), in the presence of UO and VO space, A_g^{-1} minimizes the length of the error vector

$$(A\underline{x} - \underline{b})^T (A\underline{x} - \underline{b}) = |A\underline{x} - \underline{b}|^2$$

in the data space and the length of the solution vector

$$\underline{x}^T x = |\underline{x}|^2$$

in the model space simultaneously. This second property is useful in that the perturbations to the model are kept small which tends to stabilize the inversion.

A measure of uniqueness of the solution is obtained by calculating the resolution matrix, R. Let $\hat{\underline{x}}$ be the model solution and $\underline{x}$ the "true" solution. Then from equation 3 and the properties discussed above, the inverse solution is given by

$$\hat{\underline{x}} = A_g^{-1} A\underline{x} = V_p \Lambda_p^{-1} U_p^T U_p \Lambda_p U_p^T \underline{x} = V_p V_p^T \underline{x} = R\underline{x}$$

If there is no V0 space $V_p V_p^T = I$ and $\hat{\underline{x}} = \underline{x}$ and the solution is unique even in the presense of U0 space. In the presence of V0 space, $V_p V_p^T \neq I$ and the solution will be dependent on the off-diagonal terms of $V_p V_p^T$. Thus, V0 space is the source of non-uniqueness in the solution and results when various parameters are dependent. The resolution matrix R filters the true solution $\underline{x}$ to give the estimate $\hat{\underline{x}}$. It supplies information regarding the numbers of degrees of freedom (uniqueness) in the system (m-p) because the trace of R equals p. The rows of R are called resolving kernals (Jackson, 1972).

Similarly, the information density matrix, S, describes the resolution in data space. From equation 3 and the properties of the eigenvectors discussed above, the data predicted by the generalized inverse, $\underline{b}g$, is related to the observed data, $\underline{b}$, by

$$\underline{b}_g = A A_g^{-1} \underline{b} = U_p \Lambda_p V_p^T V_p \Lambda_p^{-1} U_p^T \underline{b} = U_p U_p^T \underline{b} = S\underline{b} \quad (12)$$

For a symmetric or underdetermined system U0=0, $U_p U_p^T = I$ and the predicted data equals the observed data. In the presence of U0-space (for example in an overdetermined system) $U_p U_p^T \neq I$ and the model does not have enough flexibility to predict the data. In this case the predicted data are expressed as a weighted average of the observed. The information density matrix provides information on the inter-dependency of elements of the data vector.

The covariance matrix gives an estimate of the error in the solution $\Delta\underline{x}$ due to errors in the data $\Delta\underline{b}$ and is given

by

$$\Delta \underline{x} = A_g^{-1} \Delta \underline{b} \qquad (13)$$

The covariance matrix is defined by

$$COV = \langle \Delta \underline{x} \Delta \underline{x}^T \rangle = A_g^{-1} \langle \Delta \underline{b} \Delta \underline{b}^T \rangle (A_g^{-1})^T \qquad (14)$$

If the data are uncorrelated and have the same variance σ_d^2

$$COV = \sigma_d^2 V_p \Lambda_p^{-1} U_p^T U_p \Lambda_p^{-1} V_p^T = \sigma_d^2 U_p \Lambda_p^{-2} V_p^T \qquad (15)$$

It is clear that the errors in the solution become very large when the eigenvalues become small. Wiggins (1972) suggests eliminating eigenvectors associated with small eigenvalues. This decreases the magnitude of the errors, but the number of degrees of freedom is increased and hence the resolution is degraded.

Another method of off-setting the effects of small eigenvalues on the solution is obtained using a stochastic inverse (damped least squares) Franklin (1970) and is illustrated as follows. Given a system of equations 3

$$A \underline{x} = \underline{b} \qquad (3)$$

the least squares solution is given by

$$\underline{x} = (A^T A)^{-1} A^T \underline{b} \qquad (16)$$

However, in the presence of VO space, a pure least squares solution fails. The solution can be "damped" by adding a constant term θ^2 to the diagonal elements of $A^T A$ which gives

$$\hat{\underline{x}} = (A^T A + \theta^2 I)^{-1} A^T b \qquad (17)$$

where $\theta^2 = \frac{\sigma_d^2}{\sigma_x^2}$ and σ_d^2, σ_x^2 are the variances in data and model spaces, respectively. Rather than minimizing $|A\underline{x} - \underline{b}|^2$ we are now minimizing $|A\underline{x}-\underline{b}|^2 + \theta^2 \underline{x}^T\underline{x}$.

The damped least squares operator is given by (Aki and Richards, 1980)

$$L_\theta = (A^TA + \theta^2 I)^{-1} A^T = V_p \frac{\Lambda_p}{\Lambda_p^2 + \theta^2 I} U_p^T \qquad (18)$$

where $A = U_p \Lambda_p V_p^T$ and p is the order of space spanned by non-zero eigenvalues. From 18 the resolution matrix is seen to be

$$R = (A^TA + \theta^2 I)^{-1} A^TA = V_p \frac{\Lambda_p^2}{\Lambda_p^2 + \theta^2 I} V_p^T \qquad (19)$$

For uncorrelated errors the covariance matrix is

$$Cov = \sigma_d^2 (A^TA + \theta^2 I)^{-1} R = \sigma_d^2 V_p \frac{\Lambda_p^2}{(\Lambda_p^2 + \theta^2 I)^2} V_p^T \qquad (20)$$

Note as θ^2 goes to zero, the stochastic inverse operator and its resolution and covariance matrice reduce to those of the generalized inverse discussed previously. From equations 19 and 20 it can be seen that the addition of a damping parameter to the generalized inverse has the effect of reducing the model error at the expense of resolution. Thus, in actual use, the trade-off between resolution and errors must be examined in order to select a proper damping parameter.

APPENDIX B

NON-LINEAR INVERSION OF TRAVEL-TIME DATA FOR CROSS-OVER DISTANCES AND APPARENT VELOCITIES

Given a complete set of travel time data, a fairly simple and suprizingly stable least squares technique can be used to solve for apparent velocities, critical distances and corresponding intercept times for a plane layered earth model following the technique of Mitchell and Hashim (1977).

For a layer over a half-space model, the two branches of the travel-time curve can be described by

$$t_i^{th} = u(x)\left[(x_i - x_c)/V_1 + t_c\right] - u(x_i - x_c)\left[(x_i - x_1)/V_1 + t_c\right] + u(x_i - x_c)\left[(x_i - x_c)/V_2 + t_c\right] \quad (1)$$

where

t_i^{th} - calculated travel time at distance xi

x_c, t_c - critical distance and corresponding time

V_1, V_2 - velocity of upper and lower layer, respectively

$a_i = 1/V_i$ - slope of travel time curve for branch i

$u(x)$ - Heaviside step function

To the first order, the difference between the calculated and observed travel time at distance xi is

$$R_i = t_i^{obs} - t_i^{th} = \Delta t_c + \frac{\partial t_i}{\partial x_c}\Delta x_c + \frac{\partial t_i}{\partial a_1}\Delta a_1 + \frac{\partial t_i}{\partial a_2}\Delta a_2 \quad (2)$$

where $\Delta t_c, \Delta x_c, \Delta a_1, \Delta a_2$ are perturbations to the model and from (1)

$$\frac{\partial t}{\partial a_1} = \begin{cases} x - x_c & x \le x_c \\ 0 & x_c < x \end{cases} \qquad \frac{\partial t}{\partial t_c} = 1 \text{ all } x$$

$$\frac{\partial t}{\partial a_2} = \begin{cases} 0 & x \le x_c \\ x - x_c & x_c < x \end{cases} \qquad \frac{\partial t}{\partial x_c} = \begin{cases} -a_1 & x \le x_c \\ -a_2 & x_c < x \end{cases}$$

For m observations we solve for x_c, t_c, a_1, a_2 given an initial guess using

$$\begin{bmatrix} R_1 \\ R_2 \\ \vdots \\ R_m \end{bmatrix} = \begin{bmatrix} 1 & \frac{\partial t_1}{\partial x_c} & \frac{\partial t_1}{\partial a_1} & \frac{\partial t_1}{\partial a_2} \\ \vdots & \vdots & \vdots & \vdots \\ 1 & \frac{\partial t_m}{\partial x_c} & \frac{\partial t_m}{\partial a_1} & \frac{\partial t_m}{\partial a_2} \end{bmatrix} \begin{bmatrix} \Delta t_c \\ \Delta x_c \\ \Delta a_1 \\ \Delta a_2 \end{bmatrix} \qquad (3)$$

In matrix terms, (3) becomes

$$\underline{b} = A\underline{x} \qquad (4)$$

And the least squares solution is found by solving

$$A^T\underline{b} = A^TA\underline{x} \qquad (5)$$

using LU decomposition (Steinberg, 1974)

$$\underline{x} = (A^TA)^{-1}A^T\underline{b} \qquad (6)$$

Although the problem has been linearized by neglecting higher order terms in the Taylor series expansion about t_i^{obs}, the equations (1) still contain the non-linear terms involving distance divided by refractor velocity. However, test cases show that the system (5) converges accurately and rapidly to a final solution given a reasonable initial guess.

For three travel time branches (see Figure 3.3 for definitions) the travel time is given by

$$t_i^{th} = u(x)\left[(x_i - x_{c_1})/v_1 + t_{c_1}\right] - u(x_i - x_c)\left[(x_i - x_{c_1})/v_1 + t_{c_1}\right] + u(x_i - x_{c_1})\left[(x_i - x_{c_1})/v_2 + t_{c_1}\right]$$
$$- u(x_i - x_{c_2})\left[(x_i - x_{c_1})/v_2 + t_{c_1}\right] + u(x_i - x_{c_2})\left[(x_i - x_{c_2})/v_3 + t_{c_2}\right] \qquad (7)$$

Linearizing the problem by expanding in a first order Taylor series about t_i^{obs}

$$R_i = t_i^{obs} - t_i^{th} = \Delta t_{c_1} + \frac{\partial t_i}{\partial x_{c_1}}\Delta x_{c_1} + \frac{\partial t_i}{\partial x_{c_2}}\Delta x_{c_2} + \frac{\partial t_i}{\partial a_1}\Delta a_1 + \frac{\partial t_i}{\partial a_2}\Delta a_2 + \frac{\partial t_i}{\partial a_3}\Delta a_3 \quad (8)$$

where

$$t_{c_2} = t_{c_1} + \frac{x_{c_2} - x_{c_1}}{v_2} \quad (9)$$

and the partial derivatives are given by

$$\frac{\partial t}{\partial t_{c_1}} = 1 \text{ all } x \qquad \frac{\partial t}{\partial x_{c_1}} = \begin{cases} -a_1 & x \le x_{c_1} \\ -a_2 & x_{c_1} < x \end{cases} \qquad \frac{\partial t}{\partial x_{c_2}} = \begin{cases} 0 & x \le x_{c_2} \\ a_2 - a_3 & x_{c_2} < x \end{cases}$$

(using $\frac{\partial u(x)}{\partial x} = \delta(x)$; δ-Kronecker delta)

$$\frac{\partial t}{\partial a_1} = \begin{cases} x - x_c & x \le x_{c_1} \\ 0 & x_{c_1} < x \end{cases} \quad (10)$$

$$\frac{\partial t}{\partial a_3} = \begin{cases} 0 & x \le x_{c_2} \\ x - x_{c_2} & x_{c_2} < x \end{cases} \qquad \frac{\partial t}{\partial a_2} = \begin{cases} 0 & x \le x_{c_1} \\ x - x_{c_1} & x_{c_1} < x \le x_{c_2} \\ x_{c_2} - x_{c_1} & x_{c_2} < x \end{cases} \quad \text{(using 9)}$$

As before the system (8) is transformed into the form of (5) and solved using the LU method.

Although equation (7) represents the travel time curve for three branches, the first branch generally has a small non-zero intercept time which is either due to the effects of a thin, relatively low velocity upper layer or the focal depth of the events. To calculate the velocity with depth function a three layer over a half-space model must be used where the velocity of the upper layer, v0, is fixed. Using the terminology shown in Figure 3.3, the thickness of each layer is computed by calculating the zero-distance intercept time of each travel time branch and substituting into the following equations.

$$T_{i_1} = t_1 - \frac{x_{c_1}}{v_1} \qquad z_0 = \frac{1}{2}\sqrt{\frac{v_1 - v_0}{v_1 + v_0}}\, x_{c_1} = \frac{T_{i_1}}{2}\frac{v_1 v_0}{\sqrt{v_1^2 - v_0^2}}$$

$$T_{i_2} = t_1 - \frac{x_{c_1}}{v_0} \qquad z_1 = \frac{1}{2}\left(T_{i_2} - 2z_0\frac{\sqrt{v_2^2 - v_0^2}}{v_2 v_0}\right)\frac{v_2 v_1}{\sqrt{v_2^2 - v_1^2}} \quad (11)$$

$$T_{i3} = t_2 - \frac{X_{c2}}{V_3} \qquad Z_2 = \frac{1}{2}\left(T_{i3} - 2Z_0 \frac{\sqrt{V_3^2 - V_0^2}}{V_3 V_0} - 2Z_1 \frac{\sqrt{V_3^2 - V_1^2}}{V_3 V_1}\right) \frac{V_3 V_2}{\sqrt{V_3^2 - V_2^2}} \qquad (11)$$

The convergence of the solution is checked by calculating the RMS fit of the predicted to the observed travel times (Bevington, 1969)

$$\sigma^2 = \frac{\sum_{i=1}^{m} \left(t_i^{obs} - t_i^{th}\right)^2}{f} \qquad (12)$$

where

m - number of observations

n - number of parameters

f = m - n = number of degrees of freedom
(dimension of U0 - space; see Appendix A)

The model errors caused by errors in the data are calculated from the covariance matrix. Given the solution to a system of equations (6), the covariance matrix is (see Appendix A)

$$COV = \langle \Delta x \Delta x^T \rangle = (A^T A)^{-1} A^T \langle \Delta b \Delta b^T \rangle A (A^T A)^{-1} \qquad (13)$$

For uncorrelated errors (13) becomes

$$COV = \sigma^2 (A^T A)^{-1} \qquad (14)$$

where σ^2 is the data variance (12).

Because of the large number of degrees of freedom in the determination of the apparent velocities, the variances of the calculated velocities are very small. It is therefore assumed the velocities are well-determined and that the

errors in the thickness of each layer, Δz, are proportional to the errors in the calculated critical distances, Δx_c, $\left(z_0 = \frac{1}{2}\sqrt{\frac{V_1 - V_0}{V_1 + V_0}}\, x_{c_1}\right)$. Thus, the relative errors in layer thickness are estimated by

$$\Delta z \sim \frac{\Delta x_c}{x} z \qquad (15)$$

APPENDIX C

TIME TERM ANALYSIS

Given a set of travel times for waves refracted from a given layer, it is possible to solve for the apparent velocity, V1, and the zero-distance intercept time, a, using the equation

$$T_{ij} = a + \frac{D_{ij}}{V_1} \qquad (1)$$

where Tij is the travel time from source i to receiver j, and Dij is the distance between the source and receiver. For a single layer overlying a horizontal refractor with velocities V0, V1, respectively, equation (1) becomes (Dorman, 1976)

$$T_{ij} = \frac{2Z\sqrt{V_1^2 - V_0^2}}{V_1 V_0} + \frac{D_{ij}}{V_1} \qquad (2)$$

Equation (2) indicates that the intercept time is a function of upper layer thickness, velocity, and refractor velocity.

In a time term analysis, the intercept time is broken up into a source term, Si, plus a receiver term, Rj,

$$S_i + R_j = \frac{2Z\sqrt{V_1^2 - V_0^2}}{V_1 V_0} = a \qquad (3)$$

Then (2) becomes

$$T_{ij} = S_i + R_j + \frac{D_{ij}}{V_1} \qquad (4)$$

In the case of a layer over a horizontal refractor and constant lateral velocities

$$S_i = R_j = \frac{a}{2}$$

For the case of lateral variations in layer thickness and velocities, the station time terms will reflect these variations. For example, if a station consistently shows delayed arrivals relative to all others, this station time term will have a larger positive value than the other stations. If the station terms are well-constrained, the source time terms will absorb errors in source location and origin time. To see this, consider two events at the same location where one event has an error in origin time. The calculated velocity and the distribution of the station arrival times about the mean velocity should be equal (assuming no other errors). Then the only parameter left to absorb the error in the origin time is the source term. As will be discussed below, the source and receiver time terms are non-unique because their sum can only be determined to within a constant and there are infinitely many solutions to equation (4).

The time term method is based on the fact that the travel time between a source and receiver can be represented by sum of three terms, a source and receiver time term, and a term consisting of the distance divided by the refractor velocity (Scheiddegger and Willmore, 1957; Willmore and Bancroft, 1960)

$$T_{ij} = S_i + R_j + \frac{D_{ij}}{V} \qquad (4)$$

where

T_{ij} - travel time from source i to receiver j

S_i - source time term (delay time)

R_j - receiver time term

D_{ij} - distance between source and receiver

V - mean refractor velocity

As illustrated in Figure 3.8, the travel time from S to R can be written by the sum of three terms

$$T = \frac{HS\cos\theta}{V_0} + \frac{HR\cos\theta}{V_0} + \frac{D\cos\phi}{V_1} \qquad (5)$$

The symbols are defined in Figure 3.8, ϕ is the apparent dip of the refractor. If the dip of the refractor is small (5) reduces to

$$T = \frac{HS\cos\theta}{V_0} + \frac{HR\cos\theta}{V_0} + \frac{D}{V_1}$$

or

$$T = S + R + \frac{D}{V_1}$$

The source and receiver time terms represent the time it takes for the critically refracted wavefront to travel vertically through the upper layer. For a horizontal refractor, the vertical apparent velocity is

$$\frac{HR}{t_0} = \frac{HS}{t_0} = \frac{V_0}{\cos\theta}$$

For n separate events recorded at m stations (assuming every station records the head waves), there will be n x m equations in n + m + 1 unknowns; the source and station time

terms and the average refractor velocity. However, because the signals from an event are recorded at every station only rarely, the number of equations is reduced somewhat.

The resulting system of equations (4) is written in the matrix form

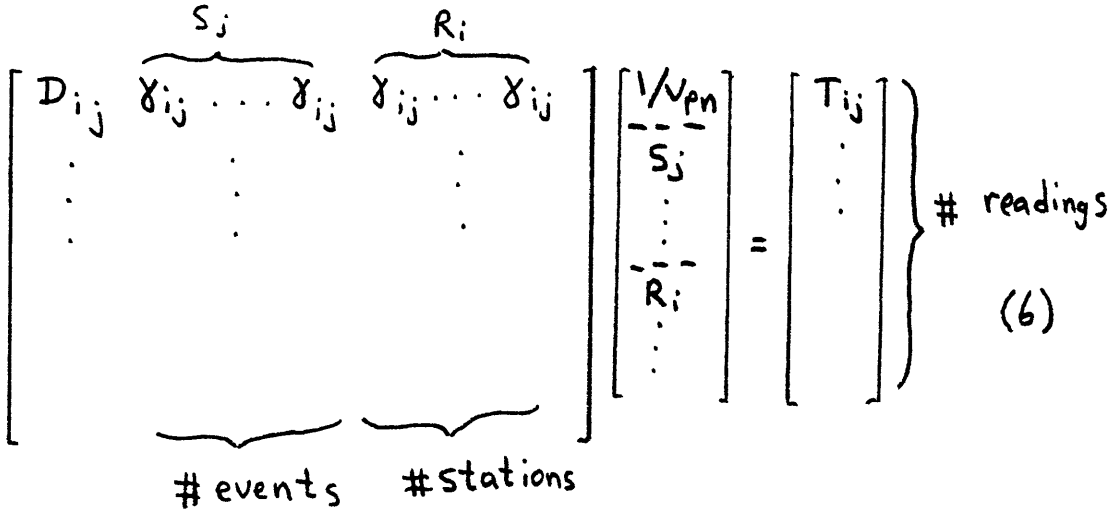

where $\gamma_{ij} = 1$ if event i is recorded at station j, otherwise $\gamma_{ij} = 0$. In matrix shorthand

$$A\underline{x} = \underline{b} \qquad (7)$$

In order to solve the system of equations (7), we decompose A into its eigenvalues and eigenvectors using a singular value decomposition (see Appendix A).

$$A = U\Lambda V^T \qquad (8)$$

Using the generalized inverse of Lancsoz (1961), the solution to (7) is given by

$$\underline{x} = V\Lambda^{-1}U^T\underline{b} \qquad (9)$$

However, because of the non-uniqueness of the source and receiver terms, the rank of A is one less than the total number of parameters resulting in one zero eigenvalue. To remove this indeterminacy, the one zero eigenvalue is truncated (Wiggins, 1972).

As discussed in Appendix A, the covariance matrix is given by (for uncorrelated errors in the data, σ_d^2)

$$COV = \sigma_d^2 V \Lambda^{-2} V^T \qquad (10)$$

and the model resolution matrix by

$$R = V V^T \qquad (11)$$

Initial runs demonstrated that the Pn velocity was perfectly resolved (i.e. R11 = 1) and that all the diagonal elements of R corresponding to the source and station terms were equal to

$$R_{ii} = 1 - \frac{1}{NT} \qquad (12)$$

where NT is the number of source and station time terms. This is a problem similar to that encountered by Aki et al. (1977) and results from the fact that the rank of A is one less than the number of parameters (number of source and time terms + 1). As discussed in Appendix A, the trace of the resolution matrix equals the rank of A and therefore the diagonal elements of the best possible resolution matrix are given by equation (12). If more than one eigenvalue was truncated, the resolution would be degraded and the values

of the Rii terms would be correspondingly less than those of equation (12).

APPENDIX D

COMPUTATION OF FREQUENCY-WAVENUMBER POWER SPECTRA

The data used in this study consist of a number of temporal signals distributed across a seismic network and is thus suitable for analysis using space-time signal processing techniques. Beamforming is the spatial analog of temporal filtering because it is possible to identify and separate out signals within a given band of wavenumbers. Each seismometer in the array acts as a temporal narrowband filter with a prescribed frequency response. Similarly, if the signal propagating across a region is sampled at given locations, the array can be used as a spatial narrowband filter with a spatial frequency response referred to as the beampattern or array response. Because of the relation between spatial and temporal frequency, $f=ck$, beamforming allows for the direct computation of phase velocity, c, group velocity, $u=df/dk$, and the direction of propagation.

Because the array elements lie along a narrow range of azimuths, we make a plane-wave approximation and assume that the stations form a linear, non-uniformly spaced array oriented radially from the source. In this way the only distance parameter for each station is a normalized distance relative to the array origin and the event.

Computation of the frequency-wavenumber power spectrum first involves the calculation of the two-dimensional

Fourier transform

$$S(f,k) = \int_{-\infty}^{\infty} \int_{-\infty}^{\infty} s(t,\Delta)\, e^{2\pi i(ft - k\Delta)}\, dt\, d\Delta \qquad (1)$$

where $s(t,\Delta)$ is the output of a single seismometer at position Δ, time t.

Opposite signs are used for the two Fourier transforms so that the waves travel in the positive Δ direction. The f-k spectrum is calculated in two steps. First, the temporal Fourier transform is computed for the signal recorded at each station

$$S(f,\Delta_j) = \sum_{n=1}^{T} s(t_n,\Delta_j)\, e^{2\pi i(m-1)(n-1)/T} \qquad (2)$$

where

f = (m-1) / TΔt , mth frequency component

t - sampling inverval

T - number of time samples

Δ_j - postition of station j

or

$$S(f,\Delta_j) = A(f,\Delta_j)\, e^{2\pi i \phi(f,\Delta_j)} \qquad (3)$$

where A and ϕ are the amplitude and phase spectrum for frequency component f.

A phase shift is then applied in the frequency domain corresponding to the distance between two stations, Δx, and a frequency-dependent phase velocity, c(f). Incrementing the wavenumber k through a given range of values,

$$k\Delta x = \frac{f}{c(f)}\Delta x \qquad (4)$$

and given that

$$c(f) = \frac{\Delta x f}{\Delta \phi} \qquad (5)$$

yields the phase shift

$$\Delta \phi = k \Delta x \qquad (6)$$

Therefore, all frequency components of all stations are phase shifted by $\Delta\phi$ corresponding to a given wavenumber (or phase velocity) and summed. This is equivalent to a delay and sum stacking technique commonly used in the time domain (Lacoss et al., 1969) and is referred to as phase stacking by Nolet and Panza, (1976).

As will be discussed below, phase stacking shifts the main lobe of the array response over any desired position in the wavenumber plane which allows for the detection of signals with a range of phase velocities and azimuths of approach. Thus, the f-k spectrum is given by

$$F(f,k) = \sum_{j=1}^{N} A(f,\Delta_j)\, e^{2\pi i (\phi(f,\Delta_j) - k\Delta_j)} \qquad (7)$$

and the f-k power spectrum in decibels is

$$P(f,k) = 20 \log |F| \qquad (8)$$

Once the power spectrum was computed, an interpolation scheme was used to select the wavenumber corresponding to the maximum power. In order to facilitate calculation of group velocities, a polynomial was fit to the f-k points of maximum power using the wavenumber as the dependent

variable. The phase velocity was calculated from

$$C = \frac{f}{k}$$

and the group velocity from

$$U = \frac{df}{dk}$$

As will be discussed in a later section, initial calculations indicated a frequency range with abnormally high phase velocities indicating the presense of laterally refracted or multipathed arrivals coming in off-azimuth. To confirm this, it was necessary to steer the array to select beams in order to identify the azimuth of approach of given frequencies. To do this, the relative distances between stations were recalculated along a given beam direction and the f-k power spectrum was computed for a set frequency as a function of azimuth using equations 7 and 8. Because the azimuth to the source was known, the spectrum was only computed for a range of azimuths of approximately 30 degrees.

If the number of stations is small, the array response will be characterized by a main lobe flanked by sidelobes (Figure 4.10). These allow for the leakage of energy into the phase stack with undesired wavenumbers, and can make it difficult to separate out overlapping modes of similar wavenumber. Also, if the recorded signal is contaminated by multipathed arrivals, the f-k spectrum along a specified beam may yield unreasonable phase velocities. One way to

eliminate these effects is to move a group velocity window function, $D_j(t,u)$, across the array where u is the group velocity (Nolet and Panza, 1976). The signals are windowed along a specified beam direction in the time domain and are given by

$$s(t_n, \Delta_j)\, D_j(t_n, u)$$

The amplitude and phase spectrum for each station is calculated and the phase shift applied before stacking is

$$\Delta\phi = \left(k - \frac{f}{u}\right)$$

Thus, the frequency wavenumber spectrum for the group velocity windowed signals is

$$F(f,k) = \sum_{j=1}^{N} A(f, \Delta_j, u)\, e^{2\pi i\left(\phi(f,\Delta_j,u) - \left(k - \frac{f}{u}\right)\Delta_j\right)} \qquad (9)$$

where the amplitude and phase spectrum are now functions of u.

Sources of errors include those caused by general data processing errors such as digitizing errors, approximations made in setting up the problem, and inadequacies in the array response. Because measurement of the f-k power spectra is essentially a delay and sum stacking technique, any influence of uncorrelated errors will decrease proportionally by $1/\sqrt{N}$, where N is the number of sensors.

The plane wave approximation used in calculating the f-k power spectrum assumes a laterally homogeneous earth and neglects local structure beneath each station. Beamsteering

allows some control on these effects by computing the arrival of energy off azimuth. The plane wave approximation also assumes that the stations lie on a narrow azimuth range and the variation of the source phase is nearly constant for all stations. This is a valid approximation assuming the stations do not lie near a nodal plane in the radiation pattern of the Rayleigh waves where the source phase can vary rapidly. Although a fault plane solution has not yet been compiled for the either earthquake, the high surface wave amplitudes suggest that New England lies along an lobe of the radiation pattern.

A significant cause of errors is probably introduced by inadequacies in the array response for the six stations used to measure the f-k power spectra. Most other short period stations in New England have an analog high-pass filter at each station site to cut down of noise caused by microseisms, and were therefore unable to detect the long-period surface waves.

To define the array response we refer to the above discussion where it was seen that beamforming is a shift and sum stacking technique. If we add the outputs, $s(t,\Delta_j)$, of the seismometers together, the stack, y(t), is given by

$$y(t) = \sum_{j=1}^{N} s(t,\Delta_j) \qquad (10)$$

where N is the number of stations. Assume that a plane wave of constant temporal and spatial frequency f0, k0 respectively, propagates across the array

$$s(t,\Delta_j) = e^{2\pi i(f_0 t - k_0 \Delta_j)} \qquad (11)$$

In electronics, a common technique to find the transfer function of a network is to input a complex exponential source and divide the output by the input (see Senturia and Wedlock, 1975). Therefore, we drive the system with the complex exponential, $e^{2\pi i f_0 t}$, and divide the output by the input giving,

$$W(k) = \sum_{j=1}^{N} e^{-2\pi i K_0 \Delta_j} \qquad (12)$$

The normalized array or spatial frequency response is then defined to be $|w(k)|^2$. The array response for the six M.I.T. stations along the beam direction of the Costa Rica the event is illustrated in Figure D.1.

Detailed analysis of the array response is important in determining the wavenumber resolution of the array and the effects that sidelobes will have on the "leakage" of unwanted energy into the system. The wavenumber resolution is determined by the width of the main lobe. Because the array response shown in Figure D.1 is for a broadside array using unshifted summation, the mainlobe is located at k = 0 which implies the array will selectively pass waves having infinite apparent wavelengths and phase velocities. As discussed in the previous section, we are using a delay and sum stacking method which has the effect of placing the main lobe over selected wavenumbers, k_s. In this case (12) becomes

$$W(k) = \sum_{j=1}^{N} e^{-2\pi i (K_0 - K_s) \Delta_j} \qquad (13)$$

The array will be selective to plane waves with phase velocities of c_s and horizontal apparent wavelengths λ_s given by

$$k_s = \frac{f}{c_s(f)} = \frac{1}{\lambda_s}$$

The width of the main lobe determines the wavenumber resolution and is mainly controlled by the length or diameter of the array. This is directly analogous to the Uncertainty Principle and analysis in the time domain which states that the length of a time series is inversely proportional to the range of resolvable frequency components (Claerbout, 1976). Similarly, the diameter of the array, Δd, is inversely proportional to the range of resolvabe wavenumbers, Δk,

$$\Delta k = \frac{2\pi}{\Delta d}$$

As can be seen from Figure D.1, the array response is characterized by sidelobes which permit the "leakage" of waves with unwanted wavenumbers into the stack. The amplitude and position of these sidelobes are governed largely by the number and position of the stations respectively. An extreme case of leakage of other spatial frequencies into the stack is illustrated in Figure D.2. Pictured is an evenly spaced, linear array recording the arrival of two plane waves with equal temporal frequencies and differing spatial frequencies. In both cases an undelayed summation of each wave will result in the same

stack. However, the delay and sum technique or steering the array will allow discrimmination of the two wavetrains. The sidelobes are caused by the finiteness of the array and again are analogous to convolving the Fourier transform of a time series with a sinc function (the Fourier transform of a rectangular truncation function). One way to minimize this effect is to taper in space before transforming to the wavenumber domain which decreases the amplitude of the sidelobes of the truncation function. As discussed by Arnold (1978), various spatial shading (or tapering) functions such as a Chebyshev or cosine taper may be used to decrease the amplitude of the sidelobes. Because only six stations were used in this study, it was difficult to select a useful shading function because the contribution of the two outermost sensors would be minimized and resolution would be degraded.

Another undesirable effect that can occur in both time and space is that of inadequate sampling or aliasing. For an evenly spaced array with station separation Δx, the array response is a periodic function of the wavenumber with a period of $1/\Delta x$. Aliasing (or folding) occurs for spatial frequencies above the Nyquist frequency

$$k_N = \frac{1}{2\Delta x}$$

The problem of aliasing is reduced somewhat by sampling at irregularly spaced points. The network used in this study have an approximate station spacing of 25 km so the highest

resolvable spatial frequency is .02 km. These correspond to arrivals with wavelengths of approximately 50 km and frequencies of obout .067 hz (T = 15 seconds) assuming a phase velocity of 3.4 km/sec.

As discussed by Clay and Hinich (1970), standard errors in the phase velocity measurements for a plane wave propagation along the line of the array are given by

$$\frac{\Delta c}{c} = \frac{1}{\sqrt{N}} \frac{|N(f)|}{|S(f)|} \frac{\lambda}{D} \qquad (14)$$

where

N - number of stations

λ -wavelength for frequency f

D - array diameter

$|S(f)|/|N(f)|$ - signal to noise ratio.

Thus, the errors in the dispersion measurements depend on the signal to noise ratio, the square root of the number of seismometers, and the number of wavelengths traversing the array. A large array aperature increases the precision of the measurements (by reducing the width of the main lobe) at the expense of spatial resolution.

FIGURE CAPTIONS

Figure D.1 Normalized array response for six MIT stations shown in Figure 4.10 as a function of wavenumber along beam direction of 204 degrees from north.

Figure D.2 Schematic illustration of energy leakage into a broadside array stack. Two plane waves of differing wavenumber produce identical array response resulting in a main lobe and a sidelobe of equal amplitudes in a figure such as that in Figure D.1.

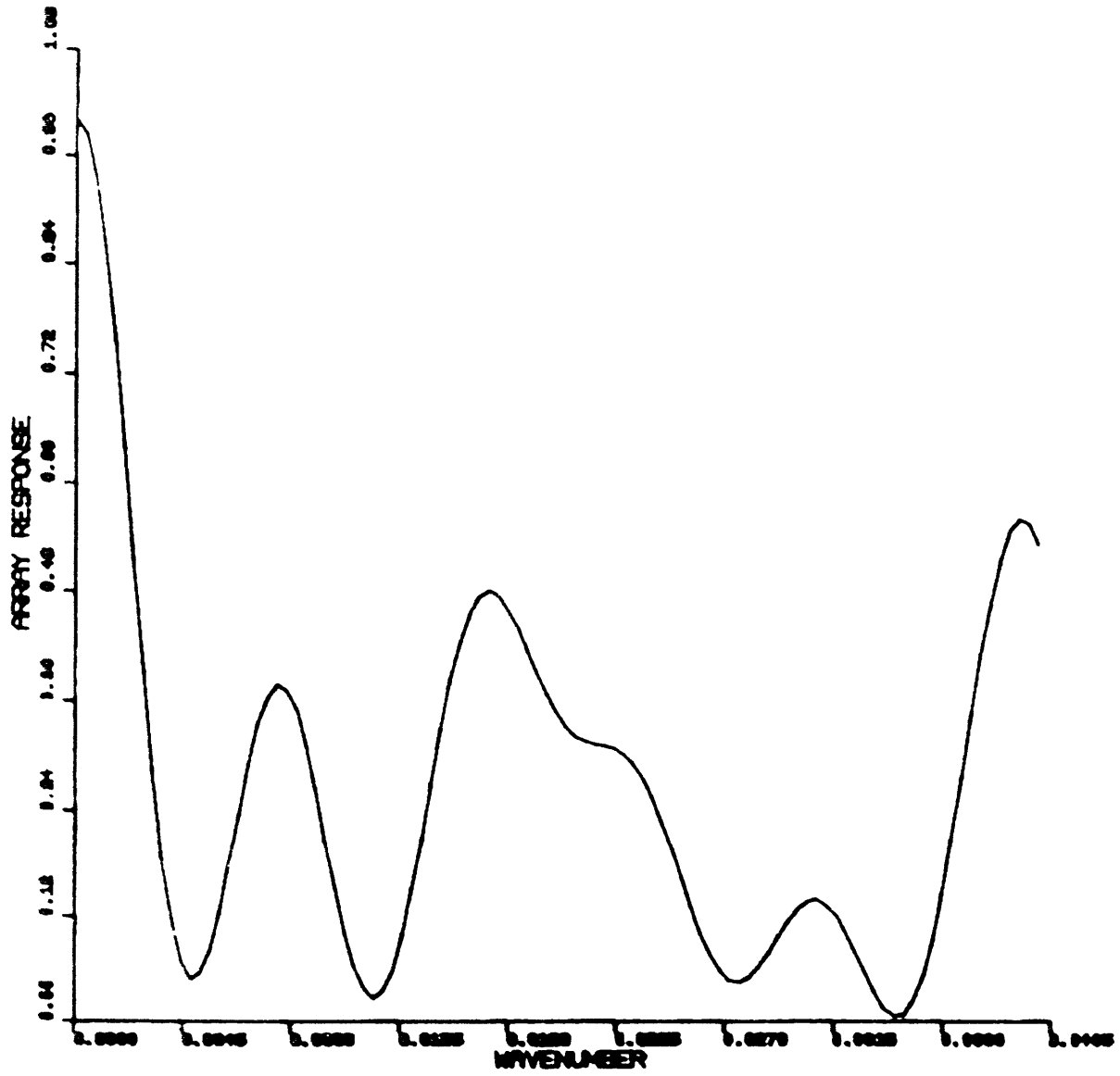

Figure D.1

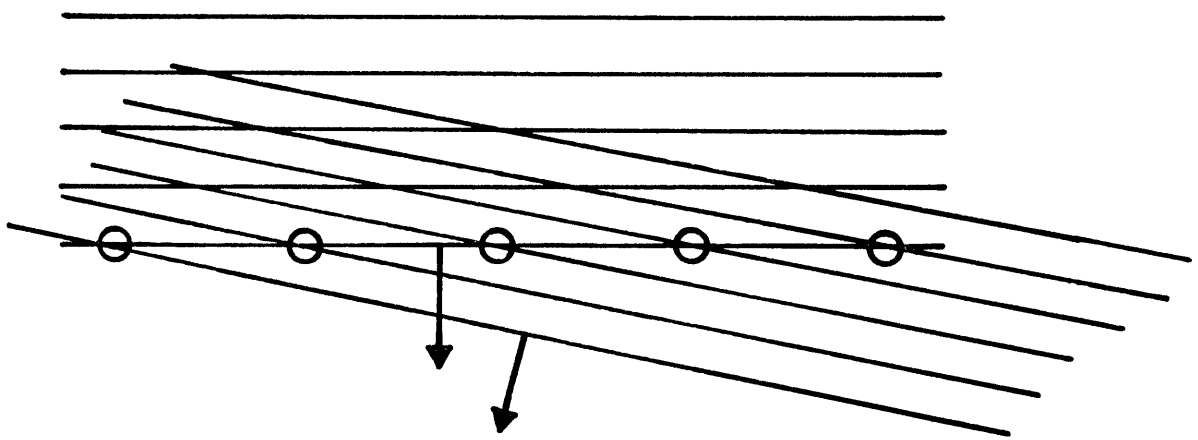

Figure D.2

APPENDIX E

CALCULATION OF PHASE AND GROUP VELOCITY PARTIAL DERIVATIVES

Because there are fewer boundary conditions to be met, it is generally more convenient to demonstrate the calculation of phase and group velocities and their partial derivatives using Love waves. Consider a plane wave of angular frequency ω, propagating in the x-direction, with the displacement parallel to the y-axis as a function of z, v(z);

$$f(k,z,\omega)=v(z)\exp(i(wt-kx))$$

The kinetic and potential energies averaged over a cycle are (Aki and Richards, 1980; Takeuchi et al., 1964)

$$T=\frac{1}{4}\int_0^\infty \rho(z)\,\omega^2\,v^2(z)\,dz \qquad V=\frac{1}{4}\int_0^\infty \mu(z)\left[k^2 v^2(z)+\left(\frac{dv}{dz}\right)^2\right]dz$$

where ρ is the density and μ is the rigidity. The 1/4 comes from averaging of cosine and sine squared terms over a cycle. Because the kinetic and potential energies averaged over a cycle are equal

$$\omega^2 I_0 = k^2 I_1 + I_2 \qquad (1)$$

where

$$I_0 = \int_0^\infty \rho v^2\,dz$$
$$I_1 = \int_0^\infty \mu v^2\,dz \qquad (2)$$
$$I_2 = \int_0^\infty \mu\left[\frac{dv}{dz}\right]^2 dz$$

Using the variational principle under the condition of no body forces or surface tractions, it can be shown that the energy equation 1 is unchanged for a perturbation of v(z) about the actual motion. As an extension of this fact, it can be shown that there exists a linear relationship between fractional changes in phase velocity with respect to small changes in elastic parameters and that for a fixed k equation 1 becomes to the first order

$$\omega^2 \delta I_2 + 2 I_0 \omega \delta\omega = \delta I_1 k^2 + \delta I_2 \qquad (3)$$

Thus, once a root of the period equation for a particular ω has been found as a function of wavenumber k

$$F(c,k) = 0 \qquad (4)$$

the phase velocity partial derivatives with respect to various layer parameters can be found immediately from equation 3. The group velocity $U = \frac{d\omega}{dk}$ can also be expressed in terms of the energy integrals (2). By differentiating equation 1 with respect to k it can be shown that

$$U = \frac{I_1}{c I_0} \qquad (5)$$

The variational principle is used in the computation of phase velocity partial derivatives in a program written by D.G. Harkrider.

A program was written to calculate the group velocity partial derivatives using numerical differention following an approach used by Rodi et al., (1975). By differentiating the group velocity U with respect to the phase velocity C and $\frac{\partial c}{\partial \omega}$ in the relationship

$$U = \frac{c}{1 - \frac{\omega}{c} \frac{\partial c}{\partial \omega}\Big|_m} \qquad (6)$$

where m represents the layer parameters, it can be shown that

$$\left.\frac{\partial u}{\partial m}\right|_f = \frac{u}{c}\left(2 - \frac{u}{c}\right)\left.\frac{\partial c}{\partial m}\right|_f + f\frac{u^2}{c^2}\left.\frac{\partial}{\partial f}\left(\left.\frac{\partial c}{\partial m}\right|_f\right)\right|_m \qquad (7)$$

Defining

$f_{+1} = f_0 + \Delta f$, $f_{-1} = f_0 - \Delta f$, $c_{+1} = c(f_{+1})$, etc.

$c_0 = \frac{1}{2}(c_{+1} + c_{-1})$, $u_0 = \frac{1}{2}(u_{+1} + u_{-1})$, and $\left.\frac{\partial c_0}{\partial m}\right|_f = \frac{1}{2}\left(\left.\frac{\partial c_{+1}}{\partial m}\right|_f + \left.\frac{\partial c_{-1}}{\partial m}\right|_f\right)$

where f0 is the frequency at which the period equation 3 is being evaluated, then

$$\left.\frac{\partial u_0}{\partial m}\right|_f = \frac{u_0}{c_0}\left(2 - \frac{u_0}{c_0}\right)\left.\frac{\partial c_0}{\partial m}\right|_f + \frac{u_0^2}{c_0^2}\frac{1}{2\Delta f}\left(\left.\frac{\partial c_{+1}}{\partial m}\right|_f - \left.\frac{\partial c_{-1}}{\partial m}\right|_f\right) \qquad (8)$$

APPENDIX F

MAXIMUM-LIKELIHOOD INVERSION OF PHASE AND GROUP VELOCITY

In Appendix A, it was assumed that the errors in the data are uncorrelated and have the same variance. As discussed in Chapter 4, the errors in the phase and group velocity vary as a function of period and, in general, the variances for the group velocity curve are greater than those for phase velocity. In addition, the partial derivatives for phase and group velocity are a function of layer thickness. Thus, it is necessary to weigh the solution in both model and data spaces.

As described in Appendix A a linearized system of equations is set up for the simultaneous inversion of phase and group velocities. For reasons discussed in Chapter 4, only the shear velocity is adjusted while the compressional velocity and density are held fixed.

$$\Delta c_i = \sum_{j=1}^{n} \frac{\partial c_i}{\partial \beta_j} \Delta \beta_j \qquad i = 1, \cdots, m \quad \text{- period index}$$

$$\Delta u_i = \sum_{j=1}^{n} \frac{\partial u_i}{\partial \beta_j} \Delta \beta_j \qquad j = 1, \cdots, n \quad \text{- layer index} \qquad (1)$$

where $\Delta c_i = c_i^{obs} - c_i^{th}$ and $\Delta u_i = u_i^{obs} - u_i^{th}$

and β_j - shear velocity in layer j

$\Delta \beta_j$ - adjustment to shear velocity in layer j

In matrix form,

$$\begin{bmatrix} \Delta C_1 \\ \Delta U_1 \\ \Delta C_2 \\ \Delta U_2 \\ \vdots \\ \Delta C_m \\ \Delta U_m \end{bmatrix}_{2m\times 1} = \begin{bmatrix} \frac{\partial C_1}{\partial \beta_1} & \frac{\partial C_1}{\partial \beta_2} & \cdots & \frac{\partial C_1}{\partial \beta_n} \\ \frac{\partial U_1}{\partial \beta_1} & \frac{\partial U_1}{\partial \beta_2} & \cdots & \frac{\partial U_1}{\partial \beta_n} \\ \vdots & & & \\ \frac{\partial C_m}{\partial \beta_1} & & \cdots & \frac{\partial C_m}{\partial \beta_n} \\ \frac{\partial U_m}{\partial \beta_1} & & \cdots & \frac{\partial U_m}{\partial \beta_n} \end{bmatrix}_{2m\times n} \begin{bmatrix} \Delta\beta_1 \\ \Delta\beta_2 \\ \vdots \\ \Delta\beta_n \end{bmatrix}_{n\times 1}$$

or

$$\underset{\sim}{b} = A\underset{\sim}{x} \qquad (2)$$

Let R_{nn} and W be the data covariance and model weighting matrices, respectively,

$$R_{nn} = \begin{bmatrix} \sigma_1^2 & & & 0 \\ & \sigma_2^2 & & \\ & & \ddots & \\ 0 & & & \sigma_{2m}^2 \end{bmatrix} \qquad W = \begin{bmatrix} 1/\Delta h_1 & & & 0 \\ & 1/\Delta h_2 & & \\ & & \ddots & \\ 0 & & & 1/\Delta h_n \end{bmatrix} \qquad (3)$$

where σ_i^2 the variance of the ith data point, and Δh_i is the thickness of the ith layer. Because R_{nn} and W are non-singular symmetric matrices they can be decomposed into a product of orthogonal eigen-vector matrices (Lancsoz, 1961).

$$R_{nn} = N\Lambda_d N^T$$
$$W = M\Lambda_m M^T \qquad (4)$$

The generalized inverse operator minimizes both $|\underset{\sim}{b}-A\underset{\sim}{x}|^2$ and $|\underset{\sim}{x}|^2$ simultaneously. With the weighting in data space it is

desired to minimize

$$(\underline{b}-A\underline{x})^T R_{nn}^{-1} (\underline{b}-A\underline{x}) = |\underline{b}^*-A^*\underline{x}^*|^2 \quad (5)$$

such that the perturbations in the model are weighted according to the errors in the data. In model space, the weighting is inversely proportional to the thickness and length of the weighted solution vector is minimized according to

$$\underline{x}^T W^{-1} \underline{x} = |\underline{x}^*|^2 \quad (6)$$

The coordinate transformation that satisfies 5 and 6 is (Wiggins, 1972; Aki and Richards, 1980)

$$\underline{b}^* = \Lambda_d^{-1/2} N^T \underline{b} \qquad \text{note:} \quad \underline{b} = N \Lambda_d^{1/2} \underline{b}^*$$

$$\underline{x}^* = \Lambda_m^{-1/2} M^T \underline{x} \quad (7) \qquad \underline{x} = M \Lambda_m^{1/2} \underline{x}^* \quad (8)$$

$$A^* = \Lambda_d^{-1/2} N^T A M \Lambda_m^{1/2} \qquad A = N \Lambda_d^{1/2} A^* \Lambda_m^{-1/2} M^T$$

Then we solve

$$\underline{b}^* = A^* \underline{x}^* \quad (9)$$

using the stochastic inverse (see Appendix A)

$$\hat{\underline{x}}^* = A_g^{*-1} \underline{b}^* = (A^{*T} A^* + \theta^2 I)^{-1} A^{*T} \underline{b}^* \quad (10)$$

Transforming back to original coordinates using 7

$$A_g^{-1} = M \Lambda_m^{1/2} A_g^{*-1} \Lambda_d^{-1/2} N^T$$

and

$$\hat{\underline{x}} = A_g^{-1} \underline{b} = A_g^{-1} A \underline{x} = R \underline{x} \quad (11)$$

where R is the resolution matrix. The covariance matrix is given by

$$COV = A_g^{-1} R_{nn} (A_g^{-1})^T \qquad (12)$$

APPENDIX G

INTERSTATION TRANSFER FUNCTION USING WIENER DECONVOLUTION

Given two seismograms positioned along the same great circle path from a source, we want to estimate the interstation transfer function (also known as the medium impulse response or Green's function). The phase of the transfer function gives the phase delay of the system which will be used to calculate the interstation phase velocity. The shape of the transfer function in the time domain provides information on the dispersiveness of the system which will be used to estimate interstation group velocity.

Figures G.1a,b illustrate the problem in the time and frequency domain where the input signal at station 1 drives the system and produces the output recorded at station 2. The convolution is given by the frequency domain representation

$$F_1(\omega)\, e^{i\phi_1(\omega)}\; F_m(\omega)\, e^{i\phi_m(\omega)} = F_2(\omega)\, e^{i\phi_2(\omega)} \qquad (1)$$

where the subscripts 1,2 and m refer to station 1, station 2, and the interstation medium, respectively. We wish to deconvolve the output by dividing (1) by the input and computing the transfer function

$$F_m(\omega)\, e^{i\phi_m(\omega)} = \frac{F_2(\omega)}{F_1(\omega)}\, e^{i(\phi_2 - \phi_1)} \qquad (2)$$

This simple deconvolution can be very unstable, particularly in the presense of spectral holes for which frequencies the filter parameters (transfer function) will be indeterminant. Various deconvolution schemes can be used to find the filter coefficients and we have chosen a least squares or Wiener deconvolution (Wiener, 1949; Treitel and Robinson, 1966; Peacock and Treitel, 1969).

Let the vector $\underline{b}$ represent the input (signal at station 1) to the system $\underline{f}$, and $\underline{d}$ be the output (signal at station 2) where

$$\underline{b} = (b_0, b_1, \cdots, b_n)$$

$$\underline{d} = (d_0, d_1, \cdots, d_{n+m})$$

$$\underline{f} = (f_0, f_1, \cdots, f_m)$$

We wish to construct a filter, $\underline{f}$, that will best estimate the desired output, $\underline{d}$, when driven by an input $\underline{b}$. Letting the n+m length vector c represent the actual output, we design $\underline{f}$ such that the difference between the actual and desired output

$$e_t = d_t - c_t$$

is minimized in a least squares sense (Figure G.1.c). This requires that the length E, of the error series, $\underline{e}$, is minimized

$$E = \underline{e}^T \underline{e} = \sum_\tau e_\tau^2 = \sum_\tau (d_\tau - c_\tau)^2 \qquad (3)$$

and we design $\underline{f}$ such that

$$\underline{b} * \underline{f} = \underline{c} \qquad (4)$$

or

$$c_\tau = \sum_{t=0}^{n+m+1} f_\tau \, b_{\tau - t}$$

where * denotes convolution. Using matrix notation, the convolution is given by

$$\begin{bmatrix} b_0 & 0 & 0 & \cdots & 0 \\ b_1 & b_0 & 0 & \cdots & 0 \\ b_2 & b_1 & b_0 & & \vdots \\ \vdots & & & & \\ b_n & b_{n-1} & \cdots & & b_0 \\ 0 & b_n & \cdots & & \vdots \\ \vdots & \vdots & & & b_n \\ 0 & 0 & & & \end{bmatrix}_{(m+n+1)\times(m+1)} \begin{bmatrix} f_0 \\ f_1 \\ \vdots \\ f_m \end{bmatrix}_{(m+1)\times 1} = \begin{bmatrix} c_0 \\ c_1 \\ \vdots \\ c_{m+n} \end{bmatrix}_{(m+n+1)\times 1} \qquad (5)$$

Introduce the desired output $\underline{d}$, which is the signal at station 2, and solve for $\underline{f}$ such that the length squared of the difference vector $d_t - c_t$ is minimized

$$\begin{bmatrix} b_0 & 0 & \cdots & 0 \\ b_1 & b_0 & 0 & 0 \\ b_2 & b_1 & \cdots & \\ \vdots & & & \\ b_n & & & \\ \vdots & & & \\ 0 & \cdots & & b_n \end{bmatrix} \begin{bmatrix} f_0 \\ f_1 \\ \vdots \\ f_m \end{bmatrix} = \begin{bmatrix} d_0 \\ d_1 \\ \vdots \\ d_{m+n} \end{bmatrix} + \begin{bmatrix} e_0 \\ e_1 \\ \vdots \\ e_{m+n} \end{bmatrix}$$

In matrix shorthand

$$B\underline{f} = \underline{d} + \underline{e}$$

Solve for $\underline{f}$ using least squares

$$B^T B\underline{f} = B^T\underline{d}$$

It turns out that the terms B^TB give the autocorrelation of the input $\underline{b}$

$$a_\tau = \sum_{t=0}^{\hat{n}} b_t d_{t+\tau}$$

and $B^T\underline{d}$ is the cross-correlation vector of $\underline{b}$ and $\underline{d}$

$$cc_\tau = \sum_{t=0}^{\hat{n}} b_t d_{t+\tau}$$

Thus, the m-length Wiener filter results from the solution of the normal equations of the form

$$\begin{bmatrix} a_0 & a_1 & a_2 & \cdots & a_m \\ a_1 & a_0 & a_1 & \cdots & a_{m-1} \\ a_2 & a_1 & a_0 & \cdots & \\ \vdots & & & & \\ a_m & \cdots & & & a_0 \end{bmatrix} \begin{bmatrix} f_0 \\ f_1 \\ \vdots \\ f_m \end{bmatrix} = \begin{bmatrix} cc_0 \\ cc_1 \\ \vdots \\ cc_m \end{bmatrix} \qquad (6)$$

or from equation (1) we are solving

$$F_2^2 F_m e^{i\phi_m} = F_1 F_2 e^{i(\phi_2 - \phi_1)} \qquad (7)$$

The autocorrelation matrix in equation (6) is in a Toeplitz form with an interesting symmetry where all of the diagonals are the same and the main diagonal is the

autocorrelation of the input at zero lag. Because of its symmetry, the system (6) can be solved efficiently and with a minimum of computer storage using Levinson recursion (Wiener, 1949; Treitel and Robinson, 1966). Although the system (6) is always nonsingular (assuming $a_o \neq 0$) (Ford and Herne, 1966), numerical instabilities may occur for large m. For this case the problem can be formulated using a stochastic framework where the input signal, $\underline{b}$, is contaminated by noise, $\underline{n}$, and the actual input $\underline{x}$, is given by

$$\underline{x} = \underline{b} + \underline{n}$$

Assuming the noise is stationary, the system can be solved using the damped least squares technique discussed in Appendix A. To do this we add a small constant to the autocorrelation function at zero lag which stabilizes the solution.

As discussed in Chapter 4, Landisman et al., (1969) suggest that the interstation cross-correlogram gives an approximation of the impulse response of the interstation medium when a source is applied at the station nearest the earthquake. Comparison of equations (2) and (7) shows that the cross-correlogram gives the phase delay of the system but not the group delay. To test this, we assume that the impulse response of the interstation medium is a delta function where the output equals the input. Using the 12/9/72 seismic records recorded at WES shown in Figure 4.2b

we compute the cross-correlation of the input with the output (Figure G.2a, which is actually the autocorrelation of the input at station WES) and the interstation transfer function using the least squares deconvolution described above (Figure G.2b). Both signals shown in Figure G.2a,b are then windowed between lags of 0-400 seconds. Comparison of Figures G.2a and b shows that the transfer function approximates a delta function much better than the "cross-correlogram". The phase and amplitude spectrum of the windowed transfer function gives a better approximation to that of a delta function than the cross-correlogram. Also shown in Figures G.2 a and b is the envelope function fit to the narrow bandpassed signals for two frequencies. As can be seen from Figure G.2a, the time of maximum amplitude is at a lag of 10 seconds which can cause group velocity errors of about 8% over distances of 500 km. Between periods of 17 to 50 seconds, the lags of the maximum amplitude for the transfer function are all within two seconds or one digital point in this case where the sampling interval was 2 seconds. For periods below 17 seconds the error increased to 4 seconds (two digital points) which is the portion of the spectrum that was not flat.

Although Landisman et al., (1969) were correct in stating that the cross-correlogram gives an approximation of the impulse response of the interstation medium, test cases show that substantial errors of interstation group velocity determinations can occur for short station separations.

FIGURE CAPTIONS

Figure G.1 Schematic illustration showing the meaning of the interstation transfer function.

Figure G.2 Comparison of performance for cross-correlogram (a) versus interstation transfer function (b) for modeling the interstation medium response. Input equals output and medium response should be a delta function. (a) Cross-correlogram, spectrum, and narrow band-passed signal and envelope function; (b) Transfer function calculated using Wiener deconvolution, spectrum,and narrow band-passed signal and envelope function

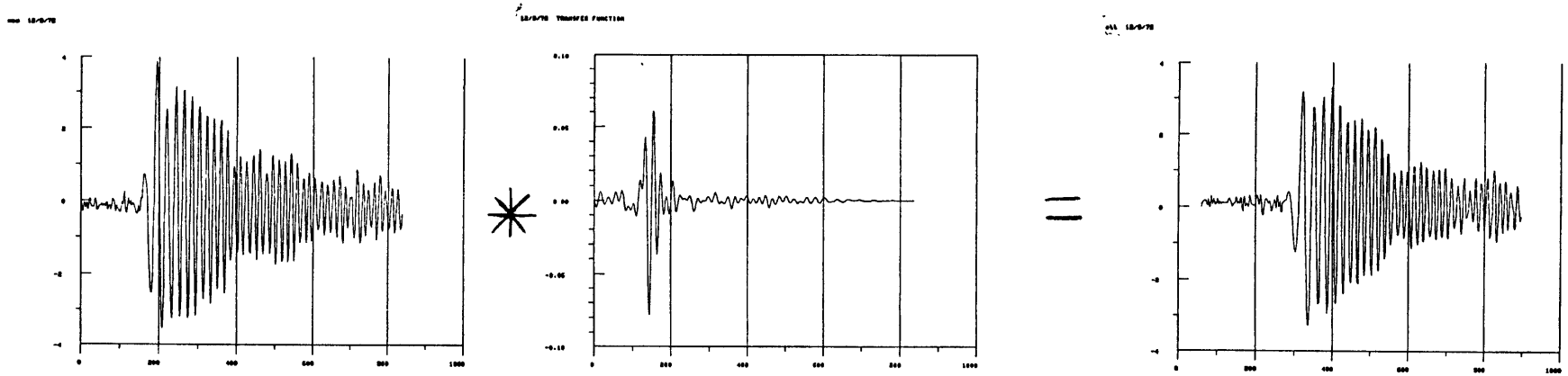

b f d

$F_1(\omega)\, e^{i\phi_1(\omega)}$ → $F_m(\omega)\, e^{i\phi_m(\omega)}$ → $F_2(\omega)\, e^{i\phi_2(\omega)}$

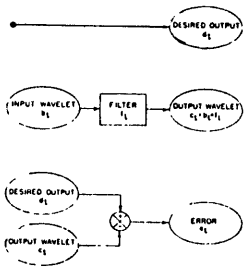

Figure G.1

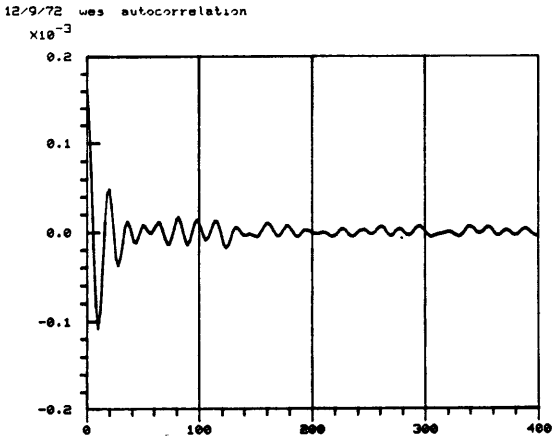
12/9/72 wes autocorrelation
X10-3
0.2
0.1
0.0
-0.1
-0.2
0
100
200
300
400

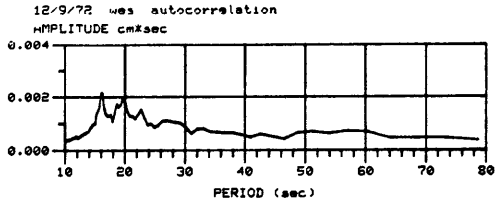
12/9/72 wes autocorrelation
AMPLITUDE cm*sec
0.004
0.002
0.000
10
20
30
40
50
60
70
80
PERIOD (sec)

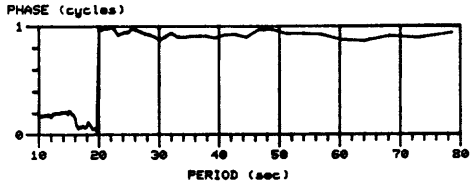
PHASE (cycles)
1
0
10
20
30
40
50
60
70
80
PERIOD (sec)

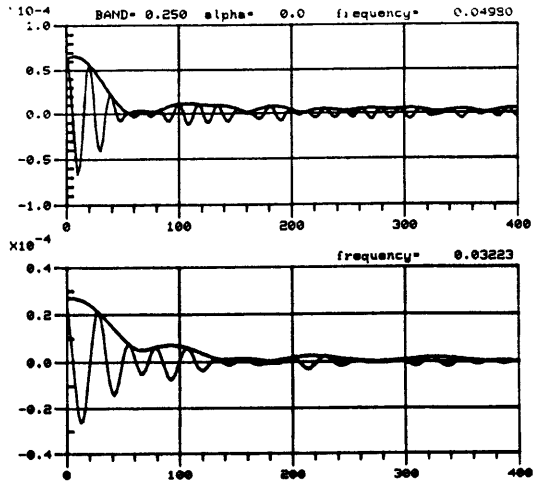
10-4
BAND= 0.250 alpha= 0.0 frequency= 0.04990
1.0
0.5
0.0
-0.5
-1.0
0
100
200
300
400
X10-4
frequency= 0.03223
0.4
0.2
0.0
-0.2
-0.4
0
100
200
300
400

Figure G.2a

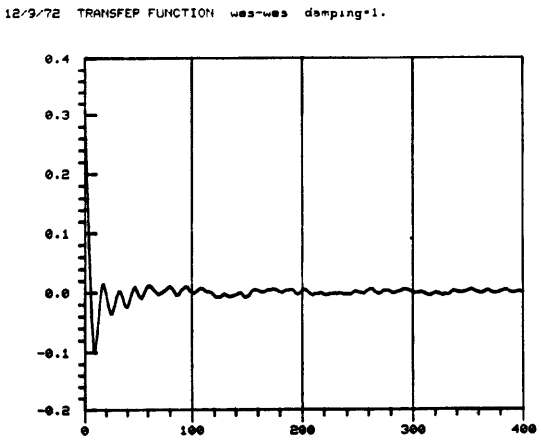
12/9/72 TRANSFER FUNCTION wes-wes damping=1.
0.4
0.3
0.2
0.1
0.0
-0.1
-0.2
0
100
200
300
400

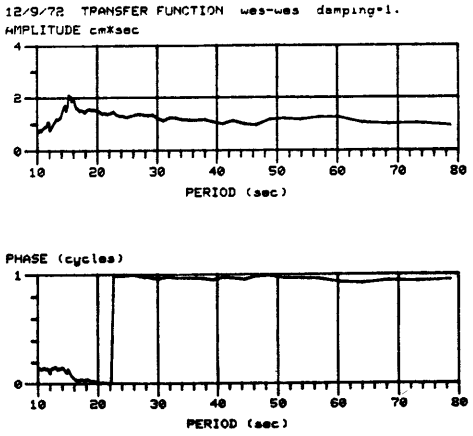
12/9/72 TRANSFER FUNCTION wes-wes damping=1.
AMPLITUDE cm*sec
4
2
0
10
20
30
40
50
60
70
80
PERIOD (sec)
PHASE (cycles)
1
0
10
20
30
40
50
60
70
80
PERIOD (sec)

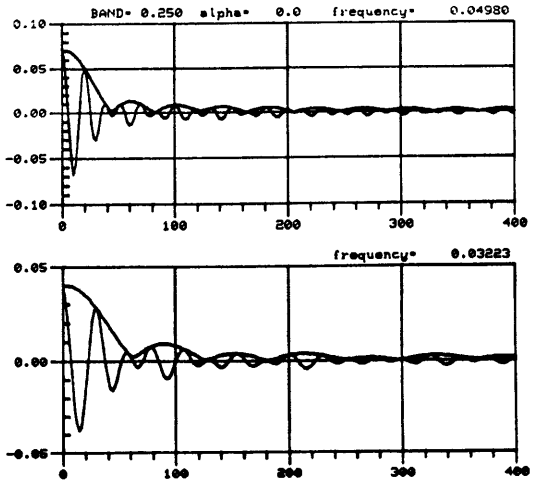
BAND= 0.250 alpha= 0.0 frequency= 0.04980
0.10
0.05
0.00
-0.05
-0.10
0
100
200
300
400
frequency= 0.03223
0.05
0.00
-0.05
0
100
200
300
400

Figure G.2b

BIOGRAPHICAL NOTE

The author was born in Rottenchester, New York on November 10, 1952. He fell in love with pizza at Ray's Pizza Place where he worked in 1968 and with Heather Goff at a party in 1969. High school earth science and experiences with Mobil Oil Co. as a Petroleum Distribution Engineer convinced him that geology for fun and profit was a suitable life endeavor.

Heather and he then set off for Athens 45701 and Ohio University where they both tooled for four years emerging with a B.S. in Geology, an AA in Science, a degree in horsemanship (from Meredith Manor) and a marriage license betwixt them.

Without knowing the difference between phase and group velocity (a concept that continues to elude him), the author naively decided to study geophysics at M.I.T. There he learned the fine arts of hand waving, computer hacking, organizing boondoggles, eating 16 inch pizzas with 1/2 of a steak and mushroom sub w/ mayo and a quart of coke, putting the puck on Arthur's stick, and telling people that they stink.

Fortunately, the author managed to finish his thesis before COCORP ran a line across New England and he prays nightly that drilling technology never enables mankind to penetrate the crust.

The author is presently living with Heather and at least

two crazy parrots in sunny California and is working at Lawrence Livermore Labs in Livermore, California.

Publications along the way include:

Taylor, S.R. and M.N. Toksoz, Three-Dimensional crust and upper mantle structure of the northeastern United States, J. Geophys. Res.,84, 7627-7644, 1979.

Taylor, S.R., M.N. Toksoz, and M.P. Chaplin, Crustal structure of the northeastern United States: Contrasts between the Grenville and Appalachian Provinces, Science,208,595-597,1980.

Chaplin, M.P., S.R. Taylor, and M.N. Toksoz, A coda-length magnitude scale for New England, Earthquake Notes (in press), 1980.